

# JOINT INSTITUTE FOR NUCLEAR RESEARCH

1

2



October 28, 2020

3

## **Conceptual design of the Spin Physics Detector**

4

Version 2020.016

# 5 Contents

6	<b>1</b>	<b>Executive summary [A. Guskov]</b>	<b>6</b>
7	<b>2</b>	<b>Polarized and unpolarized partonic structure of proton and deuteron</b>	<b>7</b>
8	1	Gluons in proton and deuteron [A. Guskov, O. Teryaev] . . . . .	7
9	1.1	Gluon probes at NICA SPD . . . . .	8
10	1.2	Gluons at large $x$ . . . . .	12
11	1.3	Tests of TMD factorization with gluon probes . . . . .	14
12	1.4	Linearly polarized gluons in unpolarized nucleon . . . . .	15
13	1.5	Hadron structure and heavy charmonia production mechanisms . . . . .	16
14	1.6	Non-nucleonic degrees of freedom in deuteron . . . . .	17
15	1.7	Gluon polarization $\Delta g$ with longitudinally polarized beams . . . . .	18
16	1.8	Gluon-related TMD and twist-3 effects with transversely polarized beams . . . . .	21
17	1.9	Gluon transversity in deuteron . . . . .	24
18	1.10	Deuteron tensor polarization and shear forces . . . . .	25
19	2	Quarks in proton and deuteron . . . . .	27
20	2.1	SSA for pions and kaons . . . . .	27
21	2.2	Drell-Yan pair production . . . . .	27
22	2.3	Generalized parton distributions . . . . .	28
23	2.4	Polarized fragmentation functions . . . . .	29
24	3	Tests of QCD basics at low energies [U. Uzikov, A. Guskov] . . . . .	30
25	3.1	Elastic $pp$ and $dd$ scattering . . . . .	30
26	3.2	Multiquark correlations and systems . . . . .	30
27	3.3	Central nucleon-nucleon collisions [Komarov] . . . . .	30
28	3.4	Exclusive hard processes with deuteron [M. Strikman] . . . . .	31
29	3.5	Polarized $pd$ elastic scattering within the Glauber model and $pN$ spin amplitudes [Yu. Uzikov] . . . . .	32
30			

---

31	3.6	Single-spin physics [V. Abramov] . . . . .	33
32	3.7	Scaling onset in exclusive reactions with lightest nuclei and spin observables	
33		[Yu. Uzikov, V. Ladygin] . . . . .	34
34	3.8	Yield of antiprotons in hadronic collisions for astrophysical dark matter search .	35
35	<b>3</b>	<b>Polarized beams [A. Kovalenko]</b>	<b>36</b>
36	1	Available species and types of collisions . . . . .	36
37	2	Beam structure, intensity and luminosity . . . . .	36
38	3	Polarization control and monitoring . . . . .	37
39	3.1	Transportation of polarized ions in the complex . . . . .	37
40	3.2	Operation modes of the NICA collider at polarized ions . . . . .	38
41	3.3	Specifications to the polarized beams in the collider . . . . .	38
42	3.4	Spin flipping system . . . . .	38
43	3.5	On-line control of the polarization in the collider . . . . .	39
44	3.6	Polarization control in the collider NICA in ST regime . . . . .	40
45	3.7	Ion polarization control in ST regime by means of two snakes . . . . .	41
46	3.8	Stability of spin motion . . . . .	42
47	3.9	Polarized beams dynamics in NUCLOTRON . . . . .	42
48	3.10	Operation modes of the NICA collider at polarized beams . . . . .	43
49	3.11	Zero Degree Calorimeter [S. Shimansky] . . . . .	44
50	3.12	Conclusion and outlook . . . . .	44
51	<b>4</b>	<b>Detector layout</b>	<b>45</b>
52	1	General design [A. Guskov] . . . . .	45
53	2	Magnetic system [A. Kovalenko] . . . . .	47
54	3	Beam pipe [A. Guskov] . . . . .	49
55	4	Vertex detector [N. Zamyatin] . . . . .	50
56	4.1	General overview . . . . .	50
57	4.2	Double-sided silicon detectors . . . . .	50
58	4.3	Mechanical layout . . . . .	52
59	5	Tracking system [T. Enik] . . . . .	53
60	5.1	Detector layout . . . . .	54
61	5.2	Mechanics . . . . .	54
62	5.3	Electronics . . . . .	54

63	6	Electromagnetic calorimeter [O. Gavrischuk] <b>[OUT OF DATE]</b> . . . . .	54
64	6.1	Calorimeter design . . . . .	54
65	6.2	Front-end electronics . . . . .	56
66	7	Range (muon) system [G. Alexeev] . . . . .	57
67	7.1	General description . . . . .	57
68	7.2	System layout . . . . .	57
69	7.3	Mini drift tubes detector . . . . .	58
70	7.4	Front-end electronics . . . . .	61
71	7.5	Performance figures . . . . .	62
72	8	Time of flight system <b>[OUT OF DATE]</b> . . . . .	63
73	8.1	SPD-ToF system . . . . .	63
74	8.2	Warm mRPC for BM@N . . . . .	65
75	8.3	Chamber for SPD . . . . .	65
76	8.4	FEE of mRPC . . . . .	66
77	8.5	SPD time resolution requirements . . . . .	66
78	9	Beam-beam counter [V. Ladygin] . . . . .	67
79	9.1	Inner part of BBC: MPC . . . . .	67
80	9.2	Outer part of BBC: scintillation tiles . . . . .	69
81	<b>5</b>	<b>Local polarimetry [V. Ladygin]</b>	<b>72</b>
82	1	Asymmetry in inclusive production of charged particles . . . . .	72
83	2	Inclusive $\pi^0$ production . . . . .	72
84	3	Single transverse spin asymmetry for very forward neutron production . . . . .	74
85	<b>6</b>	<b>Detector control system [A. S. Chepurnov]</b>	<b>76</b>
86	1	DCS concept . . . . .	76
87	2	DCS architecture . . . . .	78
88	3	SCADA for DCS . . . . .	79
89	<b>7</b>	<b>Data acquisition system [L. Afanasyev]</b>	<b>82</b>
90	1	Introduction . . . . .	82
91	2	DAQ structure . . . . .	83
92	3	Data Format . . . . .	85
93	<b>8</b>	<b>Computing and offline software [A. Zhemchugov]</b>	<b>89</b>

94	1	SPD computing model . . . . .	89
95	2	Online filter . . . . .	90
96	3	Computing system . . . . .	90
97	3.1	The computing model . . . . .	91
98	3.2	Computing services . . . . .	91
99	4	Offline software . . . . .	93
100	5	Resource estimate . . . . .	93
101	<b>9</b>	<b>Beam test facility [A. Baldin] [OUT OF DATE]</b>	<b>95</b>
102	<b>10</b>	<b>Integration and services [OUT OF DATE]</b>	<b>100</b>
103	1	Hall facilities and services . . . . .	100
104	2	SPD integration . . . . .	101
105	3	Detector assembly . . . . .	101
106	4	Technical requirements . . . . .	102
107	<b>11</b>	<b>MC simulation and physics performance</b>	<b>104</b>
108	1	General performance of the SPD setup . . . . .	104
109	1.1	Rates and spectra for minimum bias events [A. Guskov] . . . . .	104
110	1.2	Tracking [A. Guskov] . . . . .	107
111	1.3	Vertex reconstruction [A. Guskov] . . . . .	107
112	1.4	Calorimetry [A. Guskov] . . . . .	107
113	1.5	Particle identification [A. Guskov] . . . . .	109
114	2	<b>Accuracies of asymmetries measurement</b> . . . . .	111
115	2.1	Charmonia production [I. Denisenko] . . . . .	111
116	2.2	Prompt photon production . . . . .	114
117	<b>12</b>	<b>Running strategy</b>	<b>117</b>
118	1	Accelerator [A. Kovalenko] . . . . .	117
119	2	Spin Physics Detector [A. Guskov] . . . . .	119
120	<b>13</b>	<b>Cost estimate</b>	<b>120</b>
121	<b>14</b>	<b>Participating institutions and author list [OUT OF DATE]</b>	<b>121</b>
122	<b>15</b>	<b>Project timeline</b>	<b>124</b>



124 **Chapter 1**

125 **Executive summary [A. Guskov]**

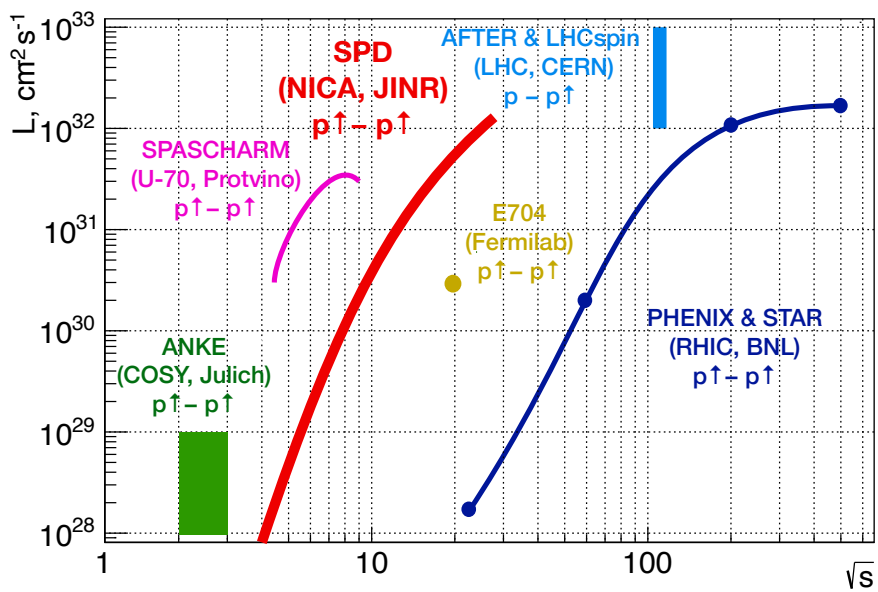


Figure 1.1

## Chapter 2

# Polarized and unpolarized partonic structure of proton and deuteron

### 1 Gluons in proton and deuteron [A. Guskov, O. Teryaev]

Gluons, together with quarks, are the fundamental constituents of the nucleon. They play a key role in generation of its mass and carry about half of its momentum in hard (semi)inclusive processes. The spin of the nucleon is also built up from the intrinsic spin of the valence and sea quarks (spin-1/2), gluons (spin-1), and their orbital angular momenta. Notwithstanding the progress achieved during the last decades in the understanding of the quark contribution to the nucleon spin, the gluon sector is much less developed. One of the difficulties is the lack of the direct probes to access gluon content in high-energy processes. While the quark contribution to the nucleon spin was determined quite precisely in semi-inclusive deep-inelastic scattering (SIDIS) experiments like EMC, HERMES, and COMPASS, the gluon contribution is still not well-constrained even so it is expected to be significant.

In recent years, the three-dimensional partonic structure of the nucleon became a subject of a careful study. Precise mapping of three-dimensional structure of the nucleon is crucial for our understanding of Quantum Chromodynamics (QCD). One of the ways to go beyond the usual collinear approximation is to describe nucleon content in the momentum space employing the so-called Transverse-Momentum-Dependent Parton Distribution Functions (TMD PDFs) [1–6].

The most powerful tools to study TMD PDFs are the measurements of the nucleon spin (in)dependent azimuthal asymmetries in SIDIS [1, 4, 5, 7] and Drell–Yan processes [8, 9]. Complementary information on TMD fragmentation process, necessary for the interpretation of SIDIS data, is obtained from  $e^+e^-$  measurements [10]. Being an actively developing field, TMD physics triggers a lot of experimental and theoretical interest all over the world, stimulating new measurements and developments in TMD extraction techniques oriented on existing and future data from lepton-nucleon, electron-positron and hadron-hadron facilities at BNL, CERN, DESY, FNAL, JLab, and KEK. For recent reviews on experimental and theoretical advances on TMDs see Refs. [11–15]. While a lot of experimental measurements were performed (and are planned) and theoretical understanding was achieved for Leading Order (LO) (twist-2) TMD PDFs such as Sivers, transversity and Boer-Mulders functions of quarks, only few data relevant for the study of gluon TMD PDFs are available [16–21].

The simplest model of the deuteron is a weakly-bound state of a proton and a neutron mainly in the S-wave with a small admixture of the D-wave state. This approach is not much helpful in the descrip-



tion of the deuteron structure at large  $Q^2$ <sup>1</sup>. Possible non-nucleonic degrees of freedom in deuteron could play an important role in the understanding of the nuclear modification of PDFs (the EMC effect). Since the gluon transversity operator requires two-unit helicity-flip it does not exist for spin-1/2 nucleons [22]. Therefore, proton and neutron gluon transversity functions can not contribute directly to the gluon transversity of the deuteron. A non-zero deuteron transversity could be an indication of a non-nucleonic component or some other exotic hadronic mechanisms within the deuteron.

Most of the existing experimental results on spin-dependent gluon distributions in nucleon are obtained in the experiments at DESY (HERMES), CERN (COMPASS), and BNL (STAR and PHENIX). Study of polarized gluon content of the proton and nuclei is an important part of future projects in Europe and the United States such as AFTER@LHC and LHCSpin at CERN, and EIC at BNL [23–25]. Notwithstanding the fact that the gluons in nucleon were successfully probed in SIDIS measurements, hadronic collisions have an important advantage since they probe the gluons at the Born-level without involving the EM couplings.

## 1.1 Gluon probes at NICA SPD

The polarized gluon content of proton and deuteron at intermediate and high values of the Bjorken  $x$  will be investigated using three complementary probes: inclusive production of charmonia, open charm, and prompt photons. Study of these processes is complementary to such proven approaches to access the partonic structure of the nucleon in hadronic collisions as the inclusive production of hadrons with high transverse momentum and the Drell-Yan process. Unfortunately, the latter one is unlikely to be accessible at SPD due to the small cross section and unfavourable background conditions. For effective registration of each aforementioned gluon probes, the SPD setup is planned to be equipped with a range (muon) system, an electromagnetic calorimeter, a time-of-flight system, straw tracker, and a silicon vertex detector. Nearly a  $4\pi$  coverage of the setup and a low material budget in the inner part of the setup should provide a large acceptance for the detection of the desired final states. In Fig. 2.1(a) the kinematic phase-space in  $x$  and  $Q^2$  to be accessed by the SPD is compared to the corresponding ranges of previous, present and future experiments. Parameters of the experimental facilities planning to contribute to gluon physics with polarized beams are listed in Tab. 2.1. Figure 2.1(b) illustrates the behavior of the cross sections for the inclusive production of  $J/\psi$ ,  $\psi'$ ,  $D$ -mesons and high- $p_T$  prompt photons in  $p$ - $p$  collisions as a function of  $\sqrt{s}$ .

### 1.1.1 Charmonia production

From the experimental point of view, for considered energies, hadronic production of charmonia seems to be particularly suited to access gluon content in hadrons. Production of prompt  $J/\psi$ -mesons looks most attractive, since large data set of  $J/\psi \rightarrow \mu^+ \mu^-$  ( $BF = 0.06$ ) events is accumulated in beam-dump experiments with proton and pion beams at  $\sqrt{s}$  close to 20 GeV. However  $J/\psi$ -meson is not the cleanest probe of the proton structure, since a significant fraction (about 20% [30]) of  $J/\psi$ -mesons observed in hadronic collisions is produced indirectly through decays of  $\chi_{cJ}$  and  $\psi(2S)$  (the so-called feed-down contribution), and modeling of this contribution introduces additional uncertainties in theoretical calculations. Hence, to provide additional constraints to production models, it is important to study production of  $\chi_{cJ}$  and  $\psi(2S)$  separately, through their decays  $\chi_{cJ} \rightarrow \gamma J/\psi$  ( $BF = 0.014, 0.343$  and  $0.19$  for  $J = 0, 1$  and  $2$ ) and  $\psi(2S) \rightarrow \mu^+ \mu^-$  ( $BF = 0.08$ ). The latter state is of special interest, because it is essentially free from feed-down contamination from higher charmonium states, due to the proximity of  $D^0 \bar{D}^0$ -threshold. However, the separation of the  $\chi_{c0,1,2}$  signals is a challenging experimental task due to the small mass

<sup>1</sup>We use  $Q^2$  (or  $\mu^2$ ) as a generic notation for the hard scale of a reaction: the invariant mass square of lepton pairs in Drell-Yan processes,  $Q^2$ , transverse momentum square  $p_T^2$  of produced hadron or its mass square  $M^2$ .

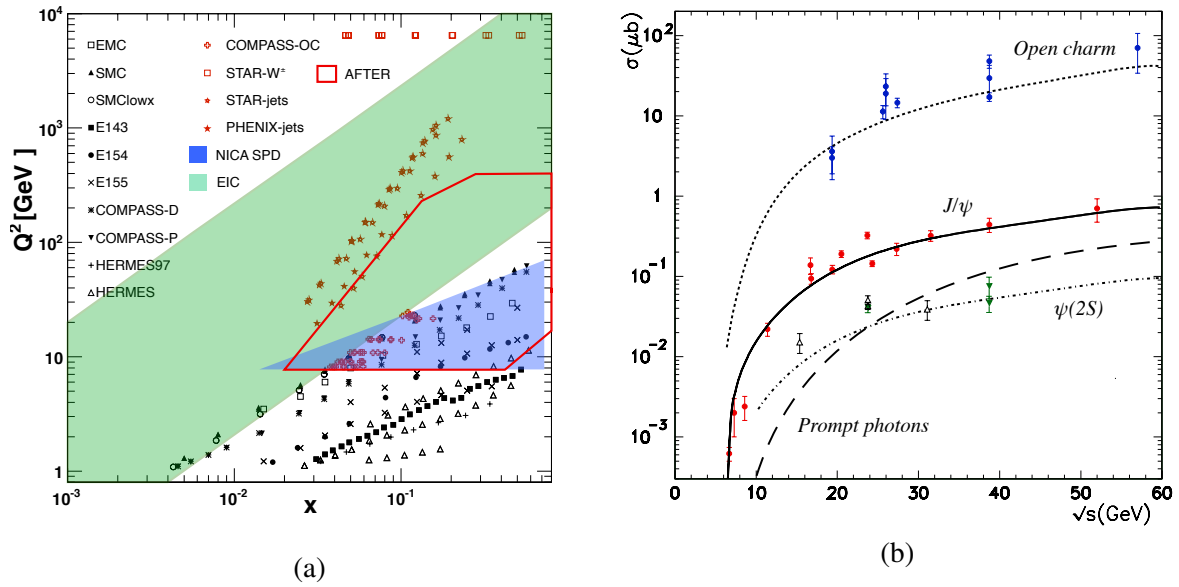


Figure 2.1: (a) The kinematic coverage, in the  $(x, Q^2)$  plane, of the hadronic cross section data for the processes commonly included in global QCD analyses of polarized quark (black) and gluon (red) PDFs [26]. The kinematic domain expected to be covered by NICA SPD by charmonia, open charm and prompt-photon production is shown in blue. (b) Cross section for the processes of open charm,  $J/\psi$ ,  $\psi(2S)$  and prompt photons ( $p_T > 3$  GeV) production as a function of center-of-mass energy (based on [27]).

Table 2.1: Main present and future actors in gluon spin physics.

Experimental facility	SPD @NICA [29]	RHIC [28]	EIC [25]	AFTER @LHC [23]	SpinLHC [24]
Scientific center	JINR	BNL	BNL	CERN	CERN
Operation mode	collider	collider	collider	fixed target	fixed target
Colliding particles & polarization	$p^\uparrow-p^\uparrow$ $d^\uparrow-d^\uparrow$ $p^\uparrow-d, p-d^\uparrow$	$p^\uparrow-p^\uparrow$	$e^\uparrow-p^\uparrow, d^\uparrow, {}^3\text{He}^\uparrow$	$p-p^\uparrow, d^\uparrow$	$p-p^\uparrow$
Center-of-mass energy $\sqrt{s_{NN}}$ , GeV	$\leq 27$ ( $p-p$ ) $\leq 13.5$ ( $d-d$ ) $\leq 19$ ( $p-d$ )	63, 200, 500	20-140 ( $ep$ )	115	115
Max. luminosity, $10^{32} \text{ cm}^{-2} \text{ s}^{-1}$	$\sim 1$ ( $p-p$ ) $\sim 0.1$ ( $d-d$ )	2	1000	up to $\sim 10$ ( $p-p$ )	4.7
Physics run	>2025	running	>2030	>2025	>2025

199 difference between the states and low energy resolution of the electromagnetic calorimeters for soft pho-  
200 tons.

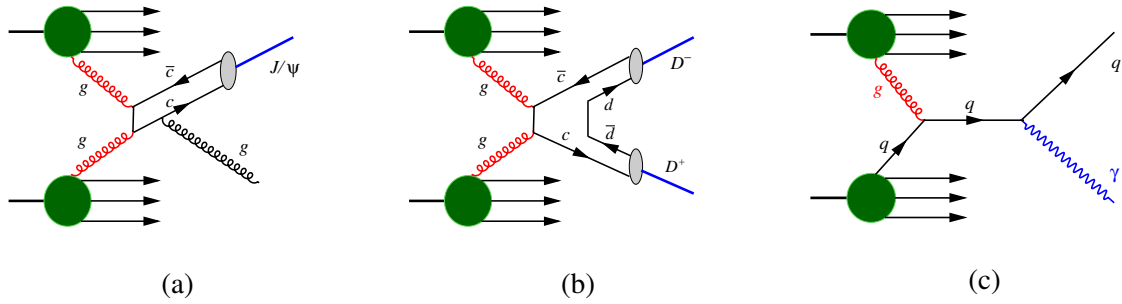


Figure 2.2: Diagrams illustrating three probes to access the gluon content of proton and deuteron in polarized collisions at NICA SPD: production of (a) charmonium, (b) open charm, (c) prompt photons.

201 Besides, from the theoretical point of view the task of accessing gluon distributions using heavy quarkonia is rather challenging. The heavy quark-antiquark pair couples directly to gluons from initial-state hadrons (Fig. 2.2(a)) and its production can be calculated perturbatively, because the hard scale of the process is limited from below by the heavy quark mass, providing the direct access to polarized and unpolarized gluon distributions. However, the process of transition of the heavy quark-antiquark pair into a physical bound-state is not well understood at present and can become a source of significant theoretical uncertainties. We review modern status of the theory of quarkonium production in more detail in Sec. 1.5 to explain the latter point.

209 Therefore, quarkonium production can be used to study the structure of hadrons only with a great caution and only if the results consistent with other probes will eventually emerge. The studies of hadronic structure and heavy quarkonium production mechanism should become complimentary. But for now the most reasonable phenomenological strategy for measurements at SPD concerning quarkonia is to study yields and polarization of different quarkonium states in a wide kinematic range, at various energies, and in polarized as well as non-polarized hadronic collisions, to provide the development of the theory with more constraints allowing to exclude various models. When the theory of production of heavy quarkonia is firmly established – it will become an invaluable tool to study the details of hadronic structure.

### 217 1.1.2 Open charm production

218 It is well-known that the heavy flavor production offers direct probes of the gluon distributions in hadrons. The basic mechanism responsible for charm pair production in  $pp$  collisions is the gluon fusion (GF, see Fig. 2.2(b)). In the framework of pQCD, the GF contributes to the hadron cross section as  $\mathcal{L}_{gg} \otimes \hat{\sigma}_{c\bar{c}}$ , where the gluon luminosity  $\mathcal{L}_{gg}$  is a convolution of the gluon densities in different protons,  $\mathcal{L}_{gg} = g \otimes g$ . At leading order in pQCD,  $\mathcal{O}(\alpha_s^2)$ , the partonic cross section  $\hat{\sigma}_{c\bar{c}}$  describes the process  $gg \rightarrow c\bar{c}$ .

223 The GF contribution to the charmonia production in  $pp$  collisions has the form  $\mathcal{L}_{gg} \otimes \hat{\sigma}_{(c\bar{c})+X} \otimes W_{c\bar{c}}$ . At the Born level, the partonic cross section  $\hat{\sigma}_{(c\bar{c})+X}$  is of the order of  $\alpha_s^3$  because its basic subprocess is  $gg \rightarrow (c\bar{c}) + g$ . Moreover, the quantity  $W_{c\bar{c}}$ , describing the probability for the charm pair to form a charmonium, imposes strong restrictions on the phase space of the final state.<sup>2</sup> For these two reasons, the  $\alpha_s$ -suppression and phase space limitation, the cross sections for charmonia production are almost two orders of magnitude smaller than the corresponding ones for open charm, see Figs. 2.1 (b).

229 To analyze the kinematics of a  $DD$  pair, each of  $D$ -mesons has to be reconstructed. The decay modes  $D^+ \rightarrow \pi^+ K^- \pi^+$  (BF=0.094) and  $D^0 \rightarrow \pi^+ K^- \pi^+$  (BF=0.04) can be used for that. To suppress a combinatorial background SPD plans to use the search for a secondary vertex of a  $D$ -meson decay that is about 100  $\mu\text{m}$  far from the interaction point (the  $c\tau$  values are 312 and 123  $\mu\text{m}$  for the charged and

<sup>2</sup>To form a charmonium, the momenta of the produced quark and antiquark should be sufficiently close to each other.

233 neutral  $D$ -mesons, respectively). Identification of a charged kaon in the final state by the time-of-flight  
 234 system would also help to do that. Production and decay of  $D^*$ -mesons could be used as an additional tag  
 235 for open-charm events. Singe-reconstructed  $D$ -mesons also carry reduced but still essential information  
 236 about gluon distribution that is especially important in the low-energy region with a lack of statistics.

### 237 1.1.3 Prompt photon production

238 Photons emerging from the hard parton scattering subprocess, the so-called prompt photons, serve as a  
 239 sensitive tool to access the gluon structure of hadrons and hadron-hadron collisions. Inclusive direct pho-  
 240 ton production proceeds without fragmentation, i.e. the photon carries the information directly from the  
 241 hard scattering process. Hence this process measures a combination of initial  $k_T$  effects and hard scat-  
 242 tering twist-3 processes. There are two main hard processes for the production of direct photons: gluon  
 243 Compton scattering,  $gq(\bar{q}) \rightarrow \gamma q(\bar{q})$  (Fig. 2.2(c)), which dominates, and quark-antiquark annihilation,  
 244  $q\bar{q} \rightarrow \gamma g$ . Contribution of the latter process to the total cross section is small.

245 Theoretical predictions for inclusive prompt photon production are shown in Fig. 2.3(a) as transverse  
 246 momentum spectrum at the energy  $\sqrt{s} = 27$  GeV. Calculations are performed in LO and NLO approx-  
 247 imations of CPM, as well as in the Parton Reggeization Approach (PRA), which is a QCD and QED  
 248 gauge-invariant version of  $k_T$ -factorization. They include direct and fragmentation contributions, the lat-  
 249 ter one is about 15-30 %. The K-factor between LO and NLO calculations in the CPM slightly depends  
 250 on  $p_{T\gamma}$  and equals about 1.8 [31]. LO prediction of PRA coincides with the result of NLO CPM calcu-  
 251 lation at moderate transverse momenta ( $p_T < 4$  GeV) while at higher  $p_T$  PRA predicts somewhat harder  
 252  $p_T$ -spectrum.

253 In experiments prompt photons are detected alongside with a much larger number of photons from decays  
 254 of secondary  $\pi^0$  and  $\eta$  mesons (minimum-bias photons). The main challenge is to subtract these decay  
 255 contributions to obtain the photons directly emitted from hard collisions. This kind of background is  
 256 especially important at small transverse momenta of produced photons ( $p_T$ ) and gives the lower limit  
 257 of the accessible  $p_T$  range. Therefore the prompt-photon contribution with  $p_T \leq 2 - 3$  GeV is usually  
 258 unreachable in the experiment [32]. Figure 2.3(b) [33] presents the comparison of the  $p_T$  spectra ( $x_T =$   
 259  $2p_T/\sqrt{s}$ ) measured in a wide kinematic range of  $\sqrt{s}$  in different fixed-target and collider experiments  
 260 and the theoretical NLO calculations performed within the JETPHOX package [34]. While high-energy  
 261 collider results exhibit rather good agreement with expectations, situation at high- $x_T$  is not pretty good.  
 262 The results of the E706 ( $\sqrt{s} = 31.6$  and  $38.8$  GeV) [35] and R806 ( $\sqrt{s} = 63$  GeV) [36] experiments  
 263 break out the trend and demonstrate some "slope". It could be an indication of possible systematic effects  
 264 that have not been not fully understood.

265 A pair of prompt photons can be produced in hadronic interactions in  $q\bar{q}$  annihilation, quark-gluon scat-  
 266 tering, and gluon-gluon fusion hard processes (at the leading, next-to-leading, and next-to-next-leading  
 267 orders, respectively). The double prompt photon production in nucleon interactions at low energies is not  
 268 yet well-studied experimentally. The production cross section for proton-carbon interaction at  $\sqrt{s} = 19.4$   
 269 GeV/c has been measured by the CERN NA3 experiment [37]. Based on this result we can expect the  
 270 cross section of the double photon production with  $p_T > 2$  GeV/c for each photon on the level of about  
 271 0.5 nb.

272 Estimations of the expected event rates are evaluated for  $p$ - $p$  collisions at  $\sqrt{s} = 27$  and  $13.5$  GeV for the  
 273 projected integrated luminosity  $1.0$  and  $0.1$  fb $^{-1}$ , respectively that corresponds effectively to one year of  
 274 data taking ( $10^7$  s). The results are listed in Tab. 2.2.

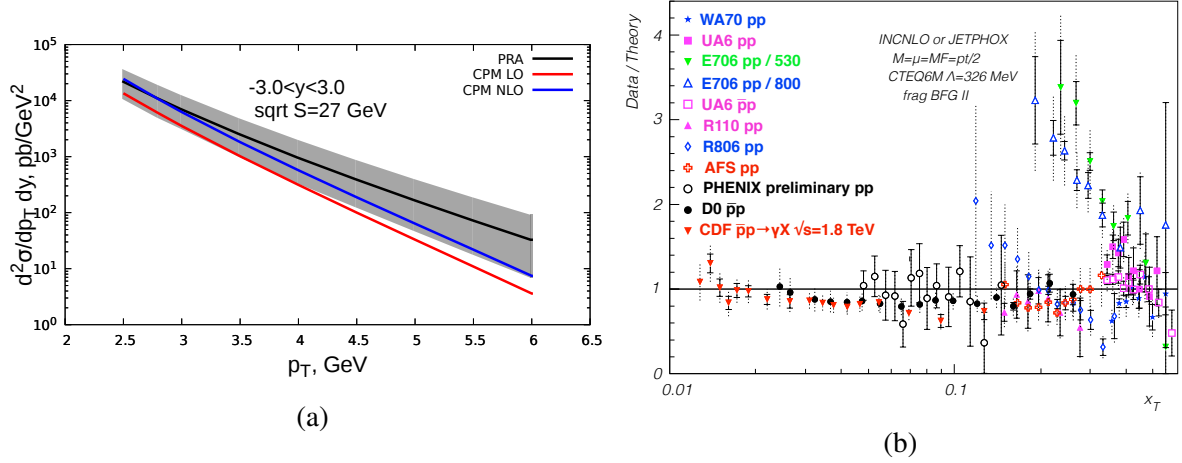


Figure 2.3: (a) Prediction for prompt photon transverse momentum spectrum at  $\sqrt{s} = 27$  GeV obtained in LO (red line) and NLO (blue line) approximations of CPM and LO of PRA (black line). Uncertainty bands for PRA predictions are due to factorization/renormalization scale variation only. (b) Data-to-theory ratio for the fixed-target and collider experiments [33].

Table 2.2: Expected rates for each of the gluon probes (per one year of SPD running).

Probe	$\sigma_{27\text{ GeV}},$ nb ( $\times$ BF)	$\sigma_{13.5\text{ GeV}},$ nb ( $\times$ BF)	$N_{27\text{ GeV}},$ $10^6$	$N_{13.5\text{ GeV}},$ $10^6$
Prompt- $\gamma$ ( $p_T > 3$ GeV/c)	35	2	35	0.2
$J/\psi$ $\rightarrow \mu^+ \mu^-$	200 12	60 3.6	12	0.36
$\psi(3686)$ $\rightarrow J/\psi \pi^+ \pi^- \rightarrow \mu^+ \mu^- \pi^+ \pi^-$ $\rightarrow \mu^+ \mu^-$	25 0.5 0.2	5 0.1 0.04	0.5 0.2	0.01 0.004
Open charm: $D\bar{D}$ pairs	$1.5 \times 10^4$	1300	$1.5 \times 10^4$	130
Single $D$ -mesons $D^+ \rightarrow K^- 2\pi^+$ and $D^- \rightarrow K^+ 2\pi^-$ $D^0 \rightarrow K^- \pi^+$ and $\bar{D}^0 \rightarrow K^+ \pi^-$	1100 730	100 65	1100 730	10 6.5

## 275 1.2 Gluons at large $x$

276 The gluon PDF is one of poorly known parton distributions in the proton because available data con-  
 277 strain weakly the quantity  $g(x, Q^2)$ , particularly for  $x$  greater than 0.5 [40, 41]. In the high- $x$  region, the  
 278 gluon density is usually parameterized as  $g(x, Q^2) \sim (1-x)^L$ , and values of  $L$  extracted from global fits  
 279 differ considerably from each other. In particular, obtained results for  $L$  vary from 3 to 11 at  $Q^2 = 1.9$   
 280  $\text{GeV}^2$  [42].

281 To improve the situation with large  $x$ , one needs precise data on the heavy flavor production at energies  
 282 not so far from the production threshold. Concerning the open charm production in  $pp$  collisions, the

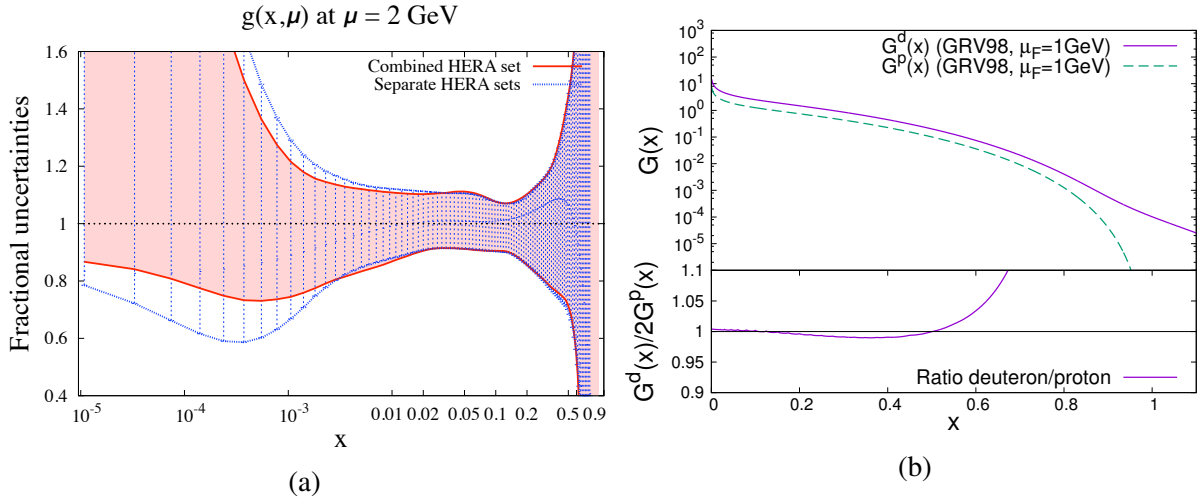


Figure 2.4: (a) Uncertainty of unpolarized gluon PDF based on HERA data ( $\mu = 2$  GeV) [38]. (b) Gluon PDF in the deuteron in comparison with the nucleon [39].

283 corresponding cross sections are poorly known for  $\sqrt{s} < 27$  GeV [43, 44].<sup>3</sup> Presently, the only available  
 284 measurements for this region were performed by the E769 experiment, which corresponds three hundred  
 285 events collected in  $pA$  collisions [45]. Unfortunately, E769 results have large uncertainties, which is  
 286 enough to estimate only the order of magnitude for the  $pp \rightarrow c\bar{c}X$  cross section at  $\sqrt{s} \approx 20$  GeV. For this  
 287 reason, future studies of the open charm production at SPD in  $pp$  and  $dd$  collisions for  $\sqrt{s} \leq 27$  GeV are  
 288 of special interest. In particular, they will allow to reduce significantly the present uncertainties in the  
 289 gluon density (and  $\alpha_s$ ) at a GeV scale, especially for high  $x$ .

290 Detailed information on the gluon distribution at large  $x$  is very important for various phenomenological  
 291 applications. For instance, it is of current interest to estimate the  $b\bar{b}$  pair production cross section at  
 292 NICA energies. Such predictions, however, are not presently reliable due to their strong dependence on  
 293 the exponent  $L$  which is known poorly. Another example is the DGLAP evolution of the PDFs. Using  
 294 precise data on  $g(x, Q^2)$  (and  $\alpha_s$ ) at  $Q^2 \sim m_c^2$  ( $m_c$  is the mass of the c-quark) as boundary conditions in  
 295 DGLAP equations, one could reduce essentially the uncertainties in evolution of PDFs for higher values  
 296 of  $Q$ .

297 From the theoretical point of view, the threshold behavior of cross sections is closely related to the so-  
 298 called infrared renormalon problem. It is well known that radiative corrections to the production cross  
 299 sections contain the mass (or threshold) logarithms whose contribution is expected to be sizable near the  
 300 threshold. These logarithms are usually taken into account within the soft gluon resummation (SGR)  
 301 formalism [46–50]. Formally resummed cross sections are, however, ill-defined due to the Landau pole  
 302 contribution, and few prescriptions have been proposed to avoid the renormalon ambiguities [51–54].  
 303 Unfortunately, numerical predictions for heavy quark production cross sections can depend significantly  
 304 on the choice of resummation prescription. Undoubtedly, anticipated data from SPD on the charm pro-  
 305 duction not so far from the production threshold will provide an excellent test for these prescriptions.

306 Another interesting problem for NICA SPD is to probe the intrinsic charm (IC) content of the proton [55,  
 307 56]. The IC contribution to open charm production is expected to be sizable near the threshold because  
 308 its PDF,  $c(x, Q^2)$ , is predicted to be harder than the gluonic one. As a result, the IC density in the proton  
 309 can be dominant at sufficiently large  $x$  independently of its overall normalization [57]. To visualize the  
 310 IC component, one needs to collect much enough events like  $D\bar{D}$  pair produced in  $pp \rightarrow D\bar{D}$  with a large  
 311 overall  $x_F$  close to 1. That events are predicted to be very rare within the GF mechanism and would

<sup>3</sup>On the contrary, the  $J/\psi$  production cross section is known well enough practically down to the threshold, see Fig. 2.1(b).

312 directly indicate the five-quark component in the proton,  $|uudc\bar{c}\rangle$

313 Investigation of the open charm production in  $pp$ ,  $pd$  and  $dd$  collisions might be one of the key points in  
 314 the NICA SPD programme. The motivation is twofold. On the one hand, production of  $D$ -mesons in  $pp$   
 315 collisions is practically unmeasured at NICA energies. On the other hand, these presently unavailable  
 316 data on open charm production rates are strongly necessary for determination of the gluon density  $g(x, \mu)$   
 317 at large  $x$  where this PDF is practically unknown.

318 Moreover, anticipated results on the open charm production are very important for many other current  
 319 issues in particle physics: from infrared renormalon ambiguities in cross sections to intrinsic charm  
 320 content of the proton.

### 321 1.3 Tests of TMD factorization with gluon probes

322 The description of hard inclusive processes in hadron collisions is based on factorization theorems. For-  
 323 mulation of factorization theorems in terms of the TMD PDFs of quarks and gluons is the most important  
 324 step towards studying the 3D structure of hadrons and the nature of their spins. The conventional TMD-  
 325 approach [58] can be applied for study of processes with colorless final states with transverse momenta  
 326 much smaller than the relevant scale of hadron interactions,  $q_T \ll Q$ . In recent years a substantial suc-  
 327 cess was achieved in the quark sector of TMD PDFs related with their correct theoretical definition and  
 328 the connection with experimentally observed cross sections within the framework of factorization theo-  
 329 rems [6]. In the case of unpolarized hadron collisions, in the leading twist approximation the production  
 330 cross section is a function of two independent TMD PDFs, i.e. distribution functions of unpolarized  
 331 quarks  $f_1^q$  and distribution functions of transversely polarized quarks  $h_1^{\perp q}$  (referred to as Boer-Mulders  
 332 function) in unpolarized nucleons. For description of cross sections in collisions of polarized hadrons,  
 333 the number of TMD PDFs increases.

334 However, the situation with gluon TMD PDFs is significantly different. Until recently, gluon TMD PDFs  
 335 were used only within the framework of phenomenological models of the type of the Generalized Parton  
 336 Model (GPM), in which the factorization formula of the Collinear Parton Model is applied if small (non-  
 337 perturbative-origin) transverse momenta of gluons from colliding hadrons are available.

338 The proof of the factorization theorem for processes with gluon TMD PDFs, as well as the formulation  
 339 of evolution equations for them, have been presented relatively recently in [59], where it was applied  
 340 to describe the Higgs boson production with small transverse momenta. However, hard processes in  
 341 which detailed information on gluon TMD PDFs can be obtained primarily, include the processes of  
 342 production of heavy mesons ( $D$ ,  $B$ ) and heavy quarkonia ( $J/\psi$ ,  $\Upsilon$ ,  $\eta_c$ ,  $\eta_b$ ,  $\dots$ ). In these processes, there  
 343 are two non-perturbative mechanisms to be factorized: the emission of soft gluons in the initial state and  
 344 the formation of a colorless hadron in the final state. Even in the case of heavy meson production with  
 345 small transverse momenta when their spectrum is determined only by a non-perturbative  $q_T$ -distribution  
 346 of initial gluons, for factorization of hard and soft interactions it is not enough to use the TMD PDFs  
 347 formalism, the introduction of new non-perturbative process-dependent hadron observables, the so-called  
 348 TMDShFs (TMD shape functions) [60, 61] is needed. Moreover, the differential cross section for the  
 349 process of production the state  $\mathcal{Q}$  in a collision of unpolarized hadrons is written as

$$\frac{d\sigma}{dyd^2q_T} \sim f_1^g \otimes f_1^g \otimes S_{\mathcal{Q}} - w_{UU} \otimes h_1^{\perp g} \otimes h_1^{\perp g} \otimes S_{\mathcal{Q}},$$

350 where  $S_{\mathcal{Q}}$  is the polarization-independent TMDShFs of this process and  $w_{UU}$  is the universal contribution  
 351 weight function of linearly polarized TMD PDFs.

352 The factorization theorem contains three or more non-perturbative hadronic quantities at low transverse  
 353 momenta: gluon TMD PDFs and TMDShFs. Thus, the phenomenological extraction of gluon TMDs

354 from quarkonium production processes is still possible, i.e., a robust factorization theorem can potentially  
 355 be obtained in any particular case of heavy meson production. However one also needs to model and  
 356 extract the involved TMDShFs.

#### 357 1.4 Linearly polarized gluons in unpolarized nucleon

358 Search for the polarized quarks and gluons in unpolarized hadrons is of special interest in studies of  
 359 the spin-orbit couplings of partons and understanding of the proton spin decomposition. The corre-  
 360 sponding intrinsic transverse momentum  $\vec{k}_T$  dependent distributions of the transversely polarized quarks,  
 361  $h_1^{\perp q}(x, \vec{k}_T^2)$ , and linearly polarized gluons,  $h_1^{\perp g}(x, \vec{k}_T^2)$ , in an unpolarized nucleon have been introduced in  
 362 Refs. [3] and [62]. Contrary to its quark version  $h_1^{\perp q}$  the TMD density  $h_1^{\perp g}$  is  $T$ - and chiral-even, and  
 363 thus can directly be probed in certain experiments.

364 Azimuthal correlations in heavy quark pair production in unpolarized  $ep$  and  $pp$  collisions as probes  
 365 of the density  $h_1^{\perp g}$  have been considered in Refs. [63, 64]. For the case of DIS, the complete angular  
 366 structure of the pair production cross section has been obtained in terms of seven azimuthal modulations.  
 367 However, only two of those modulations are really independent; they can be chosen as the  $\cos \varphi$  and  
 368  $\cos 2\varphi$  distributions, where  $\varphi$  is the heavy quark (or anti-quark) azimuthal angle [65, 66].<sup>4</sup>

To probe the TMD distributions, the momenta of both heavy quark and anti-quark,  $\vec{p}_Q$  and  $\vec{p}_{\bar{Q}}$ , in the  
 process  $pp \rightarrow Q\bar{Q}X$  should be measured (reconstructed). For further analysis, the sum and difference of  
 the transverse heavy quark momenta are introduced,

$$\vec{K}_{\perp} = \frac{1}{2} (\vec{p}_{Q\perp} - \vec{p}_{\bar{Q}\perp}), \quad \vec{q}_T = \vec{p}_{Q\perp} + \vec{p}_{\bar{Q}\perp}, \quad (2.1)$$

369 in the plane orthogonal to the collision axis. The azimuthal angles of  $\vec{K}_{\perp}$  and  $\vec{q}_T$  are denoted as  $\phi_{\perp}$  and  
 370  $\phi_T$ , respectively.

371 The angular structure of the  $pp \rightarrow Q\bar{Q}X$  cross section has the following form:

$$d\sigma_{pp} \propto A(q_T^2) + B(q_T^2)q_T^2 \cos 2(\phi_{\perp} - \phi_T) + C(q_T^2)q_T^4 \cos 4(\phi_{\perp} - \phi_T). \quad (2.2)$$

372 Assuming factorization for the TMD distributions, the terms  $A$ ,  $B$  and  $C$  can schematically be written as  
 373 the following convolutions [64]:

$$\begin{aligned} A &\propto f_1^q \otimes f_1^{\bar{q}} \otimes A_q + f_1^g \otimes f_1^g \otimes A_g + h_1^{\perp q} \otimes h_1^{\perp g} \otimes A_g^{\perp}, \\ B &\propto h_1^{\perp q} \otimes h_1^{\perp \bar{q}} \otimes B_q + f_1^g \otimes h_1^{\perp g} \otimes B_g, \\ C &\propto h_1^{\perp g} \otimes h_1^{\perp g} \otimes C_g. \end{aligned} \quad (2.3)$$

374 The order  $\alpha_s^2$  predictions for the coefficients  $A_i$ ,  $B_i$  and  $C_i$  ( $i = q, g$ ) in Eqs.(2.3) are presented in Ref.[64].  
 375 Using these results, one can, in principle, extract the densities  $h_1^{\perp q}(x, \vec{k}_T^2)$  and  $h_1^{\perp g}(x, \vec{k}_T^2)$  from azimuthal  
 376 distributions of the  $D\bar{D}$  pairs produced in  $pp$  collisions.

377 Another processes proposed to probe the linearly polarized gluons in unpolarized proton are: pseu-  
 378 doscalar  $C$ -even quarkonia (such as  $\eta_c$  and  $\chi_c$ ) [68], di-gamma ( $pp \rightarrow \gamma\gamma X$ ) [69] and  $J/\psi$ - pair ( $pp \rightarrow$   
 379  $J/\psi J/\psi X$ ) [70] production. These reactions are however strongly suppressed in comparison with  
 380  $pp \rightarrow D\bar{D}X$ .

<sup>4</sup>The function  $h_1^{\perp g}$  can also be determined from measurements of the Callan-Gross ratio in DIS [67].



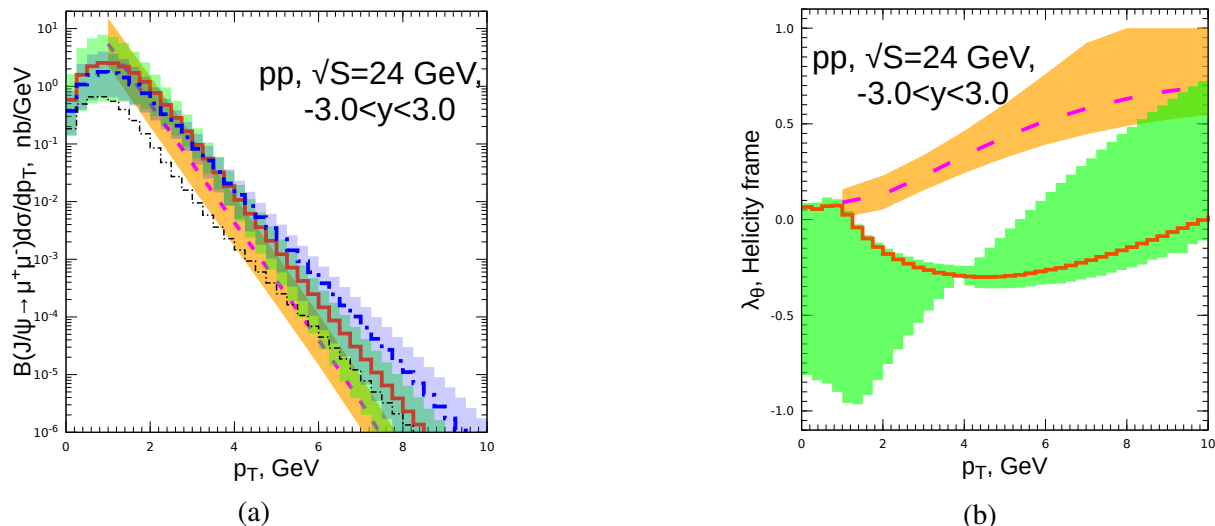


Figure 2.5: Theoretical predictions for inclusive  $J/\psi$   $p_T$ -spectrum (a) and  $p_T$ -dependence of polarization parameter  $\lambda_\theta$  (b) in various models: NLO of Collinear Parton Model + NRQCD-factorization (thick dashed line with orange uncertainty band) [88, 89], LO of PRA [90] + NRQCD-factorization (thick solid histogram with a green uncertainty band) [91, 92], and LO PRA [90] + Improved Color Evaporation Model (thick dash-dotted histogram with blue uncertainty band) [93]. The contribution of  $q\bar{q}$ -annihilation channel to the central ICEM prediction is depicted by the thin dash-dotted histogram. Uncertainty bands are due to factorization/renormalization scale variation only.

### 381 1.5 Hadron structure and heavy charmonia production mechanisms

382 In this section we give a short review of modern status of the theory of heavy quarkonium production  
 383 with an emphasis on possible applications of heavy quarkonium measurements for studies of the gluon  
 384 content of hadrons.

385 Production of heavy quarkonia proceeds in two stages: first, a heavy quark-antiquark pair is produced  
 386 at short distances, predominantly via gluon-gluon fusion but also with a non-negligible contribution  
 387 of  $q\bar{q}$  and  $qg$ -initiated subprocesses. The second stage is hadronization of quark-antiquark pair into a  
 388 physical quarkonium state, which happens at large distances (low scales) and is accompanied by a com-  
 389 plicated rearrangement of color via exchanges of soft gluons between the heavy quark-antiquark pair and  
 390 other colored partons produced in the collision. Existing approaches, aimed to describe hadronization  
 391 stage, such as Non-Relativistic QCD factorization (NRQCD-factorization) [71] and (Improved-) Color-  
 392 Evaporation Model (CEM) [72–75] are currently facing serious phenomenological challenges (see e.g.  
 393 recent reviews [76, 77]). NRQCD-factorization is challenged by the long-standing “polarization puz-  
 394 zle” [78, 79] and violation of Heavy-Quark Spin Symmetry relations between Long-Distance Matrix  
 395 Elements (LDMEs) of  $\eta_c$  and  $J/\psi$  [80], while CEM usually rather poorly reproduces the detailed shapes  
 396 of inclusive  $p_T$ -spectra of charmonia and bottomonia and, unlike NRQCD-factorization [81, 82], sig-  
 397 nificantly under-predicts bulk of cross section for pair hadroproduction of  $J/\psi$  even at NLO in  $\alpha_s$  [83].  
 398 Presently, the study of the heavy-quarkonium production mechanism is an active field of research, with  
 399 new approaches, such as subleading-power fragmentation [84] and Soft-Gluon Factorization [85–87],  
 400 being proposed recently.

401 Due to above-mentioned problems and multitude of competing theoretical approaches and models avail-  
 402 able on the market, our lack of quantitative understanding of the mechanism of hadronization can become  
 403 a source of significant theoretical uncertainties if quarkonium production is to be used as a tool to study  
 404 the proton structure. The Fig. 2.5 provides an insight on this situation at NICA SPD. In this figure,

405 predictions of three models for the  $p_T$ -spectrum (Fig. 2.5(a)) and  $p_T$ -dependence of the polarization pa-  
 406 rameter  $\lambda_\theta$  (Fig. 2.5(b)) are compared. The first one relies on the NLO calculation in Collinear Parton  
 407 Model (with LO being  $O(\alpha_s^3)$ , see Fig. 2.2(a)) to describe short-distance part of the cross section and  
 408 uses the NRQCD-factorization formalism for the long-distance part, with LDMEs of the latter tuned to  
 409 charmonium production data in hadronic collisions, DIS and  $e^+e^-$ -annihilation [78, 79, 88, 89]. In the  
 410 second prediction, the short-distance part of the cross section is calculated in the LO ( $O(\alpha_s^2)$  for color-  
 411 octet and  $P$ -wave contributions and  $O(\alpha_s^3)$  for color-singlet  $S$ -wave ones) of PRA [90], while LDMEs  
 412 in this calculation had been fitted to the charmonium hadroproduction data from RHIC, Tevatron and  
 413 LHC [91, 92]. The third prediction is performed in the LO ( $O(\alpha_s^2)$ ) of PRA with the same uninte-  
 414 grated PDFs as for the second one, but interfaced with an improved Color-Evaporation Model (ICEM)  
 415 of Ref. [93] for description of hadronization. Non-perturbative parameters of the ICEM had been taken  
 416 from the Ref. [93] where they had been fitted to charmonium hadroproduction data at Tevatron and LHC  
 417 energies. Predictions of all three models for inclusive  $J/\psi$   $p_T$ -spectrum at NICA SPD appear to be  
 418 consistent within their uncertainty bands. However, the structure of this predictions is significantly dif-  
 419 ferent, with NRQCD-based predictions being dominated by gluon-gluon fusion subprocess, while ICEM  
 420 prediction containing significant contamination from  $q\bar{q}$ -annihilation (thin dash-dotted histogram in the  
 421 Fig. 2.5(a)), which reaches up to 50% at low  $p_T < 1$  GeV and contributes up to 10% at higher  $p_T > 3$   
 422 GeV. Also ICEM tends to predict significantly harder  $p_T$ -spectrum at  $p_T > 5$  GeV, than NRQCD-based  
 423 PRA prediction which was performed with the same unintegrated PDFs.

424 Discussion above shows, that  $J/\psi$   $p_T$ -spectrum can be reliably predicted only in the limited range of  
 425 transverse momenta, approximately from 3 to 6 GeV at  $\sqrt{s} = 24$  GeV. At higher  $p_T$  the shape of the  
 426 spectrum becomes highly model-dependent and at lower  $p_T < M_{J/\psi}$  the TMD-factorization effects (in-  
 427 cluding possible violation of factorization, see [60, 61]) come into the game and the contribution of  
 428  $q\bar{q}$ -annihilation subprocess becomes uncertain. Nevertheless, predictions and measurements of rapidity  
 429 or  $x_F$ -differential cross-sections even in this limited  $p_T$ -range could help to further constrain the gluon  
 430 PDF, e.g. to rule-out the extreme values of  $L$  in the  $x \rightarrow 1$  asymptotics of the PDF  $\sim (1-x)^L$ .

431 Predictions of NLO CPM and LO of PRA for polarization parameter  $\lambda_\theta$  (see the Fig. 2.5(b)) are sig-  
 432 nificantly different, with PRA predicting mostly un-polarized production ( $\lambda_\theta \simeq 0$ ) while CPM predicts  
 433 transverse polarization ( $\lambda_\theta = +1$ ) at high  $p_T$ . Disagreement of the predictions for polarization param-  
 434 eters mostly reflects the difference of LDMEs obtained in two fits and their large uncertainty bands are  
 435 due to significant uncertainties of LDMEs. Measurements of heavy quarkonium polarization at NICA  
 436 energies will provide additional constraints on models, however due to well-known problems with de-  
 437 scription of polarization at high energies [78, 79] constraints coming from polarization measurements  
 438 should be interpreted with great care and one should try to disentangle conclusions for gluon PDF from  
 439 the results related to heavy quarkonium polarization.

## 440 1.6 Non-nucleonic degrees of freedom in deuteron

441 The naive model describes the deuteron as a weakly-bound state of a proton and a neutron mainly in  
 442 S-state with a small admixture of the D-state. However, such a simplified picture failed to describe the  
 443 HERMES experimental results on the  $b_1$  structure function of the deuteron [94]. Modern models treat  
 444 the deuteron as a six-quark state with the wave function

$$|6q\rangle = c_1|NN\rangle + c_2|\Delta\Delta\rangle + c_3|CC\rangle, \quad (2.4)$$

445 that contains such terms as the nucleon  $|NN\rangle$ ,  $\Delta$ -resonance  $|\Delta\Delta\rangle$  and the so-called hidden color compo-  
 446 nent  $|CC\rangle$  in which two color-octet baryons combine to form a color singlet [95]. Such configurations  
 447 can be generated, for example, if two nucleons exchange a single gluon. The relative contribution of the  
 448 hidden-color term varies from about 0.1% to 80% in different models [96]. The components other than

449  $|NN\rangle$  should manifest themselves in the high- $Q^2$  limit. Possible contributions of the Fock states with a  
 450 valent gluon like  $|uuudddg\rangle$  could also be discussed [39, 97].

451 The unpolarized gluon PDF of the deuteron in the light-front quantization was calculated in the Ref. [39]  
 452 under the approximation where the input nuclear wave function is obtained by solving the nonrelativistic  
 453 Schrödinger equation with the phenomenological Argonne v18 nuclear potential as an input. Gluon PDFs  
 454 calculated per nucleon are very similar for the proton one in the range of small and intermediate  $x$  values  
 455 while for  $x > 0.6$  the difference becomes large due to the Fermi motion (see Fig. 2.14(a)). A similar  
 456 work was performed in Ref. [98] for determination of spatial gluon distribution in deuteron for low- $x$   
 457 that could be tested in the  $J/\psi$  production at EIC. Today the gluon content of deuteron and light nuclei  
 458 becomes the matter of interest for the lattice QCD studies [99]. Apart from the general understanding of  
 459 the gluon EMC effect, the measurement of the gluon PDF at high- $x$  for deuteron could provide a useful  
 460 input for high-energy astrophysical calculation [39].

461 SPD can perform an explicit comparison of the differential inclusive production cross sections  $d\sigma/dx_F$   
 462 for all three gluon probes: charmonia, open charm, and prompt photons using  $p$ - $p$  and  $d$ - $d$  collisions  
 463 at  $\sqrt{s_{NN}} = 13.5$  GeV and possibly below. Such results could be treated in terms of the difference of  
 464 unpolarized gluon PDFs in deuteron and nucleon.

### 465 1.7 Gluon polarization $\Delta g$ with longitudinally polarized beams

466 The gluon helicity distribution function  $\Delta g(x)$  is a fundamental quantity characterizing the inner structure  
 467 of the nucleon. It describes the difference of probabilities to find in the longitudinally polarized nucleon  
 468 a gluon with the same and opposite spin orientations. The integral  $\Delta G = \int \Delta g(x)dx$  can be interpreted as  
 469 the gluon spin contribution to the nucleon spin. After the EMC experiment discovered that only a small  
 470 part of proton spin is carried by the quarks [100], the gluon spin was assumed to be another significant  
 471 contributor. So  $\Delta G$  is a key ingredient of the nucleon helicity sum rule

$$\frac{1}{2} = \frac{1}{2}\Delta\Sigma + \Delta G + L_q + L_g, \quad (2.5)$$

472 where  $\Delta\Sigma \approx 0.25$  [15] is the net contribution from the quark spin and  $L_q, L_g$  represent contribution of the  
 473 orbital angular momenta of quarks and gluons, respectively.

474 The first attempt to measure the gluon polarization in the nucleon was made by the FNAL E581/704 Col-  
 475 laboration using a 200 GeV polarized proton beam and a polarized proton target [101]. They measured  
 476 the longitudinal double-spin asymmetries  $A_{LL}$  for inclusive multi- $\gamma$  and  $\pi^0\pi^0$  production to be consistent  
 477 with zero within their sensitivities. In the following years a set of SIDIS measurements was performed  
 478 by the HERMES [102], SMC [103] and COMPASS [104–108] experiments. The production of hadron  
 479 pairs with high transverse momenta and the production of the open charm where the photon-gluon fusion  
 480 mechanism dominates were studied. It was figured out that with a large uncertainty the value of  $\Delta G$  is  
 481 close to zero. Nevertheless, for gluons carrying a large fraction  $x$  of the nucleon momentum, an evidence  
 482 of a positive polarization has been observed, see Fig. 2.6(a). New results for  $\Delta G$  were obtained from the  
 483 measurement of the  $A_{LL}$  asymmetries in the inclusive production of high- $p_T$  neutral pions [109–111],  
 484  $\eta$ -mesons [109], jets [112], heavy flavors [113] and, recently,  $J/\psi$ -mesons [114] in polarized  $p$ - $p$  colli-  
 485 sions at RHIC. The new data in general are in agreement with SIDIS measurements, which demonstrates  
 486 the universality of the helicity-dependent parton densities and QCD factorization.

487 At the moment the most recent sets of polarized PDFs extracted in the NLO approximation are LSS15 [115],  
 488 DSSV14 [116, 117], NNPDF-pol1.1 [26], and JAM17 [118]. To obtain them, different approaches, pa-  
 489 rameterizations, and sets of experimental data were used, see Ref. [119] for more details. Fit results for  
 490  $\Delta g(x)$  from DSSV14 and NNPDF-pol1.1 are presented in Fig. 2.6(b) [117]. The RHIC  $p$ - $p$  data put a  
 491 strong constraint on the size of  $\Delta g(x)$  in the range  $0.05 < x < 0.2$  but cannot determine its sign as soon as

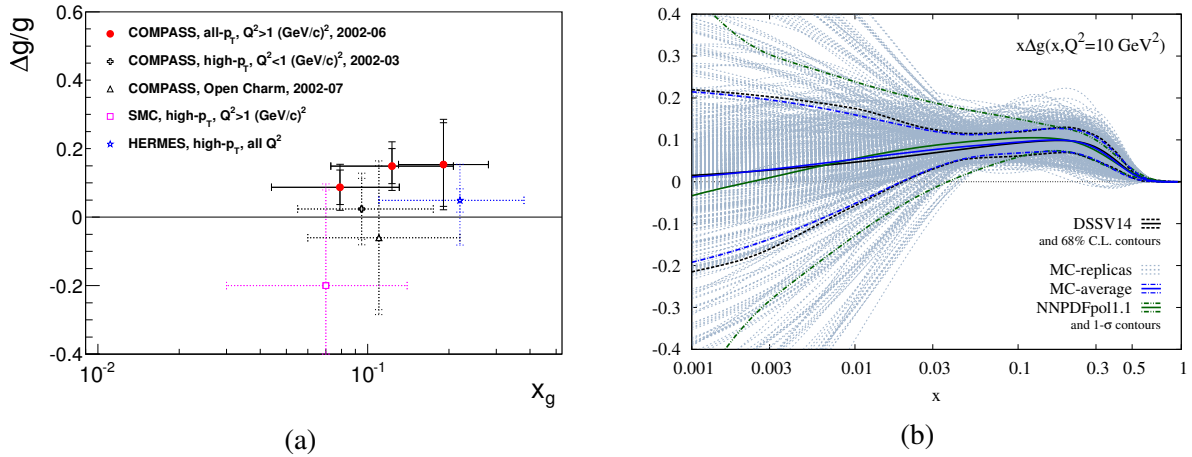


Figure 2.6: (a) SIDIS data on  $\Delta g(x)/g(x)$  extracted in LO [108]. (b) Global fit results for the gluon helicity distribution  $\Delta g(x)$  [117].

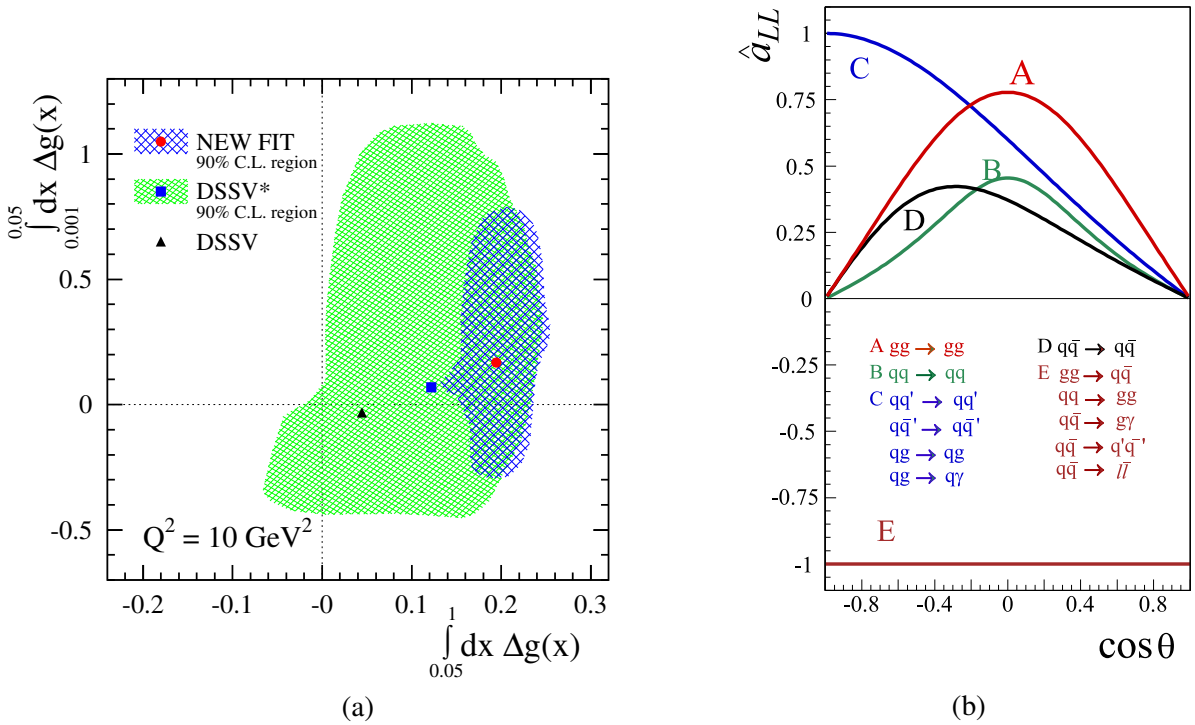


Figure 2.7: (a) Estimates of contributions of low- $x$  and high- $x$  kinematic ranges into  $\Delta G$  for the DSSV series of the global fit. The 90% C.L. areas are shown [116]. (b) Partonic longitudinal double-spin asymmetries  $A_{LL}$  for different hard processes as a function of center-of-mass scattering angle [121].

492 they mainly probe  $\Delta g$  squared (see details below). The small  $x$  region remains still largely unconstrained  
 493 and could be covered in future by measurements at EIC [25]. Region of high  $x$  is covered at the moment  
 494 only by SIDIS measurements which still lack a proper NLO description [120]. The uncertainty of the  
 495 contribution to  $\Delta g$  from the kinematic range  $0.001 < x < 0.05$  vs. the corresponding contribution from  
 496 the range  $x > 0.05$  for the DSSV global fits is shown in Fig. 2.7(a) [116].

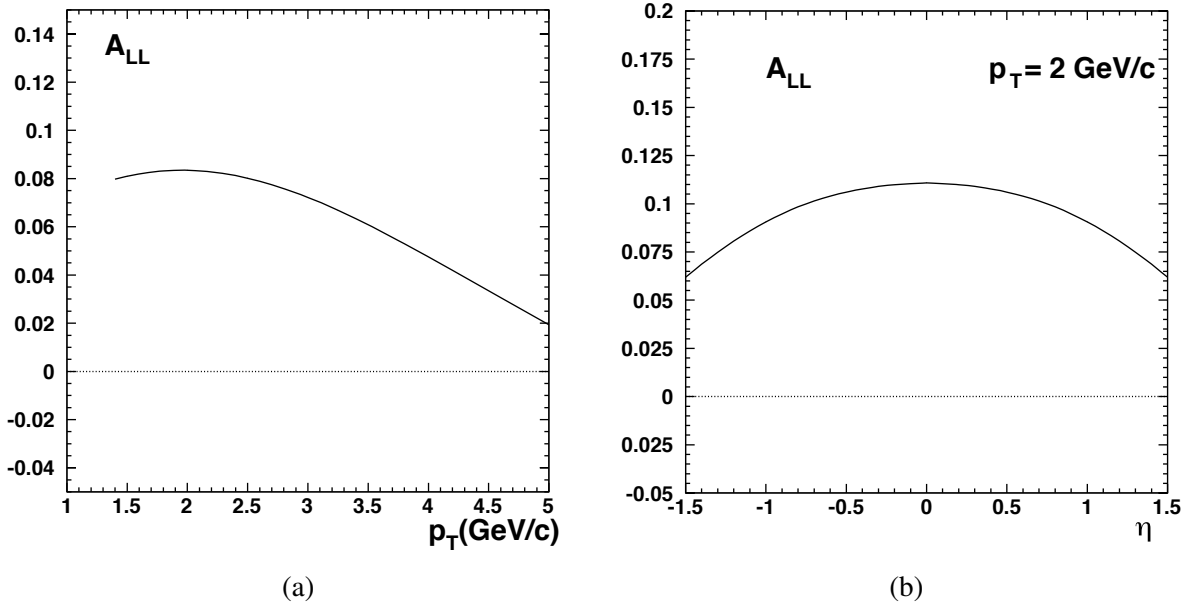


Figure 2.8: Longitudinal double spin asymmetry  $A_{LL}$  for inclusive  $J/\psi$  production calculated for  $p$ - $p$  collisions at  $\sqrt{s} = 39$  GeV in the LO approximation as a function of a) transverse momentum  $p_T$  and b) pseudorapidity  $\eta$  [122].

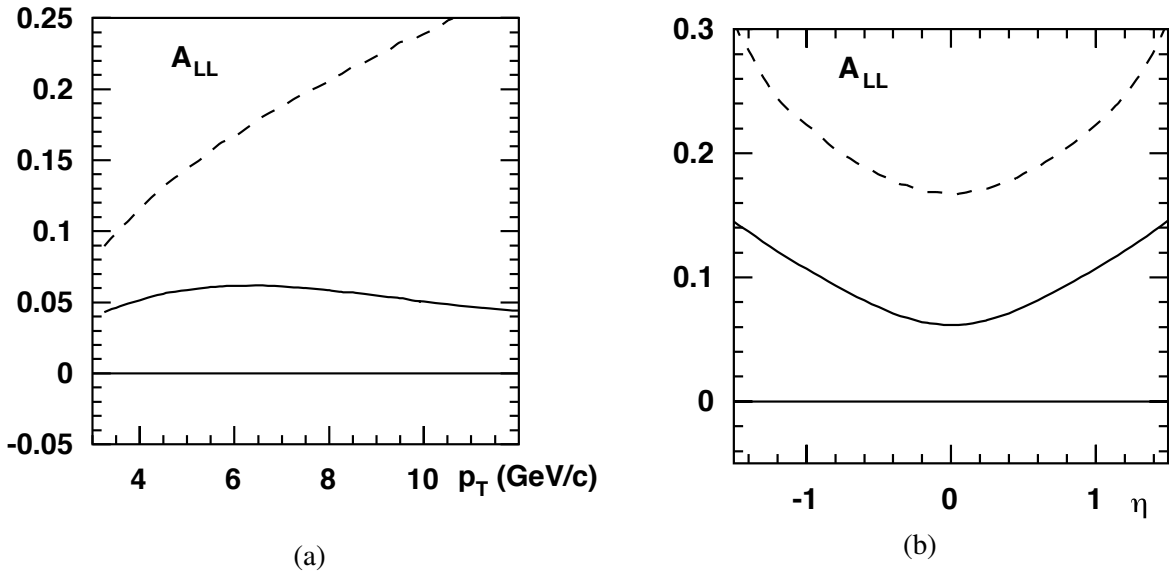


Figure 2.9: Longitudinal double spin asymmetry  $A_{LL}$  for inclusive prompt-photon production calculated for  $p$ - $p$  collisions at  $\sqrt{s} = 39$  GeV in the LO approximation as a function of a) transverse momentum  $p_T$  and b) rapidity  $\eta$  ( $p_T = 6$  GeV/c) [122].

497 In case of the longitudinally polarized  $p$ - $p$  collisions the asymmetry  $A_{LL}$  is defined as

$$A_{LL} = \frac{\sigma^{++} - \sigma^{+-}}{\sigma^{++} + \sigma^{+-}}, \quad (2.6)$$

498 where  $\sigma^{++}$  and  $\sigma^{+-}$  denote the cross sections with the same and opposite proton helicity combinations,

499 respectively. For the prompt photons produced via the gluon Compton scattering

$$A_{LL}^\gamma \approx \frac{\Delta g(x_1)}{g(x_1)} \otimes A_{1p}(x_2) \otimes \hat{a}_{LL}^{gq(\bar{q}) \rightarrow \gamma q(\bar{q})} + (1 \leftrightarrow 2). \quad (2.7)$$

500 Here  $A_{1p}(x)$  is the asymmetry well-measured in a wide range of  $x$  and  $\hat{a}_{LL}^{gq(\bar{q}) \rightarrow \gamma q(\bar{q})}$  is the asymmetry of  
 501 the corresponding hard process. The Fig. 2.7(b) shows the behavior of  $\hat{a}_{LL}$  for different hard processes  
 502 as a function of the center-of-mass scattering angle. For charmonia and open charm production via the  
 503 gluon-gluon fusion process the expression for the corresponding asymmetry reads

$$A_{LL}^{c\bar{c}} \approx \frac{\Delta g(x_1)}{g(x_1)} \otimes \frac{\Delta g(x_2)}{g(x_2)} \otimes \hat{a}_{LL}^{gg \rightarrow c\bar{c}X}. \quad (2.8)$$

504 This asymmetry on the one hand is more sensitive to the gluon polarization than the corresponding one  
 505 for the prompt photons due to the quadratic dependence on  $\Delta g$ . On the other hand the sign of the  $\Delta g$   
 506 value can not be determined from it. So the measurements with prompt photons and heavy-quark states  
 507 are complementary. The contribution of  $q\bar{q}$  annihilation processes to the above-mentioned asymmetries  
 508 is negligible despite  $\hat{a}_{LL} = -1$  because of the smallness of the sea-quark polarization in the nucleon.

509 It is important to emphasise that a sizable systematic uncertainty of  $A_{LL}$  measurements in the inclusive  
 510  $J/\psi$  production comes from our limited knowledge of charmonia production mechanisms including  
 511 the feed-down contribution. Each of them has different partonic asymmetries  $\hat{a}_{LL}$  [123]. For the  $\Delta g$   
 512 estimation in Ref. [114] the value of  $\hat{a}_{LL}^{J/\psi}$  has been forced to  $-1$ . The SPD setup will have the possibility  
 513 to reconstruct  $\chi_c J$  states via their radiative decays and resolve  $J/\psi$  and  $\psi(2S)$  signals in a wide kinematic  
 514 range and disentangle contributions of different production mechanisms. The quality of the  $\Delta g$  estimation  
 515 could be significantly improved by measuring  $A_{LL}$  separately for each charmonium state.

516 Predictions for the longitudinal double-spin asymmetries  $A_{LL}$  in  $p$ - $p$  collisions can be found in Refs. [124]  
 517 ( $J/\psi$ ) and [125] (prompt photons). They mostly cover the kinematic range of the RHIC experiments.  
 518 Some estimates for  $A_{LL}$  in charmonia [122] and prompt-photon [122, 126, 127] production at  $\sqrt{s} =$   
 519 39 GeV (see Figs. 2.8 and 2.9, respectively) have been done in preparation of the unrealized HERA- $\vec{N}$   
 520 project.

521 The authors of the Ref. [128] proposed to extract information about the gluon helicity  $\Delta g$  via studying  
 522 of the production of high- $p_T$  prompt photons accompanied by  $\Sigma^+$  hyperons. To do that the single lon-  
 523 gitudinal spin asymmetry  $A_L^{\Sigma^+}$  and the polarization of the produced  $\Sigma^+$  hyperons should be measured.  
 524 However, further elaboration of this method is needed.

## 525 1.8 Gluon-related TMD and twist-3 effects with transversely polarized beams

526 One of the promising ways to investigate the spin structure of the nucleon is the study of transverse single-  
 527 spin asymmetries (SSAs) in the inclusive production of different final states in high-energy interactions.  
 528 The SSA  $A_N$  is defined as

$$A_N = \frac{\sigma^\uparrow - \sigma^\downarrow}{\sigma^\uparrow + \sigma^\downarrow}, \quad (2.9)$$

529 where  $\sigma^\uparrow$  and  $\sigma^\downarrow$  denote the inclusive production cross sections with opposite transverse polarization of  
 530 one of the colliding particles. At the moment, more than forty years after the transverse spin phenom-  
 531 ena were discovered, a wealth of experimental data indicating non-zero  $A_N$  in the lepton-nucleon and  
 532 nucleon-nucleon interactions was collected. However, our understanding of the SSA phenomenon is not  
 533 yet conclusive.

534 Theoretically two dual approaches are used to explain the transverse single-spin asymmetries: the collinear  
 535 twist-3 formalism and the transverse momentum dependent (TMD) factorization approach. In the first

one at large transverse momenta  $p_T \gg \Lambda_{QCD}$  of a produced particle, the collinear factorization involving twist-3 contributions for three-parton (Efremov-Teryaev-Qiu-Sterman) correlations [129–132] are used. Here  $\Lambda_{QCD} \approx 200$  MeV is the QCD scale. An alternative approach assumes the TMD factorization, valid for  $p_T \ll Q$ , where the SSAs come from the initial-state quark and gluon Sivers functions or the final-state Collins fragmentation functions. The Sivers function  $f_{1T}^{\perp, q(g)}(x, k_T)$  is a TMD PDF that describes the left-right asymmetry in the distribution of the partons w.r.t. to the plane defined by the nucleon spin and momentum vectors. Originating from the correlation between the spin of the nucleon and the orbital motion of partons, it is an important detail of the three-dimensional picture of the nucleon. This function is responsible for the so-called Sivers effect (for both quarks and gluons) that was first suggested in [133] as an explanation for the large single transverse spin asymmetries  $A_N$  in the inclusive production of the nucleon. More on the theoretical and experimental status of the transverse spin structure of the nucleon can be found in Refs. [13, 134]. The first attempt to access the gluon Sivers function (GSF) studying azimuthal asymmetries in high- $p_T$  hadron pair production in SIDIS of transversely polarised deuterons and protons, was performed by COMPASS [20]. Using neural network techniques the contribution originating from Photon–Gluon Fusion (PGF) subprocess has been separated from the leading-order virtual-photon absorption and QCD Compton scattering subprocesses. The measured combined proton-deuteron PGF-asymmetry was found to be negative and more than two standard deviations below zero, which supports the possible existence of a non-zero Sivers function. In the meantime, COMPASS did not see any signal for the PGF Collins asymmetry, which can analogously be related to the gluon transversity distribution. COMPASS studied GSF also through Sivers asymmetry in the  $J/\psi$ -production channel [21], again obtaining an indication of a negative asymmetry.

Recently, in Ref. [135] a first estimate of the GSF was obtained using the midrapidity data on the  $A_N$  SSA, measured in  $\pi^0$  production at RHIC [16]. The extraction was performed within the GPM framework using GRV98-LO set for the unpolarized PDF and available parameterizations for the quark Sivers functions (SIDIS1 from Ref. [136] and SIDIS2 from Ref. [137]). The two parameterizations were obtained using different options for fragmentation functions, namely Kretzer [138] and DSS07 [139] sets, which give significantly different results for gluons. The latter point has a strong impact on the extracted GSF especially in low- $x$  region. First  $k_T$ -moments of the GSF  $\Delta_N^{q(g)}(x, k_T)$  for the SIDIS1 and SIDIS2 sets are shown in Fig. 2.10 (a) and (b), respectively.

The gluon Sivers function is expected to satisfy the positivity bound defined as two time the unpolarized TMD gluon distribution. Although, some theoretical expectations are that the gluon Sivers function at relatively high  $x$  is about 1/3 of the quark one [134].

Several inclusive processes were proposed to access the gluon-induced spin effects in transversely polarized  $p$ - $p$  collisions. Single spin asymmetries for production of charmonia [140] (RHIC, AFTER), open charm [141–144] (RHIC) [144] (AFTER), and prompt photons [131, 145] (E704), [146] (RHIC) were estimated using both approaches for the experimental conditions of the past, present, and future experiments.

The SSA  $A_N^{J/\psi}$  in the  $J/\psi$  production was measured by PHENIX in the  $p$ - $p$  and  $p$ -A collisions at  $\sqrt{s_{NN}} = 200$  GeV/ $c$  [17, 18]. The obtained values for  $A_N^{J/\psi}$  are consistent with zero for negative and positive  $x_F$ . Theoretical predictions [140] based on the Color Evaporation Model with TMD approach and the gluon Sivers function from Ref. [147] for different center-of-mass energies are shown in Fig. 2.11(a) as functions of rapidity  $y$ . Since the  $J/\psi$  production mechanism is not well understood, the measurement of the  $A_N^{J/\psi}$  may bring a valuable input to that matter as well. Predictions for  $A_N^{J/\psi}$  in proton-proton collisions at NICA energy  $\sqrt{s} = 27$  GeV, obtained in GPM + NRQCD approach, as function of  $x_F$  and  $p_T$  are shown in the Figure (2.12). For comparison, results are presented for SIDIS1 [136] and D’Alesio et al. [148, 149] parameterizations of proton Sivers function.

582 A measurement with open-heavy hadrons (both  $D$ - and  $B$ -mesons) was performed at RHIC (PHENIX,  
 583  $\sqrt{s} = 200$  GeV) [19] using high- $p_T$  muons from their semileptonic decays. Obtained results are affected  
 584 by relatively large statistical uncertainties and do not exhibit any significant non-zero asymmetry. Never-  
 585 theless, the results do not contradict the predictions of the twist-3 approach from Ref. [142]. The Siv-  
 586 ers effect contribution to the  $A_N^D$  asymmetry calculated within the Generalized Parton Model for  $\sqrt{s} = 27$   
 587 GeV is presented in Fig. 2.11(b).

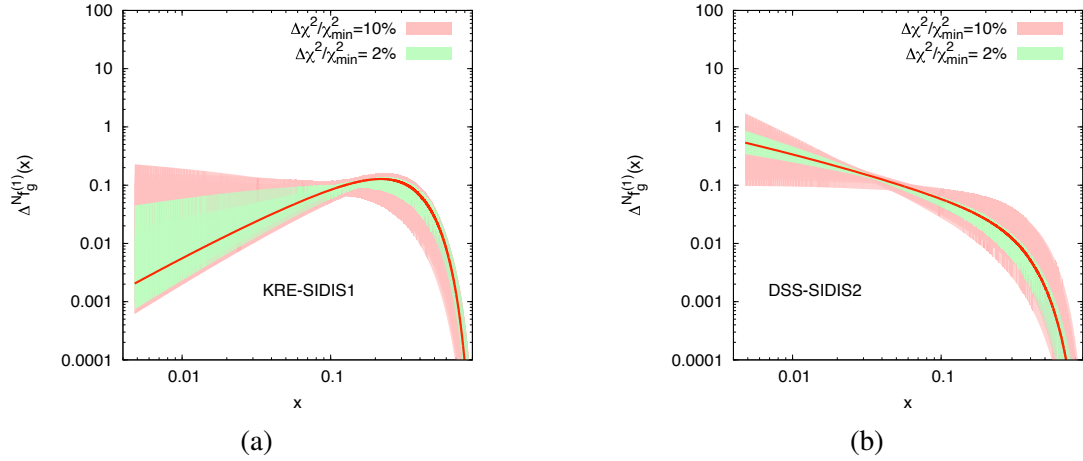


Figure 2.10: The first  $k_T$ -moment of the gluon Siv-ers function for SIDIS1 [136] and SIDIS2 [137] extractions of the quark Siv-ers functions [135].

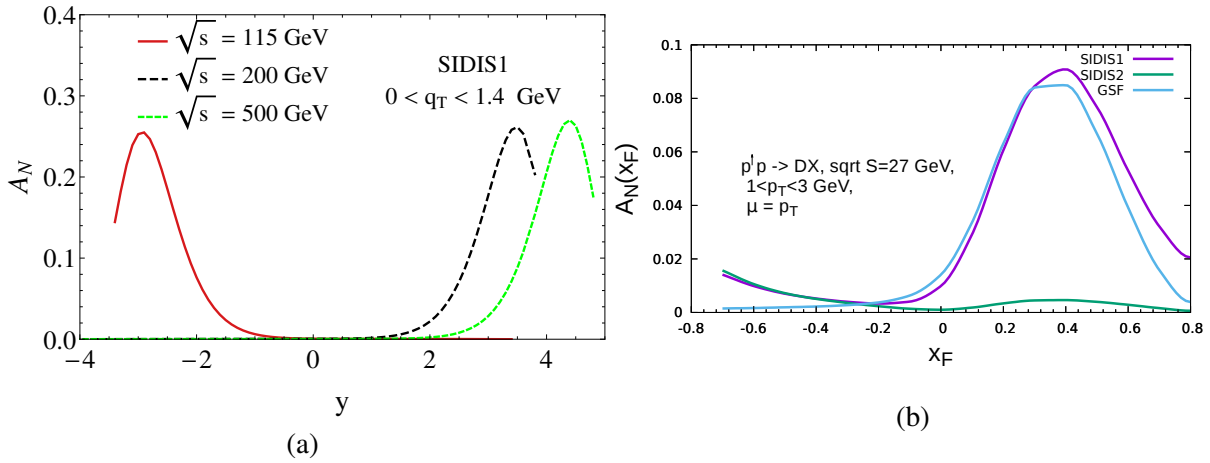


Figure 2.11: (a) Predictions for  $A_N^{J/\psi}$  for  $\sqrt{s} = 115$  GeV (AFTER), 200 GeV and 500 GeV (RHIC) as a function of rapidity  $y$  [140]. (b) Siv-ers effect contribution to the  $A_N^D$  asymmetry calculated within the Generalized Parton Model.

588 Measurement of the  $A_N^\gamma$  SSA with prompt photons provides a unique opportunity to study the Siv-ers PDF  
 589 and twist-3 correlation functions, since the corresponding hard process does not involve fragmentation  
 590 in the final state and thus is exempt from the Collins effect. The first attempt to measure  $A_N^\gamma$  at  $\sqrt{s} = 19.4$   
 591 GeV was performed at the fixed target experiment E704 at Fermilab in the kinematic range  $-0.15 < x_F <$   
 592  $0.15$  and  $2.5 \text{ GeV}/c < p_T < 3.1 \text{ GeV}/c$ . The results were consistent with zero within large statistical and  
 593 systematic uncertainties [150]. Figure 2.13(a) shows the expected  $A_N^\gamma$  asymmetry as a function of  $x_F$  for  
 594  $\sqrt{s} = 27$  GeV based on the SIDIS1 extraction of the gluon Siv-ers function. Quark and gluon contributions  
 595 from the gluon Compton scattering, dominating at positive and negative values of  $x_F$ , respectively, are  
 596 shown separately. The  $q\bar{q}$  annihilation contribution is also presented. Dashed lines illustrate the twist-3



597 predictions for  $\sqrt{s} = 30$  GeV and  $p_T = 4$  GeV/c for negative [145] and positive [131] values of  $x_F$ . The  
 598  $p_T$  dependence of the  $A_N^\gamma$  asymmetry at  $x_F = -0.5$  is shown for different values of  $\sqrt{s}$  in Fig. 2.13(b).

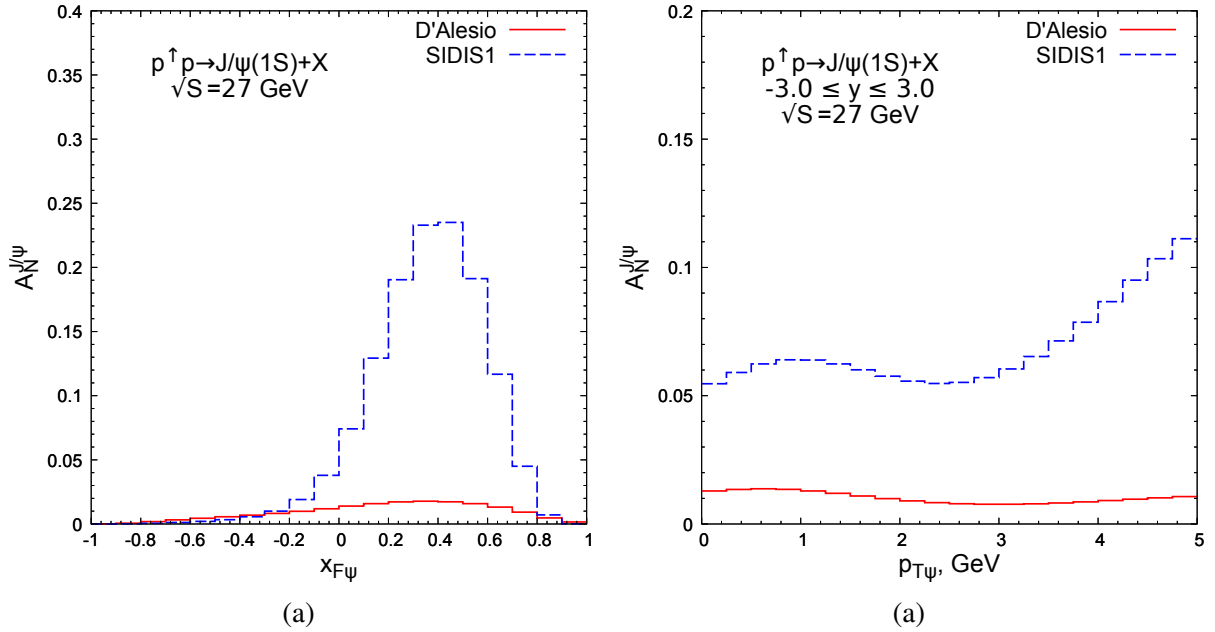


Figure 2.12: Predictions for  $A_N^{J/\psi}$  as function of  $x_F$  (a) and  $p_T$  (b) in  $p$ - $p$  collisions at the energy  $\sqrt{s} = 27$  GeV obtained in GPM + NRQCD approach.

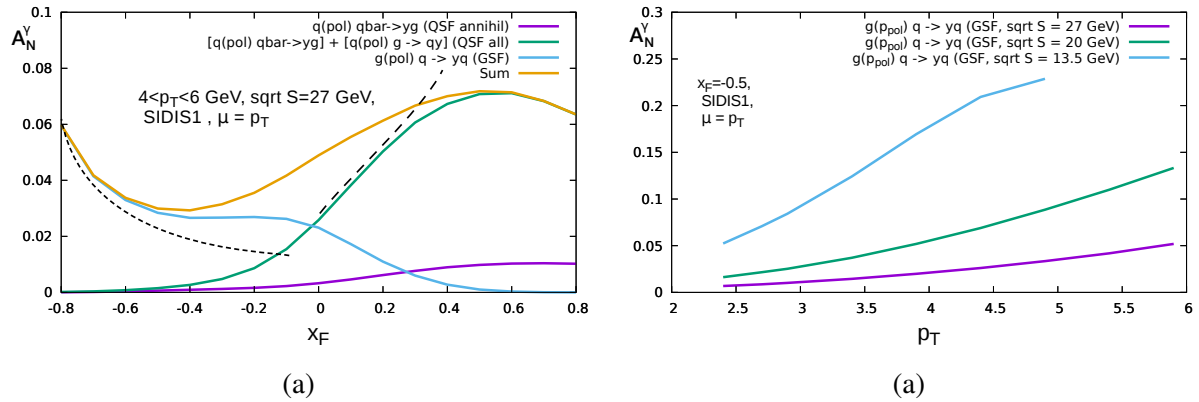


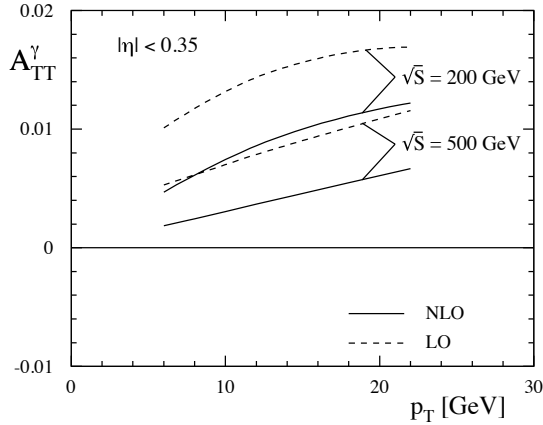
Figure 2.13: (a)  $x_F$  dependence of the asymmetry  $A_N^\gamma$  calculated based on the SIDIS1 Siverts function for  $\sqrt{s} = 27$  GeV and  $4 < p_T < 6$  GeV. Gluon and quark contributions are shown separately by color solid lines. Dashed lines illustrate the twist-3 predictions for  $\sqrt{s} = 30$  GeV and  $p_T = 4$  GeV for negative [145] and positive [131] values of  $x_F$ . (b)  $p_T$  dependence of the  $A_N^\gamma$  asymmetry for different values of  $\sqrt{s}$  at  $x_F = -0.5$ .

## 599 1.9 Gluon transversity in deuteron

600 The transversity function  $\Delta_T q(x)$  is defined for partons as the difference of probabilities to find in a  
 601 transversely polarized nucleon a parton with the same and opposite spin orientations. In spite of the  
 602 definition is similar to the helicity function  $\Delta q(x)$ , the transversity describes a completely different aspect  
 603 of the nucleon spin structure. This function is known quite well after a series of SIDIS and Drell-Yan  
 604 experiments. As soon as the transversity is related with the spin flip, for the spin-1/2 nucleon only a  
 605 quark contribution ( $\Delta s = 1$ ) is possible while  $\Delta s = 2$  for the spin-1 gluons is forbidden in the twist-2.

606 Nevertheless, a tiny nonzero gluon transversity is allowed due to higher-twist effects and possible physics  
 607 beyond the Standard model like electric dipole moment of the neutron [151]. The transverse double spin  
 608 asymmetry  $A_{TT}$  defined for interaction of transversely polarized hadrons by the similar manner as  $A_{LL}$   
 609 is a way to access the transversity. But due to the absence of a gluonic contribution in the leading order  
 610 in the case of the nucleon interactions  $A_{TT} \ll A_{LL}$ . As an example, the asymmetry  $A_{TT}^\gamma$  for the prompt-  
 611 photon production at 200 and 500 GeV coming from the  $q\bar{q}$  annihilation process calculated in LO [152]  
 612 and NLO [153] is shown in Fig. 2.14(b).

613 Situation changes [154] for the spin-1 deuteron where a gluon component not embedded into the nucleons  
 614 is possible. So in the collision of transversely polarized deuterons a nonzero contribution of the gluon  
 615 transversity  $\Delta_T g(x)$  to  $A_{TT}$  asymmetries is possible already in the twist-2. At the moment there is no any  
 616 experimental data on the gluon transversity in the deuteron. The gluon-induced (NLO) Drell-Yan process  
 617  $qg \rightarrow q\gamma^* \rightarrow q\mu^+\mu^-$  was proposed in Ref. [151] as a way to access it in the polarized  $p$ - $d$  collisions at  
 618 the SpinQuest experiment at Fermilab. A measurement of the double transverse spin asymmetries  $A_{TT}$   
 619 in the gluon-induced processes at polarized  $d$ - $d$  collisions at NICA SPD could be an alternative way to  
 620 access the  $\Delta_T g(x)$ .



(a)

Figure 2.14: (a)  $A_{TT}^\gamma$  asymmetry for the prompt-photon production at 200 and 500 GeV coming from the  $q\bar{q}$  annihilation process calculated in LO [152] and NLO [153].

### 621 1.10 Deuteron tensor polarization and shear forces

622 The availability of tensor polarized deuteron beam opens a possibility to study shear forces generated  
 623 by quarks and gluons [155]. The natural way to get the traceless part of the energy-momentum tensor  
 624 related to shear is provided just by tensor polarization, as the relevant tensor  $S^{\mu\nu}$  is a traceless one by  
 625 construction. The contribution of the "tensor polarized" parton distribution  $C^T$  [156, 157] (introduced as  
 626 an "aligned" one [158]) is constrained by the zero sum rule [158] for its second moment (complementing  
 627 the Close-Kumano sum rule [157]) which may be decomposed into quark and gluon components [159]:

$$\sum_{i=q,\bar{q}} \int_0^1 C_i^T(x) dx = \delta_T(Q^2), \quad (2.10)$$

$$\int_0^1 C_G^T(x) dx = -\delta_T(Q^2). \quad (2.11)$$

628 As a result, the matrix elements of energy momentum tensors of quarks and gluons look like

$$\sum_i \langle P, S | T_i^{\mu\nu} | P, S \rangle_{Q^2} = 2P^\mu P^\nu (1 - \delta(Q^2)) + 2M^2 S^{\mu\nu} \delta_T(Q^2) \quad (2.12)$$

$$\langle P, S | T_g^{\mu\nu} | P, S \rangle_{\mu^2} = 2P^\mu P^\nu \delta(Q^2) - 2M^2 S^{\mu\nu} \delta_T(Q^2), \quad (2.13)$$

629 where the second terms describe the average (integrated over transverse distance) shear force. Here  $M$  is  
630 the nucleon mass.

631 The zero sum rules (2.10) were later interpreted [160] as yet another manifestation of Equivalence Prin-  
632 ciple (EP), as it was done earlier [161] for Ji sum rules. In turn, the smallness of  $\delta_T$ , compatible with  
633 the existing HERMES data, was suggested [160] to be the new manifestation of Extended Equivalence  
634 Principle (ExEP) [162–164] valid separately for quarks and gluons in non-perturbative QCD due to the  
635 confinement and chiral symmetry violation. It was originally suggested for anomalous gravitomagnetic  
636 moments [162, 164]. In particular, it provides the rotation of spin in the terrestrial experiment with the  
637 angular velocity of Earth rotation. Let us stress, that it may seem trivial if spin is considered just as a  
638 vector. However, it became highly non-trivial if the measurement of spin by the device rotating together  
639 with Earth is taken into account. This is a particular example of the practical importance of the quantum  
640 theory of measurement. Another example may be represented by the Unruh radiation in heavy-ion colli-  
641 sions [165], which implies that the particles production may be also considered as a quantum-mechanical  
642 measurement in the non-inertial hadronic medium.

643 Recently, ExEP was also discovered for the pressure [166].

644 To check ExEP for shear force one may use future studies of DIS at JLab and of Drell-Yan process with  
645 tensor polarized deuterons [167]<sup>5</sup>.

646 Note that tensor polarized parton distribution may be also measured in *any* hard process with the relevant  
647 combination of deuteron polarizations, in particular, for large  $p_T$  pions production, providing much better  
648 statistics. The correspondent quantity can be the P-even Single Spin asymmetry

$$A_T = \frac{d\sigma(+)+d\sigma(-)-2d\sigma(0)}{d\sigma(+)+d\sigma(-)+d\sigma(0)} \sim \frac{\sum_{i=q,\bar{q},g} \int d\hat{\sigma}_i C_i^T(x)}{\sum_{i=q,\bar{q},g} \int d\hat{\sigma}_i q_i(x)}, \quad (2.14)$$

649 where the differential cross section with definite polarization of deuteron appear.

650 Note that due to the tensor polarization tensor being traceless the sum rule for the three mutually orthog-  
651 onal orientations of coordinate frame is valid [158]:

$$\sum_i S_{zz}^i = 0. \quad (2.15)$$

652 As a result, the leading twist kinematically dominant "longitudinal" tensor polarization can be obtained  
653 by accelerating *transverse* polarized deuterons which will be accessible at NICA.

---

<sup>5</sup>Complementary probes are provided by vector mesons [163].

654 **2 Quarks in proton and deuteron**

 655 **2.1 SSA for pions and kaons**

 656 **2.2 Drell-Yan pair production**

657 Production of Drell-Yan (DY) pairs in polarized hadronic collisions  $pp \rightarrow \gamma^* \rightarrow \mu^+ \mu^-$  is a promising  
 658 way to touch TMD PDFs of valence quarks and sea antiquarks via the measurement of azimuthal asymmetries.  
 659 A tiny DY cross section and huge combinatorial background coming from decays of secondary  
 660 pions and kaons into muons make this task rather difficult. A typical detector configuration for such  
 661 kind of studies at  $\sqrt{s} \sim 20$  GeV is a fixed-target beam-dump setup where due to the Lorentz boost the  
 662 most of secondary pions and kaons are stopped in a thick absorber before their decay. At the moment  
 663 only the COMPASS experiment at CERN has presented the results for the three azimuthal asymmetries  
 664 measured in pion-induced polarized DY [168, 169]. The observed glimpse of the sign change in Sivers  
 665 asymmetries is found to be consistent with the fundamental prediction of QCD that the Sivers TMD PDF  
 666 extracted from DY has a sign opposite to the one extracted from SIDIS data. Unique results for the Sivers  
 functions of  $\bar{u}$  and  $\bar{d}$  are expected from the SpinQuest experiment at Fermilab [170, 171].

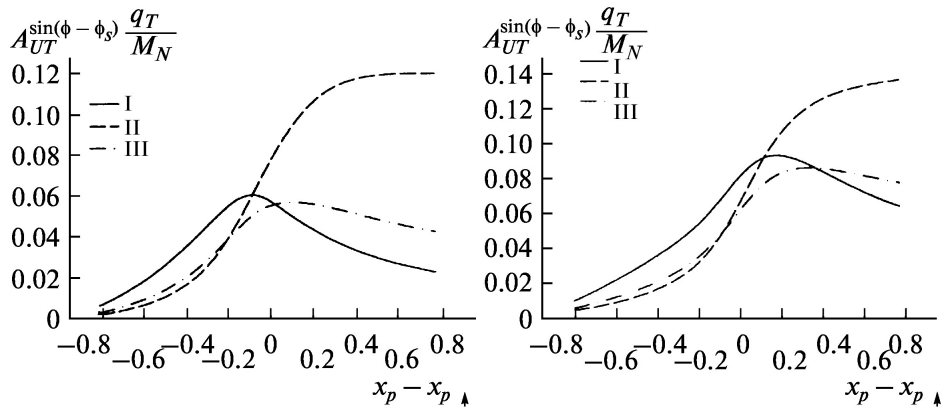


Figure 2.15: Estimated Sivers asymmetries for NICA conditions  $s = 20$  GeV,  $Q^2 = 4$  GeV<sup>2</sup> (left) and  $s = 20$  GeV,  $Q^2 = 15$  GeV<sup>2</sup> (right). Fits for Sivers functions are taken from [172].

667

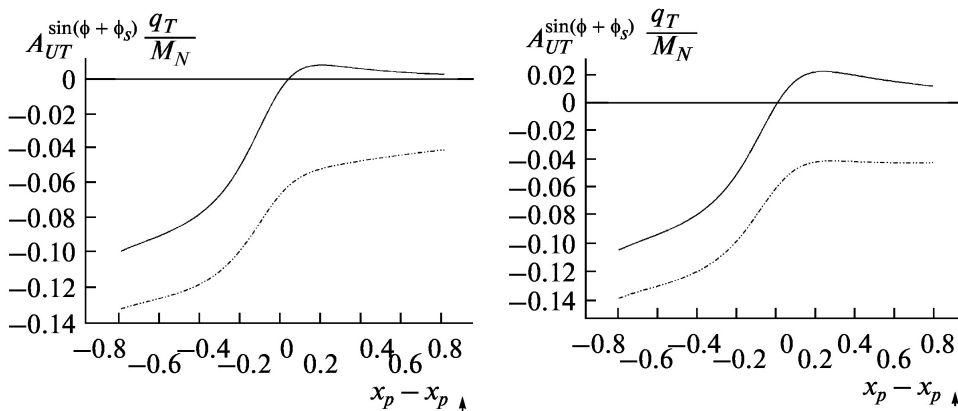


Figure 2.16: Estimated Boer-Mulders asymmetries for NICA conditions.

668 Unfortunately the Spin Physics Detector cannot use the advantage of fixed-target beam-dump setups and  
 669 expected background conditions for the Drell-Yan measurements are rather untoward. However further  
 670 improvement of experimental techniques and analysis procedures could give a chance to access polarized  
 671 DY at SPD. Estimated Siverts and Boer-Mulders asymmetries for SPD conditions are presented at Fig.  
 672 2.15 and 2.16, respectively.

### 673 2.3 Generalized parton distributions

674 The concept of Generalised Parton Distributions (GPDs) is a complementary to TMD PDFs approach  
 675 to describe the three-dimensional structure of hadrons. Study of the deeply virtual meson production  
 676 (DVMP) is one of the proven ways to access GPDs. This process has been investigated at [] ... using  
 677 lepton and photon beams. An exclusive electromagnetic process  $pp \rightarrow ppM$  Fig. 2.17(a) where the  
 678 first proton radiates a photon with low virtuality that interacts with the other proton and produce the  
 679 meson, could be used to access Generalised Parton Distributions at SPD. At SPD energies the meson  
 680 photoproduction amplitude can be presented in a factorized form as a convolution of the hard scattering  
 681 part which can be calculated perturbatively and the GPDs [173, 174]. In case of vector mesons production  
 682 the odderon exchange (that could be described as exchange by at least 3 gluons) is also possible and  
 683 the interference of these two channels is the matter of special interest. Ultrapерipheral  $p$ - $A$  collisions  
 684 at SPD which enhance the photoproduction contribution by several orders of magnitude could also be  
 685 considered. Ultrapерipheral processes could be also used for test of the most general non-perturbative  
 686 concept of the Generalized Transverse Momentum dependent Distributions (GTMD). This possibility  
 687 was explored for high energies in Ref. [175] but the approach could be extended down to the SPD  
 688 energies.

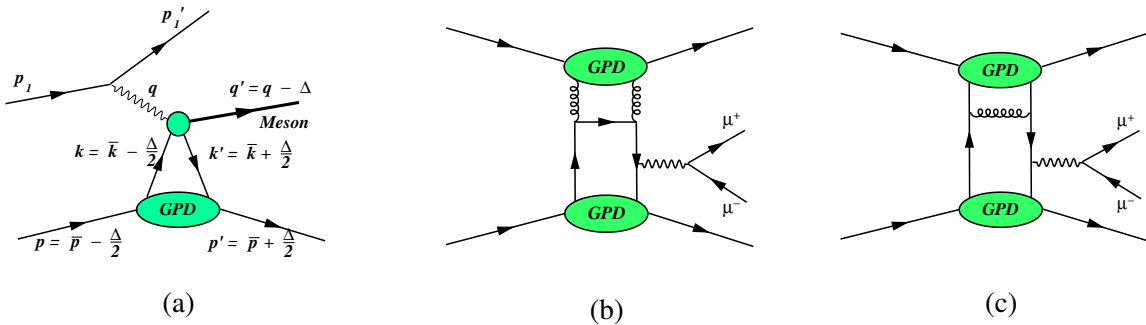


Figure 2.17: (a) Vector meson production at NICA via photoproduction mechanism or odderon exchange.  
 (b) Drell-Yan process with gluon and quark GPDs.

689 The exclusive production of the  $J/\psi$  meson can be studied at SPD at energies  $W = \sqrt{(q+p)^2} \sim 5 -$   
 690  $15$  GeV. Here  $q$  and  $p$  are the 4-momenta of a virtual photon (odderon) and a proton, respectively.  
 691 Large meson mass makes possible to perform perturbative calculations at sufficiently low  $Q^2$  where  
 692 the the photon exchange should dominate. The corresponding cross section is estimated to be of about  
 693  $\sigma_{J/\psi} \sim 10$  nb. The main contribution to the cross section is coming from the gluon GPDs.

694 The exclusive Drell-Yan (exDY) process was proposed for study of GPDs in  $p$ - $p$  collisions in Ref. [176].  
 695 The kinematics of this process is defined by convolution of two GPDs. Both quark and gluon GPDs  
 696 contribute to the exDY cross section via the diagrams shown schematically at Fig. .

697 Investigation of the cross section determined by two-GPDs effects is in progress now [177]. It is shown  
 698 that the gluon and sea quark GPDs lead to the cross section which does not decrease with the grows of  
 699 energy. The exDY cross section  $d\sigma/dQ^2$  at NICA kinematics  $\sqrt{s} = 24$  GeV and  $Q^2 = 5$  (GeV/c) $^2$  is  
 700 estimated as 3 pb/(GeV/c) $^2$  that is much smaller with respect to the inclusive Drell-Yan cross section.

701 Nevertheless exclusivity requirement applied in the analysis of future SPD dimuon data could increase  
702 the signal-to-background ratio. It should be mentioned that  $J/\psi$  could also be produced exclusively in  
703 the similar way.

#### 704 **2.4 Polarized fragmentation functions**

### 705 3 Tests of QCD basics at low energies [U. Uzikov, A. Guskov]

#### 706 3.1 Elastic $pp$ and $dd$ scattering

#### 707 3.2 Multiquark correlations and systems

#### 708 3.3 Central nucleon-nucleon collisions [Komarov]

709 The main experimental basis for clarification of the non-perturbative QCD (NPQCD) baryon structure  
 710 is the baryon spectroscopy and the short-range nucleon-nucleon interaction. The more the nucleons  
 711 are overlapped during collision, the higher sensitivity of the latter to the NPQCD structure. Maximum  
 712 sensitivity can be reached in conditions of overlapping of the quark core of nucleons and sufficiently  
 713 long time of this overlapping. Unfortunately, these conditions practically are not met in the available  
 714 nucleon-nucleon experimental data: at relatively low energies the effective momentum transfers are not  
 715 sufficiently high, and at high energies the contents of colliding nucleons diverge too quickly. This cir-  
 716 cumstance explains why the region of the  $NN$  collisions at distances smaller than the radius of the nucleon  
 717 core still remains unexplored. Access to this area is possible through the central collisions (CC) of the  
 718 nucleons at adequate energies. The collisions are usually named central if the corresponding impact  
 719 parameter  $R$  is small,  $R < r_{core} \approx 0.4 fm$ .

720 Overlapping of the nucleon cores can be achieved at the center-of-mass (CM) energies  $\sqrt{s_{min}} = U_{rep}(0) +$   
 721  $2m_N$ , where  $U_{rep}(0)$  is the repulsive potential of the  $NN$  interaction at zero distance,  $U_{rep}(0) \approx 1 GeV$ .  
 722 Then the minimal energy of interest is  $\sqrt{s_{min}} \approx 2.9 GeV$ . At the energies less than 7.5 GeV (correspond-  
 723 ing the chiral symmetry breaking momentum  $\Lambda_{\chi SB} \approx 1.2 GeV/c$  [178, 179]) the resulting intermediate  
 724 state is an excited  $(6q)^*$  system of six chiral constituent quarks interacting via goldstone boson, gluon  
 725 exchange and confinement potential. This interaction is supposed to be much more intensive than in the  
 726 perturbative quark-gluon system, and provides therefore relatively long lifetime of the system, sufficient  
 727 for manifestation of the NPQCD structure. In some conditions, it can even produce quasi-bound states,  
 728 resonance dibaryons. It should be stressed that the  $(6q)^*$  system under consideration is characterized by  
 729 very high baryon and energy densities since two baryons and the whole CM energy is concentrated in a  
 730 small volume of about  $4/3\pi(r_{core})^3$  size.

731 Decay of the  $(6q)^*$  system leads to reconstruction of hadronic states in the form

$$p + p \rightarrow (6q)^* \rightarrow N + N + Mesons, \quad (2.16)$$

732 where  $Mesons$  denotes the system of light mesons, predominantly pions.

733 Peripheral  $NN$  collisions proceed mainly via production of excited baryons  $N^*$  in the intermediate state

$$p + p \rightarrow \{(N + N^*) \text{ or } (N^* + N^*)\} \rightarrow N + N + Mesons \quad (2.17)$$

734 and have, in general, the final states similar to that in the central collisions (2.16). Therefore, in order  
 735 to distinguish the central collision process (2.16) from the peripheral (2.17), one needs special centrality  
 736 criteria. According to [180, 181], there are two such criteria: A) using of the reaction

$$N + N \rightarrow d(90^\circ) + Mesons, \quad (2.18)$$

737 where  $d(90^\circ)$  is a deuteron emitted at the angle close to  $90^\circ$ <sup>6</sup>; B) smallness of the interaction region size  
 738  $r_{int} < r_{core}$ , where  $r_{int} = 1/(-Q^2)^{1/2}$  with  $Q = P_1 - D/2$ . Here  $P_1$  is the four-momentum of one of the  
 739 initial nucleons and  $D$  is the four-momentum of the final joined nucleon pair.

<sup>6</sup>or reaction  $N + N \rightarrow \{pp\}_{S_0}(90^\circ) + Mesons$ , where  $\{pp\}_{S_0}$  is a proton pair in the  $^1S_0$  state

740 Evaluation of feasibility of experiments with the above centrality criteria shows [181] that at the expected  
 741 luminosity [29] the event rate in SPD will be at the level of tens events per second. Hence, rather large  
 742 amount of information about the processes of interest can be obtained in a reasonable time.

743 The following goals can be aimed, in particular, in experiments with central collisions:

- 744 – study of known and search for new dibaryon resonances in the region of  $\sqrt{s} \approx 2.5 - 7.5$  GeV;
- 745 – search for the predicted dominance of the  $\sigma$ -meson production [182];
- 746 – search for the expected effects caused by the chiral symmetry partial restoration (drop of mass and  
 747 width of mesons) [183, 184];
- 748 – study of the energy dependence of the reaction (2.18) cross section, what is sensitive to the strength  
 749 of the confinement forces and the value of the chiral symmetry breaking momentum;
- 750 – first measurement of the analyzing power of the reaction (2.18) for transverse and longitudinal  
 751 beam polarization.

752 It is worth to mention that experiments of this kind have never been carried out systematically. There  
 753 exists a possibility to observe new unexpected effects that can induce new approaches in solving the  
 754 fundamental problems of the non-perturbative QCD.

### 755 **3.4 Exclusive hard processes with deuteron [M. Strikman]**

756 Questions involved in studies of the short-range / high momentum nuclear structure and understanding  
 757 microscopic nucleon structure and dynamics of large momentum transfer processes are delicately inter-  
 758 twined: understanding of hard dynamics of two body processes is also necessary for precision studies of  
 759 the short range nuclear structure. Exclusive large  $t$  reactions like  $p^2H \rightarrow ppn$  process can address many  
 760 of these questions. Advantages of such reaction is a good knowledge of the nonrelativistic deuteron  
 761 wave function and ability to choose both kinematics sensitive to dynamics of elastic NN scattering and  
 762 the kinematics sensitive to short range deuteron structure. The collider kinematics presents a number  
 763 of advantages as all particles in the reactions in question have large momenta and hence can be easily  
 764 detected.

#### 765 **3.4.1 Probing dynamics of NN interaction**

766 The simplest kinematics is production of two nucleons approximately back to back large transverse  
 767 momenta and spectator nucleon with longitudinal momentum  $p \sim p_{2H}/2$  and transverse momentum  $\geq$   
 768 200 MeV/c [185, 186].

769 In the impulse approximation this process corresponds to elastic scattering of the projectile proton off  
 770 a quasifree nucleon of the target. In this kinematics soft rescatterings of the initial and final nucleons,  
 771 which accompany the hard  $pp(pn)$  reaction are large. The eikonal approximation, which accounts for  
 772 relativistic kinematics as dictated by the Feynman diagrams, reveals the important role played by the ini-  
 773 tial and final state interactions in the angular and momentum dependences of the differential cross section  
 774 in well defined kinematics. The condition for the applicability of the generalized eikonal approximation  
 775 [187] is that the c.m. scattering angle and invariant mass of the two nucleon system are large enough so  
 776 that  $-t, -u \geq 2 \text{ GeV}^2$ .

777 It was suggested in [188, 189] that nucleons in the elementary reaction interact in small size configura-  
 778 tions with a small cross section - so called color transparency phenomenon. This effect is suppressed by  
 779 the space - time evolution of nucleon wave packets [190, 191]. However effect of evolution is very small



780 for the deuteron where typical distances between nucleons in the rescattering amplitude are is  $\leq 1.5$  fm.  
 781 Hence the discussed process allows to measure the wave packet size of a nucleon practically right in the  
 782 interaction point.

783 It was pointed out that the hard dynamics in  $pp$  and  $pn$  elastic scattering may be rather different [192].  
 784 Hence it would be instructive to compare the channels where  $pp$  and  $pn$  are produced with large  $p_t$ .

785 Experiments with polarized beams would greatly add to this program: due to a better separation of kine-  
 786 matic domains where impulse approximation, double and triple scattering dominate, while the studies  
 787  $\vec{p}\vec{d} \rightarrow pNN$  processes will allow both to study spin structure of  $pp$  and  $pn$  elastic scattering at large  $t$  (the  
 788 later is practically not known). Also, it would be possible to find out whether the a strong difference be-  
 789 tween the cross sections of elastic scattering of protons with parallel and antiparallel spins[193] involves  
 790 collisions of protons in configurations with sizes depending on the spin orientation.

791 It would be possible also to study effects of coherence in the channels where exchange by gluons in  
 792 t-channel is not possible, for example  $pd \rightarrow \Delta NN$ . In particular, it would be possible to test the effect of  
 793 chiral transparency suggested in [194] - suppression of the pion field in the nucleons experiencing large  
 794  $-t$  scattering.

### 795 3.4.2 Probing microscopic deuteron structure

796 It is established now that the dominant source of the short range/ high momentum correlations (SRC)  
 797 in nuclei are proton - neutron correlations with the same quantum numbers as the deuteron and with  
 798 high momentum tail similar to that in the deuteron, see review in [195, 196]. Hence the deuteron serves  
 799 as a kind of the hydrogen atom of the SRC physics. Only after it would be tested experimentally that  
 800 approximations currently used for the description of the  $p^2H$  reaction work well, it would be possible to  
 801 perform high precision studies of SRC in heavier nuclei.

802 It was demonstrated in Ref.[185, 186] that under specific kinematical conditions (in particular low trans-  
 803 verse momenta of a slow nucleons in the deuteron rest frame)) the effect of initial and final state inter-  
 804 actions can be accounted for by rescaling the cross section calculated within the plane wave impulse  
 805 approximation. In this kinematics it would be possible to check universality of the wave function - in  
 806 particular its independence on the momentum transfer in the elementary reaction. Such factorization is  
 807 expected to break down at sufficiently large  $-t$  and  $-u$  where scattering involves interaction of nucleons  
 808 in the small size configurations (the color transparency regime) since the small size configurations are  
 809 suppressed in bound nucleons with suppression growing with the nucleon off shellness [191].

810 Studies of the nonnucleonic configurations in the deuteron as well as relativistic effects. in the scattering  
 811 off a polarized deuteron are of separate interest. In particular, it would be possible to a search for non-  
 812 nucleonic degrees of freedom like 6 quark, two  $\Delta$  isobars via production reaction  $p^2H \rightarrow \Delta^{++} + p + \Delta^-$   
 813 with  $\Delta^{++}$  and proton back to back and  $\Delta^-$  being slow in the deuteron rest frame.

### 814 3.5 Polarized $pd$ elastic scattering within the Glauber model and $pN$ spin amplitudes [Yu. Uzikov]

815 Nucleon-nucleon elastic scattering contains fundamental information on the dynamics of the  $NN$  inter-  
 816 action and constitutes a basic process in physics of atomic nuclei and hadrons. Full information about  
 817 spin amplitudes of  $pp$  and  $pn$  elastic scattering can be obtained, in principle, from complete polarization  
 818 experiment, which, however, requires to measure dozen independent observables at given collision en-  
 819 ergy that constitutes too complicated experimental task. A systematic reconstruction of these amplitudes  
 820 from scattering data is provided by the SAID data base [197] and covers laboratory energies up to 3 GeV  
 821 ( $p_{lab} \approx 3.8$  GeV/c) for  $pp$  and 1.2 GeV ( $p_{lab} \approx 1.9$  GeV/c) for  $pn$  scattering. At higher energies there  
 822 are only non-complete data on  $pp$  scattering, whereas information about the  $pn$  system is very scarce.  
 823 In the literature there are some models and corresponding parametrizations for  $pN$  amplitudes, obtained

824 in the eikonal approach [198] for the lab momentum 6 GeV/c and within the Regge phenomenology  
 825 [199] for 3-50 GeV/c (corresponding to  $2.77 < \sqrt{s} < 10$  GeV). Another Regge-type parametrization for  
 826 values of  $s$  above 6 GeV<sup>2</sup> ( $p_{lab} \geq 2.2$  GeV/c) was presented in Ref. [200]. A possible way to check ex-  
 827 isting parametrizations is to study spin effects in proton-deuteron ( $pd$ ) and neutron-deuteron ( $nd$ ) elastic  
 828 and quasi-elastic scattering. At high energies and small four-momentum transfer  $t$ ,  $pd$  scattering can  
 829 be described by the Glauber diffraction theory of multistep scattering, which involves as input on-shell  
 830  $pN$  elastic scattering amplitudes. Applications of this theory with spin-dependent effects included [201]  
 831 indicate a good agreement with the  $pd$  scattering data at energies about 1 GeV if the SAID data on  $pN$   
 832 scattering amplitudes are used as starting point of the calculations [202, 203].

833 The spin-dependent Glauber theory [201, 202] is applied recently [204] to calculate spin observables  
 834 of  $pd$  elastic scattering at 3-50 GeV/c utilizing the  $pp$  elastic scattering amplitudes  $f_{pp}$  established and  
 835 parametrized in Ref. [199] within the Regge formalism. As a first approximation, for the  $pn$  amplitudes  
 836 was used likewise the ones for  $pp$  from [199]. The Regge approach allows one to construct  $pn$  (and  $\bar{p}N$ )  
 837 amplitudes together with the  $pp$  amplitudes. However, in view of the scarce experimental information  
 838 about the spin-dependent  $pn$  amplitudes and taking into account that the spin-independent parts of the  $pp$   
 839 and  $pn$  amplitudes at high energies are approximately the same, it was assumed in [204] that  $f_{pn} = f_{pp}$ .

840 The differential cross section of  $pp$ - elastic scattering and vector analyzing power  $A_y$  in the interval of  
 841 transferred four momentum  $0 < -t < 1.5$  GeV<sup>2</sup> are reasonable reproduced with the parameters from  
 842 Ref. [199]. Numerical results for the observables of  $pd$  elastic scattering obtained at  $p_l = 4.85$  GeV/c  
 843 and 45 GeV/c using  $pN$  amplitudes from [199] As shown in Ref. [204] available data on  $pd$ -elastic  
 844 differential cross section in forward hemisphere are well described by this model. Vector analyzing  
 845 power  $A_y^p$  decreases in absolute value with increasing energy and similar behaviour demonstrates the  
 846  $A_y^d$ . In contrast, the spin correlation coefficients  $C_{x,x}$  and  $C_{y,y}$  show an opposite tendency. One should to  
 847 note, that tensor analysing powers  $A_{xx}$  and  $A_{yy}$  are weakly changed with increasing energy, moreover  
 848 these observables are not changing qualitatively in forward direction if all spin-dependent amplitudes  
 849 are excluded and only the spin-independent  $pN$  amplitude is taken into account. On the hand, spin  
 850 correlation parameters  $C_{x,x}$ ,  $C_{y,y}$  vanishing in this case. The calculated in [204] polarization observables  
 851 of the  $pd$ -elastic scattering can be measured at SPD NICA that will provide a serious test of the used  
 852  $pN$  amplitudes. The corresponding differential cross section is rather large in the considered region  
 853  $p_{lab} = 3 - 50$  GeV/c and  $|t| = 0 - 2$  GeV<sup>2</sup> being  $d\sigma/dt > 0.1$  mb/GeV<sup>2</sup>. Expected counting rate  $N$   
 854 at  $p_{lab} = 50$  GeV/c ( $q_{pp}^{cm} = 5$  GeV/c) for the luminosity  $L = 5 \times 10^{30} cm^{-2} s^{-1}$  and for the solid angle  
 855  $\Delta\Omega = 0.03$  is  $N \geq 10^2 s^{-1}$ .

### 856 3.6 Single-spin physics [V. Abramov]

857 A systematic study of such single-spin phenomena as the transverse single-spin polarization of hadrons  
 858 ( $A_N$ ) and the polarization of hyperons ( $P_N$ ) in  $p+p$ ,  $d+d$ ,  $C+C$  and  $Ca+Ca$  collisions is proposed. A  
 859 systematic study means a detailed study of the dependence of the observed  $A_N$  and  $P_N$  for dozens of  
 860 reactions on variables such as collision energy ( $\sqrt{s}$ ), Feynman variable ( $x_F$ ), transverse momentum ( $p_T$ ),  
 861 the atomic weights of the colliding particles ( $A_1$  and  $A_2$ ), the multiplicity of charged particles ( $N_{ch}$ )  
 862 in the event, and the centrality of collisions. The study of a large number of reactions will reveal the  
 863 dependence of  $A_N$  and  $P_N$  on the quantum numbers (spin, isospin, flavor, etc.) of the hadrons participating  
 864 in the reaction. A systematic study also implies a global analysis of all available single-spin data within  
 865 a single model in order to identify general behavior and the mechanism of the origin of polarization  
 866 phenomena.

867 One of such models is the model of chromomagnetic quark polarization (CPQ) developed by the author  
 868 [205]. The CPQ model assumes the presence of an inhomogeneous circular transverse chromomagnetic  
 869 field  $\mathbf{B}^a$  in the interaction region of colliding hadrons. The interaction of the chromomagnetic moments

of test quarks, which later form the observed hadron, with the field  $\mathbf{B}^a$  leads, as a result of the Stern-Gerlach effect, to the appearance of spin effects (with nonzero  $A_N$  and  $P_N$ ). The spin precession of test quarks leads to the phenomenon of oscillations  $A_N(x_F)$  and  $P_N(x_F)$  depending on the Feynman variable  $x_F$ , and the frequency of these oscillations depends on the number of spectator quarks, color charges of quarks and antiquarks, and the direction of their motion in the c.m. of reactions. The frequency of these oscillations is a linear function of the number of quarks and antiquarks - spectators interacting in pairs with each of the test quarks, taking into account the color state of the pair. The highest oscillation frequencies are expected in the case of antibaryon production in baryon collisions and in ion collisions.

The CPQ model also predicts for a number of reactions such a phenomenon as the resonance dependence of  $A_N$  and  $P_N$  on energy ( $\sqrt{s}$ ), which occurs if the sign of the color charge of the test quark and spectators is opposite. The most interesting reaction in this respect is the production of anti-lambda in various initial states of the beams of the NICA collider, for which the resonance energy is close to 7 GeV in the c.m.

The threshold dependence of  $A_N$  on the hadron production angle in the c.m. is also predicted. An example of the manifestation of the threshold dependence  $A_N$  is the reaction  $p^\uparrow p(A) \rightarrow \pi^- X$ , for which the threshold angle is  $74^\circ$ , since the test quark is the  $d$ -quark, which is heavier than the  $u$ -quark.

An important advantage of hyperons is the ability to measure  $A_N$  and  $P_N$  for them, which makes it possible to compare them with each other and with model predictions.

The rate of pion production in  $pp$  collisions varies from  $3 \cdot 10^7/s$  at 23 GeV to  $2 \cdot 10^5/s$  at 7 GeV. In C + C and Ca + Ca collisions, it will be three orders of magnitude lower. The rate of production of hyperons is two orders of magnitude lower than that of pions. Antihyperones are produced 5 to 10 times less frequently than hyperons.

### 3.7 Scaling onset in exclusive reactions with lightest nuclei and spin observables [Yu. Uzikov, V. Ladygin]

The structure of the lightest nuclei at short distances  $r_{NN} < 0.5$  fm or high relative momenta ( $q > \hbar/r_{NN} \sim 0.4$  GeV/c) constitutes a fundamental problem in nuclear physics. One of the most important questions is related to search for onset of transition region from meson-baryon to quark-gluon picture on nuclei. A definite signature for transition to the valence quark region is given the constituent counting rules (CCR) [206, 207]. According the dimensional scaling the differential cross section of a binary reaction at enough high incident energy can be parametrized as  $d\sigma/dt \sim s^{-(n-2)} f(t/s)$ , where  $n$  is the sum of constituent quarks in all participants,  $s$  and  $t$  are Mandelstam variables. Many hard processes with free hadrons are consistent with CCR at energies of several GeV. The CCR properties of the reactions with the lightest nuclei were observed in photodisintegration of the deuteron  $\gamma d \rightarrow pn$  at  $E_\gamma = 1 - 4$  GeV and  ${}^3\text{He}$  nucleus  ${}^3\text{He}(\gamma, pp)n$ ,  $\gamma{}^3\text{He} \rightarrow dp$ . More earlier data on the reaction  $dd \rightarrow {}^3\text{H}p$ ,  $dd \rightarrow {}^3\text{H}n$  [208] and  $pd \rightarrow pd$ , as was show in Ref.[209] also follow CCR behavior  $s^{-22}$  and  $s^{-16}$ , respectively, at surprising low energies, 0.5 GeV. Recently the CCR behaviour of the reaction  $pd \rightarrow pd$  was observed in [210, 211] at higher energies. On the other hand, the reaction with pion production  $pp \rightarrow d\pi^+$  does not follow CCR rule demonstrating the differential cross section  $\sim s^{-9}$  instead of  $s^{-12}$ . One possible way to explain this is a partial restoration of chiral symmetry at enough high excitation energy [212]. However, systematic study of these properties of the reactions with lightest nuclei are absent. So, important to know whether reaction  $pn \rightarrow dp^0$  follows the CCR behavior and at what minimal energy there is the CCR onset. Assuming the model of the vector meson dominance and taking into account the observed CCR behavior of the  $\gamma d \rightarrow pn$  reaction, one may expect the  $\sim s^{-12}$  dependence of the cross section of the reaction  $pn \rightarrow dp^0$ . Furthermore, possible relation between CCR behavior of the unpolarized cross section and spin observables of the same reaction are practically not known. The SPD NICA facility provides a good opportunity for this study using polarized beams in  $pp$ ,  $dd$  and  $pd$  collisions.

915 The tensor  $A_{yy}$  and vector  $A_y$  analyzing power in  $dp$ - elastic scattering obtained at  $60^\circ$ ,  $70^\circ$ ,  $80^\circ$  and  $90^\circ$   
 916 in cms versus transverse momentum  $p_T$  [213, 214] demonstrates the negative and positive asymptotics,  
 917 respectively. Note, that negative sign of  $A_{yy}$  is observed also in deuteron inclusive breakup at large  $p_T$  [?  
 918 ].It would be interesting to extend the range of the measurements to larger  $p_T$ , where the manifestation  
 919 of non-nucleonic degrees of freedom is expected. New precise measurements with small statistical and  
 920 systematic uncertainties at the energies higher than  $\sqrt{s} \geq 3.3$  GeV and at different scattering angles are  
 921 required to make a conclusion about the validity of CCR [206, 207] in  $dp$  - elastic scattering. We propose  
 922 to measure also different vector and tensor analyzing powers in  $dp$ - elastic scattering at SPD energies.

923 The measurements of  $dp$ - elastic scattering can be performed either with polarized deuterons and unpo-  
 924 larized protons, or with unpolarized deuterons and polarized deuterons. The  $dp$ - elastic scattering events  
 925 can be selected using cuts on the azimuthal and polar scattering angles correlations. The vector  $A_y$  and  
 926 tensor  $A_{yy}$  and  $A_{xx}$  analyzing powers will be measured simultaneously in the case of the vertically polar-  
 927 ized deuteron beam. The precision on the tensor  $\Delta A_{yy} \sim 0.09$  and  $\Delta A_{xx} \sim 0.09$  and on the vector  $\Delta A_y \sim 0.03$   
 928 analyzing powers can be achieved for the scattering angle  $\sim 90^\circ \pm 5^\circ$  at  $\sqrt{s} \sim 4.5$  GeV ( $p_T \sim 1.7$  GeV/c)  
 929 for 30 days of the beam time at the luminosity  $\mathcal{L} \approx 10^{29} \text{ cm}^{-2} \cdot \text{s}^{-1}$ . We assume  $\sim 75\%$  of the beam  
 930 polarization from the ideal values of polarization for different spin modes. The spin correlations can be  
 931 obtained in quasi-free  $dp$ - elastic scattering using  $dd$ - collisions.

### 932 3.8 Yield of antiprotons in hadronic collisions for astrophysical dark matter search

## Chapter 3

# Polarized beams [A. Kovalenko]

### 1 Available species and types of collisions

Basic specification to available polarization states and combinations is the following:

- protons: vector polarization, longitudinal and transverse direction in respect to a particle velocity;
- deuterons (possibly helium-3 ions at the second stage): vector and tensor polarization, vertical direction of polarization, changing of the polarization direction at  $90^\circ$  up to about 4 GeV/c momentum;
- possibility to collide any available polarized particles: proton – deuteron, proton – helium-3, deuteron – helium-3 with the luminosity of  $10^{30} \text{ cm}^{-2} \text{ s}^{-1}$  at the collision energy equivalent to the proton-proton collisions;
- possibility of asymmetric collisions should be considered as an option for the future development of the facility;
- for efficient estimates of systematic error it is desirable (or necessary) to realize rotation of a bunch polarization direction on  $90^\circ$  within one turn;

Technical realization of the above mentioned conditions is feasible [215].

### 2 Beam structure, intensity and luminosity

Beam structure of polarized proton and deuteron beams at the first stage will be corresponded to that was optimized for the NICA heavy ion regime. Some of the important, for the SPD, operation parameters in case of bunched beam are the following: bunch number 22, bunch length  $\sigma = 60$  cm, the collider orbit length - 503 m, bunch velocity  $v \approx c = 3 \times 10^8$  m/s, revolution time  $\tau = 1.67 \times 10^{-6}$  s, bunch revolution frequency  $f \approx 0.6$  MHz, time gap between bunches  $\Delta\tau = 76.0 \times 10^{-9}$  s. The dependence of the pp-collision luminosity on the energy and number of protons is presented in Fig. 3.1.

As it is clear from the calculations the luminosity level of  $1 \times 10^{30} \text{ cm}^{-2} \text{ s}^{-1}$  is reached at a bunch intensity of  $10^{11}$  polarized protons, whereas to obtain the level of  $1 \times 10^{32} \text{ cm}^{-2} \text{ s}^{-1}$  multi-bunch storage mode should be used [216].

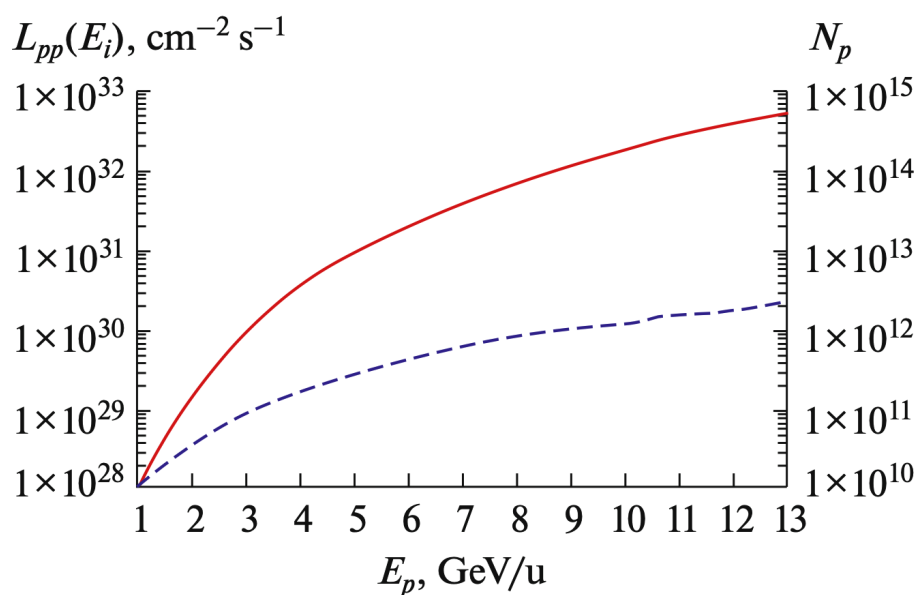


Figure 3.1: Normalized dependence of the pp-collision luminosity  $L$  and the beam intensity  $N$  on proton kinetic energy.

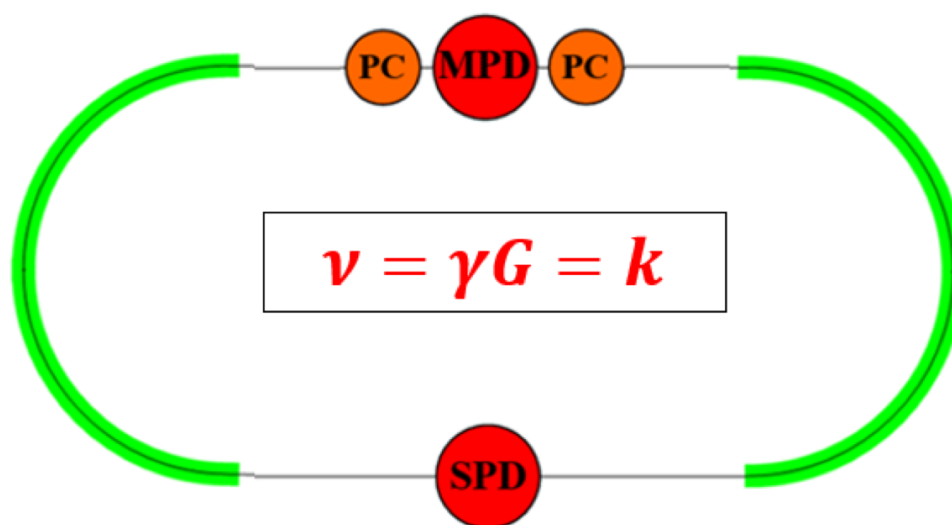


Figure 3.2: General scheme of the polarization control at integer spin resonance points.

### 959 3 Polarization control and monitoring

#### 960 3.1 Transportation of polarized ions in the complex

961 Polarized protons and deuterons from the source SPI are accelerated first in the linac LU-20M and after  
 962 that are injected and accelerated in the Nuclotron to the specified energy and extracted to the collider via  
 963 long transfer line. The main tasks at this stage are the following: i) preservation of the ion polarization  
 964 during acceleration in the Nuclotron (and in the collider also) and ii) the polarization control in the  
 965 collider mode. Moreover, it is necessary to adjust the polarization direction at the beam transfer between  
 966 the Complex elements.

### 967 **3.2 Operation modes of the NICA collider at polarized ions**

968 From the spin dynamics point of view, NICA collider can operate in two regimes (modes), namely: in  
 969 a Preferred Spin mode (PS-regime) and in the Spin Transparency mode (ST-regime) In the PS - regime  
 970 periodic motion of the spin along the particle orbit is the only possible, i.e. – stationary magnetic structure  
 971 select the only one stable direction of the polarization vector in any point of the particle orbit, non-integer  
 972 part of the spin tune is not equal to zero, whereas in the ST – regime the direction of the spin vector is  
 973 reproduced in any point at every turn, i.e. magnetic structure of the accelerator ( or storage ring) is  
 974 transparent for the spin – non-integer part of the spin tune is equal to zero.

975 The main difference between the PS- and ST- regimes is occurred at the manipulations of the spin di-  
 976 rection during physics data taken. In the ST- regime the spin motion is very sensitive to the magnetic  
 977 field changes, because particles are moved in the vicinity of the integer resonance In this case the use of  
 978 additional ”weak” magnetic field, rotating spin at small angles  $\Psi \ll 1$  provides the needed polarization  
 979 direction at any specified point of the collider. It is possible to use a pair of solenoids with the field  
 980 integral of  $1 T \cdot m$ , introduced negligible distortions of the particle closed orbit, to produce necessary  
 981 variation of the spin angle in the NICA collider over the momentum range up to 13.5 GeV/c. In the case  
 982 PS regime similar procedure will require spin rotators base on a strong fields, rotating the spins at the  
 983 angles of  $\Psi \sim 1$ . Thus, in the case of the changing the polarization direction from the longitudinal to  
 984 the transverse one, it would be necessary to apply the transverse field with the total integral of 20-30  
 985  $T \cdot m$ , which would be resulted in a strong distortions of the particle close orbit. The amplitude of the  
 986 distortions can reach of tens of centimeters at low energies. Thus, efficient polarization control of ions,  
 987 deuterons especially, by means of quasi-stationary weak fields is possible the only if the ST- regime is  
 988 used.

### 989 **3.3 Specifications to the polarized beams in the collider**

990 Different experiments are planning with polarized proton, deuteron and helium-3 (in the future) particles  
 991 to identify and study different observables for different physics tasks: Drell-Yan,  $J/\psi$ , high hadron  
 992 physics, exotic states etc. The polarization control system should be satisfied to the following main  
 993 conditions:

- 994 – to obtain both longitudinal and transverse polarization in the MPD and SPD detectors with the  
 995 polarization degree not less 70% and the polarization lifetime not less than the beam lifetime;
- 996 – to provide the collision luminosity of  $\sim 10^{30} - 10^{32} \text{ cm}^{-2} \text{ s}^{-1}$  over the particle momentum range  
 997 from 2 to 13.5 GeV/c;
- 998 – to provide the particle energy scan with a step of 1.0 GeV (Drell-Yan,  $J/\psi$ ) and 0.3 MeV (high- $p_T$   
 999 hadron physics, exotic states);
- 1000 – to adopt operation in asymmetric on the particle momentum mode;
- 1001 – make simultaneous spin-flips for all bunches in the case of the Spin Flipping experiments (SF  
 1002 system).

### 1003 **3.4 Spin flipping system**

1004 The SF system makes it possible to carry out the spin physics experiments at much higher level of the  
 1005 accuracy [217]. Being equipped by such system the SPD set-up will have real privileges, in particular:

- 1006 – revers of the polarization direction at the polarized ion source is not necessary;

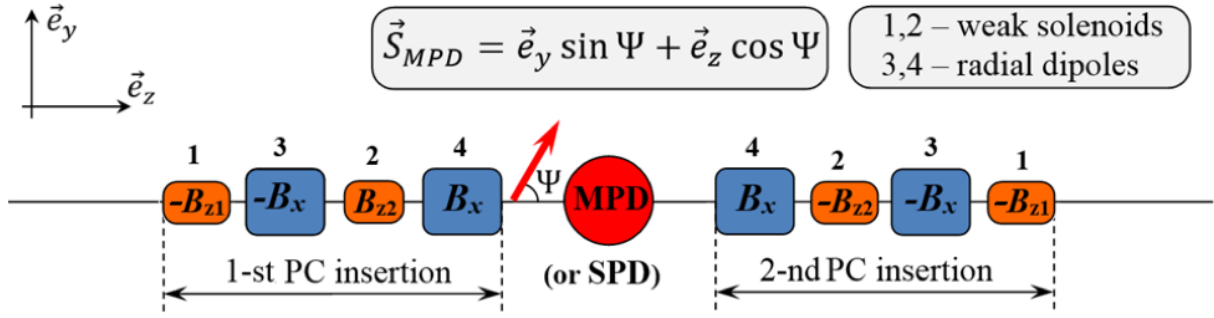


Figure 3.3: Detail scheme of the PC's insertions in the collider in the ST regime.

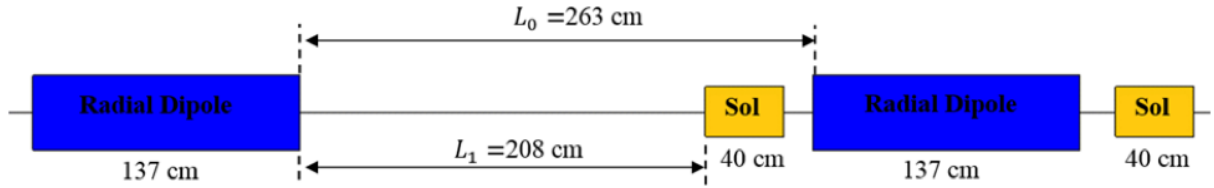


Figure 3.4: Placement of weak control solenoids in horizontal plane.

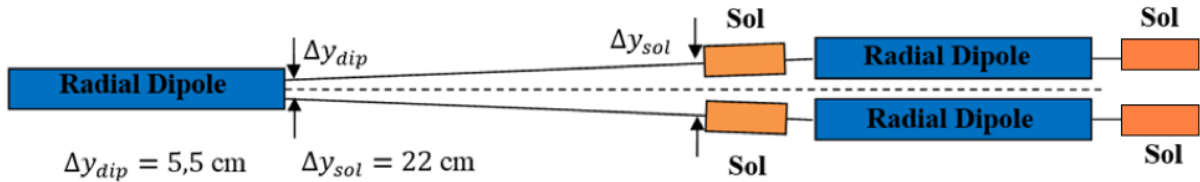


Figure 3.5: Placement of weak control solenoids in vertical plane together with radial dipoles.

- 1007 – no necessity of a bunch-to-bunch luminosity measurements and bunch monitoring system;
- 1008 – the possibility of comparison collisions of bunches with any directions of the particle spin (vertical-
- 1009 longitudinal, vertical – radial, radial – longitudinal, etc.). The SF system based on quasi-stationary
- 1010 fields is naturally realized in the ST collider regime. The pair of "weak" controlled solenoids
- 1011 provides simultaneous influence on the polarization direction and the spin tune. Thus, possibility
- 1012 of the spin tune stabilization during the spin flipping is occurred, preventing both as the zero
- 1013 spin tune and higher order spin resonances crossing. The polarization degree will be kept with
- 1014 an exponential accuracy, if the field of "weak" controlled solenoids will be changed slowly. For
- 1015 realization of SF system in the collider operating in a PS regime it would be necessary to introduce
- 1016 in the lattice RF-field of a MHz's range and the field total integral of  $1 \text{ T} \times \text{m}$ , that's not so easy
- 1017 technical task.

### 1018 3.5 On-line control of the polarization in the collider

1019 The unique possibility of the on-line polarization control is occurred if the collider operates in the ST-

1020 regime. Because the field ramp in a "weak" solenoids ( $t_{\text{change}} \sim 0.2 \text{ s}$ ) is much larger of the spin pre-

1021 cession period around the induced spin field ( $t_{\text{rev}} \sim 10^{-4} \text{ s}$ ), any manipulations with the spin direction at

1022 spin tune will be occurred adiabatically and the polarization degree during the experiment time will be

1023 supported constant with the exponent accuracy. The direction of polarization vector will be a function

1024 of the weak solenoids field and can be defined by mean of the field measurements. The comparison of

1025 the ST- and PS- regimes in the NICA collider is presented in Table 3.1. Thus, the ST-regime makes it

1026 possible to carry out the experiments at the NICA collider at the new level of the accuracy.



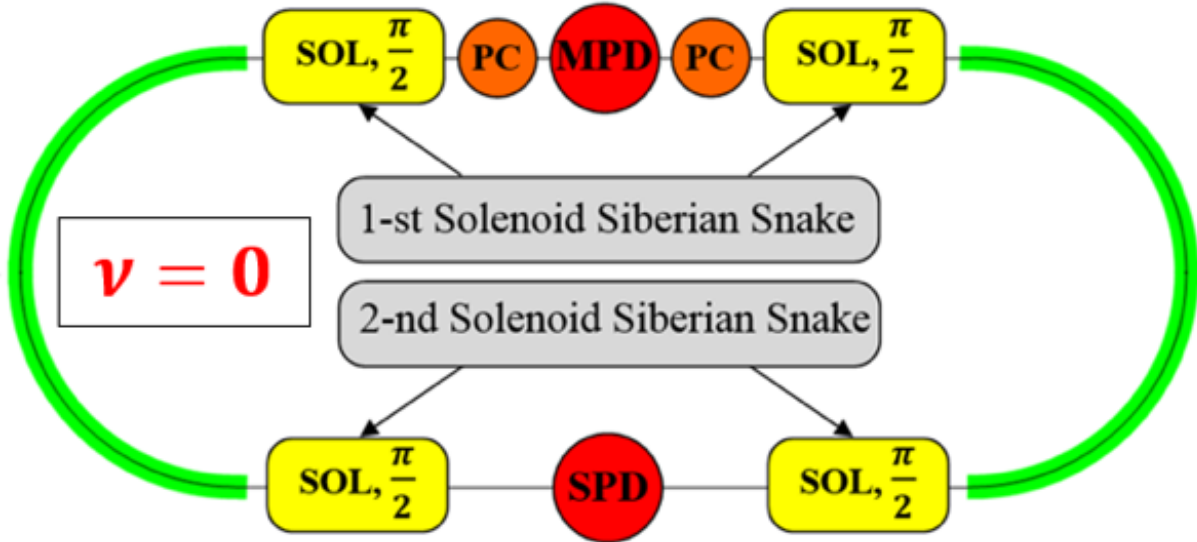


Figure 3.6: Scheme of realization ST regime in NICA collider.

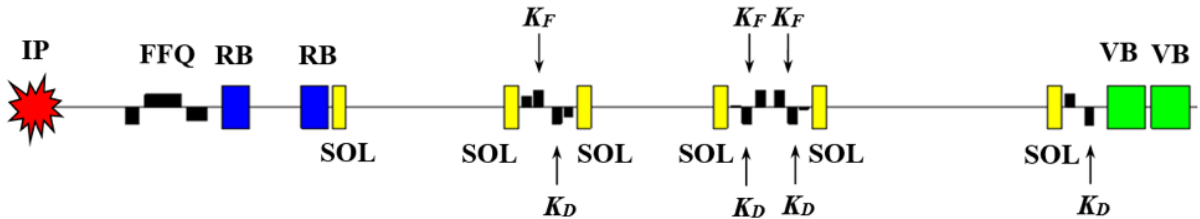


Figure 3.7: Distributed snake (one half) based on short 6 T SC solenoids.

Table 3.1: Comparison of two regimes.

Possibility of realization	PS regime	ST regime
Stationary longitudinal/transverse polarization in the detectors	yes	yes
Polarization control in any point of the orbit	no	yes
Spin Flipping systems based on quasi- static fields	no	yes
on-line polarization control	no	yes

1027 **3.6 Polarization control in the collider NICA in ST regime**

1028 **Use of integer spin resonances in ST-regimes.** Stable polarization direction in the NICA collider is  
 1029 vertical (orthogonal to the particle orbit), whereas the spin tune is proportional to the particle energy:  
 1030  $\nu = \gamma G$ , where G is anomalous part of the gyromagnetic ratio. The collider is operated in the PS- regime  
 1031 practically over the total energy range because  $\gamma \neq k/G$ , where k is an integer. The ST regime is realized  
 1032 at discrete energy points corresponding to integer spin resonances:  $\gamma = k/G$ . For protons the number of  
 1033 points corresponding to ST- regime is 25 starting from minimal energy  $E_{kin}^{min} = 108$  MeV with the step of  
 1034  $\Delta E = 523$  MeV. There is only one point  $E_{kin} = 5.63$  GeV/u, corresponding to the momentum 13 GeV/c  
 1035 i.e. the ST-regime for deuterons in the Nuclotron/NICA complex.

1036 Possible scheme of ion polarization control in the collider at the integer spin resonances is presented  
 1037 in Fig. 3.2. Two PC-insertions (marked with orange circles in Fig. 3.2) placed near MPD are used  
 1038 to stabilize the needed polarization direction at any point of the collider ring, including the collision

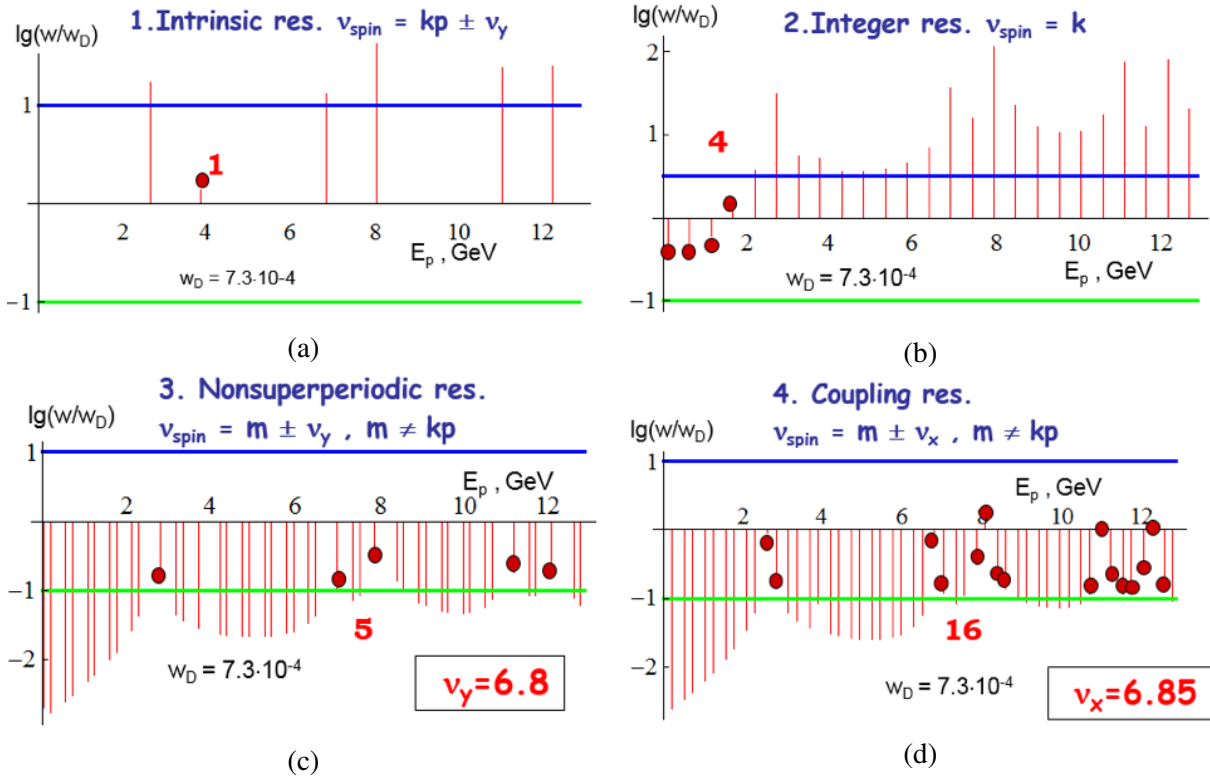


Figure 3.8: Linear spin resonances in the Nuclotron at polarized proton mode.

1039 points, at injection, etc. Detail scheme of the PC's is presented in Fig. 3.3. Weak solenoids ( $B_{z1}$  and  $B_{z2}$   
 1040 generated longitudinal magnetic field  $\pm B_{z2}$  are placed between the collider structural magnets, generated  
 1041 radial field  $\pm B_x$  (marked as 3 and 4), providing deflection the beams to the collision plane of the MPD.

1042 The scheme make it possible the ion polarization control in vertical plane ( $yz$ ) in the MPD ( or SPD) ( $\Psi$   
 1043 is angle between polarization and particle velocity vectors). The scheme provides necessary spin rotation  
 1044 for all discrete points over NICA energy range if integral magnetic field will reach  $0.6 \text{ T} \times \text{m}$  in each of  
 1045 four solenoids. If we limit the field maximum to  $1.5 \text{ T}$ , the magnetic length of the solenoid unit of  $40$   
 1046 cm. Real relative scale of the control solenoid ( $40 \text{ cm}$  long), radial dipole and distances between them is  
 1047 shown in Fig. 3.4.

1048 The scheme of installation weak control solenoids in vertical plane together with the collider lattice  
 1049 elements is presented in Fig. 3.5. The beam convergence angle in vertical plane, defined by the dipoles  
 1050 with transverse to the beam axis magnetic fields is:  $a_x = 0.04 \text{ rad}$ . The distance between the collider  
 1051 rings in vertical is  $32 \text{ cm}$ . The distances in vertical plane between the particle closed orbits are  $\Delta y_{dip} =$   
 1052  $L_x a \approx 5.5 \text{ cm}$ . and  $\Delta y_{sol} = \Delta y_{dip} + 2L_1 a \approx 22 \text{ cm}$ . at the output of common radial dipole and at the exits  
 1053 of control solenoids respectively.

### 1054 3.7 Ion polarization control in ST regime by means of two snakes

1055 Two solenoidal snakes installed symmetrically in respect to both MPD and SPD set-ups will provide ST  
 1056 regime in NICA collider (Fig. 3.6).

1057 The configuration make it possible to turn the spin in vertical plane ( $yz$ ) of MPD or SPD detector,  
 1058 whereas in the collider magnet arcs the polarization vector is moving in the median plane ( $xz$ ) [218].  
 1059 The ST scheme with two snakes provides the zero spin tune at any point of the particle energy. It is  
 1060 very important for optimization of the NICA effective operation at the highest possible luminosity of

1061 pp - collisions, due to necessity of the particle store at an energy level that gives proper conditions for  
 1062 electron cooling of stored beam. Only in this case it is possible to form particle bunches with high number  
 1063 of particles and high degree of the polarization at low energy (about 1 GeV) with further acceleration up  
 1064 to the experiment energy. The total integral of longitudinal solenoidal field should reach  $4 \times 25 \text{ T} \times \text{m}$  per  
 1065 ring at the proton momentum of  $13.5 \text{ GeV}/c$  and  $4 \times 80 \text{ T} \times \text{m}$  for deuterons respectively. The distributed  
 1066 system consisting of a short solenoids is possible, i.e. In the case of 6 T solenoids the total length of 4.2  
 1067 m is sufficient to form a half-length snake. It is possible to adopt the collider lattice structure optimized  
 1068 for heavy ion beam for the case of ST regime at the protons mode over the total energy range. Weak  
 1069 control solenoids don't disturb practically orbital motion in the collider whereas, strong solenoids of  
 1070 the snakes led to a strong betatron tunes coupling. Because longitudinal field of the snakes is changed  
 1071 proportionally to the particle momentum, the collider magnetic optics will stay adequate to the polarized  
 1072 particle stable motion during the beam acceleration phase. Matching of the solenoids with the collider  
 1073 structure is provided by means of proper choice of the work point by means of structural KF (focusing)  
 1074 and KD (defocusing) quadrupole lenses. Possible scheme of the distributed snake (one half) based on  
 1075 short 6T superconducting solenoids (SC) is shown in Fig. 3.7. The elements are the following: SOL-SC  
 1076 solenoid, FFQ - final focus triplet of the collider, VB - structural dipole magnets; RB - bending dipoles  
 1077 with transverse field for converging the bunches in the collision point IP.

### 1078 3.8 Stability of spin motion

1079 In the ST regime precession of the polarization vector is caused by the field of solenoids, by the field  
 1080 imperfections of the collider lattice elements, by a finite beam emittance and depends on a power of  
 1081 zero spin tune resonance. To stabilize the polarization during acceleration process or during control  
 1082 the polarization direction in the ST regime it will be necessary to provide spin tune level caused by the  
 1083 control solenoids much higher of a power of zero spin tune resonance: The calculations have showed that  
 1084 the level of  $10^{-2}$  for protons and  $10^{-4}$  for deuterons would be sufficient. These values put limitations on  
 1085 the minimum field integral in each of weak control solenoids –  $0.6 \text{ T} \times \text{m}$ .

Table 3.2: Polarization in the SPD and MPD detectors in PS and ST regimes.

Snake SPD	Snake MPD	Spin tune	Control regime	Polarization in SPD	Polarization in MPD
off	off	$\nu \neq \gamma G$	PS	vertical	vertical
off	off	$\nu = \gamma G$	ST	any	any
off	on	1/2	PS	longitudinal	in the collider median plane, direction angle depends on energy
on	off	1/2	PS	in the collider median plane, direction angle depends on energy	longitudinal
off	off	$\nu = \gamma G$	ST	any	any

### 1086 3.9 Polarized beams dynamics in NUCLOTRON

1087 Stable polarization direction in the Nuclotron is vertical, and the spin tune is proportional to the beam  
 1088 energy:  $\nu = \gamma G$  (  $G$  is anomaly part of the gyromagnetic ratio of the particle,  $\gamma$  is Lorentz factor) that  
 1089 definitely lead to crossing of spin resonances during the particle acceleration and, as consequence, to  
 1090 resonance depolarization of the beam. There is no problem with deuterons: the only one integer spin  
 1091 resonance can be excluded by means of weak solenoid (  $0.1 \text{ T} \times \text{m}$ ) inserted into the accelerator lattice.

Table 3.3: Polarization in the SPD and MPD detectors in PS and ST regimes.

Snake SPD	Snake MPD	Spin tune	Control regime	SF system	Online polarization control	Possibility of acceleration in collider	Influence of RF modulation on polarization lifetime
off	off	$\nu \neq \gamma G$	PS	no	no	no	reduce
off	off	$\nu = \gamma G$	ST	yes	yes	no	reduce
off	on	1/2	PS	no	no	yes	no influence
on	off	1/2	PS	no	no	yes	no influence
off	off	$\nu = \gamma G$	ST	yes	yes	yes	no influence

1092 The number of different spin resonances in the proton mode is much larger. Logarithmic graphs of  
 1093 linear spin resonances power scaled to the specific power corresponding to complete depolarization of  
 1094 the beam are presented in Fig. 3.8 [219, 220]. The proton energy range  $E_p$  corresponds to the available  
 1095 at Nuclotron. Each graph is divided onto three areas that correspond to intermediate crossing (between  
 1096 horizontal lines), fast crossing (below green line) and adiabatic crossing (upper blue line). The lines of a  
 1097 fast and adiabatic crossing are corresponding to 1% loose of the polarization degree.

1098 The parameters taken for calculation of the resonances power were the following: the magnetic field ramp  
 1099 - 1 T/s; beam emittance (horizontal and vertical) at the injection energy -  $45\pi$  mm $\times$ mmrad; quadrupole  
 1100 misalignment errors – 0.1 mm; errors of angular alignment of structural dipole and quadrupole magnets  
 1101 - 0.01 rad; and the relative error of the quadrupole gradients - 0.001. The resonances marked with red  
 1102 circles are dangerous and lead to the beam depolarization after their crossing. To keep the polarization  
 1103 of proton beam at proper level, partial Siberian snake based at a solenoid will be used. Two options  
 1104 have been considered: 1) The use of a weak 5% snake with the field integral of 0.65 T $\times$ m, which can  
 1105 save the proton beam polarization up to 3.4 GeV/c and 2) The use of 25% snake ( $\sim 12$  T $\times$ m). The  
 1106 first one is efficient if the collider operates in the ST regime with two snakes and injection of the beam  
 1107 is provided at low energy (around 1 GeV), whereas strong enough snake that is used in option 2 could  
 1108 save the polarization over the total energy range in the NUCLOTRON and is suitable to the operation at  
 1109 integer resonances. The choice of energy points is limited to the points of integer resonances.

### 1110 3.10 Operation modes of the NICA collider at polarized beams

1111 Collider NICA with two solenoidal snakes will make it possible the following operation configurations  
 1112 (see Table 3.2) [221].

1113 If the snakes installed in SPD and MPD sections are switched off, the PS regime with vertical polarization  
 1114 at any point of the collider orbit is occurred. Some narrow energy gaps which the ST regime at integer  
 1115 resonances is exists in, gives possibility to have any direction of the polarization in the both detectors.  
 1116 After switching one of the snakes on, the collider will operate in PS regime with the spin tune 1/2. The  
 1117 snake transform completely spin motion providing stable longitudinal direction of the polarization in  
 1118 opposite respect to the snake section of the collider orbit.

1119 If two dynamic solenoid snakes are switching on, the unique spin transparency (ST) regime is realized.  
 1120 The spin tune don't depend on particle energy and equal to zero that's gives possibility to obtain any  
 1121 direction of the polarization at any point of the collider orbit. The features of the collider operation in  
 1122 polarized modes are shown in Table 3.3.

1123 It is very important to realize the possibility of polarized beam acceleration in the NICA collider without  
 1124 loose the polarization degree. The problem of reaching the highest possible luminosity of polarized

1125 proton collisions is connected with the particle multi-bunch storage in the collider and electron cooling  
1126 of the stored beam during the process. The optimal proton beam kinetic energy at the beam injection into  
1127 the collider is about 1 GeV [222, 223].

### 1128 **3.11 Zero Degree Calorimeter [S. Shimansky]**

### 1129 **3.12 Conclusion and outlook**

1130 The proposed scheme of the ion polarization control in the NICA collider is adopted easily to the collider  
1131 magnetic optics at any regimes of the polarization control. Important advantages could be obtained with  
1132 the applying spin transparency regime. Polarization degree of about 70% is provided at the collision  
1133 points. The polarization life time is expected to be at the level of hours comparable with the beam life  
1134 time. We didn't describe some specific measurement and monitoring systems should be designed at the  
1135 stage of preparation technical project. In particular: precise measurement of the luminosity (bunch-to-  
1136 bunch?), absolute polarimeter based on a gas jet, targeting stations etc.

## Chapter 4

# Detector layout

### 1 General design [A. Guskov]

The physics tasks represented in the Chapter 2 impose general requirements to the concept of the Spin Physics Detector. Unlike a case of high-energy collisions where the collision energy  $\sqrt{s}$  is a few orders of magnitude larger than a typical hard scale  $Q$  of the studied reactions, at SPD energies for all the probes planned to be used for access gluon content of the colliding particles  $Q \sim M_{J/\psi} \sim 2M_D \sim p_{T\gamma min}$  is just a few times less than  $\sqrt{s}/2$ . Therefore one should expect quite uniform distribution of all signal particles (muons from the  $J/\psi$  decay, prompt photons, products of  $D$ -mesons decay etc.) over the kinematic range. In other words, there is no preferable range in rapidity could be specified for each probe for the optimal overall performance. Together with relatively small cross sections of the discussed probes, this fact leads one to a requirement of  $\sim 4\pi$  coverage of the SPD setup.

The Spin Physics Detector must have sufficient tracking capabilities and a magnetic system for spectrometric purposes for the most of the addressed physics tasks. It has to be equipped with a thick enough muon system for effective separation of muons and hadrons to be able to deal with the decay  $J/\psi \rightarrow \mu^+ \mu^-$ . Precision vertex detector is needed for recovering of the secondary vertices from decays of  $D^{\pm/0}$  mesons and other short-lived particles. Electromagnetic calorimeter ensures capability to detect signal and background photons. Low material budget and general transparency of the setup should also provide favorable conditions for the photon physics. Hadron identification capability is needed for any physics task with protons and/or kaons in the final state, in particular, to enforce a signal-to-background ratio for  $D$ -mesons selection, and also to improve tracking at low momenta. Since tiny effects are intended to be investigated, a triggerless DAQ system is planned in order to minimize possible systematic uncertainties of the measurements.

Strict limitations to the SPD detector layout are coming from an external conditions such as the maximal possible load to the floor of the SPD experimental hall (1500 tons together with a lodgement and a detector moving system). Together with a requirement to have overall thickness of the muon system not less than 4 nuclear interaction lengths ( $\Lambda_I$ ) this limits an outer size of the SPD detector and a size of an inner part of the detector. Location of the collider infrastructure, in particular, focusing elements also defines the size of the SPD setup along the beam axis. More details could be found in Chapter 3.

General layout of the SPD is shown schematically in Fig. 4.1. The detailed description of each subsystem could be found below. Table 4.1 brings together the elements of the SPD physics program and the requirements to the experimental setup.

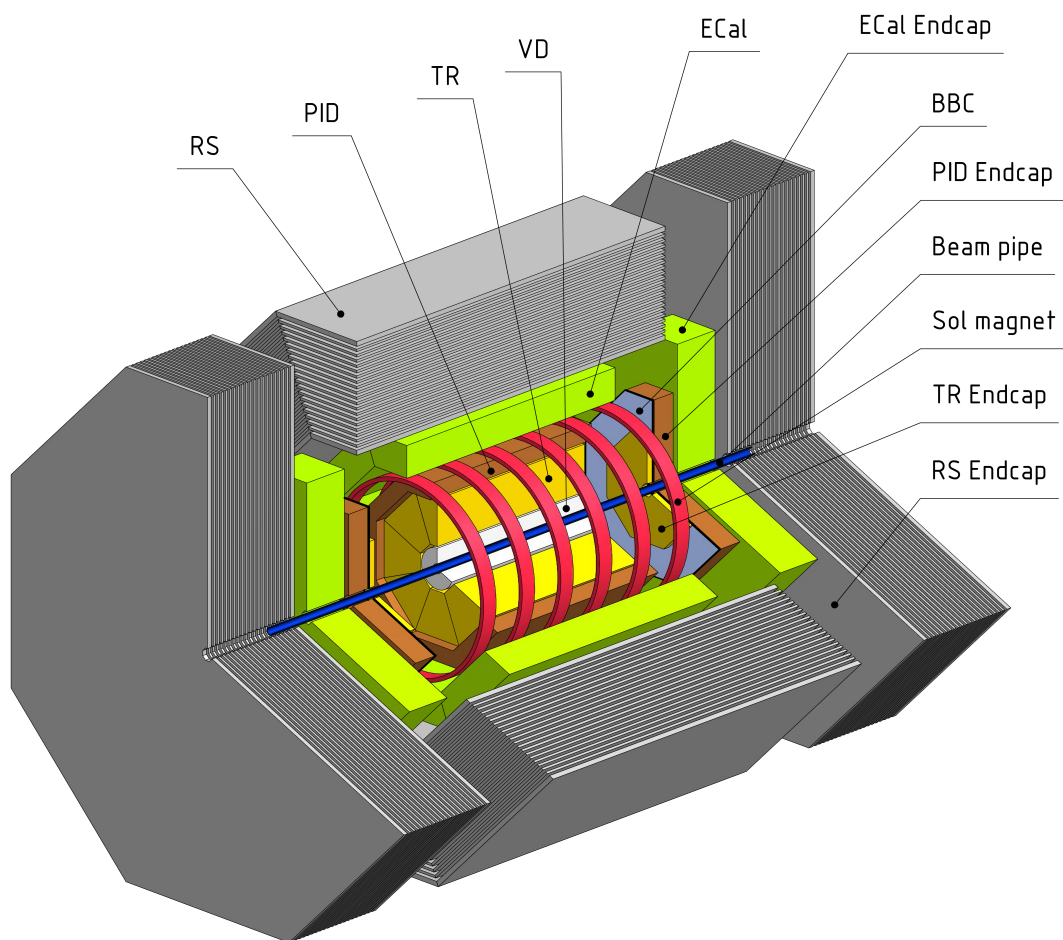


Figure 4.1: General layout of the Spin Physics Detector.

Table 4.1: Required setup configuration for each point of the SPD physics program. (+++) - absolutely needed, (++) - extremely useful, (+) - useful, (-) - not needed.

Program	Vertex detector	Straw tracker	PID system	Electromagnetic calorimeter	Beam-beam counter	Range system
Gluon content with: charmonia (and DY)	+	++	-	++	-	+++
open charm	+++	++	++	-	-	+
prompt photons	+	+	-	++	-	-
SSA for $\pi$ and $K$	+	++	+++	++	-	-
Light vector meson production	+	++	-	+	-	-
Elastic scattering	+	++	-	-	++	-
$\bar{p}$ production	+	++	+++	++	-	-

## 1169 2 Magnetic system [A. Kovalenko]

1170 The SPD Magnetic System (MS) should satisfy to the following criteria:

- 1171 – minimization of the material inside the detector inner part;
- 1172 – the magnetic field integral of (1-2) T m along the particle tracks, whereas the peak value of the  
1173 field should be limited to 0.8T over the straw tacker volume;
- 1174 – minimization of the total weight, cross section of the current coil (coils) and overall amount of the  
1175 MS material, i.e. the MS should have perfect mechanics.

1176 Several options of the MS's were considered:

- 1177 1. Solenoid - uniform multi-turn coil placed between the ECAL and the muon range (RS) systems;
- 1178 2. Toroidal MS (inside ECAL):  $3 \times 8 = 24$  coils forming toroidal distribution of the field in the detector  
1179 volume only,
- 1180 3. Hybrid system consisting of toroidal coil composition in a barrel and solenoidal in a forward/backward  
1181 parts. Both as room and cryogenic temperatures were considered;
- 1182 4. System of a 4 separate coils inside the ECAL: a) all coils are connected in series, and b) right and  
1183 left hand pairs are connected opposite to each other;
- 1184 5. Hybrid system consisting of 8 toroidal coil composition in a barrel and 2 pairs of separate solenoidal  
1185 coils in a forward/backward parts. Both as room and cryogenic temperatures were considered;
- 1186 6. System of a 6 separate coils placed between the ECAL and RS system of the reduced diameter.

1187 Thus, more than 10 different options of the 3D configurations of the magnetic fields were analyzed,  
1188 calculated field maps were presented to the collaboration and part of them have been used for the SPD  
1189 simulation [...]. Conceptual analysis of the considered MS systems was performed also. Some data  
1190 were reported at the European Conference on Apply Superconductivity EUCAS2019 [...]. General  
1191 conclusion are briefly summarized below.

- 1192 1. The most well-known system is classic solenoid. The experience of design and construction of su-  
1193 perconducting solenoids have been collected by many groups in the world including MPD NICA.  
1194 The MPD solenoid manufacturing is completed and the assembling is started in the experimental

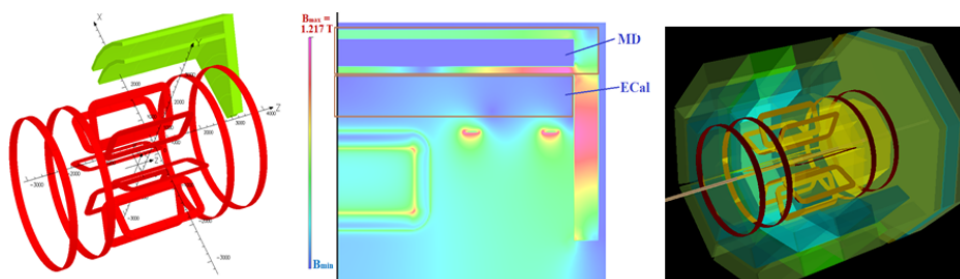


Figure 4.2: Hybrid MS: toroidal magnet consisting of 8 coils in barrel part and double coil system in forward and backward parts of the detector.



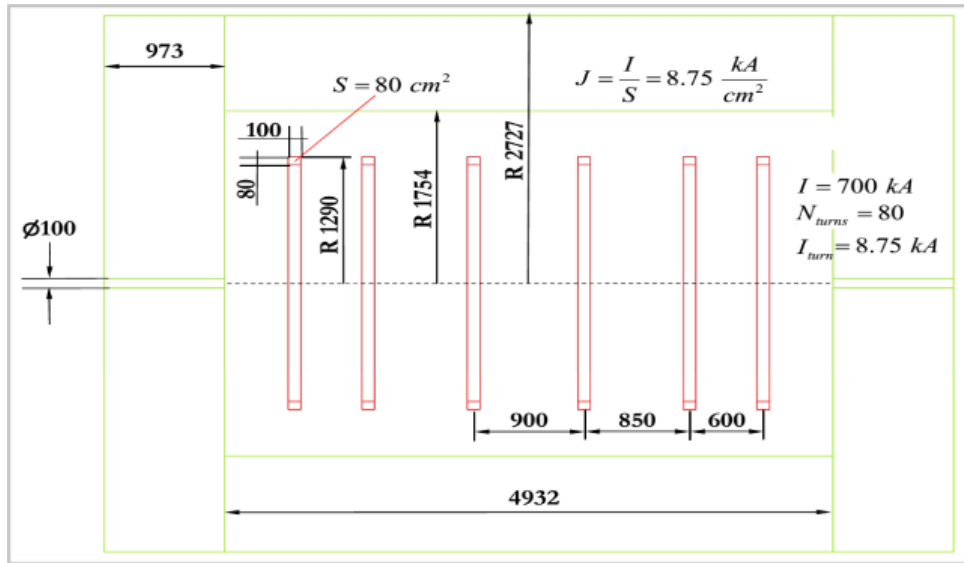


Figure 4.3: Geometrical model of the 6-coil magnetic system

1195 hall. Main disadvantage of similar solenoid as the SPD MS would be a lot of material front of the  
 1196 ECAL and high cost as well. Moreover, fixed geometry of the field gives no any universality of  
 1197 the SPD experimental program.

1198 2. The toroidal MS was considered in “warm” and “cold” options. The warm one was rejected due  
 1199 to the material budget: necessary ampere-turns led to unacceptable cross section of the coils that  
 1200 means amount of copper. The problem is solved partially in the case of superconducting coils,  
 1201 nevertheless the complexity of construction of the coil system is very high in any case. The most  
 1202 important negative effect can occur due to concentration of the coil material closer to the bunch  
 1203 crossing area.

1204 3. The MS consisting of separated coils is transparent absolutely for the particles passing through  
 1205 inner volume of the detector and contain “target” material for the secondary particles in limiting  
 1206 volume at the ECAL inner part. The amount of material depends directly on necessary amper-  
 1207 turns of the coil and achievable current density. The last point gives evidence in favor of a su-  
 1208 perconducting approach. The magnetic field radial and axial distribution is not so uniform in  
 1209 comparison with a solenoid especially in the area close to the coils. Nevertheless, the accuracy of  
 1210 modern 3D calculation codes for a nonlinear magnetic fields and precise magnetic measurements  
 1211 can guarantee necessary accuracy of real field mapping. Optimization of the coil cross section is  
 1212 very important also.

1213 4. Hybrid MS consisting of toroidal system in barrel part of the SPD and two pairs of separate coil was  
 1214 considered as some compromise, namely: minimization of the magnetic field near the polarized  
 1215 particles interaction zone and solenoidal-type distribution in front and backward parts of the SPD.  
 1216 The MS scheme is shown schematically in Fig. 4.2.

1217 More advanced analysis of the detector and the collider system have shown that partial compensation of  
 1218 the magnetic field at the axis will give not so much advantages. It would be positive, somehow, if there  
 1219 was no the spin control system in the collider lattice. The NICA collider will be equipped with such  
 1220 one. The elements aimed at the particle spin control at NICA collider was proposed and under technical  
 1221 design now. General description of the spin control system is presented in section 3. Thus, the condition

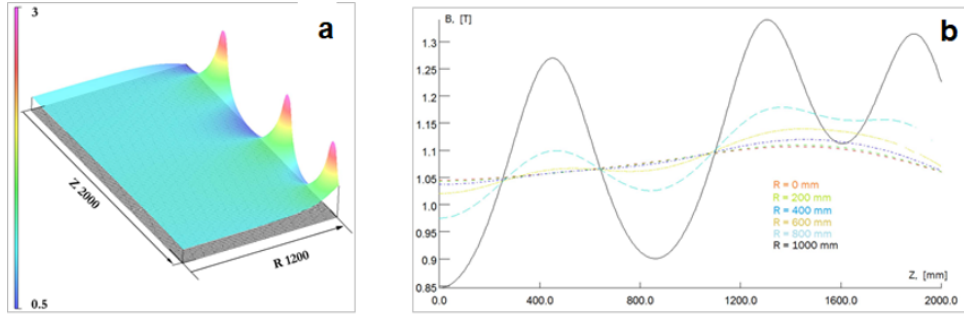


Figure 4.4: The field calculation results: (a)  $B_z$  as function of  $r$ ,  $z$ ; (b).  $B_z$  as function of  $z$  at different  $r$ .

1222 of “zero” magnetic field along the beam axis is not a critical issue in our case. Updated choice of the SPD  
 1223 MS was made in favor of a separate 6-coil design. Geometrical model of the coil system is presented in  
 1224 Fig. ??, whereas the field calculation data in Fig. 4.4.

1225 As it clear from Fig. 4.4, longitudinal variation of an axial magnetic field is varied from about 5% at the  
 1226 beam axis to about 12% at the radial distance of 2 cm from the coil inner turns. The number of 12% can  
 1227 be further improved by the coils system optimization. We consider the technology of a superconducting  
 1228 coils manufacturing based on a hollow high current cable similar to that is used for the Nuclotron magnet  
 1229 or that is used in ITER systems. Manufacturing technology of a hollow cable made of NbTi/Cu composite  
 1230 wires cooled at 4.5 K with forced He flow is well developed at the Laboratory. The magnets of NICA  
 1231 booster and collider are manufacturing at our Laboratory magnet facility. The coil containing 80 turns  
 1232 will provide  $800 \text{ kA} \times \text{turns}$  and generate necessary magnetic field in the detector volume. Some of the  
 1233 SPD 6 coil MS are presented in the Table 4.2 in comparison with the other detectors.

Table 4.2: Comparison of the SPD (NICA) and CMS (LHC) [] magnetic systems.

Parameter	SPD/NICA	CMS/LHC
Size (diam./length), m/m	3.6/6.0	6.5/12.7
Magnetic system	6 coils	solenoid
Peak magnetic field, T	2.0	4.5
Coil average diam., m	$\sim 3.6$	$\sim 6.5$
Field volume, $\text{m}^3$	$\sim 65$	$\sim 414$
Stored energy, MJ	$\sim 100$	$\sim 2800$
Coil turns	$6 \times 40$	2112
Operating current, kA	10	20
Total inductance, H	$\sim 2$	12.6

### 1234 3 Beam pipe [A. Guskov]

1235 A beam pipe separates the detector and high vacuum of the accelerator. It must be mechanically sturdy  
 1236 on the one hand and thin enough in terms of number of radiation lengths to minimize multiple scattering  
 1237 and radiation effects. The beam pipe is also protects the closest detectors from soft particles produced in  
 1238 the interaction point. A diameter of the beam pipe is a compromise between a radial size of the beams  
 1239 and a requirement to put coordinate detectors as close as possible to the interaction point for the better  
 1240 reconstruction of primary and secondary vertices. A beryllium beam pipe of 6 cm diameter and 0.5 mm  
 1241 of thickness is proposed to be used.

1242 A construction of the beam pipe and its positioning inside the SPD is shown in Fig. 4.5. ...

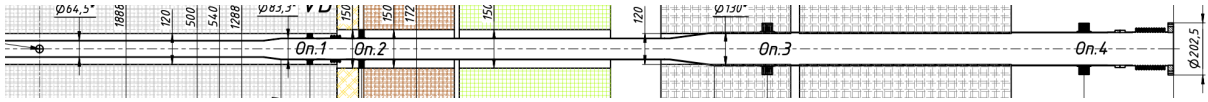


Figure 4.5: SPD beryllium beam pipe [DUMMY PLOT].

1243 At the first stage of SPD running a cheap steel beam pipe could be used.

## 1244 4 Vertex detector [N. Zamyatin]

### 1245 4.1 General overview

1246 The SPD Vertex Detector (VD) is a silicon-based part of the spectrometer responsible for precise de-  
 1247 termination of a primary interaction point and measurement of secondary vertices from the decays of  
 1248 short-lived particles (first of all  $D$ -mesons). The Vertex Detector is divided into the barrel and two end-  
 1249 cap parts (Fig. 4.6). Two different versions of the VD design are discussed: 1) five layers based on  
 1250 double side silicon detectors (DSSDs) and 2) three inner layers based on Monolithic Active Pixel Sen-  
 1251 sors (MAPS) and two outer layers based on DSSDs. The Barrel of VD consists of five layers based on  
 1252 double side silicon detectors (approximately  $4.2 \text{ m}^2$ ). The end-cap regions are each consists of five disks  
 1253 (approximately  $7 \text{ m}^2$ ). The Barrel of VD covers a radius an area between 96 mm and 500 mm (Fig. 4.7).  
 1254 All five cylindrical layers set with rectangular two-coordinate silicon strip detectors and give informa-  
 1255 tion on coordinates of the tracks  $(r, \phi, z)$  (enable to measure a point in each layer). The end-cup regions  
 1256 detect particles in the radial region between 96 mm and 500 mm. Each of the five disks set with DSSD  
 1257 with concentric ( $r$ ) strips and radial ( $\phi$ ) strips. The VD has length about 1.1 m and covers the region of  
 1258 pseudo-rapidity up to  $|\eta| < 2.0$ . Each DSSD has  $300 \mu\text{m}$  thickness and strip pitch in the range from  $95$   
 1259  $\mu\text{m}$  to  $281.5 \mu\text{m}$ . The DSSDs are assembled into detector modules by two detectors per module, form-  
 1260 ing strips 18 cm long. Detectors and Front-end electronics boards (FEE-PCB) connected via low-mass  
 1261 polyimide microcabels and assembled low-mass on mechanical supports with cooling system.

1262 From general conditions of SPD VD performance requirements are 1) close to  $4\pi$  geometry; 2) track  
 1263 reconstruction efficiency for muons greater than 99% at  $p \leq 13 \text{ GeV}/c$  (for  $0 \leq |\eta| \leq 2.5$ ); 3) low material  
 1264 budget less than  $2X_0$  per layer; 4) coordinates resolutions for vertexing:  $\sigma_{r,\phi} < 50 \mu\text{m}$ ,  $\sigma_z < 100 \mu\text{m}$ .  
 1265 The lifetime of Vertex Detector is required to be not less than 10 years of NICA running.

Table 4.3: Relevant numbers of the barrel VD.

Parameter	Layer 1	Layer 2	Layer 3	Layer 4	Layer 5	Total
$N_{DSSD}/\text{module}$	2	2	2	2	2	
$N_{\text{modules}}/\text{ladder}$	2	4	4	6	6	
$N_{\text{ladders}}/\text{layer}$	6	10	14	19	23	72
$N_{DSSD}/\text{layer}$	24	80	112	228	276	720
$N_{\text{chip}}/\text{module}$	10	10	10	10	10	
$N_{\text{chip}}/\text{layer}$	120	400	560	1140	1380	3600
$N_{\text{channel}}/\text{layer}$	15360	51200	71680	145920	176640	460800

### 1266 4.2 Double-sided silicon detectors

1267 Concept of Barrel DSSD module shown in Fig. 4.8. The module consists of two silicon detectors wire  
 1268 bonded strip to strip for p+ side (to reduce read-out channels), glued to the plastic frame and connected

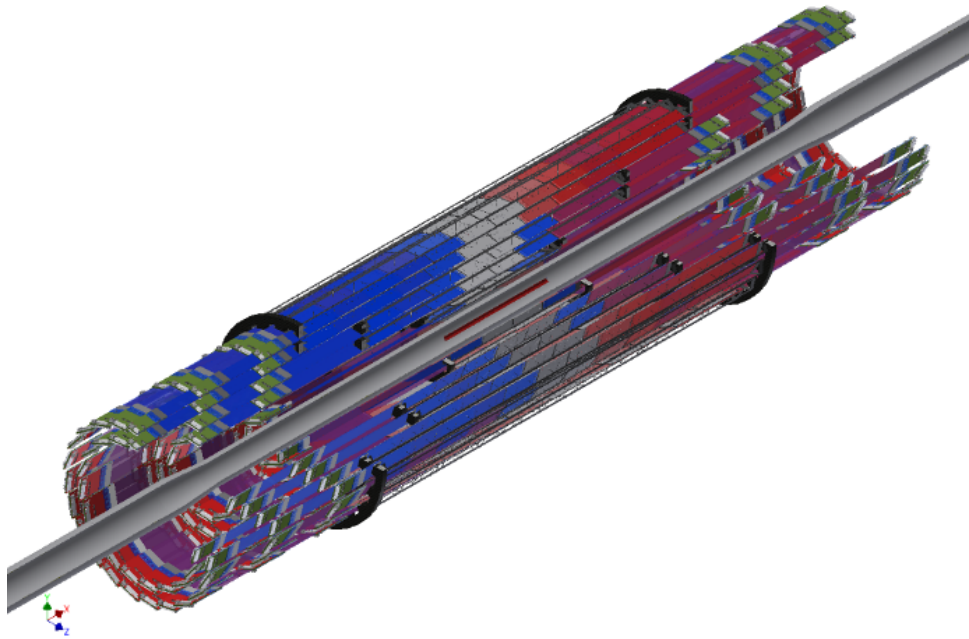


Figure 4.6: General layout of the SPD Vertex Detector.

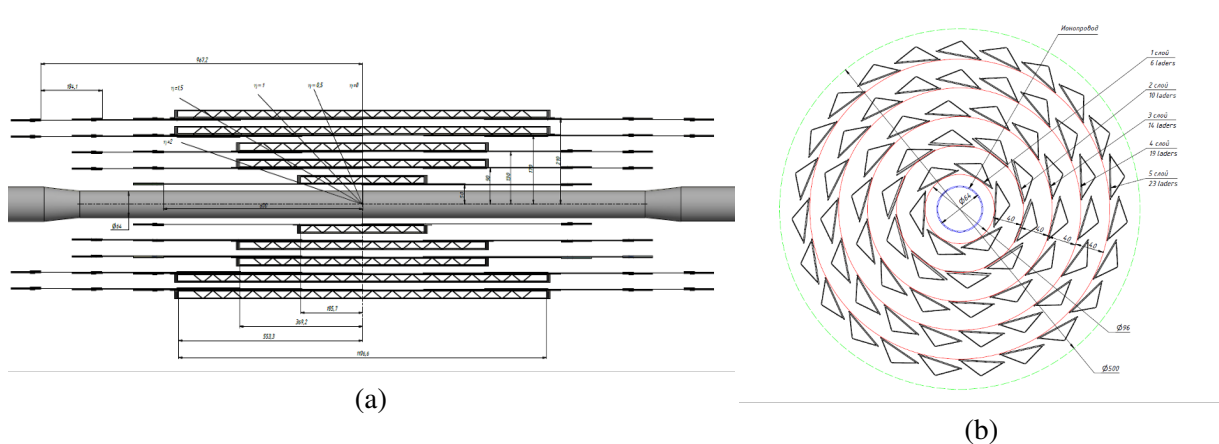


Figure 4.7: Longitudinal (a) and transversal (b) cross-sections of the barrel part of the Vertex Detector.

1269 with two front-end electronic boards via low-mass polyamide cable.

1270 The Silicon Detector made with planar double side technology based on n-type conductivity 6-inch  
 1271 float-zone Silicon wafers (produced by ZNTC, Zelenograd, Russia). It has  $63 \times 93 \text{ mm}^2$  size and  $300 \mu\text{m}$   
 1272 thickness. Pitch for  $p+$  side is  $95 \mu\text{m}$ , for  $n+$  side  $281.5 \mu\text{m}$ . Number of strips is 640 and 320 for the  $n+$   
 1273 and  $p+$  side, respectively. Stereo angle between strips  $90$  is degrees. Excepted spatial resolution for such  
 1274 detector topology is  $pitch_{p(n)+} / \sqrt{12} = 27.4 (81.26) \mu\text{m}$ , respectively for  $r - \phi$  and  $r - z$  projections. As  
 1275 mentioned before Barrel DSSD module contains two DSSDs ( $p+$  strips wire bonded strip to strip) and  
 1276 has 640 at each side.

1277 To bring the front-end electronics out of the tracker volume, will be used thin two polyimide cables with  
 1278 aluminum traces (for each side of module). Cable consists of few layers: signal layer, perforated or solid  
 1279 dielectric (polyimide) and shielding layer. Cable pins designed for TAB bonding with detector and pitch  
 1280 adapter sides. Maximum cable length is 60 cm total thickness of all cable layers less than  $0.15\% X0$ .

1281 Since DSSDs has DC topology it's necessary to supply bias voltage to detector and electrically decouple  
 1282 DC current from ASICs electronics inputs. For this purpose, integrated RC circuit (sapphire plates with  
 1283 Si-epitaxial layer Silicon On Insulator (SOI)) Pitch Adapter (PA) will be used for each side of module  
 1284 (produced by ZNTC, Zelenograd) designed with different topologies for each side. After pitch adapter  
 1285 detector's signal goes to ASIC. Table 1 shown possible ASIC read-out solution. Optimal choice should  
 1286 be done after ongoing R&D.

Table 4.4: default

ASIC	APV25	VATAGP7.3	n-XYTER	TIGER
Number of channels	128	128	128	64 (128?)
Dynamic range	-40fC – 40fC	-30fC – 30fC	Input current 10nA, polarity + and –	1–50fC
Gain	25mV/fC	20 $\mu$ A/fC		10.35mV/fc
Noise	246 e <sup>-</sup> +36 e <sup>-</sup> /pF	70e <sup>-</sup> +12 e <sup>-</sup> /pF	900 e <sup>-</sup> at 30pF	2000 e <sup>-</sup> at 100pF
Peaking time	50ns	50ns/500ns	30ns/280ns	60ns/170ns
Power consumption	1.15mW/ch.	2.18mW/ch.	10mW/ch.	12mW/ch.
ADC	No	No	16fC, 5 bit	10-bit Wilkinson ADC
TDC	No	No		10-bit Wilkinson ADC

### 1287 4.3 Mechanical layout

1288 Concept of barrel DSSD ladder shown in Fig. 4.9. Silicon modules are laying on carbon fiber support  
 1289 from center to edge. Detectors connect with FFE via thin low-mass cables. Front-end electronics are  
 1290 located at the edges of ladder and placed to conical caves as shown in Fig. 4.10 to provide connection to  
 1291 voltage supply, DAQ and cooling ASIC chips subsystems.

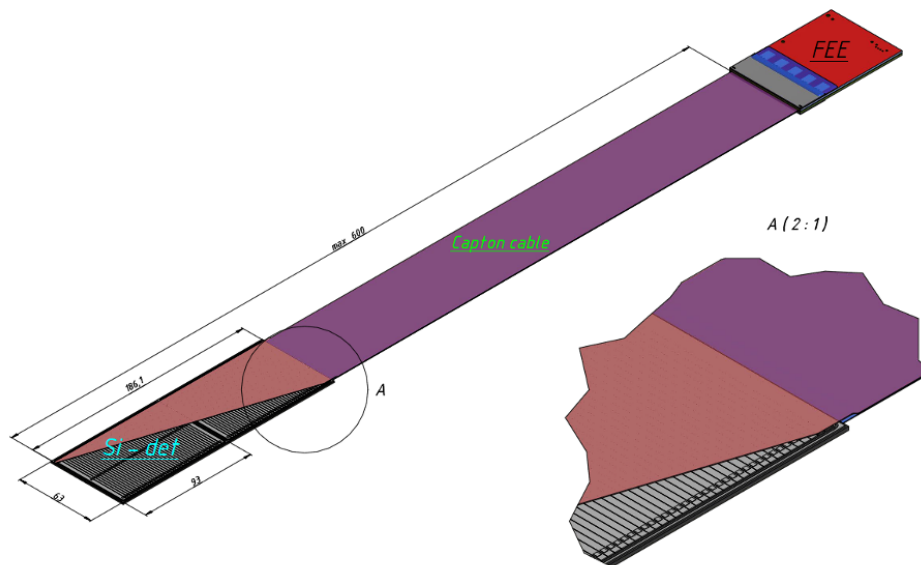


Figure 4.8: Concept of the barrel DSSD module.

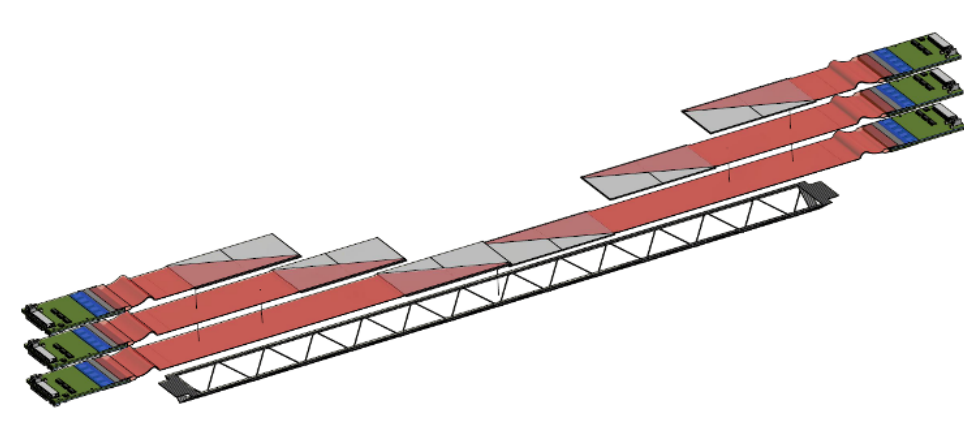


Figure 4.9: Conceptual layout of the barrel ladder.

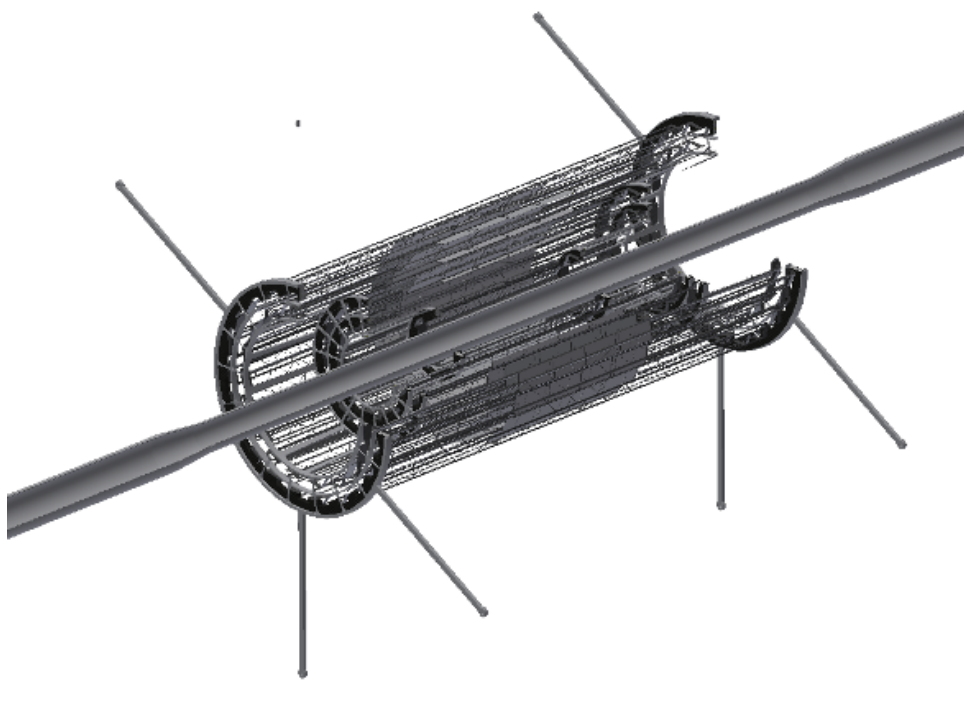


Figure 4.10: Concept of the VD mechanical support structure with conical caves for FEE.

## 1292 5 Tracking system [T. Enik]

1293 The Straw Tracker (ST) based on the gas-filled drift tubes in the main detector for determination of the  
 1294 particle momentum at SPD. It has to provide spatial resolution below  $150 \mu\text{m}$  in the magnetic field up  
 1295 to 1 T in order to reconstruct the charged particle tracks and event topology with good confidence. It  
 1296 has to be a low-material budget detector to minimize the multiple scattering effect and does not affect  
 1297 physics with photons. The core technologies required to build the Straw tracker are well established.  
 1298 The concept of the SPD ST s similar to the ATLAS TRT [2, 3, 5] and COMPASS [28, 71] straw trackers.  
 1299 Low mass straws have been successfully developed for various modern projects including NA62 [76],  
 1300 COMET [69], SHiP [19], Mu2e [59], and PANDA [48].

## 1301 5.1 Detector layout

1302 Thin-wall gas-filled drift tubes are used as a basic detecting element. Each tube (straw) is fabricating  
 1303 using polyethylene terephthalate film  $36\ \mu\text{m}$  thick by ultrasonic welding. Each tube has a diameter of  
 1304  $10\ \text{mm}$  and consists of a single anode wire in the centre that is made of  $30\ \mu\text{m}$  gold plated tungsten.  
 1305 The joint breaking strength of a tube is  $31.9\ \text{kg}/\text{mm}^2$ . A gas mixture used in the detector,  $\text{Ar} + \text{CO}_2$ ,  
 1306 provides gas gain not greater than  $10^5$  that warrants a long-lasting stable detector operation. Gas leakage  
 1307 from a tube volume of  $188.6\ \text{cm}^3$  under a pressure gradient of  $1.0$  atmosphere does not exceed  $0.3 \times 10^3$   
 1308  $\text{cm}^3/\text{min}$ . The high strength, the low tensile creep due to the absence of glued layers, negligible gas  
 1309 leakage and reliability in long-term operation make these tubes an excellent candidate for the detector  
 1310 elements of the main tracker.

1311 The SPD Straw tracker consists of three main parts: a barrel part (BST) and two end-caps. The BST has  
 1312 a cylindrical shape with an inner radius of  $800\ \text{mm}$ , an outer radius of  $1700\ \text{mm}$  and a length of  $2360$   
 1313  $\text{mm}$ . It consists of 8 stations. Each station has 40 intersecting perpendicular layers of straw and looks  
 1314 like a wedge. Stations of three modules with eight layers of straws. These are 4 double layers of straws  
 1315 along the X,Y,U and V axes. the external dimensions of the station are  $D=1700\ \text{mm}$ , and the thickness is

## 1316 5.2 Mechanics

## 1317 5.3 Electronics

## 1318 6 Electromagnetic calorimeter [O. Gavrischuk] [OUT OF DATE]

### 1319 6.1 Calorimeter design

1320 The electromagnetic calorimeter (ECAL) of the SPD setup should be placed inside the Range System  
 1321 and will consist of three parts: the barrel part and two end-caps. The ECAL should meet the following  
 1322 requirements coming from the physics tasks:

- 1323 – energy range from  $50\ \text{MeV}$  to  $10\ \text{GeV}$ ;
- 1324 – energy resolution of about  $5\%/\sqrt{E\ [\text{GeV}]}$ ;
- 1325 – granularity  $\sim 5\ \text{cm}$ ;
- 1326 – time resolution  $\sim 0.5\ \text{ns}$ ;
- 1327 – operation in the magnetic field;
- 1328 – long time stability of the basic parameters  $\pm 5\%$ .

1329 The proposed calorimeter is based on the experience of the KOPIO sampling calorimeter [224] consisted  
 1330 of alternating layers of lead and scintillator with fine granularity. A four-tower block of the KOPIO  
 1331 calorimeter is shown in Fig.4.11. The SPD calorimeter should consist of 220 layers of scintillator ( $1.5$   
 1332  $\text{mm}$ ) and lead ( $0.3\ \text{mm}$ ) plates. The scintillator tiles and the lead plates within the four-tower block  
 1333 should have transverse size  $5.5 \times 5.5\ \text{cm}^2$  and  $5.5 \times 5.5\ \text{cm}^2$ , respectively. They are fixed on the common  
 1334 plate with the help of 4 stainless rods. The wave length shifting fibers pulled inside the block should  
 1335 collect light to four avalanche multipixel diodes. The length of the active part of the module will not  
 1336 exceed  $450\ \text{mm}$ . Together with the readout electronics it should be fitted into  $600\ \text{mm}$ . The schematic  
 1337 layout of the SPD ECAL is shown in Fig. 4.12.

1338 The barrel part of the ECAL is designed as 3 rings (one middle and two side) with 8 azimuthal sectors.  
 1339 Side rings will consist of 2080 towers while the central one of 2288 towers (6448 towers in total). The

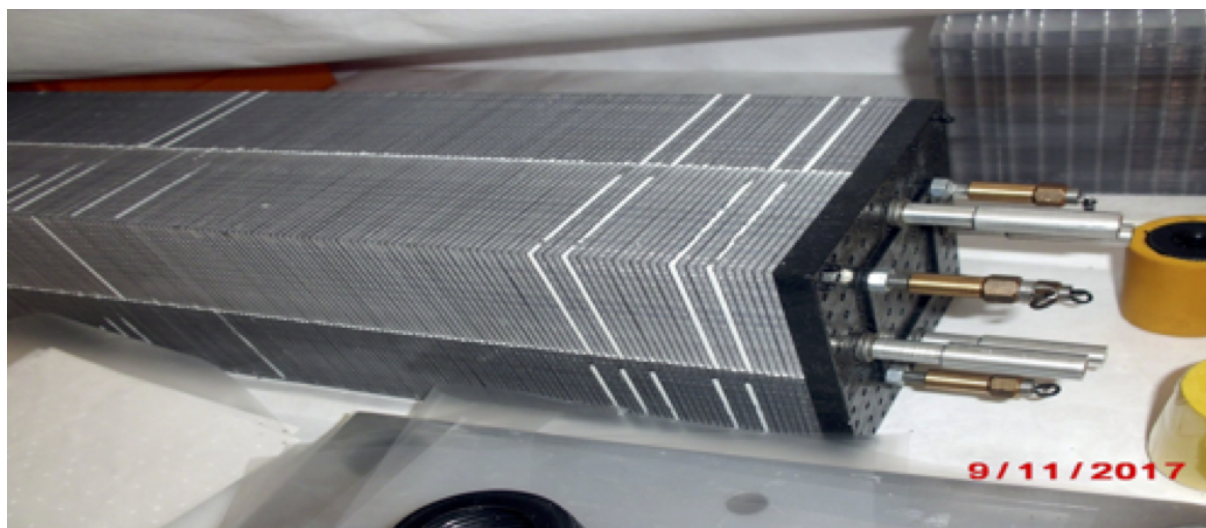


Figure 4.11: Two by two modules of the KOPIO sampling calorimeter assembled in the single block with 320 layers of lead and scintillator of 0.3 mm and 1.5 mm thick, respectively.

1340 end-cap part is planned as two discs with the diameter of about 3.6 m and the beam hole of about 20 cm.  
 1341 It will consist of the modules of the same type as the barrel part. The total amount of towers in the each  
 1342 end-cap disc is planned to be 850. The expected weight of the barrel part and the end-cap part is 81 tons  
 1343 and 11+11 tons, respectively. Assuming that the weight of the supporting structures is about 15%, the  
 1344 total weight of the SPD ECAL could be estimated as 118.5 tons.

1345 The prototype of the SPD ECAL module could be produced using the existing matrix form and moulding  
 1346 machine (shown in Fig. 4.13).

1347 The best possible resolution of the proposed sampling calorimeter is

$$\sigma_E/E = (1.96 \pm 0.1)\% \oplus (2.74 \pm 0.05)\%/\sqrt{E}. \quad (4.1)$$

1348 Photostatistics and nonuniformity of the light collectors add to the total energy resolution the additional  
 1349 terms  $2.1\%/\sqrt{E}$  and  $1.8\%/\sqrt{E}$ , respectively.

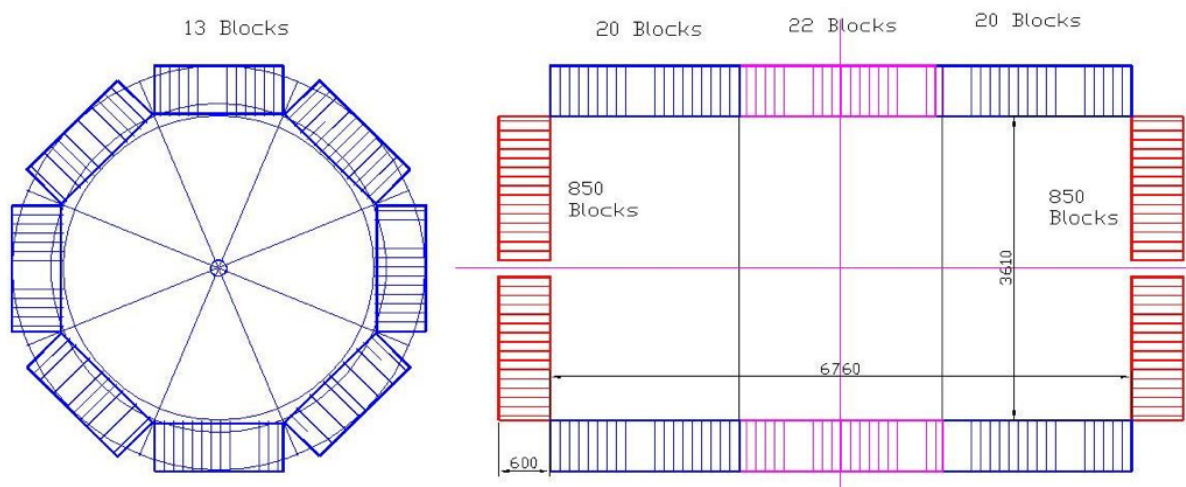


Figure 4.12: Schematic layout of the SPD electromagnetic calorimeter.





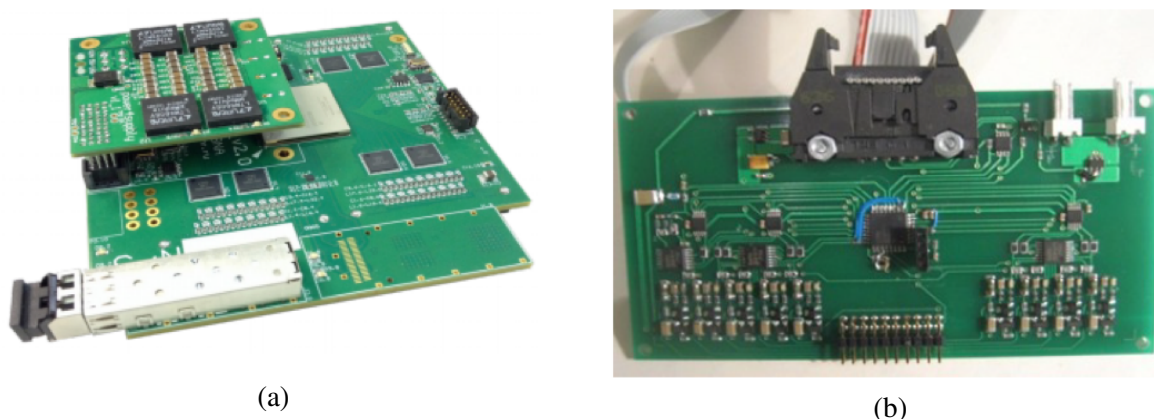
Figure 4.13: The scintillator production facility: moulding machine.

## 1350 6.2 Front-end electronics

1351 ECAL totally has 32592 channels and 510 64-channel front-end boards is needed to readout organization.  
1352 It is planned to use the board ADC64s [225] that is a 64-channel 12-bit 50MS/s ADC device with signal  
1353 processing core and Ethernet interface. It has dedicated serial links for clock synchronization and data  
1354 readout that allows system scalability to arbitrary number of channels. The power consumption is +12V  
1355 and 1.5A with proper air cooling. The board size is 145x106 mm, Fig.4.14 (a). It digitize the analogue  
1356 input signal and samples it at fixed time intervals. Zero suppression logic is based on baseline estimation  
1357 and threshold value. Signal shaping is performed in digital form with FIR filters. It allows to reduce the  
1358 number of waveform points required for digital signal representation with minimum loss of accuracy.  
1359 The ring type memory allows the read back of last 30  $\mu s$  of waveforms. The ADC64s board is used  
1360 successfully at NICA BM@N.

1361 The High Voltage (HV) control for SIPM will be based on equipment designed by the HVSYS company  
1362 [226]. Such modules are used successfully at NICA BM@N and COMPASS (CERN). Multichannel HV  
1363 system consists of the Control Box (Fig.11, left) which is able to control and supply power for 127 cells  
1364 with SIPM diodes. It has a remote Ethernet control and optionally USB-2 or RS-232 interface. The  
1365 patch way (10 pair flat cable) distributes the necessary signals for powering of 127 diodes and provides  
1366 feedback for taken their temperature stability. The thermo sensor is installed nearly from SIMP for these  
1367 purposes. HV board for supplying of 8 channels is shown in Fig. 4.14 (b).

1368 The slow control system is considered to be based on the LED control. For this purpose the light pulse  
1369 will be distribute by via the transparent fibers from the LED driver to all SIPMs. The LED driver  
1370 developed by the HVSYS company is assumed to be used.



(a) (b)  
Figure 4.14: (a) ADC64s board and (b) HV board.

## 1371 7 Range (muon) system [G. Alexeev]

### 1372 7.1 General description

1373 The Range System of the SPD detector serves for the following purposes: (i) identification of muons  
 1374 in presence of a remarkable hadronic background and (ii) estimation of hadronic energy (coarse hadron  
 1375 calorimetry). It is important to stress that the system is the only device in the SPD setup, which can  
 1376 identify neutrons (by combining its signals with the electromagnetic calorimeter and the inner trackers).  
 1377 Muon identification (PID) is performed via muonic pattern recognition and further matching of the track  
 1378 segments to the tracks inside the magnets. The precise muon momentum definition is performed by the  
 1379 inner trackers in the magnetic field. The Mini Drift Tubes [227, 228] are used in the Range System as  
 1380 tracking detectors providing two-coordinate readout (wires and strips running perpendicularly). Such  
 1381 readout is mostly needed for the events with high track multiplicity and also for the reconstruction of the  
 1382 neutron space angle.

1383 As for the design and construction of the present system, we assume to capitalize on the experience  
 1384 gained by the JINR group in the development of the PANDA (FAIR, Darmstadt) Muon System [? ].  
 1385 These two systems (PANDA and SPD), dealing with muons of comparable momentum ranges and solv-  
 1386 ing the same PID tasks, should look very similar in their design and instrumentation.

### 1387 7.2 System layout

1388 The Range System serves as an absorber for hadrons and a ‘filter’ for muons. It also forms the magnet  
 1389 yoke. It consists of a Barrel and two End Caps. Each End Cap, in its turn, consists of an End Cap Disk  
 1390 and a Plug. The schematic 3D view of the system and its main sizes are shown in Fig.4.15 (a). The  
 1391 absorber structure is shown in Fig.4.15 (b). The outer 60-mm Fe layers are used for bolting the modules  
 1392 together. The interlayer gaps of 35 mm are taken for reliable mounting of the detecting layers comprising  
 1393 the MDTs proper, the strip boards and the front-end electronic boards on them. The 30-mm thickness  
 1394 of the main absorber plates is selected as comparable with muon straggling in steel, thus giving the best  
 1395 possible muon-to-pion separation, and also providing rather good sampling for hadron calorimetry.

1396 The Barrel consists of eight modules, and each End Cap Disk consists of two halves divided vertically.  
 1397 Such subdivision of the system (14 pieces in total) is chosen to optimize its further assembly and to  
 1398 satisfy the constructional requirements of the SPD experimental hall (cranes capability and floor load).  
 1399 The total weight of the system is about 810 tons, including 30 tons of detectors. The total number of  
 1400 MDT detectors is about 8000 units. The MDTs are deployed in the following way: along the beam  
 1401 direction in the Barrel, and perpendicular to the beam (horizontally) in the End Caps.

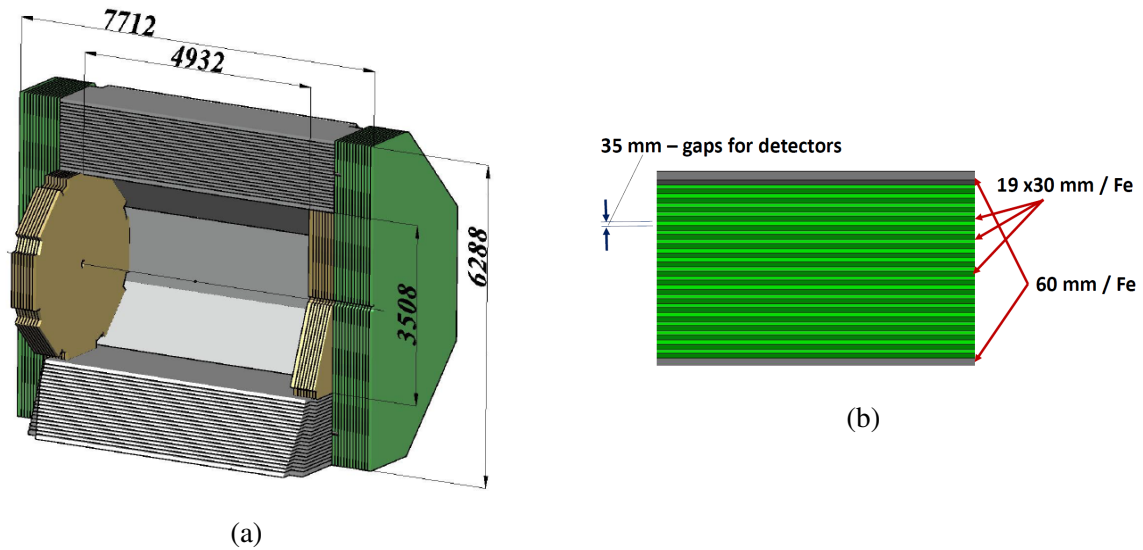


Figure 4.15: 3D view (half cut) of the Range (muon) system: (a) Barrel is shown in grey, End Cap Disks – in green, and End Cap Plugs – in yellow; (b) absorber structure.

1402 The absorption thicknesses of Barrel and End Caps are selected to be equal - to 4 nuclear interaction  
 1403 lengths ( $\lambda_I$ ) each. It provides uniform muon filtering in all directions. Together with the thickness of the  
 1404 electromagnetic calorimeter ( $\sim 0.5 \lambda_I$ ) the total thickness of the SPD setup is about  $4.5 \lambda_I$ .

### 1405 7.3 Mini drift tubes detector

1406 The Mini Drift Tubes (MDT) detector was initially developed and produced at JINR for the Muon System  
 1407 of the D0 experiment at FNAL [229]. Later on, an MDT-based muon system was also produced for the  
 1408 COMPASS experiment at CERN [230]. Developed two-coordinate readout modification of the MDT  
 1409 with open cathode geometry and external pickup electrodes was proposed to and accepted by the PANDA  
 1410 collaboration at FAIR for the muon system of their experimental setup. This new version of the MDT  
 1411 is proposed for the SPD project, as it has all the necessary features – radiation hardness, coordinate  
 1412 resolution and accuracy, time resolution, robustness, as well as advanced level of already conducted  
 1413 R&D within the PANDA project.

1414 The cross-section and layout of the MDT with open cathode geometry are shown in Fig.4.16. The detec-  
 1415 tor consists of a metallic cathode (aluminum extruded comb-like 8-cell profile), anode wires with plastic  
 1416 supports, and a Noryl envelope for gas tightness. The comb-like profile of the cathode provides each wire  
 1417 with an opening left uncovered to induce wire signals on the external electrodes (strips) perpendicular to  
 1418 the wires. The strips are applied to obtain the second coordinate readout. The shape of the induced signal  
 1419 repeats the initial one, having the opposite polarity, but the amplitude is about 15% of the wire signal (see  
 1420 Fig.4.17). Thus, the strip signal readout requires higher signal amplification and proper electromagnetic  
 1421 shielding.

1422 Application of an open cathode leads to the loss of the electric field symmetry in each of the 8 detec-  
 1423 tor cells, resulting in lower gas gain for the applied voltage comparing to the standard MDT (cathode  
 1424 openings closed with stainless steel lid). The conducted R&D proved that the MDT with open cathode  
 1425 geometry easily achieves the parameters of the one with a closed cathode at higher voltages. The com-  
 1426 parative plots of the counting rate, efficiency, and gas gain for both detector types (see Fig.4.18) show  
 1427 that the MDT with open cathode geometry repeats the standard MDT performance at a high voltage shift  
 1428 of + 100V. The drift time and the amplitude spectra of both detector variants also match, if we set this  
 1429 voltage shift between their operating points.

MDT with open cathode geometry and external pickup electrodes (strips) cross-section

External board with strips perpendicular to MDT wires

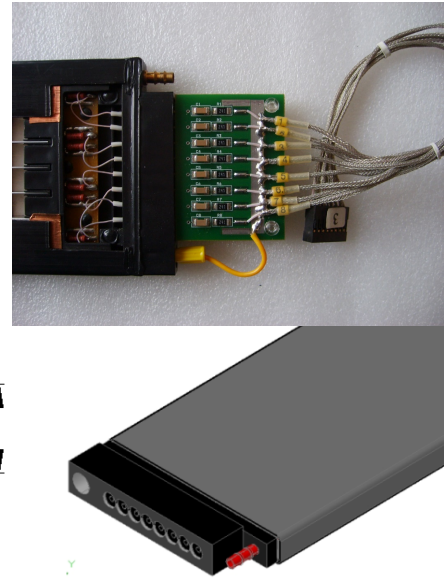
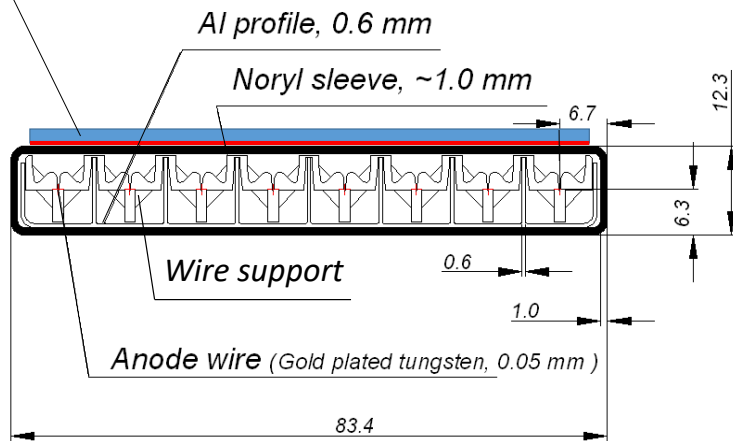


Figure 4.16: Mini Drift Tube with open cathode geometry cross-section (left) and layout (right).

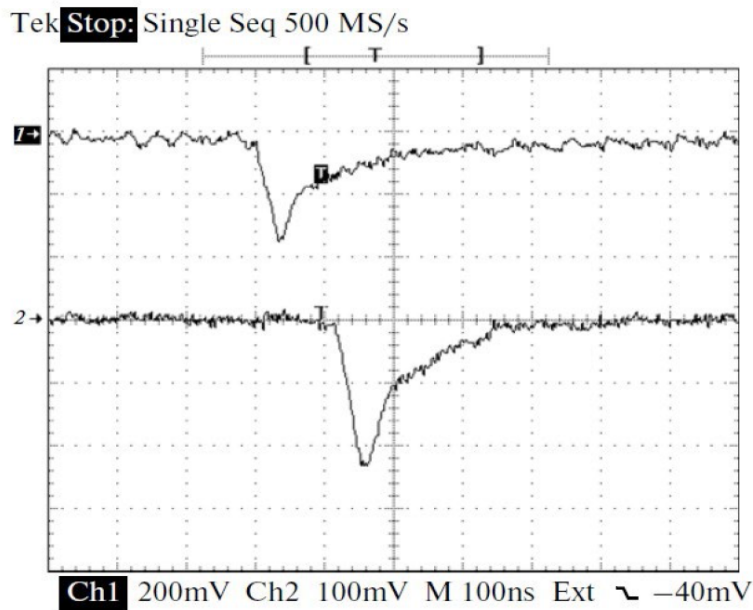


Figure 4.17: Oscillograms of single signals: from the anode wire (1) and the strip (2, inverted); the conversion factors are 60 and 480 mV/ $\mu$ A, respectively.

1430 According to the results of the MDT (open cathode geometry) ageing tests, accumulation of a 1 C/cm  
 1431 total charge does not produce any significant effect on the detector performance. To monitor the ageing  
 1432 effects, measurements of the counting rate curves (Co-60 source) together with oscilloscopic observa-  
 1433 tions of the MDT average signals (256 events) for Co-60 and X-rays were made twice a week over the  
 1434 whole period of intense irradiation (see Fig.4.19). Later on, this measurement (with X-rays) was con-  
 1435 ducted up to 3.5 C/cm of irradiation without any visible degradation of the MDT performance. It should  
 1436 ensure stable MDTs performance for the lifetime of the SPD project.

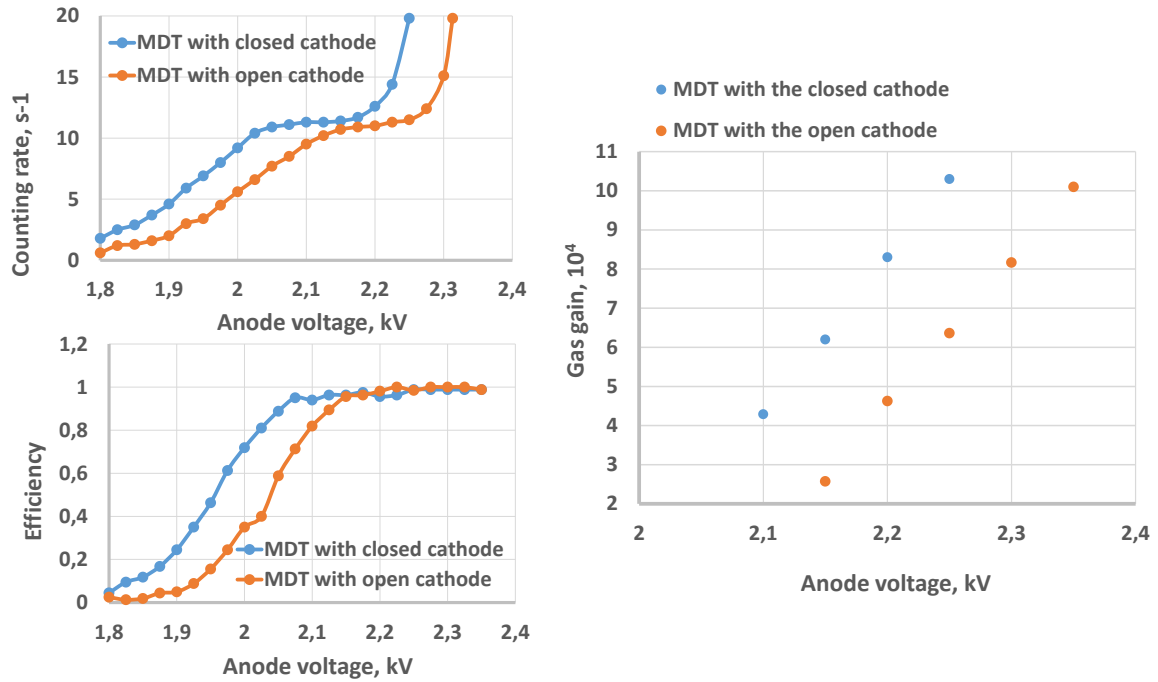


Figure 4.18: Comparative plots of the counting rate, efficiency, and gas gain versus the supply voltage for the MDT with closed and open cathode geometry.

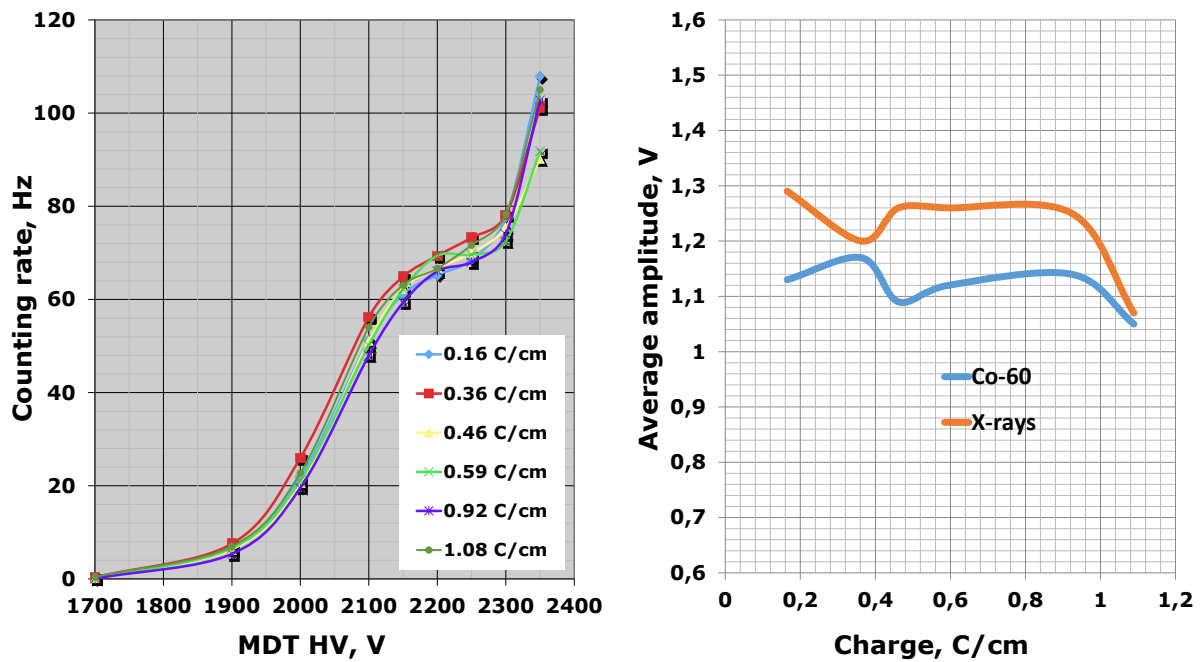


Figure 4.19: Counting rate curves for different accumulated charges (0.16÷1.08 C/cm) (left); average wire signal amplitudes vs accumulated charge for Co-60 and X-ray sources (right).

1437 All R&D studies were made with a gas mixture of 70% Ar + 30% CO<sub>2</sub> at atmospheric pressure, the one  
 1438 to be used in the proposed SPD Muon System. It is inflammable, radiation hard and fast enough (150-  
 1439 200 ns drift time). The wire pitch in the present design equals 1 cm, and a 3-cm strip width is selected  
 1440 for the second coordinate. These spatial parameters provide the Range System with coordinate accuracy  
 1441 well enough for identification of muons and give the system the features of a digital hadron calorimeter.

## 1442 7.4 Front-end electronics

1443 We plan to use the analog front-end electronics (with probable minor modifications) developed for  
1444 the D0/FNAL and COMPASS/CERN experiments and also accepted by PANDA/FAIR. It is based on  
1445 two ASIC chips: 8-channel amplifier Ampl-8.3 [231] and 8-channel comparator/discriminator Disc-8.3  
1446 [232].

1447 The HVS/A-8 card serves for two purposes - as an MDT high voltage distributor and a signal amplifier  
1448 designed to be the first stage of the Barrel and the End Cap Plugs wire signal readout. It is followed by  
1449 Disc-8.3 based discriminating electronics (design in process) to fulfill the readout.

1450 The ADB-32 card (initially designed for D0/FNAL) [233] is used for the End Cap Disks wire readout.  
1451 It amplifies and discriminates the MDT signal, shaping it to the LVDS standard for further treatment by  
1452 the digital front-end electronics.

1453 An A-32 preamplifier card is used to start the strip signal readout in the whole system. It should be  
1454 terminated (similarly to wire readout) by Disc-8.3-based discriminating electronics. In case of the End  
1455 Cap Disks an ADB-32 card will be used for this purpose. The view of the basic FEE cards is shown in  
1456 Fig.4.20.

1457 Totally, the Range System has 106000 readout channels ( 65000 of which are wires and 41000 strips).

1458 After having been shaped to the LVDS standard, the signals from the analog electronics go to the digital  
1459 front-end electronics for further treatment.

1460 The digital electronics being created for the Muon System is based on the use of FPGA chips. The  
1461 prototype of the digital 192-channel MFDM module (Muon FPGA Digital Module) that we have devel-  
1462 oped includes a XC7A200T chip of the Xilinx Artix 7 family. This unit is functionally, mechanically, in  
1463 data format and DAQ interface, compatible with the previously developed MWDB (Muon Wall Digital  
1464 Board) unit [?] made on the basis of TDC F1 (ASIC) and successfully used for data readout from the  
1465 Muon System of the COMPASS experiment (CERN). This approach allows both types of units to be  
1466 used in the same readout system, thus making it possible for the new MFDBs cards to be tested under  
1467 actual operating conditions.

1468 The unit includes three electronic boards (Fig.4.21): motherboard, mezzanine card, and interface card.  
1469 The motherboard accepts 96 LVDS signals from the analog electronics through 3 high-density connec-  
1470 tors, converts them to LVTTTL levels and writes to the FPGA, and also communicates with two other  
1471 boards. The mezzanine card also accepts 96 LVDS signals through 3 connectors, converts them to  
1472 LVTTTL levels and transmits through the 120-pin board-to-board connector to the motherboard. The in-  
1473 terface card is designed to connect the MFDM module with the DAQ via the HotLink interface (RJ45  
1474 connector), to download the firmware to the FPGA from a local computer, as well as to download the  
1475 firmware via the RS-485 interface (RJ45 connector) from a remote computer.

1476 Tests performed at CERN with the Muon System prototype on cosmic muons gave encouraging results.  
1477 The further tests will be conducted with a prototype of the SPD range system ( $\sim 1200$  channels of wire  
1478 and strip readout) at the Nuclotron test beam area.

1479 In the future, after the final tuning of the unit, we are planning to replace the HotLink interface in the  
1480 MFDM module with the S-Link interface for direct connection of the Muon System digital electronics  
1481 to the FPGA-based SPD DAQ. A general view of the data flow structure for the Muon System is shown  
1482 in Fig.4.22.

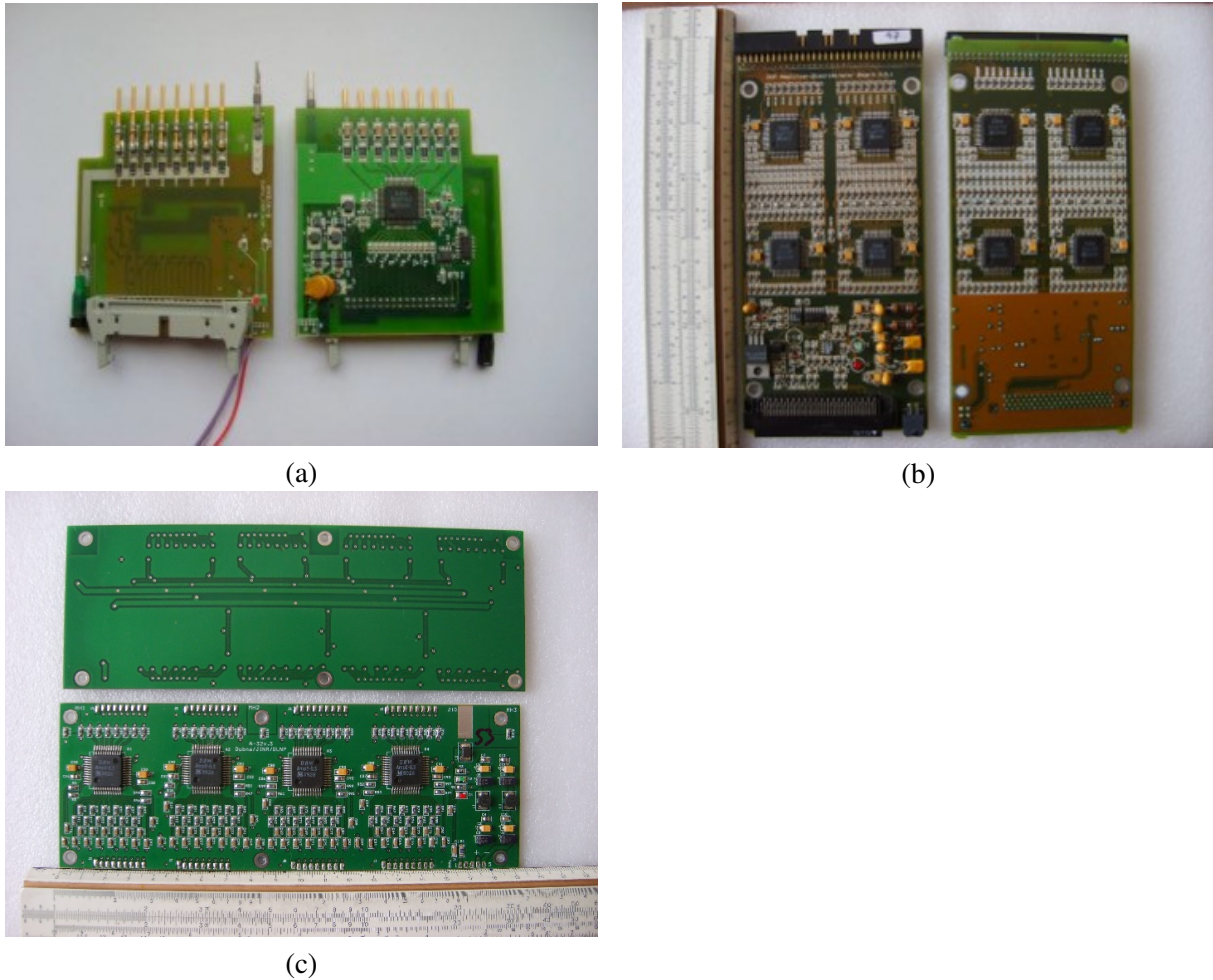
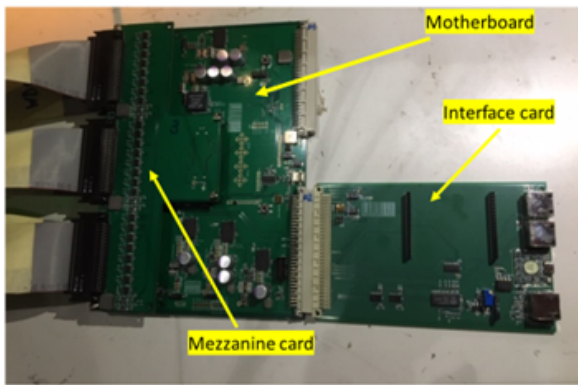
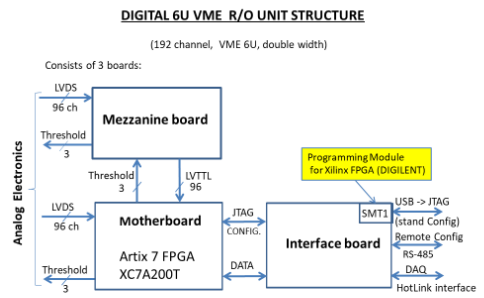


Figure 4.20: Front-end analog electronics cards: HVS/A-8 (a), ADB-32 (b) and A-32 (c).



(a)



(b)

Figure 4.21: Digital 192-channel MFDM module (a) and its block-diagram (b).

1483 **7.5 Performance figures**

1484 The evaluation of the main parameters of the proposed Range System is being performed with big proto-  
 1485 type installed at CERN within the PANDA program. The prototype (Fig.4.23) has a total weight of

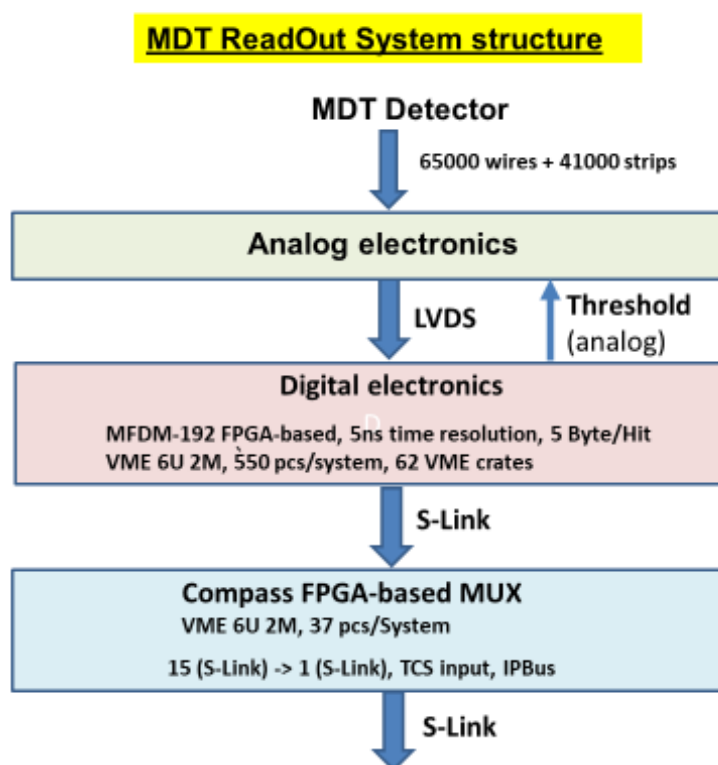


Figure 4.22: Data flow diagram – from detector to DAQ.

1486 about 10 tons (steel absorber and detectors with electronics) and comprises 250 MDT detectors with  
 1487 4000 readout channels (2000 for the wires and 2000 for the strips, 1 cm wide). It has both samplings  
 1488 (3 cm and 6 cm) present in the system (Barrel and End Caps), thus providing an opportunity for direct  
 1489 calibration of the response to muons, pions, protons, and neutrons.

1490 Fig.4.24 gives the examples of the prototype response to different particles. The patterns demonstrate  
 1491 excellent PID abilities of the Range System. The data were taken during the May and August runs of  
 1492 2018 at the T9/PS/CERN test beam. The beam particles hit the prototype from the top of the picture.  
 1493 The beam momentum for all the particles is 5.0 GeV/c. Neutrons were generated by a proton beam on a  
 1494 carbon target placed in the very vicinity of the first detecting layer. The points on the pictures represent  
 1495 hit wires, thus giving the impression of a typical device response with an accuracy  $\sim 1$  cm.

## 1496 8 Time of flight system [OUT OF DATE]

### 1497 8.1 SPD-ToF system

1498 Newest SPD detector should allow identifying different particles with good resolution. In this case it  
 1499 has to have good time-of-flight (TOF) system. Estimate time resolution of such TOF system should  
 1500 not be worse than (60?) ps. The efficiency of particle registration at high rate (few kHz/cm<sup>2</sup>) must be  
 1501 above 98%. Based on the experience of built similar systems in experiments as ALICE [1], HARP [2],  
 1502 STAR [3], PHENIX [4] and BM@N the glass multigap Timing Resistive Plate Chamber (mRPC) could  
 1503 be proposed as base time detector. For example, ToF-700 wall in BM@N experiment provides us with



## PANDA Muon System Prototype @ PS/T9/CERN Beam Line

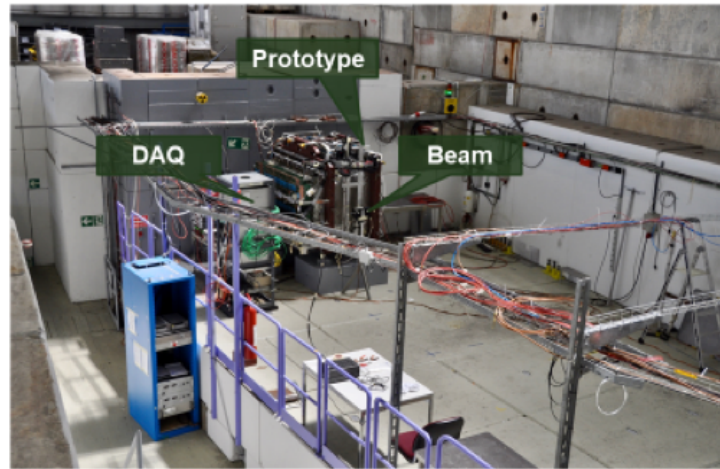


Figure 4.23: Range System prototype (10 ton, 4000 readout channels) at CERN.

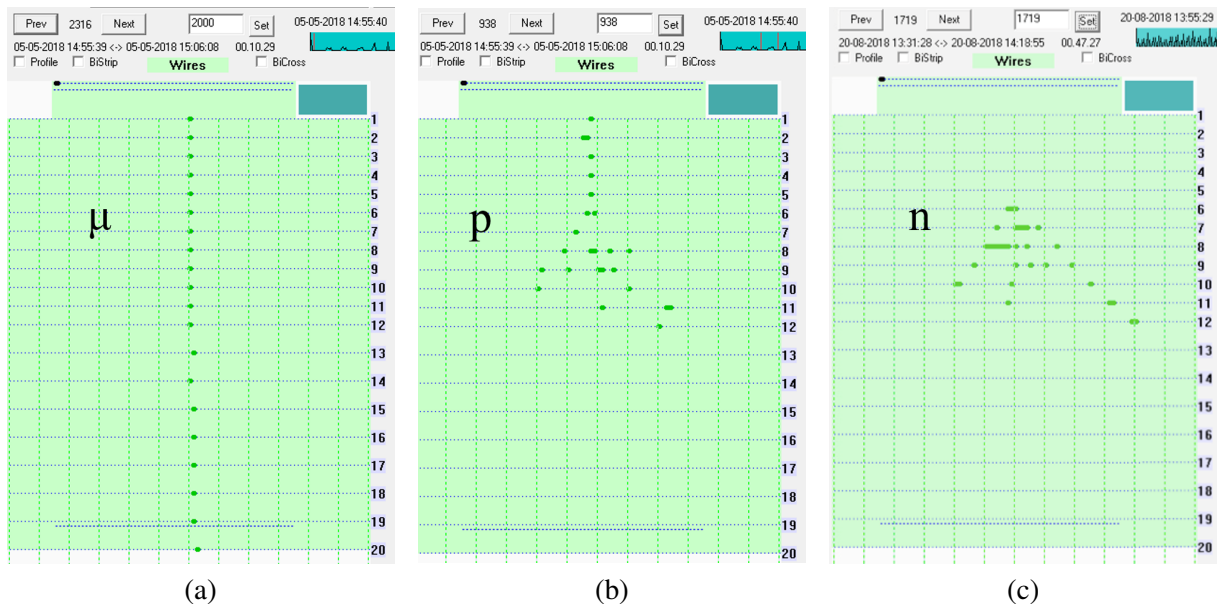


Figure 4.24: Demonstration of PID abilities: patterns for - (a) muon, (b) proton and (c) neutron.

1504 the pion/kaon separation up to 3 GeV/c and proton/kaon separation up to 5 GeV/c. In an assumption that  
1505 time resolution of start timing detector will be <40 ps.

1506 Design of the BM@N ToF-700 wall was based on experimental results obtained during multiple tests of  
1507 various modifications of glass mRPC exposed in charge particles beam [38, in preparation]. The counting  
1508 rate for standard glass mRPC is limited to several hundreds Hz/cm<sup>2</sup> due to the use of conventional float  
1509 glass plates with a bulk resistivity in the range 10<sup>12</sup> – 10<sup>13</sup> Ω·cm. Therefore, the extension of the  
1510 counting rate capabilities of mRPC has become an important issue.

1511 One of the way to increase the mRPCs performance at high rates is to use the low resistivity glass (less  
1512 than 10<sup>10</sup> – 10<sup>11</sup> Ω·cm) [24, 25, 26, 27] or ceramics [28] as the electrode materials. For instance,

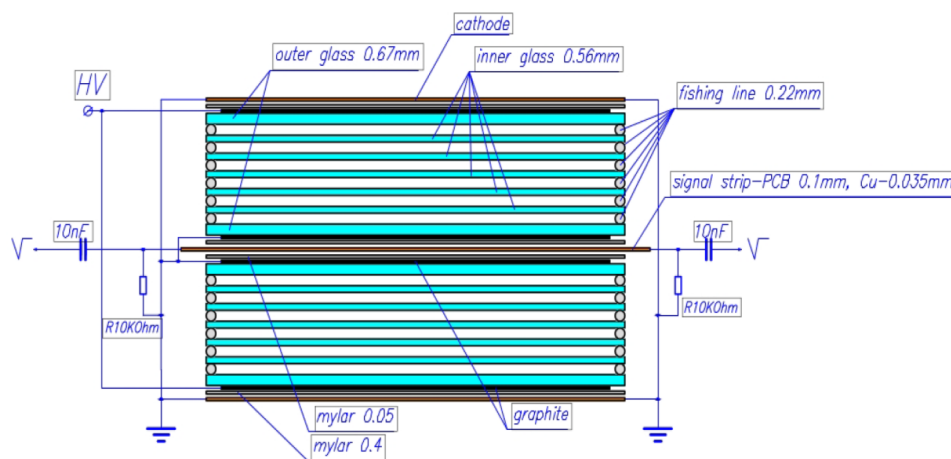


Figure 4.25: Schematic cross-section of the twelve gap MRPC.

1513 time resolutions below 90 ps and efficiencies larger than 90% were obtained for particle fluxes up to 25  
 1514 kHz/cm<sup>2</sup> for the 10-gap mRPC [26]. An alternative method is to reduce the glass stack resistance by  
 1515 minimizing of the used electrodes thickness and to increasing a temperature of the glass [29, 30]. It was  
 1516 shown that such method can provide high time resolution at continuous rate up to 20 kHz/cm<sup>2</sup> [31].

## 1517 8.2 Warm mRPC for BM@N

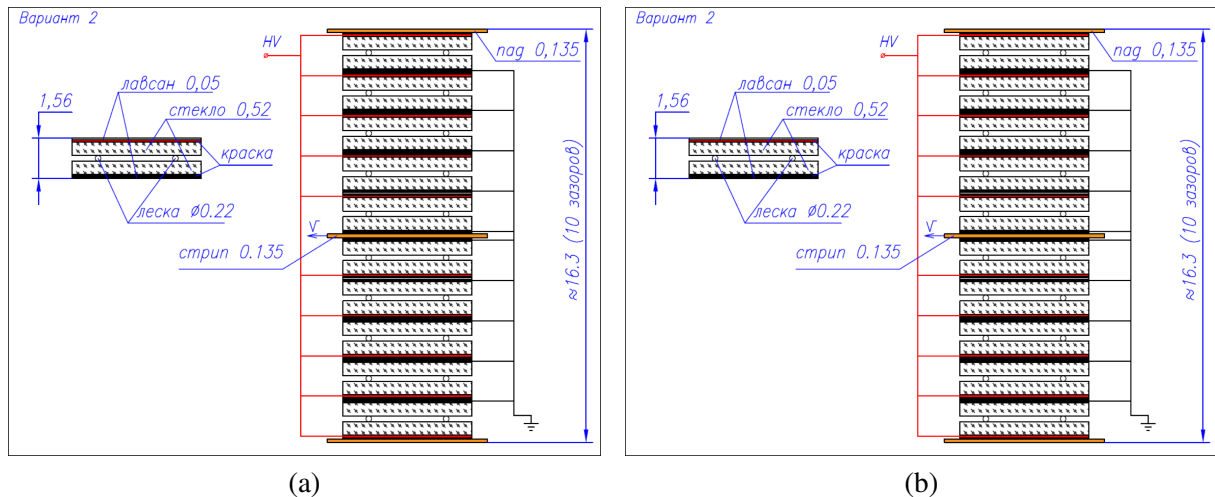
1518 Schematic cross section of mRPC is shown in Fig. 4.25. It consists of two identical 6-gap stacks with  
 1519 anode strip readout plate in between. The size of mRPC is 473×279×17 mm<sup>3</sup> with the working area of  
 1520 351x160 mm<sup>2</sup>. Each mRPC has 32 10x160 mm<sup>2</sup> readout strips with 1 mm gaps between them.

1521 Each stack is formed by seven glass plates with the  $2 \times 10^{12} \Omega\cdot\text{cm}$  bulk resistivity. The gap between the  
 1522 glasses 0.22 mm is fixed by spacers – usual fishing-lines, which ran directly through the RPC working  
 1523 area. Graphite conductive coating with surface resistivity of  $\sim 1 \text{ M}\Omega$  is painted to outer surfaces of  
 1524 external glass plates of each stack to distribute both the high voltage and its separate ground and thus to  
 1525 form the uniform electrical field in the stack sensitive area. The anode readout strips plate is a one-sided  
 1526 printed PCB with the thickness of 100 mm, the thickness of the copper is 35 microns. Signals are taken  
 1527 from the both ends of anode strips. The entire mRPC assembly is put into a gas-tight box. Bottom of box  
 1528 is made of a double side PCB (motherboard) with a thickness of 2.5 mm, side frame of the box is made  
 1529 of aluminum profile, the top of box is closed by aluminum cover having thickness of 1.5 mm. Paper  
 1530 [38] presents the performance of 12-gap mRPC in the range of the counting rate from 0.45 kHz/cm<sup>2</sup>  
 1531 up to 10 kHz/cm<sup>2</sup> obtained using secondary muon beam from U70 at Protvino. The measurements at  
 1532 different rates were performed in the mRPCs temperature range 25-45 °C with the step of 5 °C. The time  
 1533 resolution is reached up to 50-60 ps with good and stable efficiency under temperature of 40-45 °C.

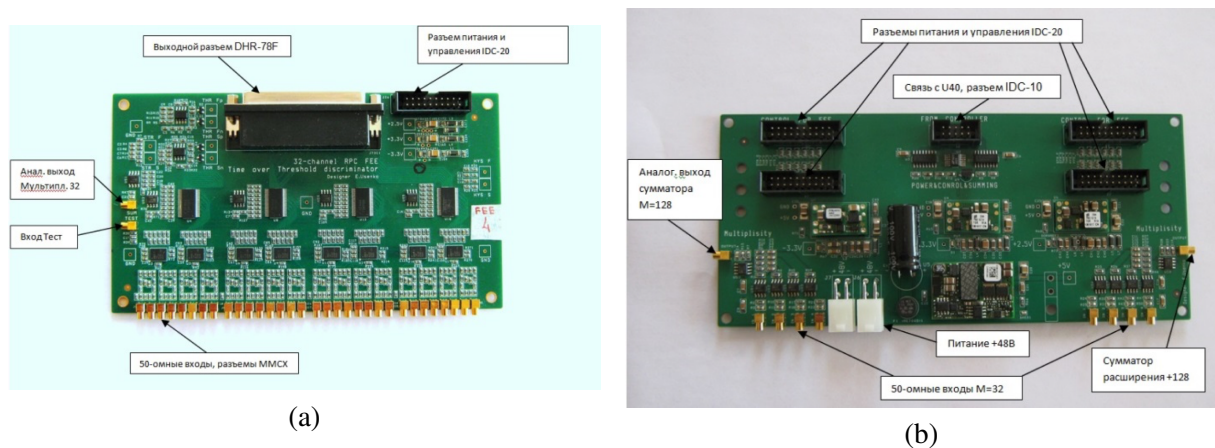
## 1534 8.3 Chamber for SPD

1535 Particle flux in SPD experiment is expected up to 10 and more kHz/cm<sup>2</sup> (?). Therefore the high-speed  
 1536 performance of TOF system is important parameter. In order to increase the high-speed performance of  
 1537 mRPC now is decided to make new chamber using of glass plate with less thickness and cover each plate  
 1538 by graphite (Fig. 4.26). It should decrease the time dissipation of charge inside glass.

1539 Using such structures we expect to increase high-speed performance twice with time resolution better  
 1540 than 50 ps



(a) (b)  
Figure 4.26: Schematic cross-section of the new MRPC.



(a) (b)  
Figure 4.27: The 32RPC (a) and PWR&CTRL (b) modules.

#### 1541 8.4 FEE of mRPC

1542 The 32-channels FEE module (32RPC board) designed for our mRPCs bases on NINO chip. The output  
 1543 signal of NINO amplifier-discriminator is the time-over-threshold pulse whose leading edge provides  
 1544 with the time of the hit while its pulse width is proportional to the input signal charge [9]. The signals  
 1545 from mRPC to the module 32RPC are coming by 50Ω coaxial cables with use MMCX connectors.  
 1546 Output LVDS signals are transmitting to the module of digitization with use of DHR-78F sockets. At  
 1547 present a 64-channel VME time-to-digital converter TDC64VHLE based on the HPTDC chip is used for  
 1548 digitization [10]. Power supply, threshold settings, stretch time settings and hysteresis settings of the four  
 1549 32RPC boards are made by a special designed module power and control (PWR&CTRL). PWR&CTRL  
 1550 module is controlled by the U-40 VME module [11] via digital SPI interface.

#### 1551 8.5 SPD time resolution requirements

- 1552 – Diameter = 2 m
- 1553 – Time of flight = ~10 ns
- 1554 – Required time resolution = 20 ps (??)

## 1555 9 Beam-beam counter [V. Ladygin]

1556 Two Beam-Beam Counters are located just in front of the PID system endcaps. The main goal of the  
 1557 Beam-Beam Counter is the local polarimetry at SPD using the measurements of the azimuthal asymmetry  
 1558 in inclusive production of charged particles in collision of transverse polarized proton beams.

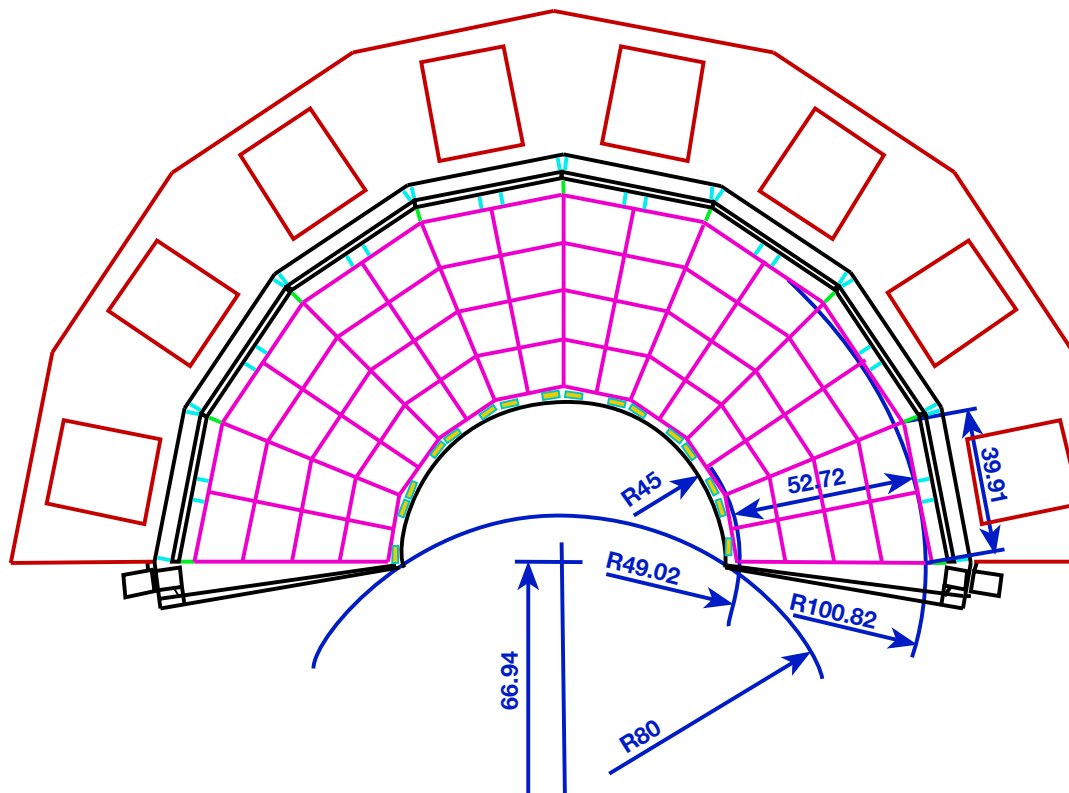


Figure 4.28: Beam-beam counter azimuthal and polar angle segmentation.

1559 Another goal of BBC is the fast selection of the different types of events. The simulation performed at  
 1560  $\sqrt{s}=27 \text{ GeV}/c^2$  for minbias  $pp$ - collisions gives that at least one BBC will have a signal for 72% events  
 1561 (only 41% in both BBCs). However, in the case of hard processes at least one BBC will hit in 96.5% of  
 1562 events, while both BBCs will have signals in 67% cases. Therefore, the requirement of the BBC signals  
 1563 allows to select hard processes.

1564 The concept of the BBC is shown in Fig.4.28. It consists of two major part: inner and outer, which are  
 1565 based on different technologies. BBC inner part will be based on fast segmented Micro Channel Plate  
 1566 (MCP) detectors, while BBC outer part will be produced from fast plastic scintillator tiles. The inner part  
 1567 covers 30-60 mrad and should be separated on to 4 layers consisting of 32 azimuthal sectors. The  
 1568 outer part covers 60-500 mrad divided on 5-6 layers on the polar angle each of them has 16 azimuthal  
 1569 sectors. Final segmntation will be obataied from the ptimization of the polar angle granularity for the  
 1570 whole energy range of NICA.

### 1571 9.1 Inner part of BBC: MPC

1572 Two compact detector systems are proposed to meet the challenges of the fast beam-beam collisions  
 1573 monitoring, event selection and the precise timing determination in proton-proton and nucleus-nucleus  
 1574 collisions at NICA. Beam Position Monitor (BPM) and Fast Beam-Beam Collision (FBBC) monitor  
 1575 are capable to provide the information for each bunch crossing both on the beams location and on the

1576 intensity of collisions, as well as on the azimuthal distribution of the particles in the event. The systems  
 1577 use fast Micro Channel Plate detectors (MCPs). The ultra-high vacuum (UHV) compatibility and low-  
 1578 mass compact design of the BPM and FBBC components allow one to consider their application inside  
 1579 the vacuum beam line of NICA collider. The BPM is based on the effect of the residual gas ionization  
 1580 and provides high accuracy, fast, bunch-by-bunch measurements of the beam position. FBBC uses the  
 1581 concept of the fast isochronous timing for the multi-pad readout of short ( $\sim 1$ ns) MCP signals, produced  
 1582 by the particles in the collisions of the beams. Studies of the polarization phenomena in light- and heavy-  
 1583 ion interactions at SPD NICA is another goal of research at NICA, and the FBBC is also considered for  
 1584 the local polarimetry at SPD.

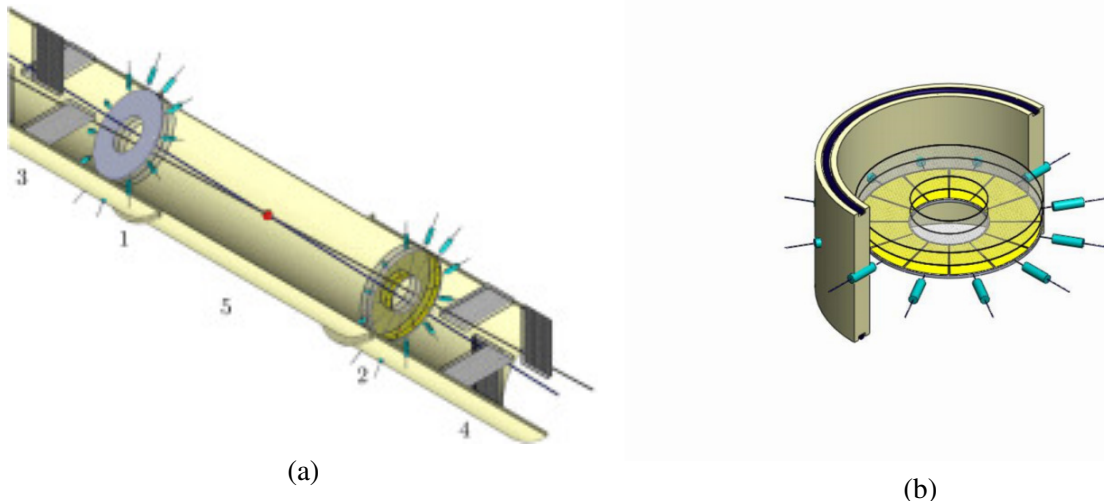


Figure 4.29: (a) General layout: the Fast Beam-Beam Collision (FBBC) monitor composed of MCP discs (1 and 2) in combination with the Beam Position devices (BPM) (3 and 4) are situated symmetrically to the Interaction Point (5) inside the vacuum beam-pipe of NICA collider. (b) Compact module of the Fast Beam-Beam Collision Monitor (FBBC) based on the circular MCPs. Sector cathode readout pads and two MCP set-ups are embedded into a separate flange with hermetic 50 Ohm signal and HV feedthroughs (the last ones are not shown).

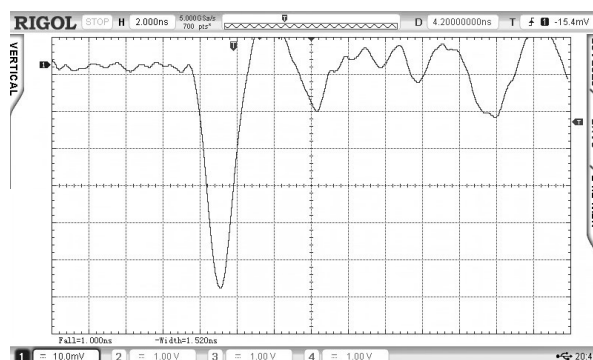


Figure 4.30: Compact module of the Fast Beam-Beam Collision Monitor (FBBC) based on the circular MCPs. Sector cathode readout pads and two MCP set-ups are embedded into a separate flange with hermetic 50 Ohm signal and HV feedthroughs (the last ones are not shown).

1585 One of the promising directions of beam diagnostics is the registration of residual gas ionization prod-  
 1586 ucts by the fast MCP based detector. Such detectors work in high vacuum conditions and are used for

1587 registration of circulating beam profile at many accelerators, including Nuclotron (JINR), and heavy ion  
1588 colliders.

1589 To meet the challenges of fast monitoring of beam-beam collisions for high intensity NICA beams, the  
1590 MCP-based Fast Beam-Beam Collisions (FBBC) detector with high timing properties is proposed in  
1591 combination with the Beam Position Monitor (BPM). This will provide monitoring of bunch-by-bunch  
1592 crossing, the beams location and their profiles, the collision intensity, and the azimuthal distribution of  
1593 produced particles.

1594 Two compact systems based on the application of Micro Channel Plates (MCPs) are proposed to meet  
1595 the challenges of the fast beam-beam collisions monitoring, event selection and determination of the  
1596 precise timing signal (T0) of the collisions, see Fig.4.29. These systems of monitor detectors consist  
1597 of 2D position-sensitive beam imaging detectors (BPM) and two ring beam-beam collision detectors  
1598 (FBBC-left and FBBC-right) that are situated inside the vacuum beam line. The ultra-high vacuum  
1599 (UHV) compatibility and low-mass compact design of the Fast Beam-Beam Collisions (FBBC) monitor  
1600 in combination with the Beam Position device (BPM)[10], allow their application inside the vacuum  
1601 beam line of NICA collider. FBBC uses the concept of the isochronous multi-pad fast readout and the  
1602 precise timing determination of short ( $\sim 1$ ns) MCP signals. New MCPs with the improved characteristics,  
1603 such as small diameter ( $8\mu\text{m}$ ) channels, low resistivity (100-500 MOhm), high gain ( $\sim 10^7$ ), short fast  
1604 rise-time ( $\sim 0.8$ ns) signals, will be used.

1605 Fig.4.30 shows a typical MCP signal from the testing of the prototype detector. The colliding beams  
1606 pass through the central opening of the MCP, and the outer edges of the MCP capture secondary particles  
1607 flying some definite distance from the interaction point (IP). Signals are recorded at 12 sector cathode  
1608 and their arrival times are digitized along with the multiplicity information.

1609 The main feature of the new MCP is a high secondary emission coefficient and fast fronts of the output  
1610 signal. The new MCPs have a fast leading edge and high gain.

1611 A compact set-up of two detectors with high timing capabilities based on the MCP applications – the  
1612 Fast Beam-Beam Collision counters (FBBC) and the Beam Position Monitor (BPM), is proposed to meet  
1613 the wide set of requirements including those of the future physics program with the polarized beams at  
1614 SPD NICA . The feasibility of the event-by-event monitoring of the beam-beam interactions at NICA is  
1615 confirmed both by the previous developments of the UHF-UHV technology and by the beam tests at JINR  
1616 and CERN of the prototype detectors and electronics, as well as by the in-lab tests of new 8-channels  
1617 MCPs with the improved characteristics.

## 1618 **9.2 Outer part of BBC: scintillation tiles**

1619 The scintillation part of BBC will consist of tiles viewed by SiPMs. The measurement of the signal  
1620 amplitude is required for time-walk correction to improve the time resolution.

1621 At single-channel prototype of detector we have the ability to measure the amplitude using developed  
1622 FEE based on the ToT technique. This technique is a well-known method that allows us to measure  
1623 the energy deposited in the material by reconstructing a given property of the output current pulse –  
1624 the total charge collected, the pulse amplitude, etc. The ToT method converts the signal pulse height  
1625 into a digital value in the early stage of the FEE, which greatly simplifies the system in comparison  
1626 to analog detectors with serial readout through ADCs. The measurement of the ToT is composed of  
1627 two measurements of time for the signal going above (leading) and returning below (trailing) a given  
1628 threshold. The first version of the prototype includes a power supply and the electronics (Fig.4.31 a))  
1629 made on a separate PCB. This PCB used for each cell of the SiPM. Power supply for SiPM with the  
1630 total (65 V) and individual (range of 0 to +10 V) voltage, built-in voltmeter, and manual interface for  
1631 voltage supply. It is possible to connect eight cells simultaneously. The amplifiers are used that do not

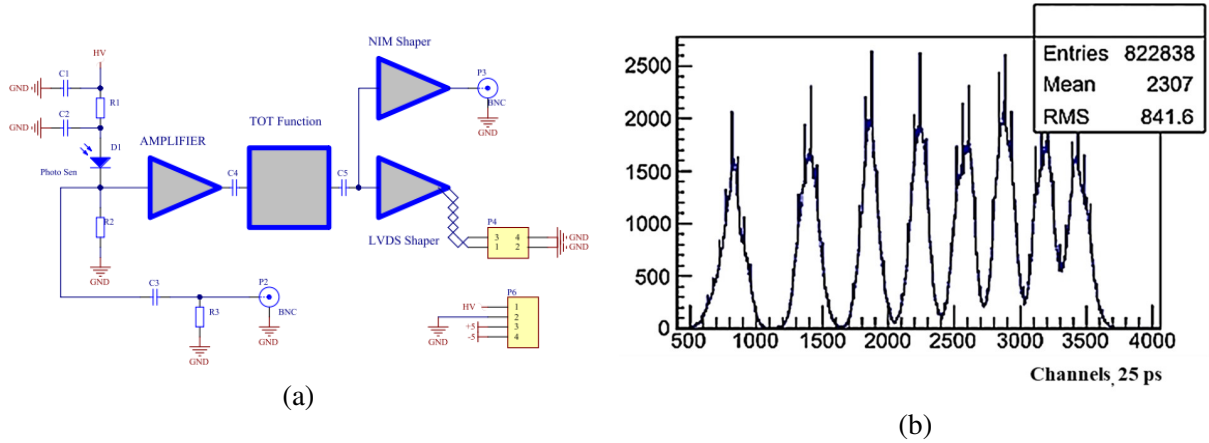


Figure 4.31: (a) The schematic view of the front-end electronics with a ToT function, (b) The distribution of the ToT for LED signal.

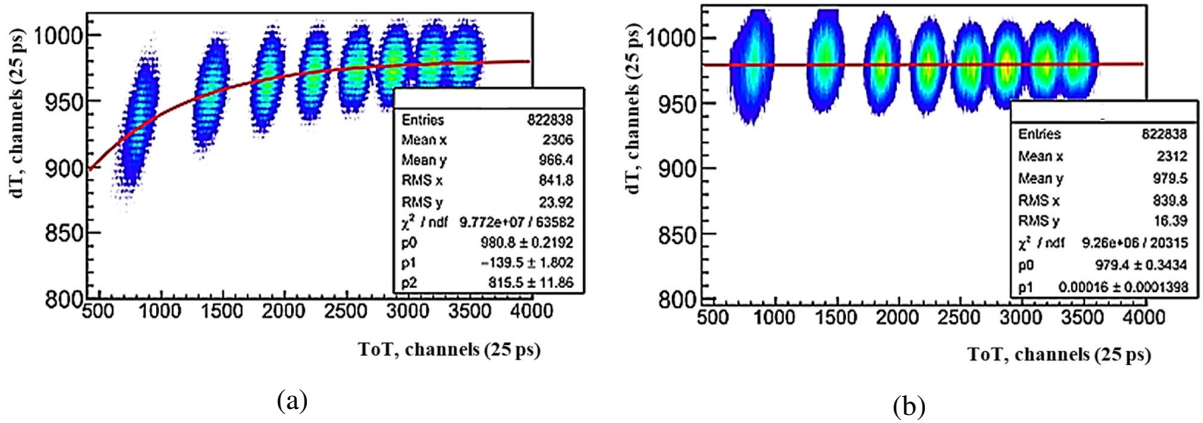


Figure 4.32: The  $dT$  ( $T_{SiPM1} - T_{SiPM2}$ ) correlation on the ToT. (b) The result after the time-walk correction for the  $dT$  ( $T_{SiPM1} - T_{SiPM2}$ ) correlation on the ToT.

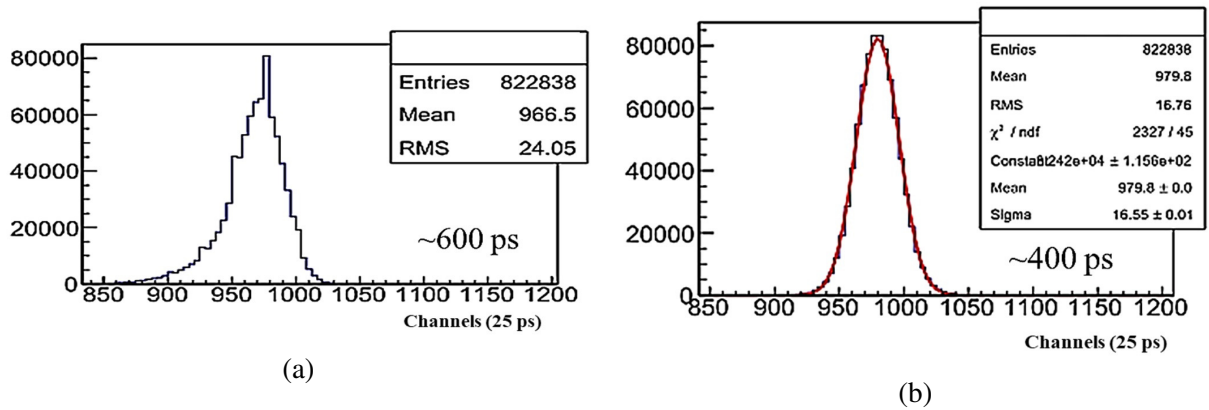


Figure 4.33: (a) The  $dT$  ( $T_{SiPM1} - T_{SiPM2}$ ). (b) The result after the time-walk correction for the  $dT$  ( $T_{SiPM1} - T_{SiPM2}$ ).

1632 change the leading edge of the signal. This allows to get the time stamp of the event. Then the signal is  
 1633 integrated and transmitted to the comparator.

1634 The response of Hamamatsu S12572-010P SiPM [234] with FEE to the LED have been studied. The

1635 electrical signal from a lemo output of the LED was used as a trigger. The illumination was performed  
1636 by uniform light in light isolated box. In addition to the ToT information (Fig.4.31 b)) the time stamp  
1637 of the event for each SiPM cell was investigated. The distribution (Fig.5.1 a)) shows the correlation of  
1638 these values and that the signal in the region of small amplitudes comes later in time. This is due to  
1639 signal latency (so called time-walking effect). This delay occurs due to the difference between the time  
1640 when a photon or charged particle passes through the detecting element and the time when the electronics  
1641 register this signal. This leads to a deterioration in the time resolution. After performing the correction  
1642 (see Fig.5.1 b)), the time-walking effect is removed [235].

1643 The time resolution was defined as the RMS and was approximately 600ps. Taking into account the  
1644 non-Gaussian waveform (Fig.5.3 a)) and the fact that the time resolution is not the maximum allowed  
1645 for this type of detector, the time-walk correction has been applied. The main and important result of the  
1646 correction was a time resolution of approximately 400 ps (Fig.5.3 b)), which is 1.5 times better before  
1647 the correction.

1648 The first version of the prototype using developed front-end electronics based on the Time-over-Threshold  
1649 method was tested. After the time-walk correction, the time resolution improved to 400 ps. Taking into  
1650 account the SiPM suboptimal for precise time measurements the result is promising. Further develop-  
1651 ment of the FEE with a ToT function allows to use standard TDCs for timing measurements.



## Chapter 5

# Local polarimetry [V. Ladygin]

The main goal of the local polarimetry at SPD is the permanent monitoring of the beam polarization during data taking to reduce the systematic error coming from the beam polarization variation. Another task is beam polarization monitoring independent on the major polarimeters (CNI and the absolute one), as well as possible usage of this tool to tune the beam polarization axis. Since the SPD energy range is relatively new for spin physics, there is a lack of precise polarization data allowing one to find the explicit solution for the local polarimetry.

### 1 Asymmetry in inclusive production of charged particles

One of the tools to control the proton beam polarization is measurements of the azimuthal asymmetry in inclusive production of charged particles in collisions of transverse polarized proton beams. Such a method is well adopted at the STAR detector. Two Beam-Beam Counters (BBCs) are used for this purpose. Each BBC consists of two zones corresponding to different rapidity range. The inner and outer zones cover  $3.3 < |\eta| < 5.0$  and  $2.1 < |\eta| < 3.3$ , respectively. The BBCs detect all the charged particles produced in the forward direction within their acceptance.

The correlation of the beam asymmetries measured by the RHIC  $pC$  CNI polarimeter [236, 237] and the STAR BBCs is demonstrated in Fig.5.1. One can see that the measurements by BBCs are sensitive to the transverse polarization of the colliding beams. The value of the effective analyzing power  $A_N$  for inclusive production of charged particles at  $\sqrt{s}=200$  GeV is about  $(6 \div 7) \times 10^{-3}$ . At NICA energies it will have, in principle, the same magnitude, or even a larger one due to a larger analyzing power for the  $pp$  elastic scattering. Therefore, the BBCs can be used for the local polarimetry at SPD. The design of the SPD BBCs is described in Sec. ??.

### 2 Inclusive $\pi^0$ production

One of the reactions to measure and to monitor the vertical component of the polarized proton beam is the inclusive  $pp \rightarrow \pi^{\pm,0}X$  reaction. Fig.5.1 demonstrates the single transverse spin asymmetries  $A_N$  obtained in the  $p$ - $p$  collision for  $\pi^+$ ,  $\pi^0$  and  $\pi^-$  inclusive production at 200 GeV ( $\sqrt{s} \sim 20$  GeV)[238, 239]. The data demonstrate large values of the single transverse spin asymmetries with their signs following to the polarization of the valence quarks in the pions. This regime occurs already at 22 GeV [240] corresponding to  $\sqrt{s_{NN}} \sim 7$  GeV for the collider option. Therefore, the inclusive neutral pion production can be used for the polarimetry over the full energy range of the SPD experiment.

The value of the single transverse spin asymmetry in the  $pp \rightarrow \pi^0X$  reaction is almost twice smaller than

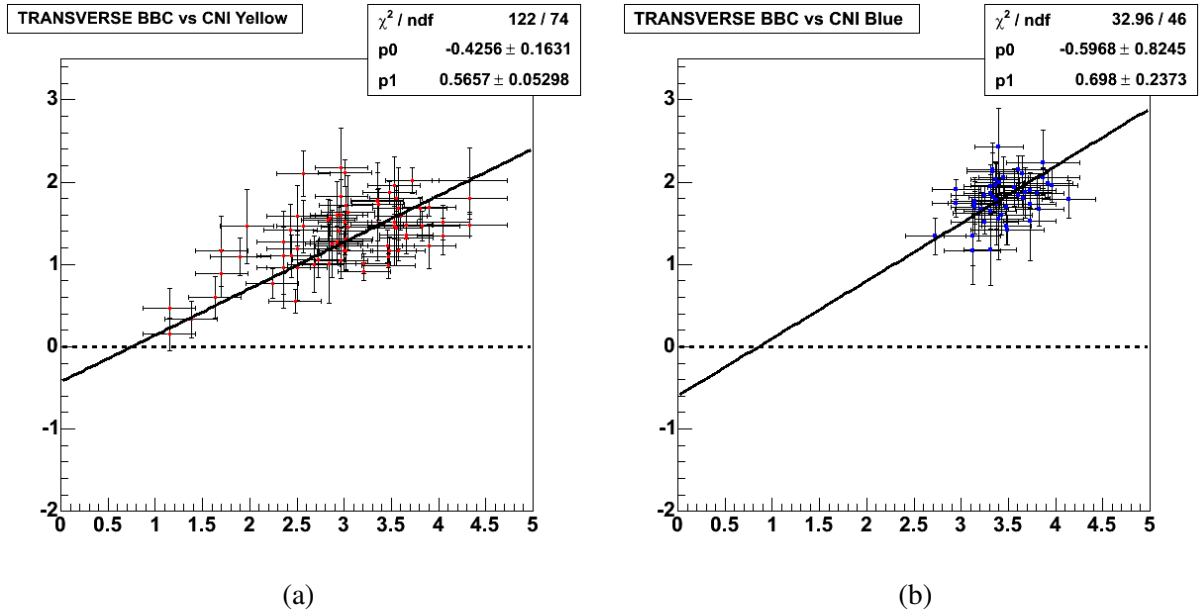


Figure 5.1: Correlation of the beam asymmetries measured by the RHIC  $pC$  CNI polarimeter [236, 237] and left (a) and right (b) STAR BBCs.

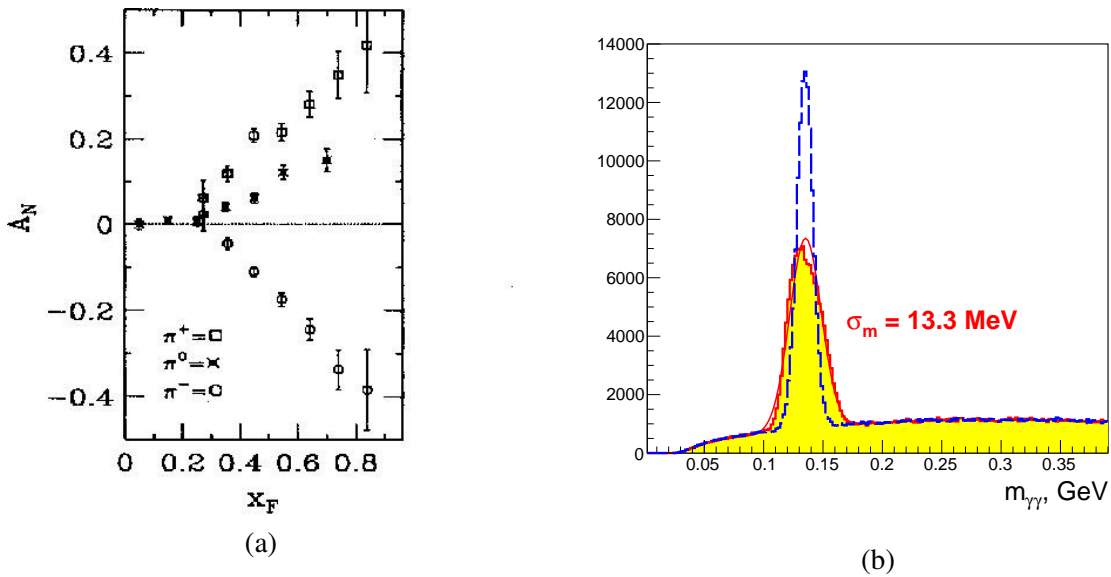


Figure 5.2: (a) Single transverse spin asymmetry  $A_N$  for inclusive pion production in  $p$ - $p$  collisions at 200 GeV [238, 239]. (b) The  $\pi^0$  reconstruction in the SPD ECAL end-cup with (red) and without (blue) vertex position information.

1683 for the charged pions production. However, the  $\pi^0$  selection can be done more easily, since it does not  
 1684 require track reconstruction.

1685 For online local polarimetry one can use the parts of the ECAL end-cups placed around the beam pipe.  
 1686 Fast  $\pi^0$  reconstruction algorithms will not include the information on the vertex position along the beam  
 1687 axis, therefore, the width of the  $\pi^0$  peak will increase. The Monte-Carlo results obtained for  $\sqrt{s_{NN}} \sim 27$   
 1688 GeV and presented in Fig.5.3 demonstrate such enlargement. However, one can see that the selection  
 1689 of  $\pi^0$  is good enough for the local polarimetry purposes. An effective analyzing power  $\langle A_N \rangle$  for  
 1690 the kinematic range of produced  $\pi^0$   $p_T > 0.5$  GeV/ $c$  and  $x_F > 0.5$  is about 0.1. The rate of  $\pi^0$  decays

1691 reconstructed in the end-caps of the calorimeter provides statistical accuracy of the beam polarization  
 1692 estimation at a few-percent level after 10 minutes of data taking at  $10 \text{ GeV} < \sqrt{s} \leq 27 \text{ GeV}$ . The corre-  
 1693 sponding accuracy of the spin direction reconstruction is about a few degrees.

### 1694 **3 Single transverse spin asymmetry for very forward neutron production**

1695 The energy dependence of the single transverse spin asymmetry,  $A_N$ , for neutron production at very  
 1696 forward angles was measured in the PHENIX experiment at RHIC for the polarized  $p$ - $p$  collisions at  
 1697  $\sqrt{s}=200 \text{ GeV}$  [241]. The neutrons were observed in the forward detectors covering an angular range  
 1698 of up to 2.2 mrad. The observed forward neutron asymmetries are large, reaching  $A_N = -0.08 \pm 0.02$  for  
 1699  $x_F = 0.8$ ; the measured backward asymmetries, for negative  $x_F$ , are consistent with zero. The results  
 1700 of  $x_F$  dependence of  $A_N$  for neutron production in the (upper) ZDC trigger sample and for the (lower)  
 1701 ZDC $\otimes$ BBC trigger sample are shown in Fig.5.2(a). The error bars show statistical uncertainties, and the  
 1702 brackets show the  $p_T$ -correlated systematic uncertainties. The data were obtained for 2 types of triggers:  
 1703 the first one is the ZDC trigger for neutron inclusive measurements, requiring an energy deposit in the  
 1704 ZDC to be greater than 5 GeV. The other one was a ZDC $\otimes$ BBC trigger, a coincidence trigger of the ZDC  
 1705 trigger with the BBC hits defined as one or more charged particles in both of the BBC detectors.

1706 The observed large asymmetry for forward neutron production was discussed within the pion exchange  
 1707 framework, with interference between the spin-flip amplitude due to the pion exchange and the non-flip  
 1708 amplitudes from all Reggeon exchanges. The numerical results of the parameter-free calculation of  $A_N$   
 1709 are in excellent agreement with the PHENIX data (see Fig.5.2(b)). One can see that  $A_N$  is increasing  
 1710 almost linearly as a function of neutron transverse momentum  $q_T$ . One can expect the  $A_N$  value of  $\sim$ -  
 1711 0.02 at  $\sqrt{s}=27 \text{ GeV}$ . Therefore, the  $pp \rightarrow nX$  reaction with the neutron emission at very forward angles  
 1712 can be used at SPD at least at a higher energy.

1713 Very forward neutrons are detected by two zero-degree calorimeters (ZDCs) [243] placed in the gaps  
 1714 between the ion tubes of the colliding beams on the left and right from the center of the detector. Two  
 1715 ZDCs will be also placed at SPD. These ZDCs can be considered as an additional tool for the local  
 1716 polarimetry for pp-collisions at the highest NICA energy.

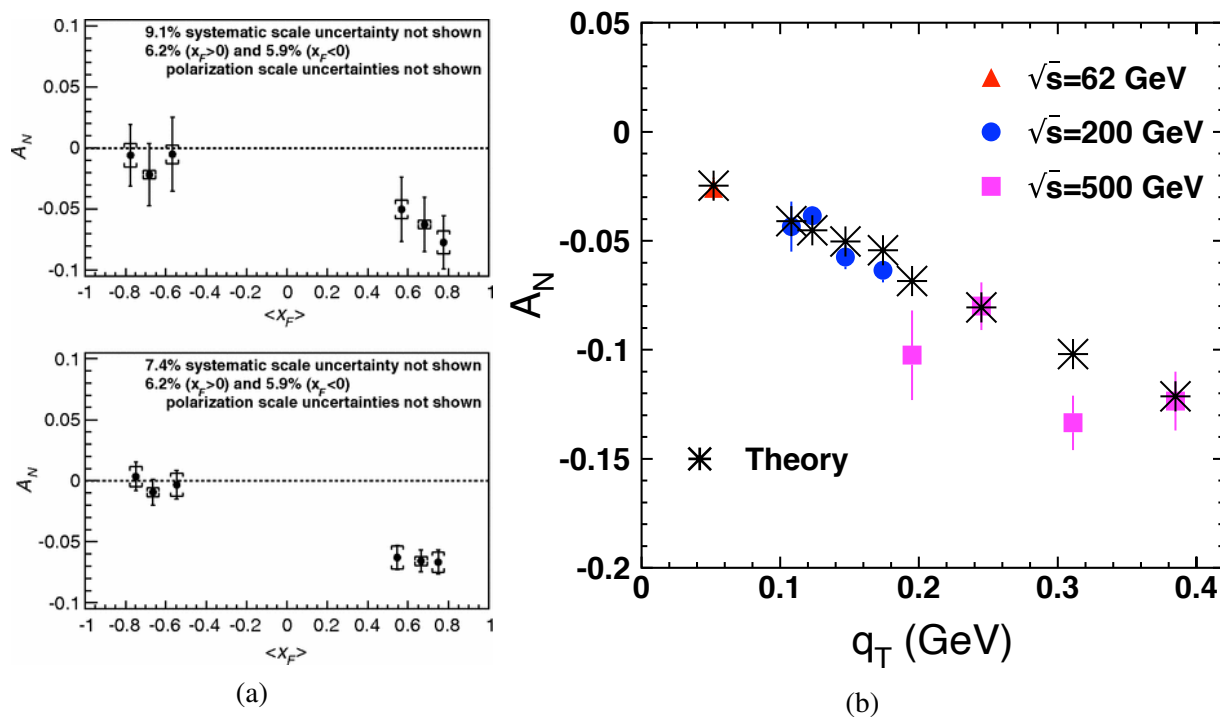


Figure 5.3: (a)  $x_F$  dependence of  $A_N$  for neutron production in the (upper) ZDC trigger sample and for the (lower) ZDC $\otimes$ BBC trigger sample. (b) Single transverse spin asymmetry  $A_N$  in the reaction  $pp \rightarrow nX$  measured at  $\sqrt{s} = 62, 200, 500$  GeV at PHENIX. The asterisks show the result of the theoretical calculations [242].

## Chapter 6

# Detector control system [A. S. Chepurnov]

SPD detector control system (DCS) is designed to control the main operating modes of the detector parts and the entire detector as a whole, for continuous monitoring of slowly changing parameters of the detector, engineering means which ensure the operation of the detector and the environment. DCS is synchronized with the main operating modes of the NICA accelerating complex through a synchronization subsystem common to DCS and DAQ. DCS provides parameterization of the control object (SPD detector), implements algorithms for normalization, measurement of parameters and control based on these parameters and provides the formation of the necessary sets of abstractions and options for representing these abstractions to the operator in an intuitive way.

When critical values of parameters go beyond the predefined boundaries in predetermined situations emergency events are caused and initiate procedures for handling such events, including the procedure for automatically detector stopping in order to prevent its damage. Parameter values are archived in a database to implement the procedure for long-term monitoring of the detector's operation and identify possible failures in the operation of the equipment and emergency situations. The configurations of the detector parameters saved in the database make it possible to start the detector promptly and use it with various preset parameters and in various operating modes in accordance with the current requirements of a physical experiment

DCS allows the autonomous operation of each detector subsystem at the stage of initial start-up, periodic maintenance, calibration and planned upgrades. The number of parameters in the system is expected to be significant, so it is assumed that the system should be extendable and flexibly configurable. When building general DCS and control systems of each part of the detector, the preference should be given to architectural and software solutions based on the event-oriented model and client-server and producer-consumer interaction models should be implemented for communication. Centralized systems operating in the master-slave polling mode should be avoided.

### 1 DCS concept

Almost all detectors used in high-energy physics include parts consisting of similar systems consists from devices, sensors and actuators with similar or identical functionality that determine the parameterization of the entire detector as a control object. Such systems include:

1. HV power supply system for powering gas detectors and light (photon) sensors (PMT and SiPM);
2. LV power supplies for powering of magnets, digital and analog electronics;

- 1748 3. cryogenic systems;
- 1749 4. gas supply and mixing systems;
- 1750 5. vacuum systems;
- 1751 6. front-end electronic LW powering control and temperature monitoring;
- 1752 7. various cooling and temperature control systems;
- 1753 8. DAQ system;
- 1754 9. accelerator interface and sync.;
- 1755 10. deneral external electricity, water cooling, etc.

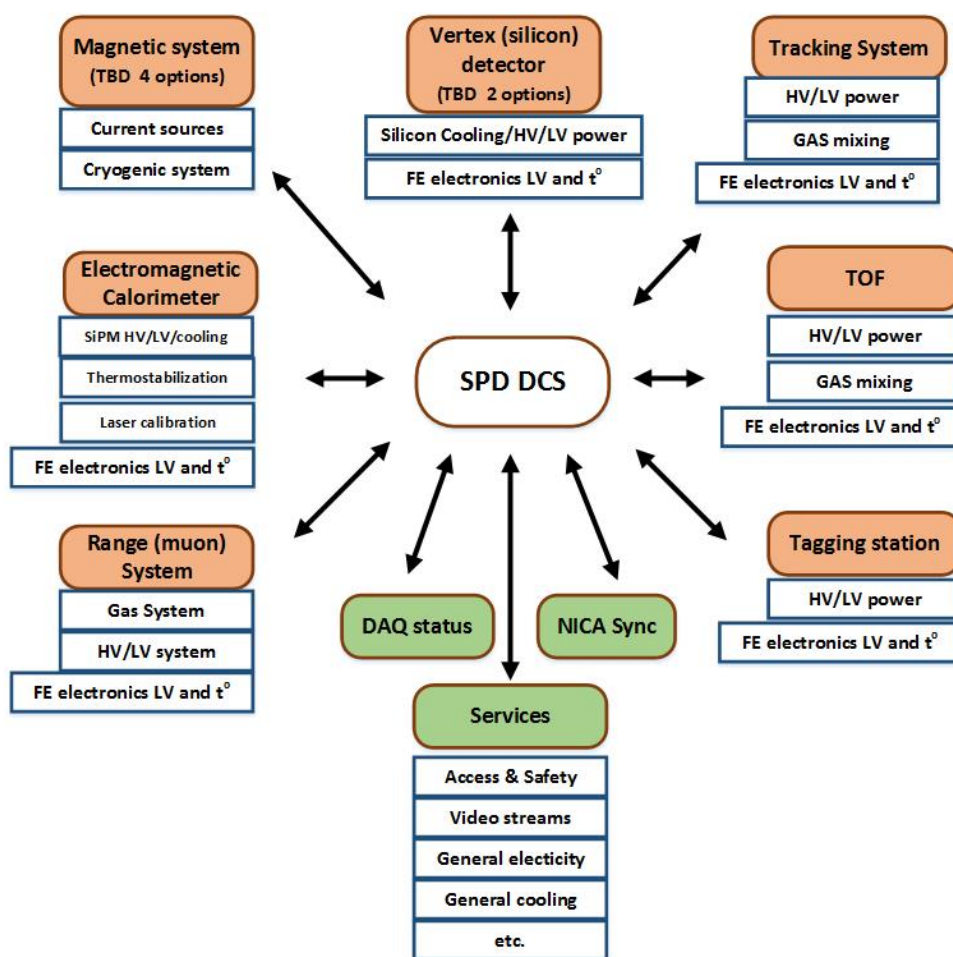


Figure 6.1: SPD detector control system layout.

1756 The SPD detector is no exception and includes almost all of these systems included in separate parts of  
 1757 the detector as shown in the layout diagram Fig. 6.1. Each part of the detector contains one or more  
 1758 subsystems. The composition of the systems will be refined as the individual parts of the detector are  
 1759 developed.

1760 All of these systems can be similarly parameterized and shown to the operator in an intuitive representa-  
 1761 tion in order to simplify the operator's decision-making algorithm. However, the physical implementa-  
 1762 tion at the hardware level of these elements may differ significantly in different parts of the SPD, which  
 1763 is due to the fact that - these parts inherit the experience of their developers gained in previous experi-  
 1764 ments, - hardware and software components are selected based on their cost and availability, - parts of  
 1765 the detector are manufactured at different times.

1766 Nevertheless, in order to optimize the cost of financial and human resources for the creation of the entire  
 1767 detector and DCS, in particular, it is necessary to recommend the developers of the detector parts to strive  
 1768 for standardization of the used hardware and embedded software. This will significantly reduce the effort  
 1769 in developing, setting up and operating the detector and will result in significant cost savings. To achieve  
 1770 these goals, it is advisable to work out at the stage of prototyping detector systems not only the detector  
 1771 itself, front-end electronics and DAQ, but also slow control systems. This work can be carried out in the  
 1772 BeamTest Zone, for which the BTZ slow control system must be made as similar as possible to the final  
 1773 DCS version.

## 1774 2 DCS architecture

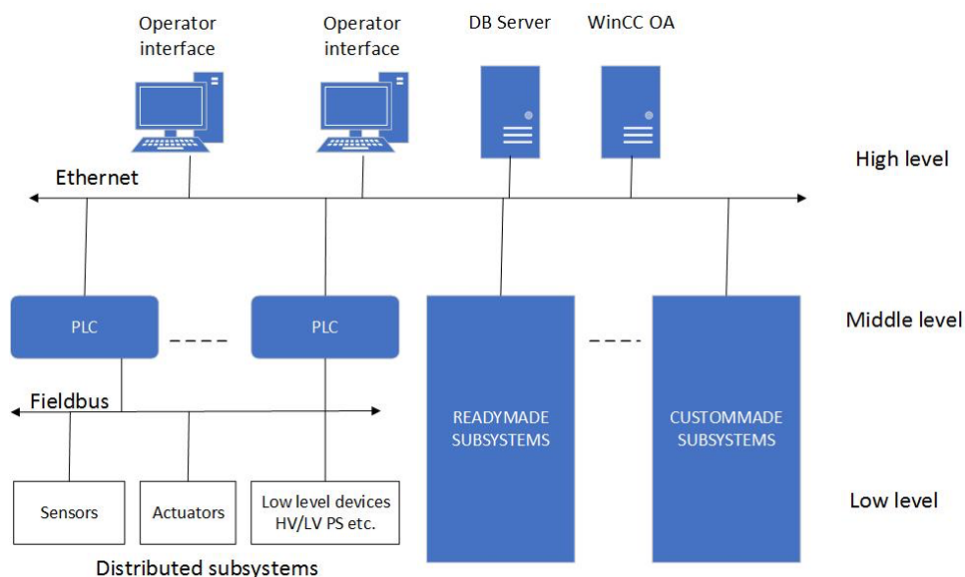


Figure 6.2: SPD detector control system architecture.

1775 The detector control system is divided into three logical levels as it is shown in Fig. 6.2. The lower  
 1776 layer includes measurement channels built into the Front End Electronics (FEE) and Data Acquisition  
 1777 (DAQ) of the detector parts, various stand-alone sensors, I/O devices, and low and high voltage power  
 1778 supplies. The middle level is represented by programmable logic controllers and integrated ready-made  
 1779 and custom made subsystems (vacuum posts, gas consoles, multichannel ready-made power subsystems  
 1780 etc.). Interfaces to the Front End Electronics (FEE) and Data Acquisition (DAQ) subsystems that provide  
 1781 data for the benefit of the detector control system are also at this level. The upper level is designed  
 1782 to provide a human-machine interface for operators, implement a database of detector parameters and  
 1783 configurations, communicate with the outside world (accelerator, engineering support systems, access  
 1784 system, etc.) and implement macro-control algorithms common for the entire detector. All these levels  
 1785 are connected in a hierarchical network using fieldbuses between the first and second level, for example  
 1786 CAN-bus with CANopen protocol. Ethernet LAN is used between the middle and upper levels. At the

1787 top level, special software such as SCADA (Supervisory Control And Data Acquisition) is used, which  
1788 provides control, collection and storage of data in real time. It is proposed to use the WinCC OA system  
1789 widely used in CERN as a SCADA system. We understand that for smooth and reliable communication  
1790 with NUCLOTORN's control system, a gateway to the Tango Controls system should be developed and  
1791 built in.

### 1792 **3 SCADA for DCS**

1793 WinCC OA is a commercial SCADA system. It is a software component constructor that allows to use  
1794 both preinstalled prototypes and templates, and software modules and system components developed of  
1795 its own in C. This system is actively used in many experiments at CERN and has support and safety  
1796 certificates in the Russian Federation. The following properties make WinCC OA an attractive solution  
1797 for use in DCS SPDs:

- 1798 – object-oriented approach built into the system ensures an efficient development process and the  
1799 ability to flexibly expand the system;
- 1800 – capability to create distributed systems - up to 2048 WinCC OA servers;
- 1801 – scalability from a simple single-user system to a distributed redundant network system with 10  
1802 million tags (physical and synthetic parameters);
- 1803 – platform independent system is available for Windows, Linux;
- 1804 – event-driven system;
- 1805 – hot standby and 2x2 redundancy (DRSystem), the required level of availability and reliability;
- 1806 – wide range of drivers and options for communication OPC, OPC UA, S7, Modbus, IEC 60870-5-  
1807 101/104, DNP3, XML, JSON, SOAP...;
- 1808 – support by major manufacturers of electronic devices for building automation systems in high  
1809 energy physics.

1810 A functional unit of the system that is programmatically implemented as a separate process is called a  
1811 manager. A set of managers forms a system. Data exchange and communications between managers are  
1812 realized via TCP. There exists a possibility to exchange data via events. The system allows to parallelize  
1813 processes (managers) by running them on different computers with different OC, which are connected  
1814 via TCP (each of these processes is called a manager). The system provides a capability of scalability  
1815 and load balancing on managing computers. The required managers are started only by necessity, and  
1816 they can also be run several times in parallel. Managers can be distributed across multiple computers /  
1817 servers. The WinCC OA block diagram is shown in figure 6.3. The main process is the Event Manager,  
1818 it contains and manages the process image (current values of all process variables), receives and qualifies  
1819 data (central message manager), distributes data across other managers, acts as a data server for others,  
1820 manages users authorization, manages the generation and status of alarm messages.

1821 The Database Manager receives data from the Event Manager and manages them based on the embedded  
1822 program. In the capacity of a historical database it can be used both as an own database (HDB) and as an  
1823 Oracle DBMS (the Oracle Real Application Clusters configuration is also supported). Parallel archiving  
1824 in Oracle and HDB databases is possible. It is also possible to record user-defined data and log system  
1825 events and messages in an external relational database (MS SQL, MySQL, Oracle, etc).

1826 The WinCC OA Report Manager supports different ways of generating reports:



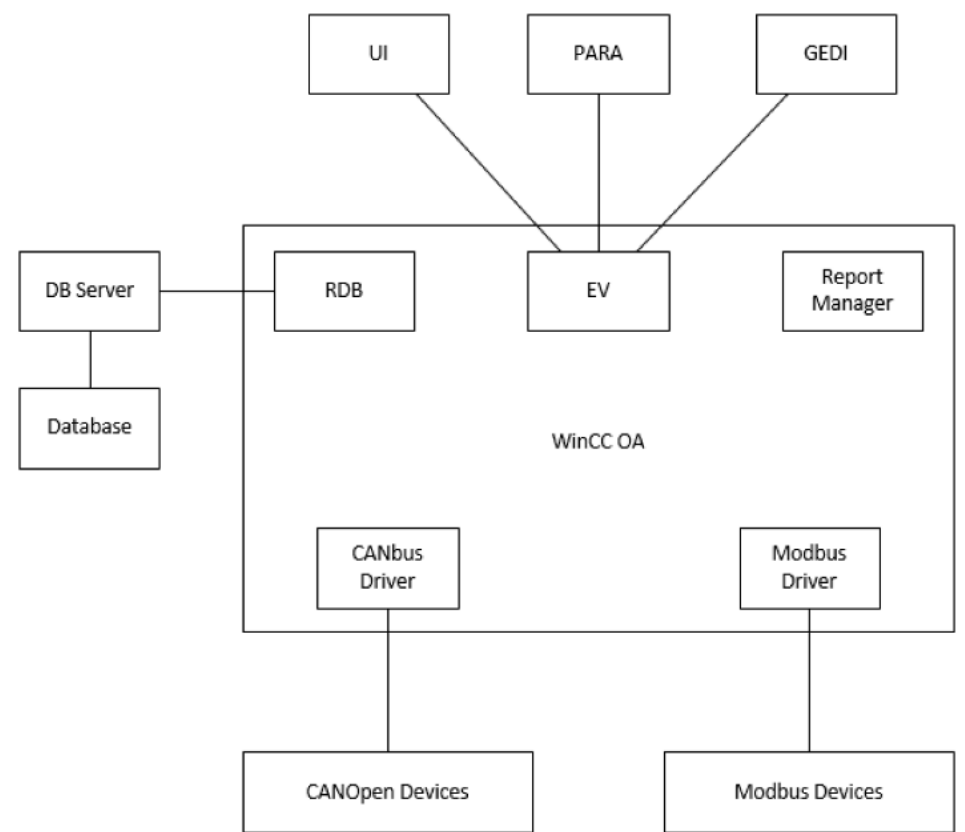


Figure 6.3: SCADA structural scheme of WinCC OA software.

- 1827 – in Microsoft Excel format;
- 1828 – in xml format with the ability to display in any external tool for working with reports (Eclipse
- 1829 BIRT, Crystal Reports, SYMATIC Information Server etc.), SOAP protocol is also supported
- 1830 (Simple Object Access Protocol).

1831 The development of projects in the WinCC OA system is based on an object-oriented approach. In the

1832 WinCC OA data model, objects are represented as data points that characterize the image of a specific

1833 physical device or process. For each data point (tag) element, properties and actions can be defined in

1834 relation to it, such as signal processing (smoothing, setting ranges, etc.), communication with external

1835 systems, archiving, generation of alarm messages (alarms), etc. Typing and inheritance are supported,

1836 due to which arbitrary hierarchical data structures can be created. Similarly, the principles of inheritance

1837 and reusability are implemented for graphical objects. The WinCC OA IDE includes the PARA configura-

1838 tion editor and the GEDI graphical editor of User Interface Manager (UI) (includes a data model editor,

1839 mass configuration tools, administration tools, an interface to version control systems, a debugger, etc.).

1840 Changes to data structures and graphics are applied without restarting the project. Writing custom scripts

1841 is carried out in CONTROL++ (syntax is similar to C / C ++). Such scripts can be both event handlers

1842 associated with elements of the graphical interface, and data processing procedures.

1843 The system has a library of standard graphical objects; it can be scaled via developing its own objects or

1844 using the Qt Toolkit widgets. It is also possible to use the JavaScript libraries available on the market or

1845 JavaScript scripts of its own. Thanks to the open API (C++ / C# API), it is possible to create managers,

1846 drivers, widgets and CONTROL++ extensions of its own. It is available a new set of tools for imple-

1847 menting the concept of High Speed Programming, which supports the formation of documentation from  
1848 the source code, unit testing and autocompletion of program structures.

1849 TANGA.

# Chapter 7

## Data acquisition system [L. Afanasyev]

### 1 Introduction

The data acquisition system of the SPD should provide continuous data taking, including data readout from front-end electronics, data consistency check, event building and writing events to a storage. The system should have no dead time or minimal dead time. *These features will be realized with the DAQ operating in a free-running (trigger-less) mode.*

Other important tasks of DAQ are:

- initialization of hardware;
- control and monitoring of the data taking process: control of the status of all hardware devices including front-end electronics, status of software, quality of collected data;
- monitoring of the parameters characterizing the detector performance (accumulation of time, amplitude and hit distribution histograms, detector rates, etc.);
- logging of information and errors;
- distribution of the data over the computing nodes for following on-line analysis;
- etc.

The data acquisition system of SPD should withstand the data flux from  $p$ - $p$ ,  $p$ - $d$  or  $d$ - $d$  interactions at the extreme conditions of high luminosity. At the highest NICA energy and luminosity,  $\sqrt{s} = 27$  GeV and  $L = 10^{32} \text{ cm}^{-2} \text{ s}^{-1}$ , the interaction rate within the SPD aperture will be 4 MHz, and the average multiplicity **about 20** ????. This drastically differs from conditions of another NICA experiment, MPD, where the collision rate of heavy ions is orders of magnitude less but multiplicity is much higher.

The structure of DAQ will be similar to recently modernized DAQ of the COMPASS experiment at CERN [244–246]. The COMPASS DAQ extensively uses the logical programmable integrated circuits FPGA at different levels of the system. This allows one to handle large data streams with minimal latency and provides very good flexibility. Unlike the COMPASS experiment, which uses the beam of the CERN SPS with a spill time structure, the SPD DAQ will deal with continuous beam.

The DAQ of SPD will operate in a free-running mode, when readout is not controlled by a trigger system, but occurs with a fixed frequency. It requires all front-end electronics running in a self-triggered mode, and readout happens synchronously with a common clock distributed by precise timing system. All the

1879 data, received between the acts of readout, are accumulated in memories implemented in the front-end  
1880 electronics modules and are preserved there until the next readout. The readout frequency value will  
1881 be chosen depending on detector rates and memory depths available in the front-end cards. The width  
1882 of the time slice between the successive readouts should be much larger than the response time of the  
1883 sub-detectors in order to minimize the probability of separating an event into two slices.

1884 Digitization of data and zero suppression occur in front-end electronics. It is expected that so-called  
1885 "feature extraction algorithm" will be implemented in front-end electronics of the Vertex detector and  
1886 the Calorimeter. This algorithm, which is under development in several collaborations (in particular,  
1887 PANDA [247], COMPASS [248–250]), allows transferring only the extracted time and amplitude, instead  
1888 of many samples of a digitizer, thus greatly decreasing the amount of data to be transferred.

1889 The expected data flux in the hardest conditions of the experiment (maximum energy and luminosity)  
1890 has been estimated without detailed simulations yet, but using the current knowledge of the sub-detector  
1891 structure, particle multiplicity per event, hit multiplicity in different detectors, expectations about the  
1892 front-end electronics parameters and, where relevant, some results of the beam tests of other experiments  
1893 (MPD, PANDA). A total number of channels to be readout is about 700 thousand, with the major part  
1894 coming from the Vertex Detector ( $\sim 460$  thousand for the VD strip option). Preliminary estimation for  
1895 the data flow is about 20 GB/s (including 7 GB/s added for safety).

## 1896 2 DAQ structure

1897 The scheme of DAQ is presented in Fig. 7.1. The data from front-end electronics cards come to detector  
1898 interface cards (FE concentrators). The Data-Handler multiplexers (DHMux) are configured on the base  
1899 of FPGA. They verify consistency of data and store them until receiving the readout signal. The existing  
1900 version of the multiplexer [246] is equipped with memory of 4 GB and has a bandwidth of 2 GB/s.  
1901 The FE concentrators and Data-Handler multiplexers are implemented on the same electronics cards by  
1902 means of different firmware.

1903 The two Data-Handler Switches (DHSw) function as  $10 \times 10$  switch and perform event building with a  
1904 maximum throughput rate of 10 GBytes/second. DHSw's perform the final level of event building and  
1905 distribute the assembled events to 20 readout computers. Each readout computer is equipped with a ded-  
1906 icated PCIe buffer card for data collection. These cards are built on a FPGA chip and are commercially  
1907 available. The current version of the card used in COMPASS has the bandwidth close to 1 GB/s [251–  
1908 254]. Finally, the continuous sequence of slices is formed below the Network Switch in each of on-line  
1909 computers to be used for on-line filtering and event monitoring.

1910 A slow control software accesses front-end electronics via the FE concentrators using UDP-based IPBus  
1911 protocol [255]. The interface cards retransmit control and clock signals provided by a time distribution  
1912 system to corresponding front-end electronics, and convert the detector information from detector spe-  
1913 cific interfaces to a common high speed serial interface running over an optical fiber. It is foreseen to use  
1914 UCF [256] as a standard high speed link protocol within the DAQ.

1915 The White Rabbit system [257, 258] is planned to be used in NICA for time synchronization. It provides  
1916 synchronization for large distributed systems with time-stamping of 125 MHz, sub-nanosecond accuracy  
1917 and  $\sim 10$  ps precision. Signals from the White Rabbit system will be used as an input for the Time  
1918 Control System (TCS) [259] which will distribute clock signals through the whole electronic system.

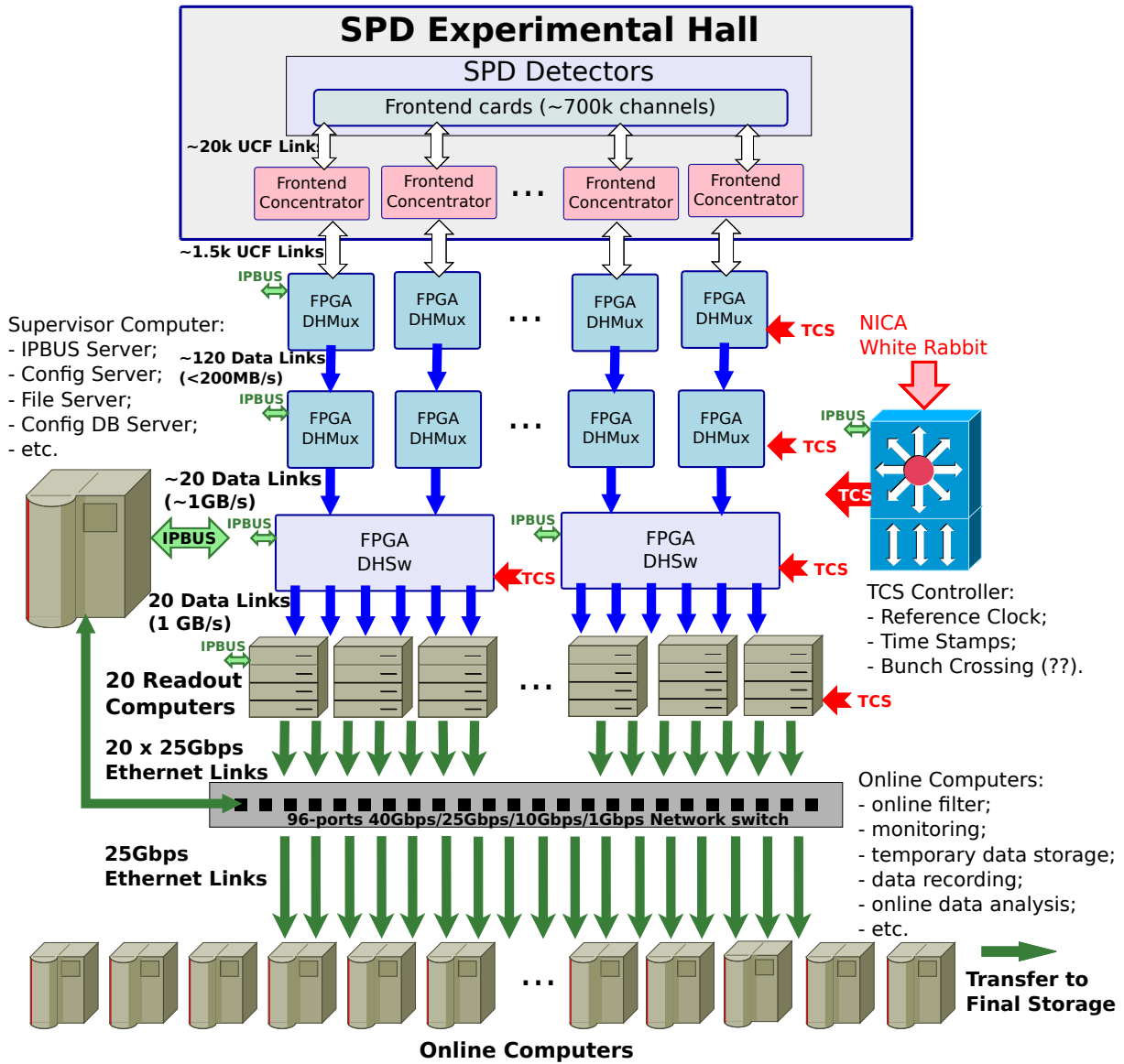


Figure 7.1: General structure of DAQ-SPD.

### 3 Data Format

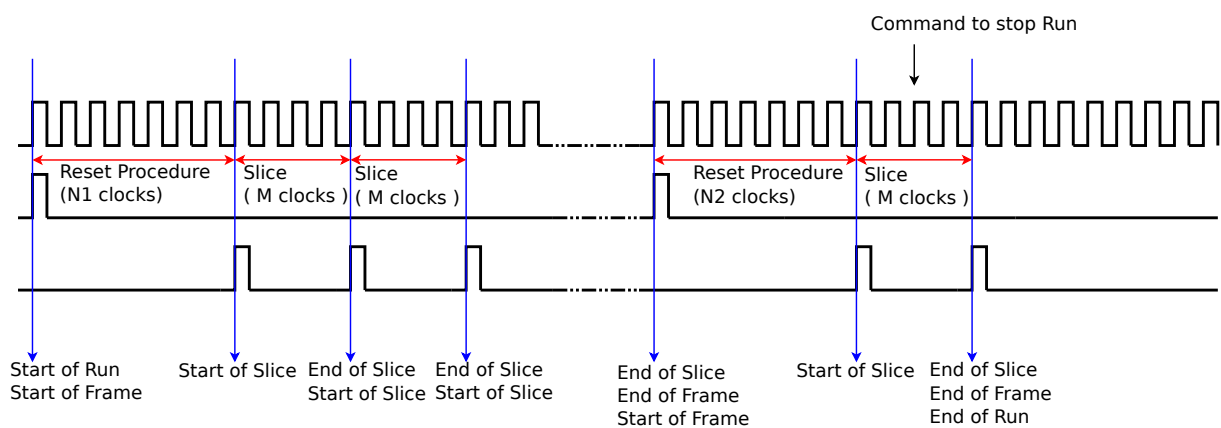
1919 **3 Data Format**  
1920 The time structure of the expected data flow during a run is shown in Fig. 7.2. All processes are syn-  
1921 chronized with 125 MHz clock coming from the White Rabbit system. A Run is started after the reset  
1922 procedure which includes all initialization processes. Then, the continuous date flow is divided into a  
1923 sequence of time slices. The proposed time slice duration can be selected in the range from 1  $\mu$ s to  
1924 8.3 ms and will be chosen according to the data flux and capacity of the whole chain of data collection.  
1925 The longer slices are preferable because the longer slice, the less probability of falling an event into two  
1926 adjacent slices. The slices have a continuous numbering within a frame, a wider time interval, which can  
1927 extend from 65 ms to 549.7 s. The slice numbering is reset every Frame by the Start of Frame signal.

1928 The proposed format of the collected data is shown in Figs. 7.3 and 7.4. The data are formatted at all  
1929 stages of transfer from Front-End Concentrators to Data-Handler Switches. The required headers and  
1930 checksums are added at all stages.

1931 In Fig.7.3 the structure of a Run and of a Frame is shown. The Run consists of a sequence of Frames  
1932 which are numbered from 0 to N, where N, the maximum number of frames in the Run, is assigned by  
1933 the TCS controller. The Frame consists of a sequence of slices numbered from 0 to K, the maximum  
1934 number of slices in the Frame, which is also assigned by the TCS controller.

1935 Fig.7.4 shows the structure of the Slice and of the Data Blocks. The Slice contains a sequence of Data  
1936 Blocks from the Data Concentrators. Finally, the lowest unit in the Data Format chain is the Data Block  
1937 of FE Concentrators which contains Physical Data from several ports whose amount depends on the FE  
1938 Data Concentrator type.

1939 The proposed format provides a unique connection of the physical information to the detectors geometry  
1940 and event time.



Tclock = 8ns (125 MHz) from White Rabbit;  
 Reset Procedure  $\leq$  300 ms (depends on electronics);

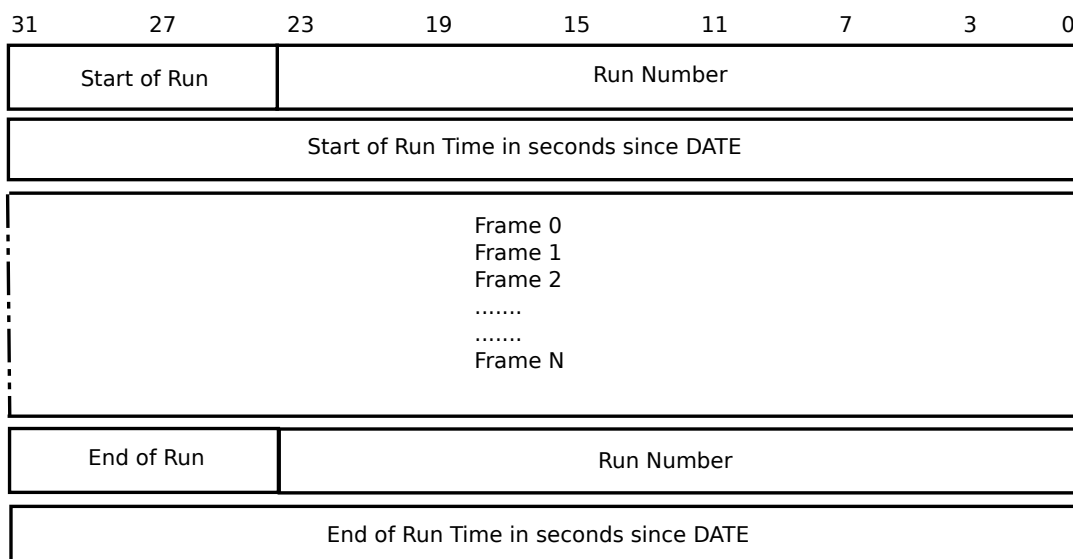
Slice Number: 24 bits (1 us - 8.3ms)  
 Data Size: max 16GB (real size < 160MB (20GB/s limit));

Frame: starts by Reset procedure, width 16 bits (min: 65ms, max: 549.7s),  
 Data Size: max 1PB (real size < 10TB (20GB/s limit))

Figure 7.2: Time diagram of a sequence of clocks, Slices and Frames within the Run.

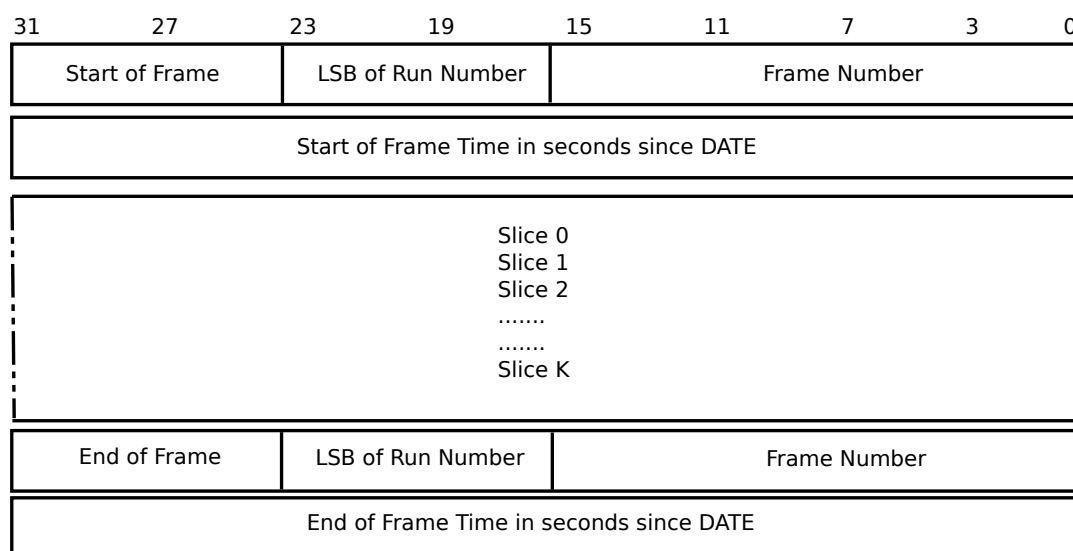
## SPD Data Format

### Run Structure:



Number of Frames in the Run: 1..N, where N is maximal number of frames in the Run (assigned by TCS Controller)

### Frame Structure:

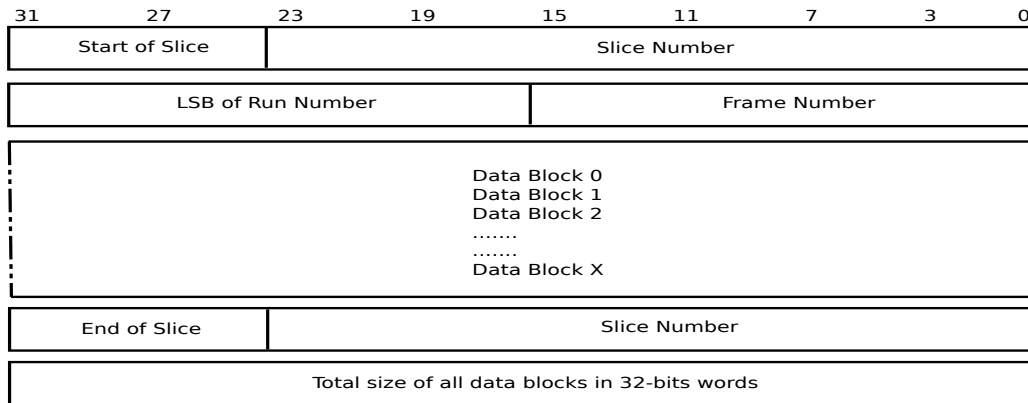


Number of Slices in the Frame: 1..K, where K is maximal number of slice in the Frame assigned by TCS Controller

Figure 7.3: Data Format: Run and Frame structure.

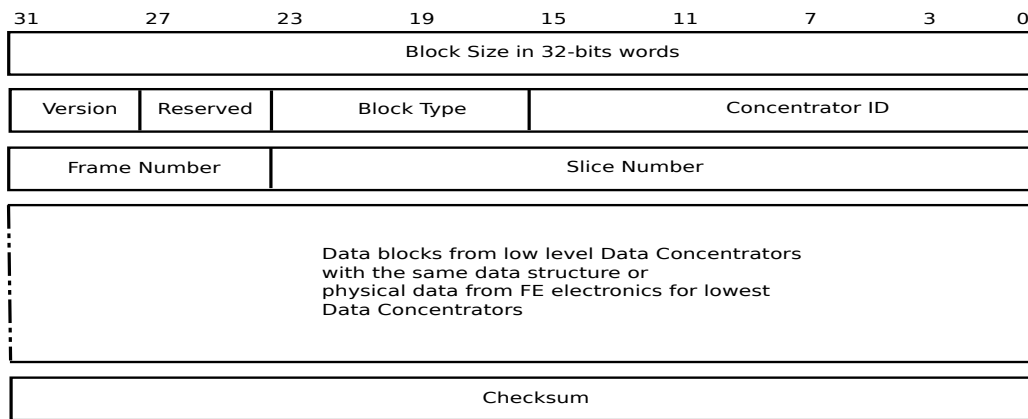


### Slice Structure:

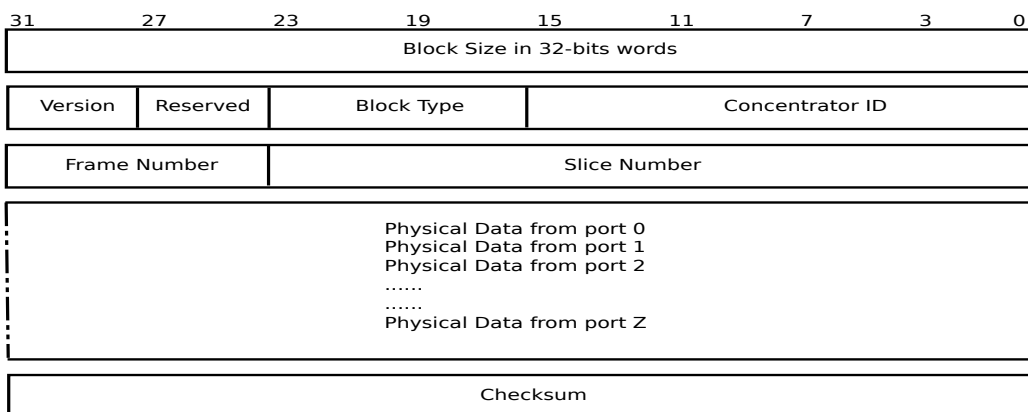


Number of Blocks in the Slice depends on DAQ configuration and data flux.

### Data Block Structure of High Level Data Concentrators (Switches, Multiplexers etc.):



### Data Block Structure of Lowest Level Data Concentrators (FE Concentrators):



Number of ports depends on FE Data Concentrator Type.  
 For instance, Igor Konorov if TDC Multiplexer has 15 input ports.

Figure 7.4: Data Format: Slice structure and structure of Data Blocks of High Level and Low Level Data Concentrators.

## Chapter 8

# Computing and offline software [A. Zhemchugov]

### 1 SPD computing model

Expected event rate of the SPD experiment is about 3 MHz ( $pp$  collisions at  $\sqrt{s} = 27$  GeV and  $10^{32}$   $\text{cm}^{-2}\text{s}^{-1}$  design luminosity). This is equivalent to the raw data rate of 20 GB/s or 200 PB/yr, assuming the detector duty cycle is 0.3, while the signal-to-background ratio is expected to be in order of  $10^{-5}$ . Taking into account the bunch crossing rate of 12.5 MHz, one may conclude that pile-up probability will be sufficiently high.

The key challenge of the SPD Computing Model is the fact, that no simple selection of physics events is possible at the hardware level, because the trigger decision would depend on measurement of momentum and vertex position, which requires tracking. Moreover, the free-running DAQ provides a continuous data stream, which requires a sophisticated unscrambling prior building individual events. That is the reason why any reliable hardware-based trigger system turns out to be overcomplicated and the computing system will have to cope with the full amount of data supplied by the DAQ system. This makes a medium-scale setup of SPD a large scale data factory.

The continuous data reduction is a key point in the SPD computing. While simple operations like noise removal can be done yet by DAQ, it is an online filter that is aimed at fast partial reconstruction of events and data selection, thus being a kind of a software trigger. The goal of the online filter is to decrease the data rate at least by a factor of 50 so that the annual upgrowth of data including the simulated samples stays within 10 PB. Then, data are transferred to the Tier-1 facility, where full reconstruction takes place and the data is stored permanently. Two reconstruction cycles are foreseen. The first cycle includes reconstruction of some fraction of each run necessary to study the detector performance and derive calibration constants, followed by the second cycle of reconstruction of full data sample for physics analysis. The data analysis and Monte-Carlo simulation will likely run at the remote computing centers (Tier-2s). Given the large data volume, a thorough optimization of the event model and performance of reconstruction and simulation algorithms are necessary.

Taking into account recent advances in the computing hardware and software, the investment in the research and development necessary to deploy software to acquire, manage, process, and analyze the data recorded is required along with the physics program elaboration and the detector design. While the core elements of the SPD computing system and offline software now exist as prototypes, the system as a whole with capabilities such as described above is in the conceptual design stage and information will be added to SPD planning documents as it is developed.

## 2 Online filter

The SPD online filter facility will be a high-throughput system which will include heterogeneous computing platforms similar to many high performance computing clusters. The computing nodes will be equipped with hardware acceleration. The software framework will provide the necessary abstraction so that common code can deliver the selected functionality on different platforms.

The main goal of the online filter is a fast reconstruction of the SPD events and suppression of the background ones at least by a factor of 50. This requires fast tracking and fast clustering in the electromagnetic calorimeter, followed by reconstruction of event from a sequence of time slices and an event selection (software trigger). Several consecutive time slices shall be considered, tracker data unpacked and given for a fast tracking. The result of the fast track reconstruction is the number of tracks, an estimate of their momentum and an estimate of primary vertex (to distinguish between tracks belonging to different collisions). Using this outcome, the online filter should combine information from the time slices into events and add a trigger mark. The events shall be separated in several data streams using the trigger mark and an individual prescale factor for each stream is applied.

One of the most important aspects of this chain is the recognition of particle tracks. Traditional tracking algorithms, such as the combinatorial Kalman filter, are inherently sequential, which makes them rather slow and hard to parallelized on modern high-performance architectures (graphics processors). As a result, they do not scale well with the expected increase in the detector occupancy during the SPD data taking. This is especially important for the online event filter, which should be able to cope with the extremely high data rates and to fulfill the significant data reduction based on partial event reconstruction 'on the fly'. The parallel resources like multicore CPU and GPU farms will likely be used as a computing platform, which requires the algorithms, capable of the effective parallelization, to be developed, as well as the overall cluster simulation and optimization.

Machine learning algorithms are well suited for multi-track recognition problems because of their ability to reveal effective representations of multidimensional data through learning and to model complex dynamics through computationally regular transformations, that scale linearly with the size of input data and are easily distributed across computing nodes. Moreover, these algorithms are based on the linear algebra operations and can be parallelized well using standard packages like Tensorflow or Torch. This approach was already been applied successfully to recognize tracks in the BM@N experiment at JINR and in the BESIII experiment in IHEP CAS in China [260, 261]. In the course of the project an algorithm, based on recurrent neural networks of deep learning, will be developed to search for and reconstruct tracks of elementary particles in SPD data from the silicon vertex detector and the straw tube-based main tracker. The same approach will be applied to the EMC clustering. The caution is necessary, though, to avoid possible bias due to an inadequacy of the training data to the real ones, including possible machine background and the detector noise. The continuous monitoring of the neural networks used in the online filter is necessary and needs to be elaborated.

Besides the high-level event filtering and corresponding data reduction, the online filter will provide input for the run monitoring by the shift team and the data quality assessment, as well as local polarimetry.

## 3 Computing system

The projected rate and amount of data produced by SPD prescribe to use High Throughput Computing (HTC) solutions for the processing of collected data. It is the experience of a decade of the LHC computing that already developed a set of technologies mature enough for the building of distributed high-throughput computing systems for HEP.

### 2017 3.1 The computing model

2018 The 'online' part of computing systems for the SPD experiment, namely the online filter described above,  
 2019 is an integral part of experimental facilities, connected with the 'offline' part using a high throughput  
 2020 backbone network. The entry point to 'offline' facilities is a high capacity storage system, connected  
 2021 with 'online facility' through a multilink high-speed network. Data from high capacity storage at the  
 2022 Laboratory of Information Technologies will be copied to the tape-based mass storage system for long  
 2023 term storage. At the same time, data from high capacity storage will be processed on different computing  
 2024 facilities as in JINR as in other collaborative institutions.

2025 The hierarchy of offline processing facilities can be introduced:

- 2026 – Tier 1 level facilities should provide high capacity long term storage which will have enough  
 2027 capacity to store a full copy of primary data and a significant amount of important derived data.
- 2028 – Tier 2 level facility should provide (transient) storage with capacity that will be enough for storing  
 2029 of data associated with a period of data taking.
- 2030 – Optional Tier 3 level are opportunistic resources, that can be used to cope with a pile-up of pro-  
 2031 cessing during some period of time or for special analysis.

2032 Offline data processing resources are heterogeneous as on hardware architecture level so by technolo-  
 2033 gies and even in JINR includes batch processing computing farms, high performance (supercomputer)  
 2034 facilities, and cloud resources. A set of middleware services will be required to have unified access to  
 2035 different resources.

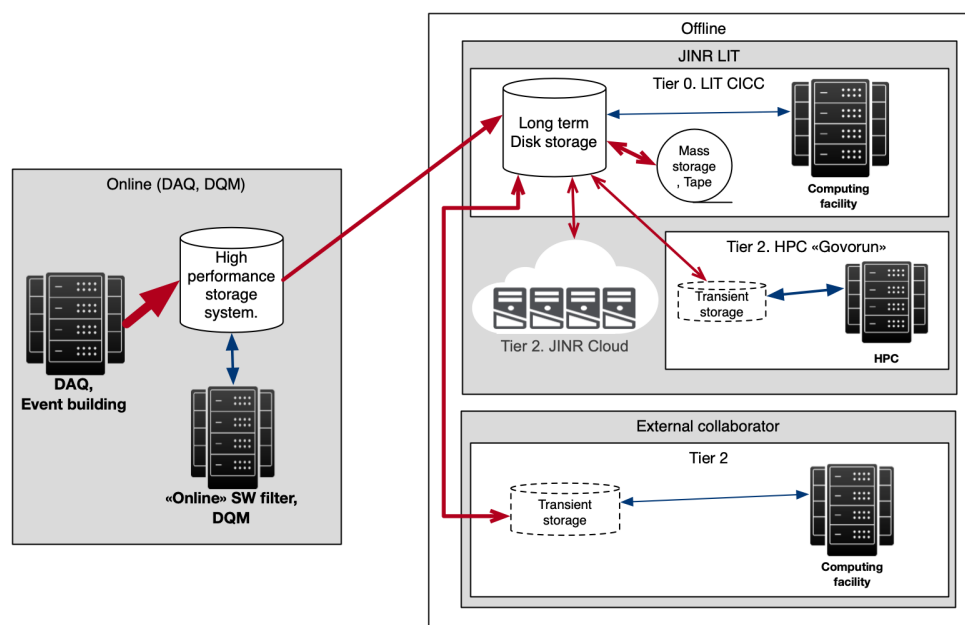


Figure 8.1: Scheme of the SPD computing system

### 2036 3.2 Computing services

2037 Computing systems for NICA in JINR are naturally distributed. Experimental facilities and main data  
 2038 processing facilities placed across two JINR sites and, sometimes, managed by different teams. That

2039 causes some heterogeneity not only on hardware systems but also on the level of basic software: different  
2040 OSs, different batch systems etc.

2041 Taking into account the distributed nature and heterogeneity of the existing infrastructure, and expected  
2042 data volumes, the experimental data processing management system must be based on services that have  
2043 proven reliability and performance.

2044 It is necessary to develop a high-level orchestrating system that will manage the low-level services.  
2045 The main task of that system will be to provide efficient, highly automated multi-step data processing  
2046 following the experimental data processing processes.

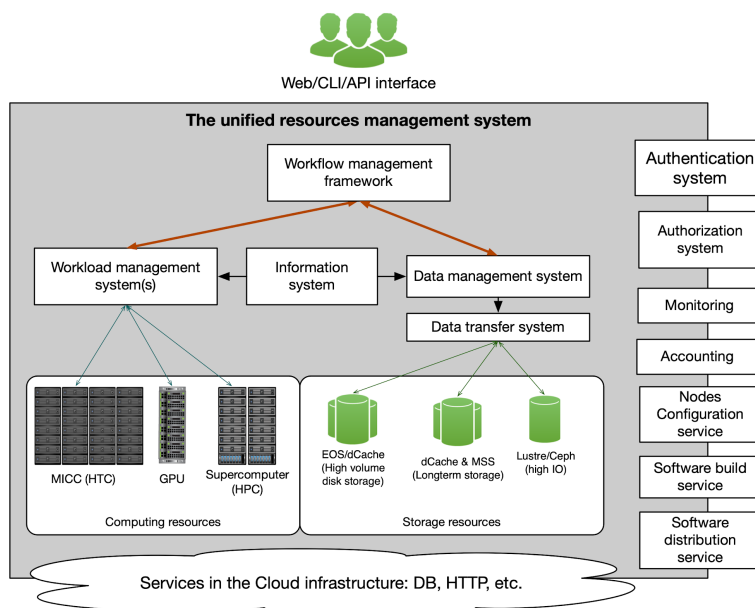


Figure 8.2: Distributed SPD computing services

2047 The Unified Resource Management System is a IT ecosystem composed from the set of subsystem and  
2048 services which should:

- 2049 – Unify of access to the data and compute resources in a heterogeneous distributed environment
- 2050 – Automate most of the operations related to massive data processing
- 2051 – Avoid duplication of basic functionality, through sharing of systems across different users (if it  
2052 possible)
- 2053 – As a result - reduce operational cost, increase the efficiency of usage of resources,
- 2054 – Transparent accounting of usage of resources

2055 Many distributed computing tools have already been developed for the LHC experiments and can be re-  
2056 used in SPD. For the task management one can use PANDA [262] or DIRAC [263] frameworks. For the  
2057 distributed data management RUCIO [264] package has been developed. For the massive data transfer  
2058 FTS [265] can be used. Evaluation of these tools for the SPD experiment and their implementation  
2059 within the SPD Unified Resource Management System is planned in scope of the TDR preparation.

## 2060 **4 Offline software**

2061 Offline software is a toolkit for event reconstruction, Monte-Carlo simulation and data analysis. Linux is  
2062 chosen as a base operating system.

2063 Currently, the offline software of the SPD experiment – SpdRoot – is derived from the FairRoot soft-  
2064 ware [266] and it is capable of Monte Carlo simulation, event reconstruction, and data analysis and visu-  
2065 alization. The SPD detector description is flexible and based on the ROOT geometry package. Proton-  
2066 proton collisions are simulated using a multipurpose generator Pythia8 [267]. Deuteron-deuteron colli-  
2067 sions are simulated using a modern implementation of the FRITIOF model [268, 269], while UrQMD [270,  
2068 271] generator is used to simulate nucleus-nucleus interactions. Transportation of secondary particles  
2069 through the material of the SPD setup and the simulation of detector response is provided by Geant4  
2070 toolkit [272–274]. Track reconstruction uses GenFit toolkit [275] and KFparticle package [276] is used  
2071 to reconstruct primary and secondary vertices. The central database is going to be established to keep  
2072 and distribute run information, slow control data and calibration constants.

2073 Recent developments in computing hardware resulted in the rapid increase in potential processing capac-  
2074 ity from increases in the core count of CPUs and wide CPU registers. Alternative processing architec-  
2075 tures have become more commonplace. These range from the many-core architecture based on standard  
2076 x86\_64 cores to numerous alternatives such as GPUs. For GPUs, the processing model is very different,  
2077 allowing a much greater fraction of the die to be dedicated to arithmetic calculations, but at a price in  
2078 programming difficulty and memory handling for the developer that tends to be specific to each processor  
2079 generation. Further developments may even see the use of FPGAs for more general-purpose tasks.

2080 The effective use of these computing resources may provide a significant improvement in offline data  
2081 processing. However, the offline software should be capable to do it by taking advantage of concurrent  
2082 programming techniques, such as vectorization and thread-based programming. Currently, the SPD  
2083 software framework, SpdRoot, cannot use these techniques effectively. The studies of the concurrent-  
2084 capable software frameworks (e.g. ALFA [277], Key4Hep [278]) are needed to provide input for the  
2085 proper choice of the offline software for Day-1 of the SPD detector operation.

2086 A git-based infrastructure for the SPD software development already established at JINR [279].

## 2087 **5 Resource estimate**

2088 For the online filter we assume the CPU consumption of 1000 SPD events/core/second. This requires  
2089 3000 cores simultaneously for the fast tracking. Taking into account additional expenditures to the event  
2090 unscrambling and data packing and including a real efficiency of CPU which will be lower than 100%,  
2091 one derives the CPU resources for the online filter as 6000 CPU cores. This number sets the upper limit  
2092 and the required computing power may decrease substantially if an efficient way to use GPU cores are  
2093 implemented for the event filtration. As for the data storage, a high performance disk buffer of 2 PB  
2094 capable to keep data of about one day of data taking is needed.

2095 For the offline computing, the data storage is determined by the data rate after the online filter? or 4  
2096 PB/year of raw data. Besides that, we may expect the comparable amount of simulated data and estimate  
2097 the long term storage as 10 PB/year, assuming two cycles of data processing and possible optimization  
2098 of the data format and data objects to be stored permanently. We assume that a half of the annual data  
2099 sample (~5 PB) is kept on disk storage, and the rest is stored on tape. The CPU power necessary to  
2100 process the amount of data like this and to run Monte-Carlo simulation is estimated as many as 30000  
2101 CPU cores. The summary of computing resources is given in Table. ???. The cost estimate is conservative  
2102 and will be defined more exactly in the TDR, when detailed hardware solutions and their actual price in  
2103 the market will be considered.

Table 8.1: Required SPD computing resources

	CPU [cores]	Disk [PB]	Tape [PB]
Online filter	6000	2	none
Offline computing	30000	5	9 per year
Cost estimate [kUSD]	4000	8000	4500 per year

2104 The burden of the SPD computing system operation is a subject of sharing between the computing centers  
2105 of the participating institutes.

## Chapter 9

# Beam test facility [A. Baldin] [OUT OF DATE]

In order to create the conditions for testing and certification of detectors and data acquisition and analysis systems at SPD close to those anticipated at the collider NICA, it is proposed to reconstruct the existing installation MARUSYA [280–283] situated in building 205 of LHEP JINR and build the additional high momentum channel (HMC) for 1–10 GeV/c beams. Both channels spectrometers are situated in the region of focus F4 of extracted beams of Nuclotron.

It should be noted that it is not planned to change the biological shielding in the considered zone. Instead, the existing channel of the spectrometer MARUSYA will be upgraded and developed to provide testing of prototypes and detector elements, as well as the electronics of the data acquisition system of SPD at secondary beams of pions, kaons, protons, neutrons, muons, electrons, and light nuclear fragments in a momentum range of 0.4 – 1.2 GeV/c. It is advantageous that there exists positive experience in working with extracted polarized beams at MARUSYA [284].

This would ensure physical measurements at extracted beams using the existing experimental installation and infrastructure. The installation MARUSYA is well suitable for applied studies with secondary beams at maximum possible intensity of the beam extracted to building 205 (up to  $10^{11}$  protons per acceleration cycle). The development of HMC requires two new magnetic elements; therefore, it is considered as an independent installation to be put in operation at the second stage of upgrade in accordance with the existing regulations for commissioning of experimental facilities.

The power supply and water cooling with the parameters sufficient for the required operation modes of all six magnetic elements are available, the approval by the LHEP engineer in chief has been received.

Each channel-spectrometer provides spatial registration, identification, and tagging of each particle hitting the detector under the condition of matching of the electronic registration system (DAC) of the installation and the tested detector or data acquisition system element.

Figure 9.1 shows the drawing of the considered magnetic elements.

It is planned to use SP12 magnet of VP1 extraction channel situated directly in front of F4 focus in order to turn the primary extracted beam toward HMC. Calculations show that the primary beam can be turned to the required angle in a proton momentum range of 1–7 GeV/c. For higher-energy particles, it is necessary to use a target in F4 focus. In this operation mode, secondary beams are formed at the installation MARUSYA and HMC simultaneously.

Note that this operation mode is possible with simultaneous (parallel) operation of other installations at



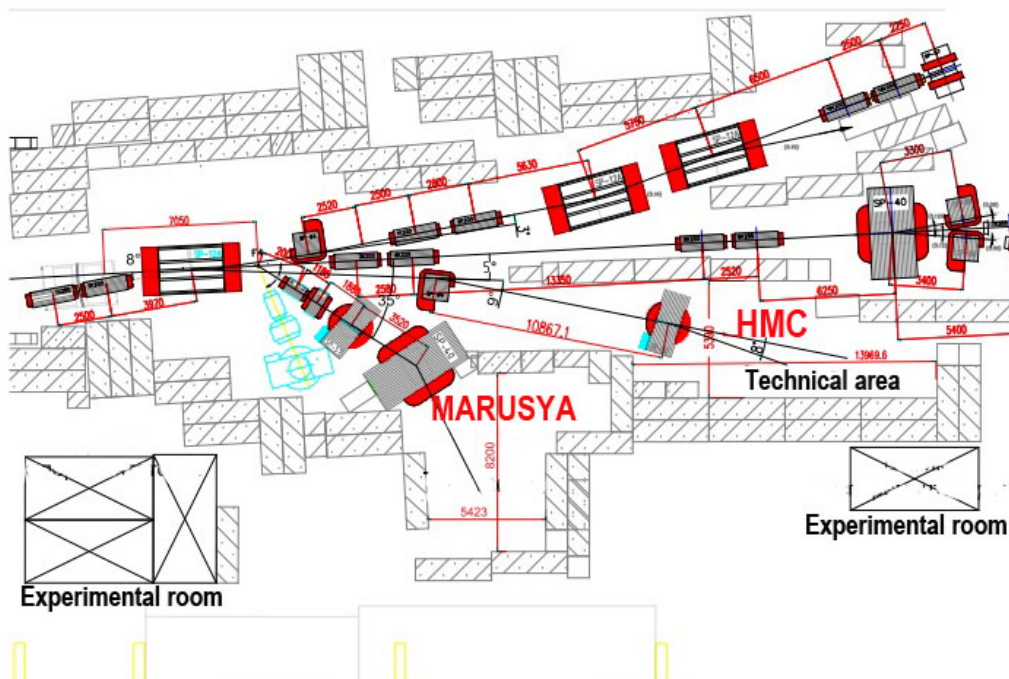


Figure 9.1: Magnetic elements of the test zone.

2138 VP1 extraction channel (in particular, the installation BM&N).

2139 Figure 9.2 shows the schematic diagram of the magneto-optical part of the installation MARUSYA and  
 2140 the detector stations:

- 2141 – M1–M3 scintillation monitors for the extracted beam (and polarization monitoring);
- 2142 – K100, ML17 magnetic lenses;
- 2143 – SP57, SP40 dipole magnets;
- 2144 – G time of flight scintillation hodoscopes;
- 2145 – PC proportional chambers;
- 2146 – acceptance  $50 - 80 \text{ msr} \times \%$ ;
- 2147 – momentum resolution  $\Delta P/P \sim 0.5\%$ ;
- 2148 – particle registration angles  $20-90^\circ$ ;
- 2149 – particle momenta  $0.3 - 1.5 \text{ GeV}/c$ .

2150 It is planned to place tested detectors behind SP40 magnet; there, a concrete-shielded region with a size  
 2151 of  $5 \times 7 \text{ m}^2$  without an upper plate is planned.

2152 This region is available for personnel during the accelerator operation and beam extraction along VP1  
 2153 channel if the target is in F4 focus.

2154 At present, the remote-controlled target station is used; it provides the target movement in three directions  
 2155 (horizontal, vertical, and along the beam axis); the target can be automatically removed out of the beam  
 2156 if a personnel member enters behind the shielding to attend to detectors behind the SP40 magnet.

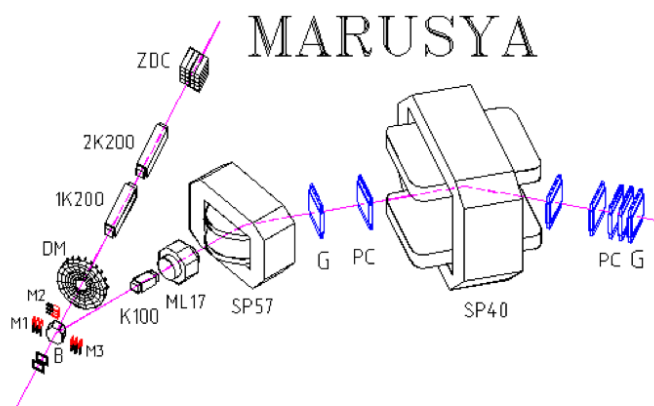
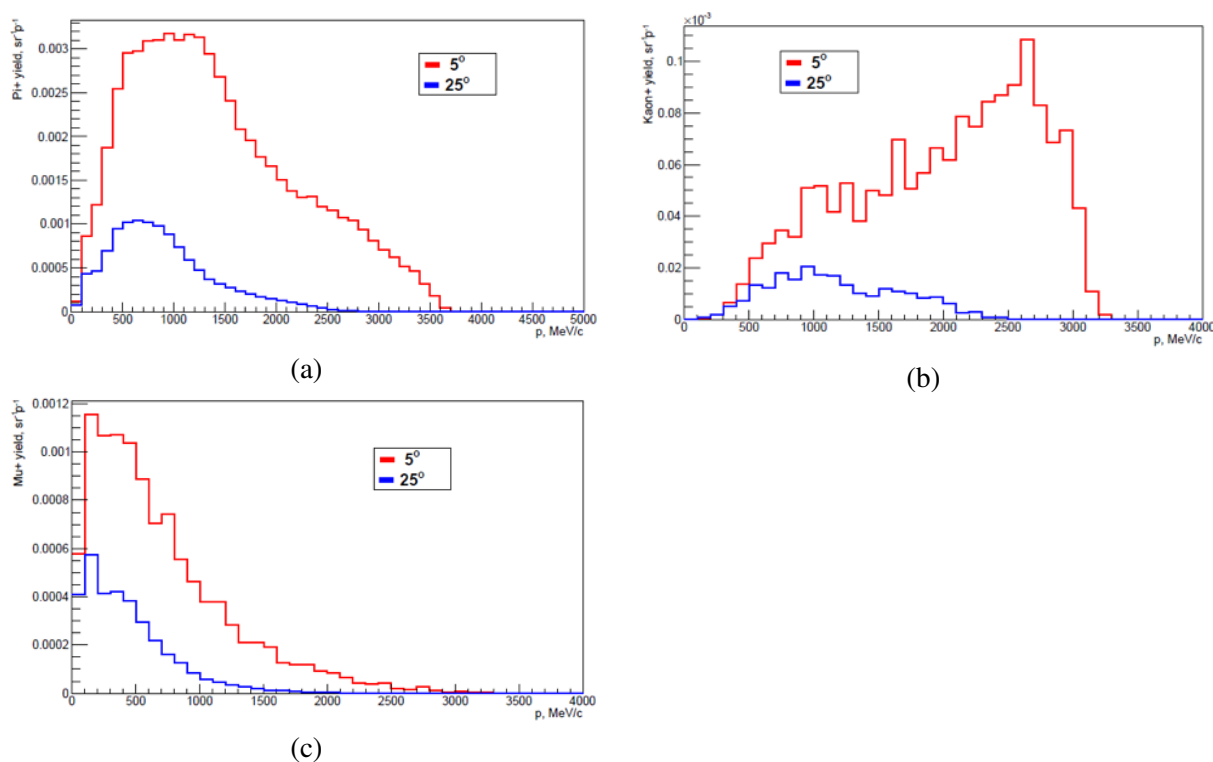


Figure 9.2: MARUSYA installation and the detector stations.

Figure 9.3: GEANT4 Monte Carlo simulation of yield of (a)  $\pi^+$ , (b)  $K^+$ , and (c)  $\mu^+$  per one incoming proton for production angles of  $5^\circ$  and  $25^\circ$  in the reaction  $4 \text{ GeV } p + C$ .

2157 Taking into account the requirement of creation of VP1 vacuum extraction channel, it is planned to  
 2158 develop, approve with the beams division staff, and manufacture a new target station in the vacuum box  
 2159 of F4 focus.

2160 Simulation using the software TRANSPORT and GEANT4, as well as experimental measurements at  
 2161 deuteron, carbon, magnesium, lithium, etc. beams showed that the channel-spectrometer MARUSYA  
 2162 provides the following parameters: for an extracted 2-4 GeV/nucleon deuteron beam with an intensity  
 2163 of  $10^{10}$  and carbon and copper targets with a thickness of  $1 \text{ g/cm}^2$ , secondary pion beams with an  
 2164 intensity of  $10^4$  can be obtained. The size of the secondary beam at a studied detector behind SP40

2165 is  $100 \times 150$  mm. The prototype time of flight system based on scintillation hodoscopes demonstrated  
2166 reliable identification of protons, pions, kaons in a momentum range of 600-1200 MeV/c.

2167 For 5 GeV/nucleon deuteron beams extracted to building 205 and carbon targets with a thickness from  
2168  $0.005$  to  $5 \text{ g/cm}^2$ , the beam parameters feasible at the channel-spectrometer MARUSYA are given in  
rows 1–3 of Table 9.1, and the parameters for the high-momentum channel, in rows 4–5 of Table 9.1.

Table 9.1: Beam parameters feasible at the channel of the spectrometer MARUSYA and the high-momentum channel.

P, MeV/c	d	p,n	$\pi^\pm$	$K^+$	$K^-$	$\mu^\pm$	$e^\pm$
400	$10^3$	$10^5$	$10^5$	$10^3$	$10^2$	$10^3$	$10^3$
800	$10^3$	$10^4$	$10^4$	$10^3$	$10^2$	$10^3$	$10^3$
1500	$10^2$	$10^4$	$10^4$	$10^3$	$10^2$	$10^2$	$10^2$
2000	$10^4$	$10^5$	$10^4$	$10^3$	$10^2$	$10^2$	$10^2$
7000	$10^4$	$10^6$	$10^3$	$10^3$	$10^2$	$10^2$	$10^2$

2169

2170 The region between magnets SP57 and SP40 is preferable for measurement of momenta below 600 MeV.

2171 In order to achieve a momentum resolution of  $0.2\%$ , it is necessary to equip the magneto-optical spec-  
2172 trometer MARUSYA with four sets of chambers with a spatial resolution of at least  $150 \mu\text{m}$  in the vertical  
2173 and horizontal directions. Two chambers will be situated between the dipole magnets and two chambers  
2174 behind SP40.

2175 For muon and electron registration and identification, it is planned to use the electromagnetic calorimeter  
2176 with a size of  $100 \times 150 \text{ mm}^2$  based on BGO crystals.

2177 It is planned to use the gas Cherenkov counter for testing of the electromagnetic calorimeter at sec-  
2178 ondary muon and pion beams; this Cherenkov counter will be provided by the SPD collaboration.

2179 The new electronics of the data acquisition system TQDC based on VME standard (developed at LHEP)  
2180 was tested during the accelerator run in 2018. The testing was successful; it demonstrated that the  
2181 experiment SPD should use this new VME-based electronics or improved data acquisition systems.

2182 The structural diagram of the data acquisition, analysis and storage system is shown in Fig. 9.4.

2183 The upgrade of the SPD test zone consists of the following stages.

2184 1. Cleaning of the zone, removal of unnecessary elements (magnets, lenses, detectors, etc.). Refur-  
2185 bishment of biological shielding and walls.

2186 2. Renovation and repair of experimental rooms, installation of electric communications. Recon-  
2187 struction of electrical control units for power supply of detectors and auxiliary equipment.

2188 3. Manufacture and installation of gas consoles.

2189 4. Manufacture of scintillation beam detectors and electronics of the data acquisition system. Manu-  
2190 facture of small-size track detectors based on straw, RPS, Si, etc. in the framework of prototyping  
2191 and production of main detectors of SPD.

2192 5. Purchase and commissioning of computer equipment for the data acquisition, communication, and  
2193 processing system.

- 2194 6. Mounting of two magnets of the new high momentum channel. Geodesy and measurement of  
2195 magnetic field maps.
- 2196 7. Manufacture of scintillation time of flight HMC system.
- 2197 8. Development and production of the channel slow control systems.

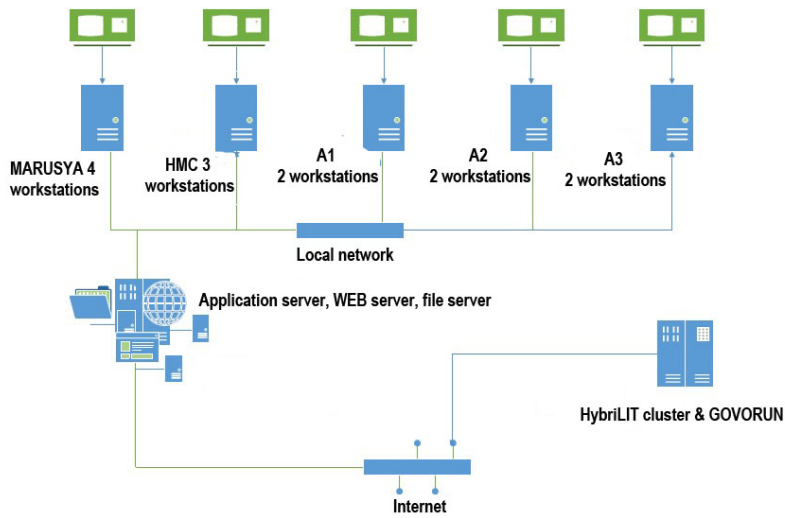


Figure 9.4: Computers and servers for MARUSYA and HMC.

## Chapter 10

# Integration and services [OUT OF DATE]

According NICA TDR [285] the SPD is allocated in southern point of beams collision. The NICA SPD location is shown in Figure 10.1.



Figure 10.1: NICA layout with SPD.

The experimental hall is designed very close to MPD hall [286].

### 1 Hall facilities and services

The hall solid concrete floor is considered to have the bearing capacity to be able to perform the operation and assembly of the SPD. It would be quite enough:

1. to bear the weight of the assembled detector with needed services,
2. to keep the integrity of the detector in the process of its transportation on the rail guided carriage and its assembling,
3. to provide a stable detector position during operation cycles with high accuracy .

A helium refrigerators has to be mounted in close to the detector to provide cryogenic fluids and gases for toroidal and solenoidal magnets operation (see chapter 3.2). The crates of the data acquisition systems and power supplies has to be placed in close the detector on special electronic platforms.

## 2213 2 SPD integration

2214 The SPD hall shown in Figures 10.2, 10.3, consists of the Production area and Experimental hall. The  
 2215 experimental area is located on the right side of the Figure 10.2, below the level of the production area.  
 2216 The production area will be used for the preparation and testing of the SPD detectors system and for  
 2217 the installation and the final assembly for the data taking. Also, the Production area will be used for  
 2218 technical work and maintenance of the set-up. It is assumed that the maximum for the power supply of  
 2219 the SPD hall will be about 1.2 MWatts.

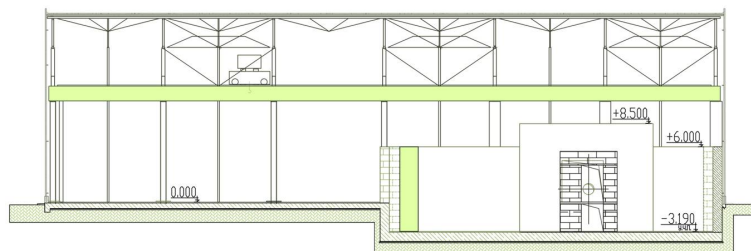


Figure 10.2: SPD experimental hall.

2220 The sizes of the SPD hall is as follows: the total area is more than  $2000 \text{ m}^2$ , the main gate for trucks -  
 2221  $4000 \text{ mm} \times 4000 \text{ mm}$ , the dismantle part of wall for widest equipment -  $8000 \text{ mm} \times 8000 \text{ mm}$ .

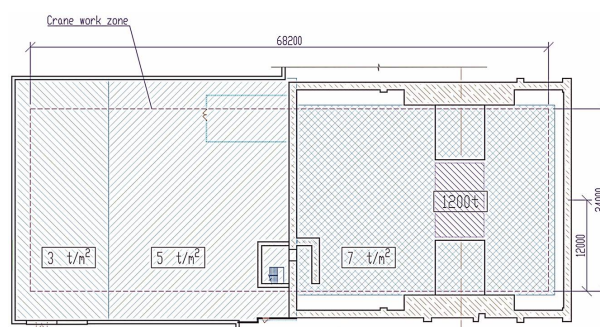


Figure 10.3: The view from the top of the SPD experimental hall.

2222 To provide access to the electronic racks and to sections of the detector, between the detector and the  
 2223 electronics platform especial radiation shielding can be installed.

2224 The Figure 10.4 shows transportation system to operate with set-up. The mark 1 is beam line, 2 -  
 2225 interaction point, 3- rails, 4- collider systems, 5,6 - walls of the hall.

2226 The integration of the SPD within the accelerator rings is given in Figure 10.5.

## 2227 3 Detector assembly

2228 The assembly of the SPD is a very critical point because of their essential weights, modularity (see  
 2229 chapter 3) and three different magnet systems.

2230 The Figure 10.6 shows possible procedure of the operating with SPD, one includes the transportation of  
 2231 the whole detector to (C) or out (A,B) beam position. Also the detector can be dismantled into three  
 2232 parts (two endcaps an barrel parts) at B position.

2233 The preliminary view of assembled SPD is shown in Figure 10.7.

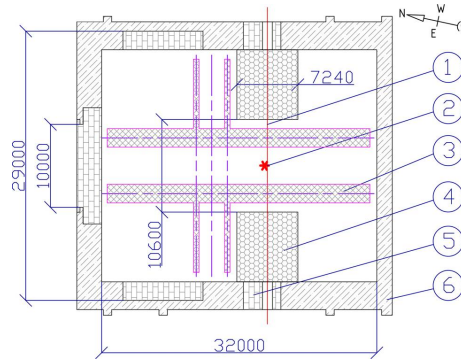


Figure 10.4: The view from the top of the SPD hall with elements of detector transportation. Descriptions given in the text.

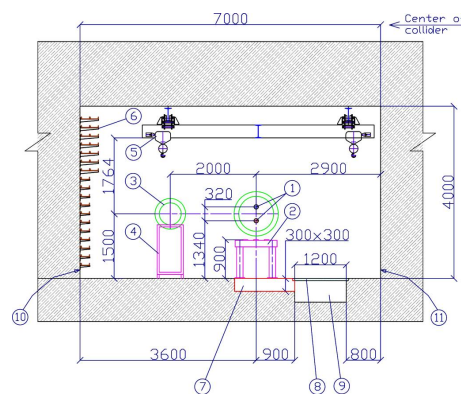


Figure 10.5: The view of the hall in section with collider beam lines (1,2) with sizes and technical cable supports (5,10), cranes (5) and garage position of collider magnets (3,4).

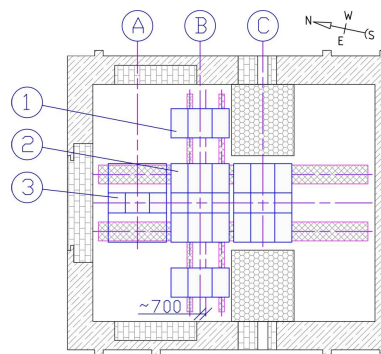


Figure 10.6: The SPD position in experimental hall. Details are given in the text.

#### 2234 4 Technical requirements

2235 Technical requirements of SPD includes subdetectors having their subsystems as follows:

2236 1. Magnet: Current source, Cryogenic system

2237 2. Vertex Detector: HV power supply system, LV power supplies for powering of digital and analog  
2238 electronics, Cooling system to provide silicon detector stable working temperature, FE temperature

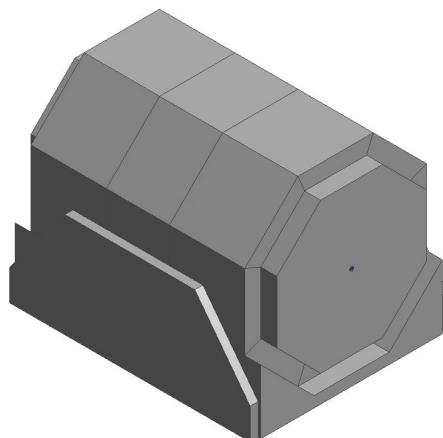


Figure 10.7: View of assembled SPD detector.

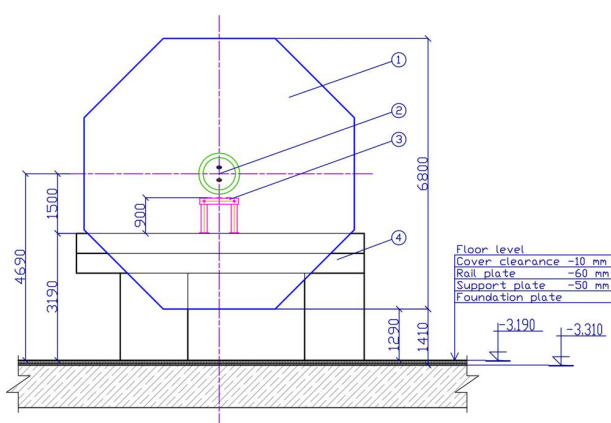


Figure 10.8: The view of the SPD with collider magnet and beam lines.

- 2239 monitoring system, FE control
- 2240 3. Tracking System: HV power supply system, LV power supply system, Gas mixing system, FE
- 2241 control
- 2242 4. TOF: HV power supply system, LV power supply system, Gas mixing system, FE control
- 2243 5. ECAL: HV power supply system, LV power supply system, Cooling, Thermo-stabilization, FE
- 2244 control, laser calibration/monitoring system
- 2245 6. Muon system(Range system): HV power supply system, LV power supply system, Gas mixing
- 2246 system, FE control
- 2247 7. Tagging station: HV, LV, FE control
- 2248 8. Local polarimetry: HV, LV, Cooling, FE control, monitoring system.



# Chapter 11

## MC simulation and physics performance

### 1 General performance of the SPD setup

#### 1.1 Rates and spectra for minimum bias events [A. Guskov]

The beam particles collision in the interaction point is the source of numerous secondary charged and neutral particles in the SPD setup. Table 11.1 shows the total cross-section of the  $p$ - $p$  collisions, the multiplicity of charged and neutral secondary particles for the different collision energy  $\sqrt{s}$ . The angular and momentum distributions for different particles produced in the primary vertex in the  $p$ - $p$  interactions at  $\sqrt{s} = 26$  GeV/ $c$  are presented in Fig. 11.1.

Table 11.1: The total cross-section and the average multiplicity for the charged and neutral particles produced in the  $p$ - $p$  collisions as a function of  $\sqrt{s}$ .

$\sqrt{s}$ , GeV	$\sigma_{tot}$ , mb	Charged multiplicity	Neutral ( $\gamma$ ) multiplicity
13	38.4	5.9	4.6 (3.8)
20	38.9	7.2	6.0 (5.0)
26	39.7	7.8	6.5 (5.5)

Secondary particles are produced in the interaction of primary particles with elements of the setup. The material budget between the interaction point and the closest internal surface of the ECAL is  $\sim 0.15X_0$  or  $\sim 0.03\lambda_I$ . The flux of charged particles and photons with an energy above 0.1 GeV at the internal surface of the ECAL for the Barrel and one End-cap for the  $p$ - $p$  collisions at  $\sqrt{s} = 26$  GeV/ $c$ . is shown in 11.2.

Energy deposit in the ECAL per one minimum bias event for the Barrel and the End-cap is shown in Fig. 11.3. Average energy deposit in the ECAL is 2.0 GeV per event (1.2 GeV from charged particles and 0.8 GeV for photons) in the barrel and 5.0 GeV per event (3.7 GeV from charged particles and 1.3 GeV for photons) in each End-cap for  $p$ - $p$  collision at  $\sqrt{s} = 26$  GeV/ $c$ .

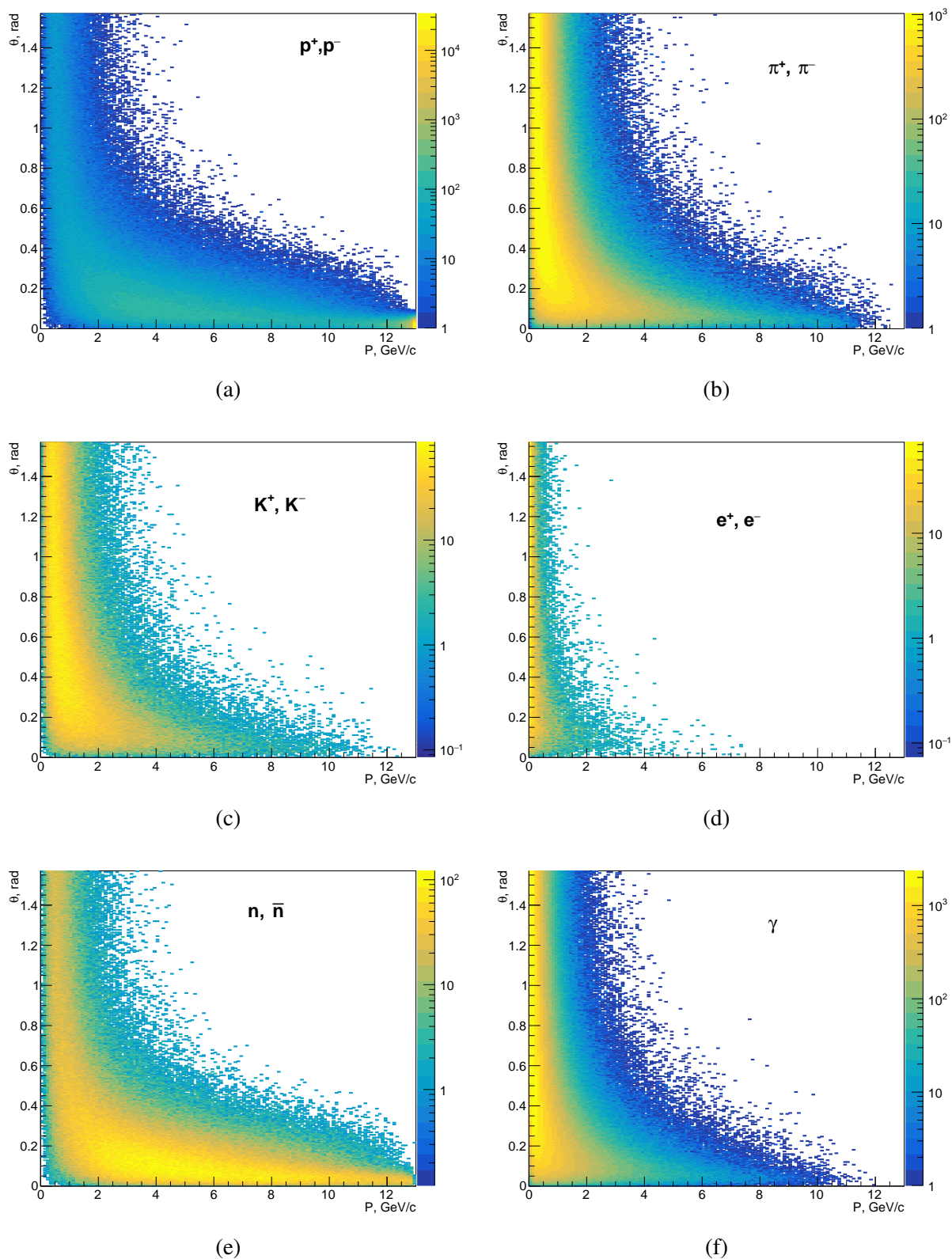


Figure 11.1: Momentum and angular distributions for particles produced in the primary vertex of  $p$ - $p$  interactions at  $\sqrt{s} = 26$  GeV/c:  $p^\pm$  (a),  $\pi^\pm$  (b),  $K^\pm$  (c),  $e^\pm$  (d),  $n$  and  $\bar{n}$  (e) and  $\gamma$  (f) per  $10^6$  minimum bias events.

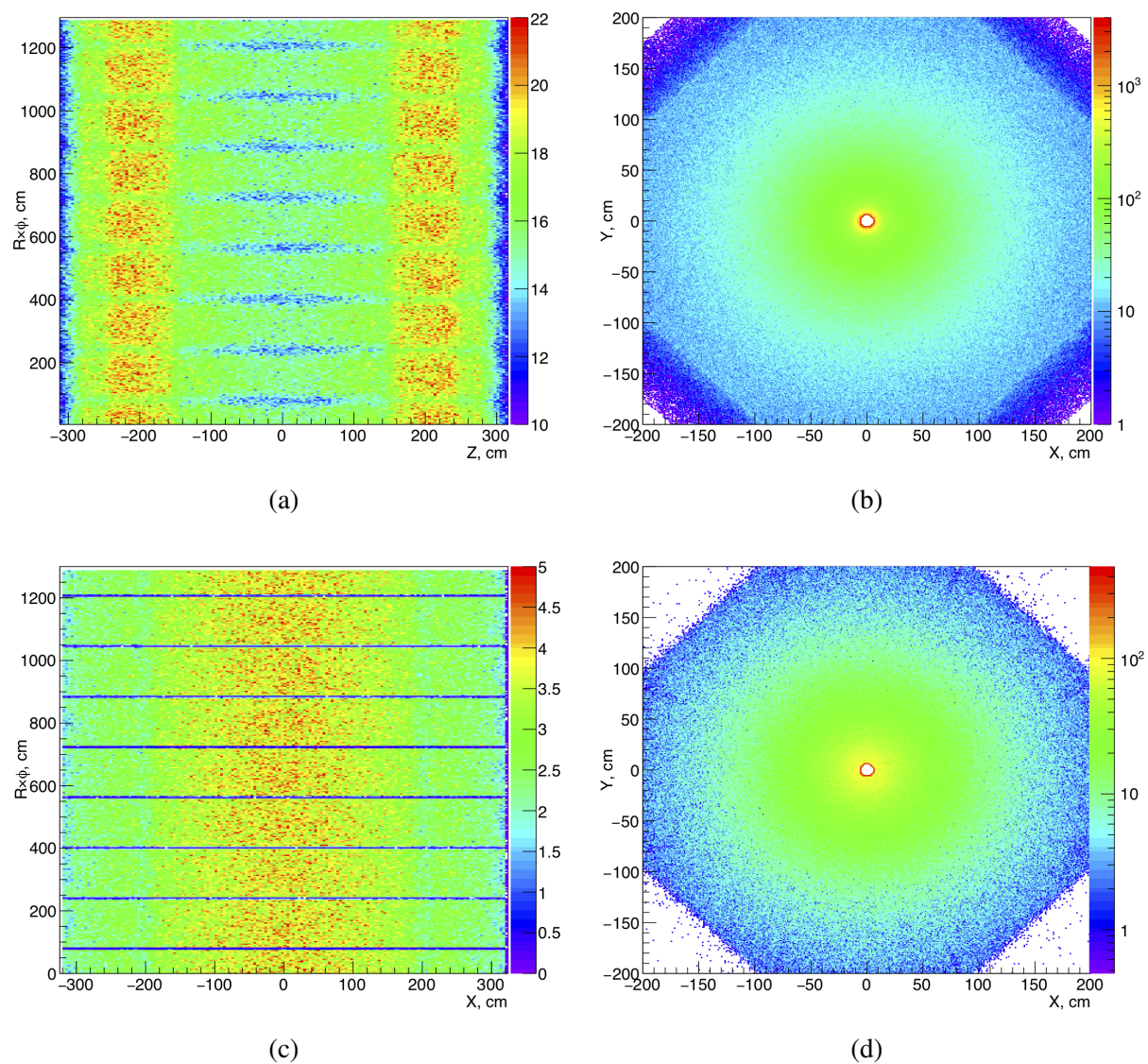


Figure 11.2: Flux of charged particles and photons with energy above 0.1 GeV at the internal surface of the ECAL for the Barrel (a, c) and one of the End-caps (b, d) in particles per  $1 \text{ cm}^2$  per  $10^6$  interactions.

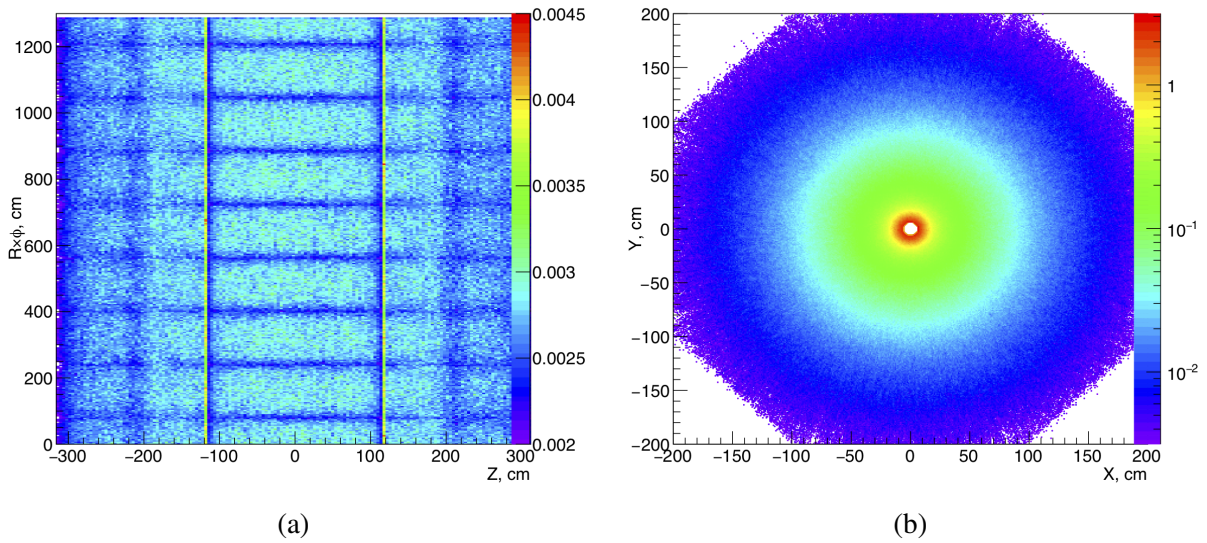


Figure 11.3: Energy deposit in the ECAL in the Barrel (a) and one End-cap (b) in  $MeV/cm^2$  per one minimum bias event.

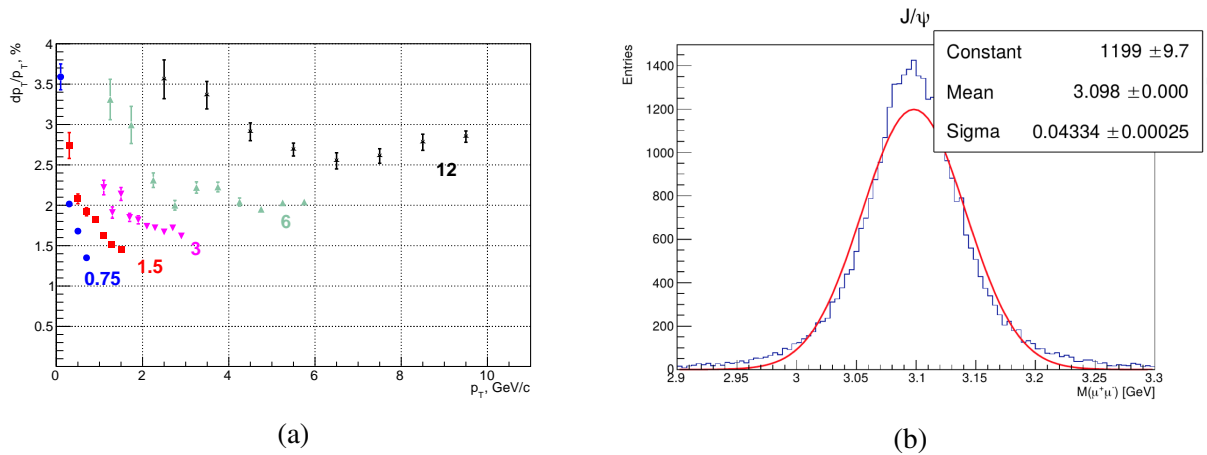


Figure 11.4

## 2267 1.2 Tracking [A. Guskov]

## 2268 1.3 Vertex reconstruction [A. Guskov]

## 2269 1.4 Calorimetry [A. Guskov]

2270 The electromagnetic calorimeter is one of the main detectors for the SPD gluon program. Its function is:  
 2271 (i) to measure the energy and position of hard prompt photons, and photons from the radiative decays of  
 2272  $\pi^0$  and  $\eta$  mesons; (ii) to reconstruct soft photons from the decays  $\chi_{c1,2} \rightarrow J/\psi\gamma$ ; (iii) to provide identifi-  
 2273 cation of electrons and positrons via comparison of an energy deposit in the ECAL and a momentum  
 2274 measured in the tracking system. End-cup part of the ECAL participates also in online polarimetry with  
 2275 inclusive  $\pi^0$  production at high  $x_F$  (see Sec. 2).

2276 Transparency of the SPD setup allows to detect photons produced in the interaction point in a wide  
 2277 kinematic range. Efficiency of photon detection as a function of a production angle  $\theta$  in respect to  
 2278 the beam direction and as a function of a transverse momentum  $p_T$  is shown in Fig. 11.5(a) and (b),  
 2279 respectively. Expected energy resolution of the ECAL obtained from the Geant4-based Monte Carlo

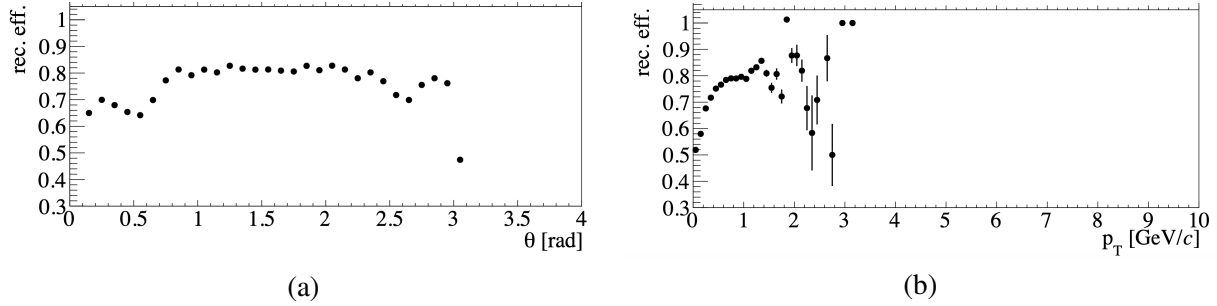


Figure 11.5: Efficiency of photon detection as a function of (a)  $\theta$  and (b)  $p_T$ . [Dummy now!]

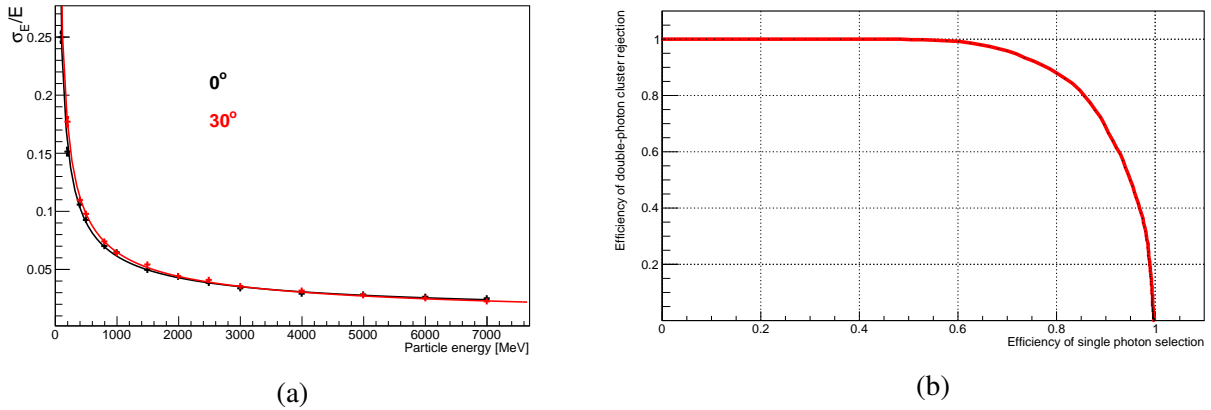


Figure 11.6: (a) Energy resolution of the ECAL for the normal incidence of photons and for an angle of  $30^\circ$ . (b) Purity of double-photon rejection vs. the efficiency of single photon reconstruction for 6 GeV photons and two 3 GeV photons separated by 4 cm of distance basing on the cluster shape analysis.

2280 simulation for the normal incidence of photons and for an angle of  $30^\circ$  in respect to the normal line is  
 2281 shown in Fig. 11.6(a). Such effects as individual cell energy threshold on the level of 50 MeV, light  
 2282 absorption in optic fibers and fluctuation of the number of photons are taken into account. The fitted  
 2283 curve has a shape:

$$\sigma_E/E = A \oplus \frac{B}{\sqrt{E/GeV}} \oplus \frac{C}{E/GeV}, \quad (11.1)$$

2284 were the sets of parameters  $A$ ,  $B$  and  $C$  are 0.9%, 5.9%, 1.7% and 0.0%, 6.0%, 2.2%, respectively, for  
 2285  $0^\circ$  and  $30^\circ$  of incidence angle. The superconducting coils of the magnetic system (0.7  $X_0$  of material)  
 2286 placed in front of the calorimeter do not reduce its acceptance and do not produce any sizable impart to  
 2287 the energy resolution. For instance, the average resolution for 1-GeV photons passed through the coil  
 2288 changes from 6.1% to 6.3%.

2289 As soon as the internal longitudinal and transverse size of the ECAL is quite small, for photons from  
 2290 the high-energy pions decay ( $E_{\pi^0} \gtrsim 6$  GeV) there is a probability to produce a single cluster and be  
 2291 misidentified as a single high-energy photon. That is especially important for the prompt-photon part of  
 2292 the physics program. But it is possible to identify such clusters with a certain precision performing the  
 2293 cluster shape analysis. Cluster shape can be characterised using variables such as dispersion, or second-  
 2294 order moment (in one or two dimensions), fourth-order moment, ratio of major and minor semiaxes of  
 2295 the ellipse corresponding to deposited energy, etc. The machine learning classification techniques are  
 2296 planned to be applied (multilayer perceptron, k-nearest neighbors, etc.) using these variables as an input  
 2297 to classify between single and double-photon clusters. Figure 11.6 illustrates the purity of double-photon  
 2298 rejection vs. the efficiency of single photon reconstruction for 6 GeV photons and two 3 GeV photons

2299 separated by 4 cm of distance (exactly the ECAL cell size) basing on the cluster shape analysis.

2300 Impact of the ECAL energy resolution to the reconstruction of such states as  $\pi^0$  and  $\chi_{c,1,2}$  via their  
 2301 radiative decays is presented in Fig. 11.7. For the latter case the  $\chi_{c1}$  and  $\chi_{c2}$  cannot be fully resolved  
 2302 ( $\Delta M/\sigma_M \approx 1.5$ ) but nevertheless a relative contribution of these states could be estimated basing on the  
 2303 detailed peak shape analysis.

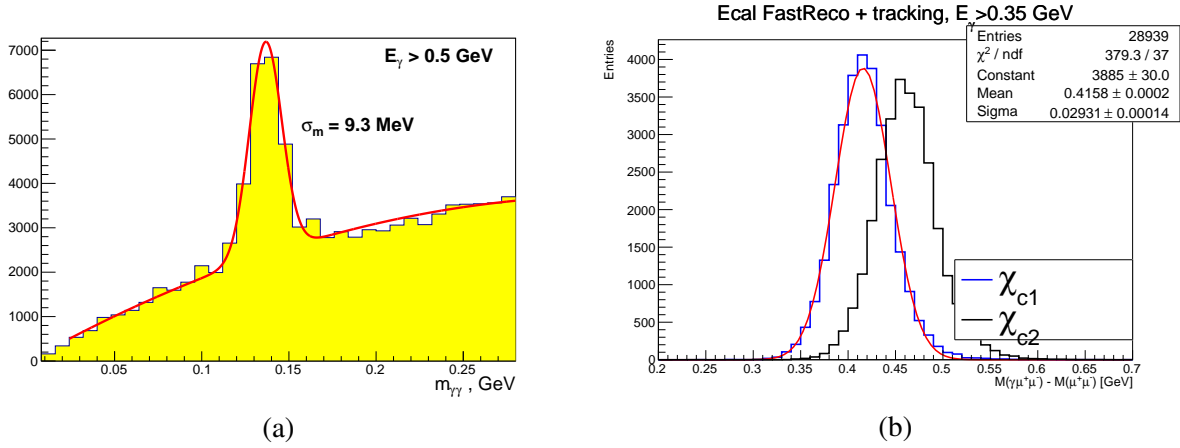


Figure 11.7: (a)  $\pi^0$  peak in the  $\gamma\gamma$  mass spectrum. (b) Mass resolution for  $\chi_{c1,2}$  reconstructed via their decay into  $J/\psi\gamma$  final state.

### 2304 1.5 Particle identification [A. Guskov]

2305 The particle identification with the TOF detector is based on the comparison between the time of flight  
 2306 of the particle from the primary vertex to the TOF detector and the expected time under a given mass hy-  
 2307 pothesis. Presence of only one plane of the TOF detector requires for particle identification the precision  
 2308 knowledge of the event collision time  $t_0$ . It can be estimated by the TOF detector on an event-by-event  
 2309 basis using  $\chi^2$  minimization procedure for events with two and more reconstructed tracks. Having in the  
 2310 event  $N$  tracks matched to a corresponding hits on the TOF plane it is possible to define certain combi-  
 2311 nations of masses  $\vec{m}_i$  assigning independently for each track the  $\pi$ ,  $K$  or  $p$  mass. The index  $i$  indicates  
 2312 one of the possible combination  $(m_1, m_2, \dots, m_{N \text{ tracks}})$  among the  $3N$  tracks ones [287].

2313 For each track the following weight is attributed

$$W_i = \frac{1}{\sigma_{TOF}^2 + \sigma_{t_{exp. i}}^2}. \quad (11.2)$$

2314 Here  $\sigma_{TOF}$  and  $\sigma_{t_{exp. i}}$  are the time resolution of the TOF detector and uncertainty of the expected time  
 2315 of flight under a given mass hypothesis  $t_{exp. i}$ , respectively. The latter is defined by uncertainty of the  
 2316 momentum and track length measurements.

2317 The following  $\chi^2$  function has to be minimized

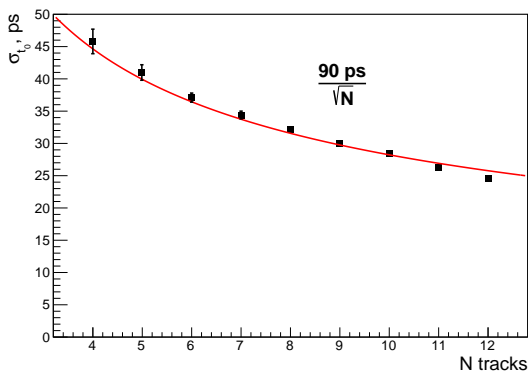
$$\chi^2(\vec{m}_i) = \sum_N W_i ((t_{TOF} - t_0(\vec{m}_i)) - t_{exp. i})^2. \quad (11.3)$$

2318 Here

$$t_0(\vec{m}_i) = \frac{\sum_N (t_{TOF} - t_{exp. i})}{\sum_N W_i}. \quad (11.4)$$

2319 The mass vector  $\vec{m}_i$  that minimizes  $\chi^2$  in Eq. 11.3 can be used in Eq. 11.4 for determination of the event  
 2320 collision time  $t_0$ . For unbiased particle mass determination, each track has to be subsequently excluded  
 2321 from the  $t_0$  calculation procedure.

2322 Figure 11.8(a) illustrates an accuracy of  $t_0$  reconstruction as a function of the number of tracks for  $\sigma_{TOF} =$   
 2323  $70$  ps. One can see that  $\sigma_{t_0}$  is proportional to  $1/\sqrt{N}$  and for the track multiplicity 10 (typical for hard  
 2324 interaction events) is about 30 ps. Pion, kaon and proton separation with the TOF detector is shown  
 2325 in Fig. 11.9.  $\pi/K$  and  $K/p$  separation power as a function of particle momenta and emission angle  
 2326 in the primary vertex is presented in Fig. 11.10 (a) and (b), respectively, for the time of flight ( $t_{TOF} -$   
 2327  $t_0$ ) resolution 80 ps. It is mostly defined by the time measurements while the accuracy of momentum  
 2328 reconstruction becomes sizable only for  $\theta < 10^\circ$ .



(a)

Figure 11.8: Accuracy of  $t_0$  reconstruction as a function of the number of tracks in the primary vertex.

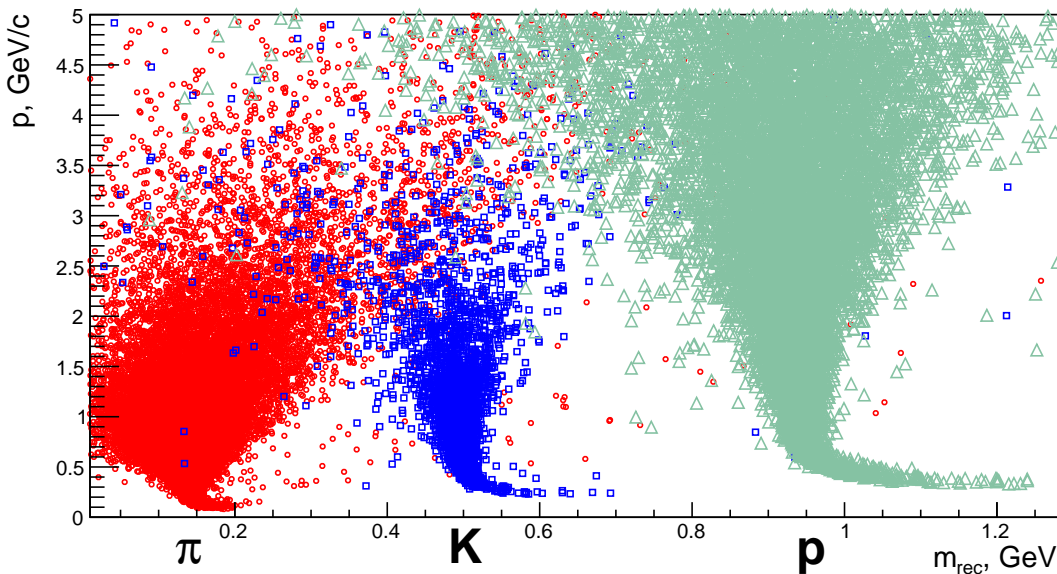


Figure 11.9: Reconstructed mass vs. particle momentum for pions, kaons and protons.

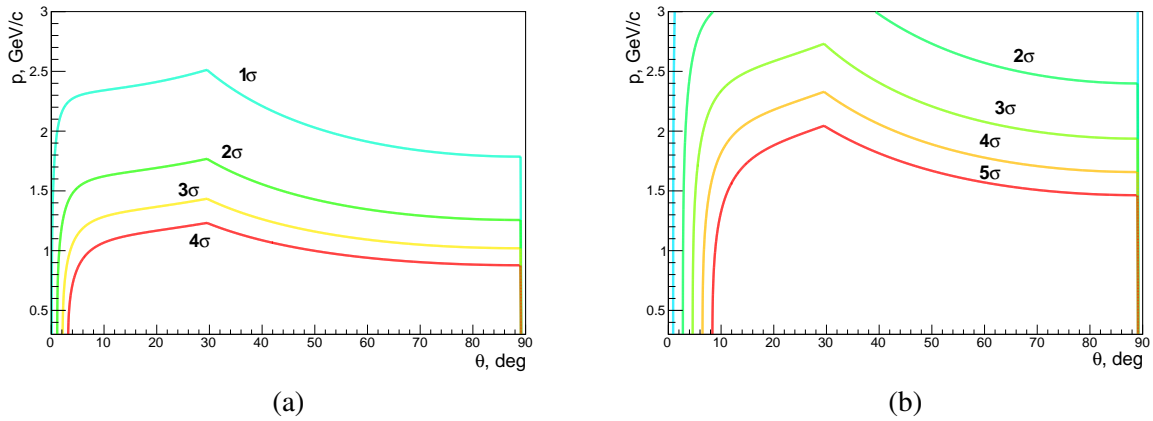


Figure 11.10:  $\pi/K$  (a) and  $K/p$  (b) separation power of the TOF system as a function of particle momenta and emission angle.

## 2329 **2 Accuracies of asymmetries measurement**

### 2330 **2.1 Charmonia production [I. Denisenko]**

2331 According to the modern theoretical approaches, the charmonia production at the SPD energies ( $10 \text{ GeV} \leq$   
 2332  $\sqrt{s} \leq 27 \text{ GeV}$ ) is dominated by gluon-gluon fusion process. The inclusive  $J/\psi$  production has a large  
 2333 cross-section (200 – 250 nb at the maximum energy) and clear experimental signature in the dimuon  
 2334 decay mode, and thus is a powerful probe of internal structure of proton [and deuteron]. The distinct  
 2335  $J/\psi$  signal allows us to also reconstruct excited charmonia states in the decays  $\chi_{c1,2} \rightarrow \gamma J/\psi$  and  
 2336  $\psi(2S) \rightarrow \pi^+ \pi^- J/\psi$ . The feasibility of physics with  $\eta_c$  (e.g. decaying to  $p\bar{p}$ ) is questionable. There  
 2337 is also a possibility to reconstruct  $J/\psi$  from  $e^+e^-$  final state, but it look less promising due larger back-  
 2338 ground, a larger observed  $J/\psi$  width and more complicated shape of the peak, which will significantly  
 2339 affect both statistical and systematic errors.

2340 Muons are identified in the RS. The system is expected to separate showers from strongly interacted  
 2341 pions and muon tracks (using standard or machine learning techniques.) The main background are  
 2342 muons from pion decays and pions that passed large distance in the RS. The pion decays result in a small  
 2343 kink of charged track (about  $2^\circ$ ), and the decay muon retains from 60% to almost 100% of the initial pion  
 2344 energy. There is a possibility that a fraction of decay muons can be suppressed by search of a kink in  
 2345 the tracker or by considering correlation between particle momentum and amount of material it crossed.  
 2346 But the results in this section are based on a simplified model (gives a lower performance boundary). A  
 2347 particle is identified as a muon based on the amount of material it passes in the active part of the RS, this  
 2348 amount is given as a number of proton nuclear lengths ( $n_\lambda$ ). Two possibilities are considered: a particle  
 2349 from the initial interaction and a muon from a pion decay (the pion must be from the initial interaction).  
 2350 In the latter case, if pion decays in the RS, the amount of material is added for pion and muon.

2351 It clear that higher running energies are preferable for physics with charmonia due to higher production  
 2352 cross-section, stronger boost for pions and more energetic muons. All estimates in this section assume a  
 2353  $pp$  collision energy of 27 GeV,  $10^7$  s time of data taking (one year) with the maximum luminosity and a  
 2354 polarization  $P$  of 0.7. At these conditions one expects about 12 million  $J/\psi \rightarrow \mu^+ \mu^-$  decays in the SPD  
 2355 detector.

2356 The  $J/\psi$  events are simulated using Pythia8 and their number normalized to the cross-section of 200 nb.  
 2357 For background minimum bias events generated with Pythia6 and Pythia8 are considered (giving almost  
 2358 the same predictions around  $J/\psi$  peak). Approximately half of background events are produced in hard



2359 interaction, but sizable fraction comes also from diffraction processes. It appears that significant amount  
 2360 of background events can be suppressed by a requirement on polar angle of a muon candidate. The  
 2361  $\mu^+\mu^-$  invariant mass spectrum for muon candidates with  $n_\lambda > 3$  and satisfying  $|\cos\theta| < 0.9$  is shown  
 2362 in Fig 11.11. The selection efficiency can be estimated to be around 35 – 45% depending on the cut  
 2363 on  $\theta$ , resulting in 4 – 5 million selected events. The statistical errors for observables can be estimated  
 2364 using a linear LSM fit []. As an example, the estimated statistical precision for polarization is shown in  
 Fig. 11.11.

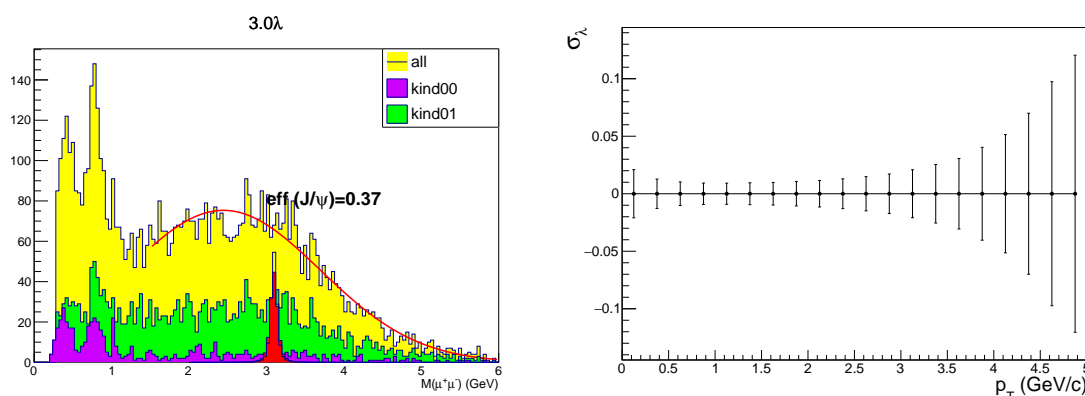


Figure 11.11: (left) The dimuon candidate spectrum and the  $J/\psi$  peak. (right) Expected statistical precision for polarization as a function of  $J/\psi$  transverse momentum [plot on predictions?]. ( $\lambda$  is the polarization in the helicity frame,  $d\sigma/d\cos\theta \propto 1 + \lambda \cos^2\theta$ ). The estimate is made assuming  $\lambda \ll 1$ .

2365

2366 The transverse single spin asymmetry  $A_N$  in  $J/\psi$  production probes the Sivers function. It is observed as  
 2367 modulation of the cross-section with respect to azimuth angle  $\phi$ :  $d\sigma/d\phi \propto 1 + PA_N \cos(\phi - \phi_0)$ , where  
 2368  $P$  and  $\phi_0$  are the beam polarization and its direction, respectively. At  $\sqrt{s} = 200$  GeV it was measured the  
 2369 PHENIX Collaboration and found consistent with zero [17, 18]. To estimate our statistical precision 8  
 2370 bins in  $\phi$  are considered. The same linear fit is used to firstly estimate error in bins based on expected  
 2371  $J/\psi$  number and secondly to extract  $A_N$ . The projected statistical uncertainties for  $A_N$  as a function of  
 2372  $x_F$  are compared to the GPM model predictions from Ref. [?] in Fig 11.12. Compared to the PHENIX  
 2373 measurement, we expect much better precision and much wider kinematic range in  $x_F$ . Our rapidity  
 2374 range is approximately  $|y| < 2$ .

2375 The longitudinal double spin asymmetry  $A_{LL}$  is sensitive to the polarized gluon distribution. It is defined  
 2376 as

$$A_{LL} = \frac{\sigma^{++} - \sigma^{+-}}{\sigma^{++} + \sigma^{+-}},$$

2377 where  $\sigma^{++}$  and  $\sigma^{+-}$  are cross-sections for protons with the same and the opposite helicities, respectively.  
 2378 In terms of  $J/\psi$  yields  $N^{++}$  and  $N^{+-}$  it reads

$$A_{LL} = \frac{1}{P_1 P_2} \frac{N^{++} - RN^{+-}}{N^{++} + RN^{+-}},$$

2379 where  $R$  is the ratio of luminosities and  $P_1$  and  $P_2$  are polarizations of beams. The asymmetry is expected  
 2380 to be small. Taking  $R = 1$  (and neglecting its uncertainty), approximating for  $N^{++}$  and  $N^{+-}$  by the  
 2381 same distribution ( $N$ ) and assuming  $P_1 = P_2 = P$ , the statistical error of  $A_{LL}$  can be approximated as  
 2382  $\sigma_{A_{LL}} \approx \frac{1}{P^2} \frac{\sigma_N}{N}$ . They projection of statistical uncertainties as functions of  $p_T$  and  $|y|$  are shown in Fig 11.13.  
 2383 Compared to previous results obtained by the PHENIX Collaboration at  $\sqrt{s} = 510$  GeV [114], we have  
 2384 much better precision and probe wider kinematic range.

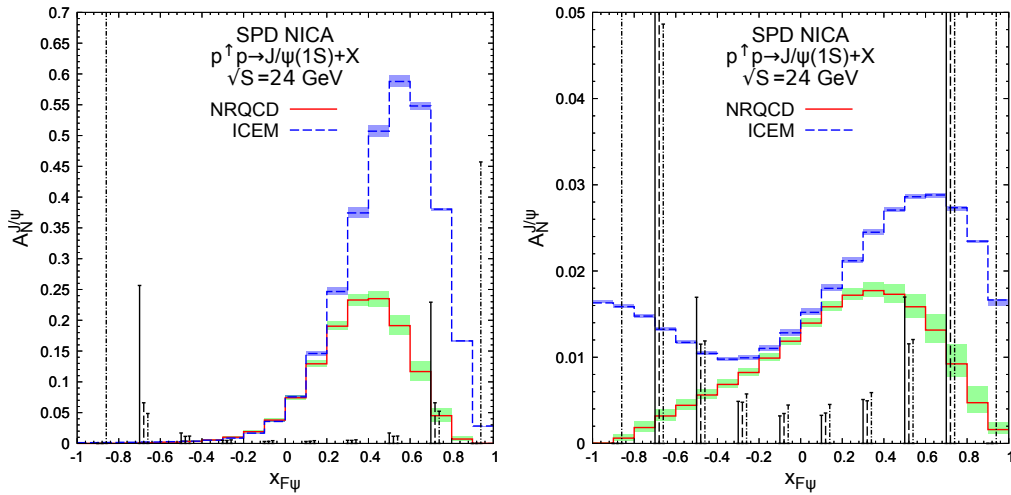


Figure 11.12: Projection of the estimated statistical uncertainties for  $A_N$  compared to GPM predictions from Ref. [?] for SIDIS1 (left) and D'Alesio PDF parameterizations (right).

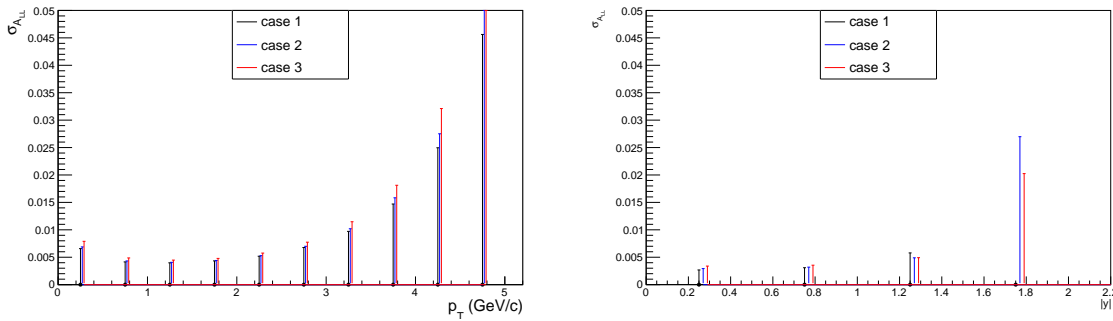


Figure 11.13: Estimated statistical precision of  $A_{LL}$  as a function of  $p_T$  (left) and  $x_F$  (right).

2385 The study of associated  $J/\psi$  production will likely strongly restricted by the small expected statistics.  
 2386 The double  $J/\psi$  production cross-section was measured by the NA3 Collaboration [?] and was found  
 2387 to be  $27 \pm 10$  pb in proton nucleus interaction at  $\sqrt{s} \approx 27$  GeV. Optimistically, such cross-section would  
 2388 result in 50-100 reconstructed events if both  $e^+e^-$  and  $\mu^+\mu^-$  modes are used to reconstruct  $J/\psi$ . It may  
 2389 be enough to determine low- $p_T$  cross-section dependence, but a study of any angular modulation will  
 2390 not be possible. The  $\gamma J/\psi$  [cs??] will be challenging experimentally due to both lack of statistics and  
 2391 high expected background. The reasonable statistics might be expected for  $J/\psi D$  production.

2392 The  $\psi(2S) \rightarrow \mu^+\mu^-$  decay is suppressed as compared to  $J/\psi \rightarrow \mu^+\mu^-$  by approximately a factor of 60  
 2393 and its reliable extraction may not be feasible. At the same time the decay  $\psi(2S) \rightarrow \pi^+\pi^- J/\psi$  can  
 2394 be reliably identified as a narrow (about 10 MeV/ $c^2$  wide) peak in the  $M_{\pi^+\pi^-\mu^+\mu^-} - M_{\mu^+\mu^-}$  distribution  
 2395 [Show?]. The expected statistics is about  $200 \times 10^3$  selected events.

2396 The  $\chi_{c1}$  and  $\chi_{c2}$  states have a large partial of decay to  $J/\psi\gamma$  and can be reconstructed using it. The pro-  
 2397 duction properties of these states at low energies are poorly known (e.g. see Ref). At SPD identification  
 2398 of these decays relies on the ECAL performance. The result of MC simulation for  $M_{\gamma\mu^+\mu^-} - M_{\mu^+\mu^-}$  is  
 2399 shown in Fig. 11.7(b). The states  $\chi_{c1}$  from  $\chi_{c2}$ , but their relative fractions should be well measurable for  
 2400 the expected statistics of approximately 0.5 million reconstructed decays (for both states together) per  
 2401 year.

## 2.2 Prompt photon production

As it was already mentioned in the Sec. , the two hard processes determine the production of prompt photons in  $p$ - $p$  collisions in the leading order: gluon Compton scattering  $gq(\bar{q}) \rightarrow \gamma q(\bar{q})$  and quark-antiquark annihilation:  $q\bar{q} \rightarrow g\gamma$ . Contribution of the latter process to the total cross section does not exceed 20% at the discussed energy range. That is what makes prompt photons a convenient probe for gluons inside the nucleon. In ultrarelativistic approximation the minimal value of the longitudinal momentum fraction of struck parton  $x_{min}$  accessible by detection of prompt photon with normalized transverse momentum  $x_T = 2p_T/\sqrt{s}$  and rapidity  $y$  could be expressed as [288]

$$x_{min} = \frac{x_T e^{-y}}{2 - x_T e^y}. \quad (11.5)$$

For the fixed  $x_T$  the minimal  $x_{min} = x_T^2$  is reached at  $y_0 = -\ln(x_T)$ . The value  $x_{min}$  as a function of rapidity  $y$  and  $p_T$  of photon for  $\sqrt{s} = 27$  GeV is shown in color in Fig. ??(a). One can see that possibility to access low- $x$  region is limited by our capability to detect prompt-photon signal at low  $p_T$  and angular acceptance of the experimental apparatus. The latter is especially important for collider experiments like SPD where large values of  $|y|$  correspond to a blind area near beam pipes.

Huge rate of decay photons makes rather difficult determination of the prompt photon production cross-section. Main source of decay photons is the two-body decay  $\pi^0 \rightarrow \gamma\gamma$ . The second most important source is the decay  $\eta \rightarrow \gamma\gamma$ . In the kinematic range  $p_T > 3$  GeV/c at  $\sqrt{s} = 27$  GeV there are 0.18 photons from the  $\eta$  decay per one photon from the  $\pi$  decay. Relative contribution of all other decay photons ( $\omega, \rho, \phi$  decays) does not exceed 0.03.

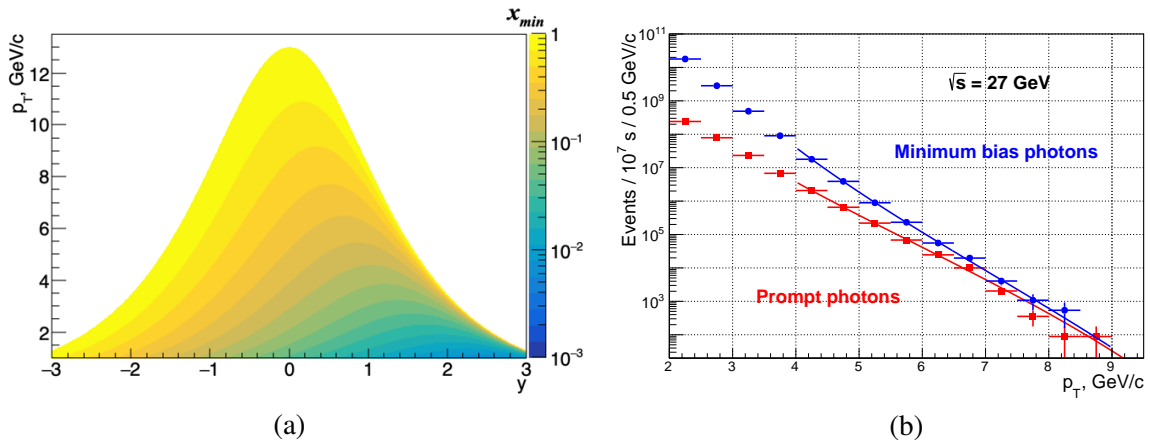


Figure 11.14: (a) A minimal value of gluon  $x$  accessible via registration of prompt photon with rapidity  $y$  and transverse momentum  $p_T$  at  $\sqrt{s} = 27$  GeV. (b)  $p_T$  spectra of produced prompt (red) and decay or minimum bias (blue) photons in  $p$ - $p$  collisions at  $\sqrt{s} = 27$  GeV. Distributions are scaled to one year of data taking ( $10^7$  s).

2419

The  $p_T$  spectra for prompt and decay photons expected at SPD after one year of running at  $\sqrt{s} = 27$  GeV are presented in FIG. (b). The result was obtained using Pythia8 generator with parameters tuned to reproduce high- $p_T$  spectra of  $\pi^0$  and prompt photons measured at similar energies by WA70 ( $\sqrt{s} = 22.96$  GeV) [289, 290] and UA6 ( $\sqrt{s} = 24.3$  GeV) [], respectively. One can see that the  $p_T$  spectrum of decay photons goes down with grows of  $p_T$  faster than for prompt photons and their rates becomes comparable at  $p_T \approx 7$  GeV/c. The fitted functions presented on the plot have shape

$$N(p_T) = A(1 - x_T)^n (p/p_0)^{-m}. \quad (11.6)$$

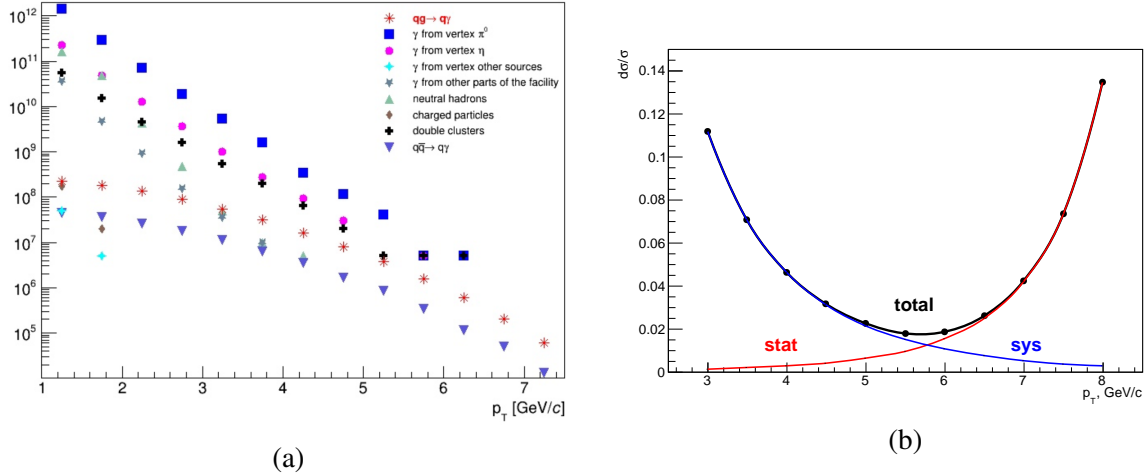


Figure 11.15: (a) Contributions of different background components for the prompt photon production in  $p$ - $p$  collisions at  $\sqrt{s} = 27$  GeV.) (b) Expected uncertainty of the unpolarized cross section  $Ed^3\sigma/dp^3$  measurement as a function of  $p_T$ .

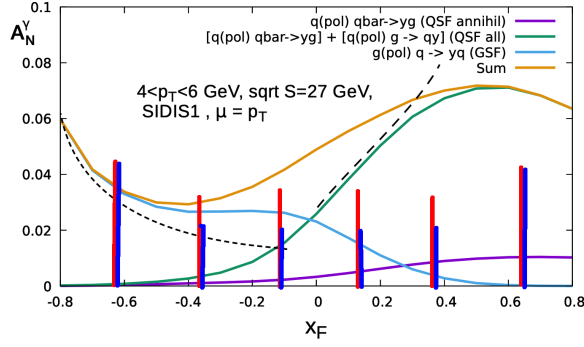
2426 Each cluster of energy deposition in the ECAL with energy above the threshold  $E_0 = 100$  MeV that is  
 2427 not associated with any reconstructed tracks is treated as a prompt photon candidate. The momentum of  
 2428 such photon is reconstructed under assumption of its production in the primary vertex. In order to reject  
 2429 photons from the  $\pi^0 \rightarrow \gamma\gamma$  decay the invariant mass of each to photons is calculated. If the difference  
 2430 between the reconstructed mass and the nominal mass of  $\pi^0$  is smaller than 10 MeV, both photons  
 2431 are removed from the list of candidates. Nevertheless this procedure removes just about 40% of false  
 2432 candidates. The photons from the  $\pi^0 \rightarrow \gamma\gamma$  decay whose partner was not reconstructed due to conversion  
 2433 in the material, too low energy or acceptance issue remain in the list of candidates. Photons from radiative  
 2434 decays of other particles are also in the list. The list of candidates includes also photons associated with  
 2435 two or more overlapping clusters, first of all clusters from the decay of energetic  $\pi^0$ . Significant part of  
 2436 such false candidates could be rejected by a sophisticated analysis of the cluster shape. Clusters produced  
 2437 by charged particles whose tracks are lost, clusters deposited by photons originated from elements of the  
 2438 setup and clusters induced by neutral hadrons are also taken into account as a background. Contributions  
 2439 of each source of background mentioned above are presented as a function of  $p_T$  in Fig. 11.15(a).

2440 As one can see, photons from unreconstructed decays of neutral pions are the main source of background.  
 2441 Fraction of such unreconstructed decays can be estimated from the Monte Carlo simulation and is about  
 2442 50%. Basing on the number  $N_{\pi^0}$  of reconstructed  $\pi^0 \rightarrow \gamma\gamma$  decays the corresponding number of remaining  
 2443 background photons  $k \times N_{\pi^0}$  should be subtracted from the number of prompt photon candidates  $N_\gamma$  in  
 2444 order to get estimation of a true number of prompt photons:

$$N_{prompt} = N_\gamma - k \times N_{\pi^0}. \quad (11.7)$$

2445 Here  $k \approx 0.3$  is a coefficient, calculated from the MC simulation and takes into account not only an  
 2446 inefficiency of the  $\pi^0 \rightarrow \gamma\gamma$  decay reconstruction but also overall contribution of all other background  
 2447 photons including photons from radiative decays of  $\eta$ ,  $\omega$ ,  $\rho$ ,  $\phi$  etc. The described subtraction procedure  
 2448 has to be performed for each bin of  $p_T$  and  $x_F$  ranges. One should keep in mind that the background  
 2449 of decay photons is also spin-dependent: there is an indication of nonzero asymmetries  $A_{LL}$  and  $A_N$  in  
 2450 inclusive  $\pi^0$  and  $\eta$  production [].

2451 An expected accuracy of the unpolarized cross section  $Ed^3\sigma/dp^3$  measurement after one year ( $10^7$  s) of  
 2452 data taking is shown in Fig. 11.15(b). At low- $p_T$  the main contribution to the total uncertainty is coming  
 2453 from the systematics of the  $\pi^0$  background subtraction procedure while at high  $p_T$  statistical uncertainty



(a)

Figure 11.16: (a) Expected accuracy of the  $A_N$  measurement for prompt photons with  $p_T > 4$  GeV/c at  $\sqrt{s} = 27$  GeV as a function of  $x_F$  (**dummy at the moment**). Model predictions are also shown.

2454 dominates. To estimate systematics  $dk/k = 1\%$  is assumed.

2455 An accuracy of the  $A_{LL}$  spin asymmetry measurement is estimated basing on the assumption of ap-  
 2456 proximately equal statistics collected under similar conditions for same ( $N^{++}$ ) and opposite ( $N^{+-}$ ) spin  
 2457 orientations of colliding protons. So

$$A_{LL} = \frac{\sigma^{++} - \sigma^{+-}}{\sigma^{++} + \sigma^{+-}} = \frac{1}{P_1 P_2} \times \frac{N^{++} - RN^{+-}}{N^{++} + RN^{+-}} \approx \frac{1}{P_1 P_2} \times \frac{N^{++} - N^{+-}}{N^{++} + N^{+-}}, \quad (11.8)$$

2458 where  $P_1$  and  $P_2$  are the absolute values of proton beams polarizations and  $R$  is the ratio of integrated  
 2459 luminosities for the samples with same and opposite spin orientations.

2460 To estimate the  $A_N$  asymmetry the function

$$f(\phi) = C + P \times A_N \cos \phi \quad (11.9)$$

2461 is fitted to the expected acceptance-corrected azimuthal distribution of prompt-photon events. Here  $\phi$  is  
 2462 the azimuthal angle of produced photon in the lab. system in respect to the direction of the proton beam  
 2463 polarization. The expected accuracy of  $A_{LL}$  and  $A_N$  measurement as a function of  $x_F$  is shown in Fig. . It  
 2464 does not include uncertainties related with luminosity and beam polarization measurement.

## Chapter 12

# Running strategy

### 1 Accelerator [A. Kovalenko]

We consider the strategy of SPD operation as successive chain of the experimental work with polarized proton and deuteron beam aimed at the obtaining of the ultimate polarized proton beam parameters at the collider and the use of the existing unique polarized deuteron beam for physics experiments from the early beginning of the collider putting into commissioning. Polarized deuterons  $d\uparrow$  was first accelerated at the old LHEP proton accelerator Synchrophasotron in 1986 and much later at the new superconducting synchrotron- Nuclotron in 2002 (see Fig. 12.1).

Polarized protons  $p\uparrow$  was first obtained in 2017. The first test was performed after analysis of the proton spin resonances in 2018. The first dangerous proton spin resonance in Nuclotron corresponds to the beam momentum of about 3.5 GeV/c, whereas in the deuteron case the spin resonance will be occurred at the particle kinetic energy of 5.6 GeV/nucleon. This limit is practically equal to the maximum achievable energy corresponding to the magnetic rigidity of the Nuclotron dipoles.



(a)

Figure 12.1: (a) View of the Nuclotron ring.

The existing polarized proton and deuteron ion source SPI provides up to 3 mA pulse current over  $t \approx 100$  mks. Thus up to  $1.5 \times 10^{11}$  can be injected in the Nuclotron during the injection time (8 mks). The spin modes (pz, pzz): (0,0), (0,-2), (2/3, 0) and (-1/3,+1) were adjusted. Polarization degree of 80 % was achieved.

The existing pre-accelerator of RFQ-type put limit for the achievable proton energy in the next element of the injector chain - linac LU-20. We can obtain only 5 MeV at its output instead of 20 MeV that we

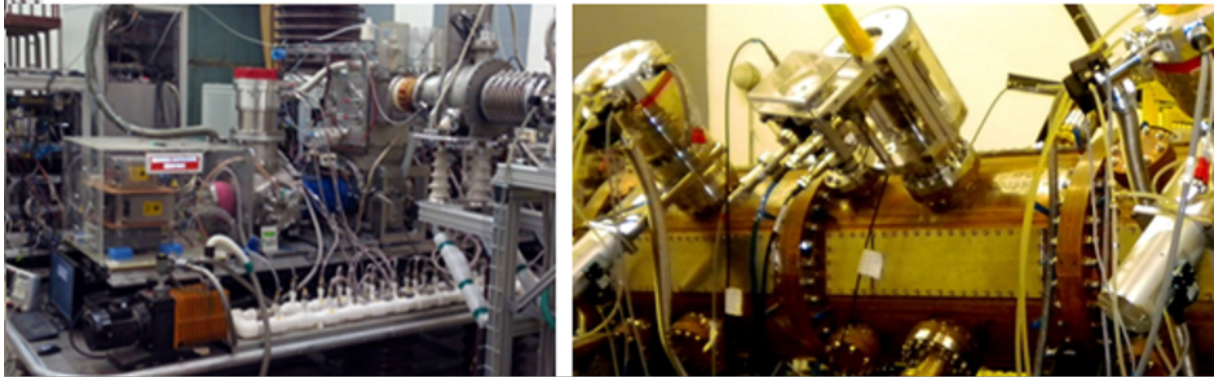


Figure 12.2: View of the SPI (left) and existing RFQ (right).

2485 have had in the past years. The new proton and light ion linac “LILAC” is now under manufacturing.  
 2486 The LILAC output energy will be of 12 MeV. Commissioning is scheduled in 2015-2016. Photos of the  
 2487 SPI and existing RFQ are presented in Fig. 12.2.

2488 The further tasks for the period of 2021-2025 are reasonable and necessary for the starting the SPD  
 2489 operation at the ultimate beam parameters:

- 2490 – continuation of operation and further improvement of polarized ion source SPI, waiting beam time  
 2491 at Nuclotron – 2021-2022;
- 2492 – upgrade of the polarimeters: linac output; coasting beam; extracted beam; new polarimeter for  
 2493 proton energy above 6 GeV – 2020-2023;
- 2494 – manufacturing of the 6T SC-solenoid model; for the SPD test bench -2021-2022;
- 2495 – design and manufacturing equipment for the SPD test bench at the collider - 2020-2023;
- 2496 – LILAC manufacturing and tests – 2020-2025;
- 2497 – analysis of  $^3\text{He}$  (2+) polarized ion source based on the SPI upgrade.

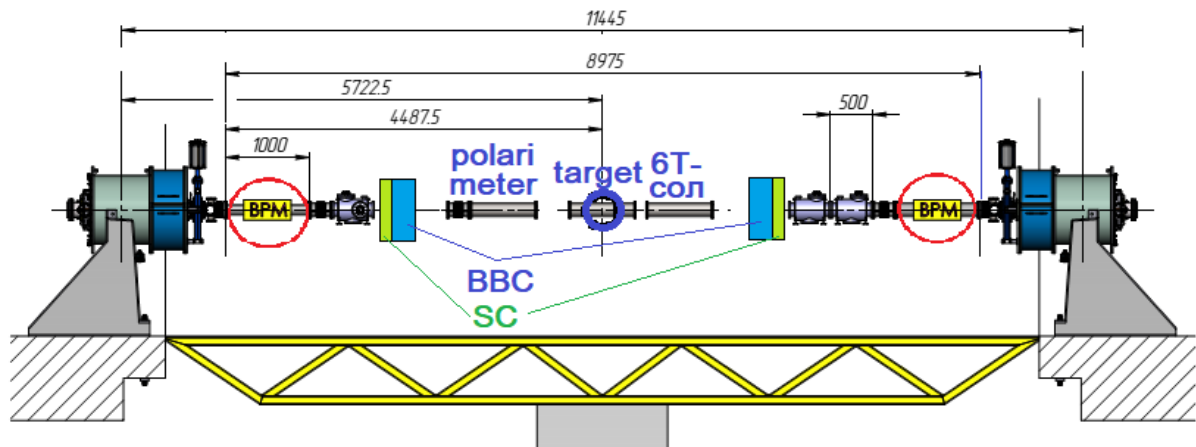


Figure 12.3: The SPD straight section equipped with the diagnostic and control units.

2498 We suppose also, the beam test experiments and preparation to getting the luminosity of  $10^{32} \text{ cm}^{-2} \text{ s}^{-1}$  at  
 2499  $\sqrt{s} = 27 \text{ GeV}$  including the proton polarization control will be demonstrated by the SPD commissioning.  
 2500 For that reason we propose installation of the diagnostic and control equipment at the SPD straight  
 2501 section (see Fig. 12.3).

2502 **2 Spin Physics Detector [A. Guskov]**



2503 **Chapter 13**

2504 **Cost estimate**

Table 13.1: **DUMMY**

	Subsystem		Cost, M\$
SPD setup	Vertex detector	detector	10
		electronics	5
	Straw tracker	detector	1
		electronics	1
	ToF system	detector	2
		electronics	0.5
	Electromagnetic calorimeter	detector	10
		electronics	5
	Range system	detector	10
		electronics	2
	ZDC	detector	1
		electronics	0.5
	Magnetic system		10
	Beam pipe		0.5
General infrastructure			5
Data acquisition system			0.5
Computing			10
<b>TOTAL COST</b>			<b>74</b>

## Chapter 14

# Participating institutions and author list [OUT OF DATE]

Host institute of the project is the Laboratory of High-Energy Physics of the Joint Institute for Nuclear Research. The main part of the human resources engaged with the project comes from there (61 researchers, 24.4 FTE). The Laboratory of Nuclear Problems is the other laboratory of the JINR that participates in the project with substantial number of researchers (29 researchers, 11.3 FTE). Altogether the JINR engagement in the project now evaluates to 37.7 full-time-equivalent (FTE) researchers.

Fourteen institutes from the JINR Member States and other countries have expressed by now their interest for participation in the project and indicate that they could allocate resources and manpower for the project. The list of institutes together with the names of researchers (in some cases only the leaders of the teams are listed) is given below. Received Expressions of Interest are collected under a separate cover.

### **Institute of Applied Physics of the National Academy of Sciences of Belarus**

Shulyakovsky R.

### **Higher Institute of Technologies and Applied Sciences (InSTEC), Havana University, Havana, Cuba**

Guzman F., Garsía Trapaga C.E.

### **Charles University, Prague, Czech Republic**

Finger M., Finger M. (jr.), Hrusovsky J., Jandek M., Prochazka I., Slunicka M., Slunickova V.,  
Stepankova H., Zemko M.

### **Czech Technical University in Prague, Czech Republic**

Jary V., Lednický D., Marcisovsky M., Neugebauer G., Nový J., Popule J., Virius M., Vrba V.

### **University of Turin and INFN Section, Turin, Italy**

Denisov O. Yu., Panzieri D., Rivetti A.

### **Joint Institute for Nuclear Research, JINR, Dubna, Russia**

Directorate

Lednický R.

**Laboratory of High-Energy Physics**

Anosov V.A., Akhunzyanov R.R., Azorskiy N.I., Baldin A.A., Baldina E.G., Barabanov M.Yu.,  
Beloborodov A.N., Dunin V.B., Enik T.L., Filatov Yu.N., Gavrishchuk O.P., Galoyan A.S., Gribovsky  
A.S., Gromov V.A., Gurchin Yu.V., Gusakov Yu.V., Ivanov A.V., Ivanov N.Ya., Isupov A.Yu.,  
Kekelidze G.D., Khabarov S.V., Kharusov P.R., Kovalenko A.D., Kovalev Yu.S., Kozhin M.A.,  
Kolesnikov A.O., Kokoulina E.S., Kopylov Yu.A., Kostukov E.V., Kramarenko V.A., Khrenov A.N.,  
Kruglov V.N., Kuzmin N., Ladygin E., Ladygin V.P., Lapshina I.V., Lysan V.M., Makankin A.M.,  
Meshcheriakov G.V., Moshkovsky I.V., Nagaitsev A.P., Nagorniy S., Nikitin V.A., Pavlov V.V.,  
Paraipan M., Parzhitskii S.S., Perepelkin E.E., Petukhov Yu., Peshekhonov D.V., Reznikov S.G.,  
Rogachevsky O.V., Savenkov A.A., Sheremeteva A.I., Shimanskii S.S., Skhomenko Ya.T., Starikova  
S.Yu., Streletskaya E.A., Tarasov O.G., Tarasova L.N., Teryaev O.V., Tishevsky A.V., Topilin N.D.,  
Topko B.L., Tsenov R., Usenko E.A., Vasilieva E.V., Veselova N.I., Volkov P.V., Yudin I.P., Zamyatin  
N.I., Zemlyanichkina E.V., Zhukov I.A., Zinin A.V., Zubarev E.V.

**Laboratory of Nuclear Problems**

Abazov V.M., Alexeev G.D., Afanasyev L.G., Denisenko I.I., Duginov V.N., Fedorov A.N., Frolov  
V.N., Golovanov G.A., Gritsay K. I., Guskov A.V., Komarov V.I., Kulikov A.V., Kutuzov S.A., Nefedov  
Yu.A., Piskun A.A., Prokhorov I.K., Romanov V.M., Rudenko A.I., Rymbekova A., Samartsev A.G.,  
Semenov A.V., Skachkov N.B., Skachkova A.N., Tsirkov D.A., Tkachenko A.V., Tokmenin V.V.,  
Uzikov Yu. N., Verkheev A.Yu., Vertogradov L.S., Zhuravlev N.F.

**Laboratory of Theoretical Physics**

Anikin I.V., Efremov A.V., Goloskokov S.V., Klopot Ya., Strusik-Kotlozh D., Volchansky N.I.

**Laboratory of Information Technologies**

Uzhinsky V.V.

**St. Petersburg Nuclear Physics Institute, Gatchina, Russia**

Kim V.T.

**Lebedev Physical Institute of the Russian Academy of Sciences, Moscow, Russia**

Andreev V.F., Baskov V.A., Dalkarov O.D., Gerassimov S.G., L'vov A.Yo., Negodaev M.A., Nechaeva  
P.Yu., Polyanskiy V.V., Soutchkov S.I., Terkulov A.R., Topchiev N.P.

**Skobeltsin Institute of Nuclear Physics of the Moscow State University, Moscow, Russia**

Boos E., Merkin M.

**Institute for Theoretical and Experimental Physics, Moscow, Russia**

Akindinov A.V., Alekseev, Golubev A., Kirin D.Yu., Luschevskaya E., Malkevich D.B., B. Morozov,  
Plotnikov V.V., Polozov P., Rusinov V., Stavinskiy A.V., Sultanov R.I., D. Svirida, Tarkovskiy E.I.,  
Zhigareva N.M.

**Institute for High-Energy Physics, Protvino, Russia**

Vorobiev A.

**Samara National Research University, Samara, Russia**

A.V. Karpishkov, M.A. Nefedov, V.A. Saleev, A.V. Shipilova

2571

**St. Petersburg Polytechnic University, St. Petersburg, Russia**

2572

Berdnikov Ya.

2573

**St. Petersburg State University, St. Petersburg, Russia**

2574

Feofilov G.A., V.Kovalenko V.N., Valiev F.F., Vechernin V.V., Zhrebchevsky V.Yo.

2575

**Tomsk State University, Tomsk, Russia**

2576

Burtsev V., Chumakov A., Dusaev R., Lyubovitskij V., Mamon S., Sharko K., Trifonov A., Vasilishin

2577

B., Zhevlakov A.

## Chapter 15

### Project timeline

We propose a five-year project for delivering of a complete technical design of the SPD facility based on the necessary simulation work, prototypes construction and test measurements.

The timeline is seen like follows:

- Approval of a formal JINR project for design of the SPD facility by the PAC for HEP in its meeting in January 2019;
- Setting up of the SPD collaboration and election of its management bodies (2019);
- Signing of MoU based on "Regulations for the organization of experiments conducted by international collaborations using the capabilities of the JINR basic facilities" [291] (2019);
- Preparation of Conceptual Design Report and its approval by the PAC for HEP at its meeting in January 2020;
- Preparation of Technical Design Report for the first stage of the facility, including prototyping and test measurements (2020 – 2022);
- Preparation of Technical Design Report for the second stage (2023);

We hope to be able to start construction of the first stage of the detector in 2022 and perform first measurements somewhere in 2025.

2596 **Chapter 16**

2597 **Conclusion**

# Bibliography

2598

- 2599 [1] A. Kotzinian, New quark distributions and semiinclusive electroproduction on the polarized nu-  
2600 cleons, Nucl. Phys. B 441 (1995) 234–248.
- 2601 [2] P. J. Mulders, R. D. Tangerman, The Complete tree level result up to order  $1/Q$  for po-  
2602 larized deep inelastic leptonproduction, Nucl. Phys. B461 (1996) 197–237, [Erratum: Nucl.  
2603 Phys.B484,538(1997)].
- 2604 [3] D. Boer, P. Mulders, Time reversal odd distribution functions in leptonproduction, Phys. Rev. D 57  
2605 (1998) 5780–5786.
- 2606 [4] K. Goeke, A. Metz, M. Schlegel, Parameterization of the quark-quark correlator of a spin-1/2  
2607 hadron, Phys. Lett. B 618 (2005) 90–96.
- 2608 [5] A. Bacchetta, M. Diehl, K. Goeke, A. Metz, P. J. Mulders, M. Schlegel, Semi-inclusive deep  
2609 inelastic scattering at small transverse momentum, JHEP 02 (2007) 093.
- 2610 [6] R. Angeles-Martinez, et al., Transverse Momentum Dependent (TMD) parton distribution func-  
2611 tions: status and prospects, Acta Phys. Polon. B 46 (12) (2015) 2501–2534.
- 2612 [7] S. Bastami, et al., Semi-Inclusive Deep Inelastic Scattering in Wandzura-Wilczek-type approxi-  
2613 mation, JHEP 06 (2019) 007.
- 2614 [8] S. Arnold, A. Metz, M. Schlegel, Dilepton production from polarized hadron hadron collisions,  
2615 Phys. Rev. D79 (2009) 034005.
- 2616 [9] S. Bastami, L. Gamberg, B. Parsamyan, B. Pasquini, A. Prokudin, P. Schweitzer, The Drell-Yan  
2617 process with pions and polarized nucleons .
- 2618 [10] A. Metz, A. Vossen, Parton Fragmentation Functions, Prog. Part. Nucl. Phys. 91 (2016) 136–202.
- 2619 [11] M. Anselmino, A. Mukherjee, A. Vossen, Transverse spin effects in hard semi-inclusive collisions  
2620 .
- 2621 [12] H. Avakian, B. Parsamyan, A. Prokudin, Spin orbit correlations and the structure of the nucleon,  
2622 Riv. Nuovo Cim. 42 (1) (2019) 1–48.
- 2623 [13] M. Grosse Perdekamp, F. Yuan, Transverse Spin Structure of the Nucleon, Ann. Rev. Nucl. Part.  
2624 Sci. 65 (2015) 429–456.
- 2625 [14] M. Boglione, A. Prokudin, Phenomenology of transverse spin: past, present and future, Eur. Phys.  
2626 J. A 52 (6) (2016) 154.
- 2627 [15] C. A. Aidala, S. D. Bass, D. Hasch, G. K. Mallot, The Spin Structure of the Nucleon, Rev. Mod.  
2628 Phys. 85 (2013) 655–691.

- 2629 [16] A. Adare, et al., Measurement of transverse-single-spin asymmetries for midrapidity and forward-  
2630 rapidity production of hadrons in polarized p+p collisions at  $\sqrt{s} = 200$  and 62.4 GeV, Phys. Rev.  
2631 D 90 (1) (2014) 012006.
- 2632 [17] A. Adare, et al., Measurement of Transverse Single-Spin Asymmetries for  $J/\psi$  Production in Po-  
2633 larized  $p + p$  Collisions at  $\sqrt{s} = 200$  GeV, Phys. Rev. D 82 (2010) 112008, [Erratum: Phys.Rev.D  
2634 86, 099904 (2012)].
- 2635 [18] C. Aidala, et al., Single-spin asymmetry of  $J/\psi$  production in  $p+p$ ,  $p+Al$ , and  $p+Au$  collisions  
2636 with transversely polarized proton beams at  $\sqrt{s_{NN}} = 200$  GeV, Phys. Rev. D 98 (1) (2018) 012006.
- 2637 [19] C. Aidala, et al., Cross section and transverse single-spin asymmetry of muons from open heavy-  
2638 flavor decays in polarized  $p+p$  collisions at  $\sqrt{s} = 200$  GeV, Phys. Rev. D 95 (11) (2017) 112001.
- 2639 [20] C. Adolph, et al., First measurement of the Sivers asymmetry for gluons using SIDIS data, Phys.  
2640 Lett. B 772 (2017) 854–864.
- 2641 [21] A. Szabelski, The gluon Sivers asymmetry measurements at COMPASS, PoS DIS2016 (2016)  
2642 219.
- 2643 [22] V. Barone, A. Drago, P. G. Ratcliffe, Transverse polarisation of quarks in hadrons, Phys. Rept.  
2644 359 (2002) 1–168.
- 2645 [23] C. Hadjidakis, et al., A Fixed-Target Programme at the LHC: Physics Case and Projected Perfor-  
2646 mances for Heavy-Ion, Hadron, Spin and Astroparticle Studies .
- 2647 [24] C. Aidala, et al., The LHCSpin Project (2020) 204–207.
- 2648 [25] A. Accardi, et al., Electron Ion Collider: The Next QCD Frontier: Understanding the glue that  
2649 binds us all, Eur. Phys. J. A 52 (9) (2016) 268.
- 2650 [26] E. R. Nocera, R. D. Ball, S. Forte, G. Ridolfi, J. Rojo, A first unbiased global determination of  
2651 polarized PDFs and their uncertainties, Nucl. Phys. B887 (2014) 276–308.
- 2652 [27] C. Brenner Mariotto, M. B. Gay Ducati, G. Ingelman, Soft and hard QCD dynamics in hadropro-  
2653 duction of charmonium, Eur. Phys. J. C23 (2002) 527–538.
- 2654 [28] <https://www.agsrhichome.bnl.gov/RHIC/Runs/>, Run overview of the relativistic heavy ion  
2655 collider .
- 2656 [29] I. N. Meshkov, Luminosity of an Ion Collider, Phys. Part. Nucl. 50 (6) (2019) 663–682.
- 2657 [30] I. Abt, et al., Production of the Charmonium States  $\chi_{c1}$  and  $\chi_{c2}$  in Proton Nucleus Interactions at  
2658  $\sqrt{s} = 41.6$ -GeV, Phys. Rev. D 79 (2009) 012001.
- 2659 [31] C.-Y. Wong, H. Wang, Effects of parton intrinsic transverse momentum on photon production in  
2660 hard scattering processes, Phys. Rev. C 58 (1998) 376–388.
- 2661 [32] W. Vogelsang, M. R. Whalley, A Compilation of data on single and double prompt photon pro-  
2662 duction in hadron hadron interactions, J. Phys. G23 (1997) A1–A69.
- 2663 [33] P. Aurenche, M. Fontannaz, J.-P. Guillet, E. Pilon, M. Werlen, A New critical study of photon  
2664 production in hadronic collisions, Phys. Rev. D73 (2006) 094007.
- 2665 [34] T. Binoth, J. Guillet, E. Pilon, M. Werlen, A Full next-to-leading order study of direct photon pair  
2666 production in hadronic collisions, Eur. Phys. J. C 16 (2000) 311–330.



- 2667 [35] L. Apanasevich, et al., Evidence for parton  $k_T$  effects in high  $p_T$  particle production, Phys. Rev.  
2668 Lett. 81 (1998) 2642–2645.
- 2669 [36] E. Anassontzis, et al., High  $p(t)$  Direct Photon Production in p p Collisions, Z. Phys. C 13 (1982)  
2670 277–289.
- 2671 [37] J. Badier, et al., Direct Photon Pair Production From Pions and Protons at 200-GeV/c, Phys. Lett.  
2672 B 164 (1985) 184–188.
- 2673 [38] H.-L. Lai, M. Guzzi, J. Huston, Z. Li, P. M. Nadolsky, J. Pumplin, C.-P. Yuan, New parton distri-  
2674 butions for collider physics, Phys. Rev. D 82 (2010) 074024.
- 2675 [39] S. J. Brodsky, K. Y.-J. Chiu, J.-P. Lansberg, N. Yamanaka, The gluon and charm content of the  
2676 deuteron, Phys. Lett. B 783 (2018) 287–293.
- 2677 [40] I. Abt, et al., Study of proton parton distribution functions at high  $x$  using ZEUS data .
- 2678 [41] A. M. Sirunyan, et al., Measurement of double-differential cross sections for top quark pair pro-  
2679 duction in pp collisions at  $\sqrt{s} = 8$  TeV and impact on parton distribution functions, Eur. Phys. J.  
2680 C 77 (7) (2017) 459.
- 2681 [42] H. Abdolmaleki, A. Khorramian, Parton distribution functions and constraints on the intrinsic  
2682 charm content of the proton using the Brodsky-Hoyer-Peterson-Saka approach, Phys. Rev. D  
2683 99 (11) (2019) 116019.
- 2684 [43] C. Lourenco, H. Wohri, Heavy flavour hadro-production from fixed-target to collider energies,  
2685 Phys. Rept. 433 (2006) 127–180.
- 2686 [44] A. Accardi, et al., A Critical Appraisal and Evaluation of Modern PDFs, Eur. Phys. J. C 76 (8)  
2687 (2016) 471.
- 2688 [45] G. Alves, et al., Forward cross-sections for production of  $D^+$ ,  $D^0$ ,  $D(s)$ ,  $D^{*+}$  and  $\Lambda_c$  in 250-  
2689 GeV  $\pi^\pm$ ,  $K^\pm$ , and p - nucleon interactions, Phys. Rev. Lett. 77 (1996) 2388–2391, [Erratum:  
2690 Phys.Rev.Lett. 81, 1537 (1998)].
- 2691 [46] G. F. Sterman, Summation of Large Corrections to Short Distance Hadronic Cross-Sections, Nucl.  
2692 Phys. B 281 (1987) 310–364.
- 2693 [47] S. Catani, L. Trentadue, Resummation of the QCD Perturbative Series for Hard Processes, Nucl.  
2694 Phys. B 327 (1989) 323–352.
- 2695 [48] H. Contopanagos, E. Laenen, G. F. Sterman, Sudakov factorization and resummation, Nucl. Phys.  
2696 B 484 (1997) 303–330.
- 2697 [49] N. Kidonakis, G. Oderda, G. F. Sterman, Evolution of color exchange in QCD hard scattering,  
2698 Nucl. Phys. B 531 (1998) 365–402.
- 2699 [50] N. Ivanov, Perturbative stability of the QCD predictions for single spin asymmetry in heavy quark  
2700 photoproduction, Nucl. Phys. B 615 (2001) 266–284.
- 2701 [51] S. Catani, M. L. Mangano, P. Nason, L. Trentadue, The Resummation of soft gluons in hadronic  
2702 collisions, Nucl. Phys. B 478 (1996) 273–310.
- 2703 [52] E. L. Berger, H. Contopanagos, The Perturbative resummed series for top quark production in  
2704 hadron reactions, Phys. Rev. D 54 (1996) 3085–3113.

- 2705 [53] N. Kidonakis, High order corrections and subleading logarithms for top quark production, Phys.  
2706 Rev. D 64 (2001) 014009.
- 2707 [54] S. Forte, G. Ridolfi, J. Rojo, M. Ubiali, Borel resummation of soft gluon radiation and higher  
2708 twists, Phys. Lett. B 635 (2006) 313–319.
- 2709 [55] S. Brodsky, P. Hoyer, C. Peterson, N. Sakai, The Intrinsic Charm of the Proton, Phys. Lett. B 93  
2710 (1980) 451–455.
- 2711 [56] S. J. Brodsky, C. Peterson, N. Sakai, Intrinsic Heavy Quark States, Phys. Rev. D 23 (1981) 2745.
- 2712 [57] L. Ananikyan, N. Ivanov, Azimuthal Asymmetries in DIS as a Probe of Intrinsic Charm Content  
2713 of the Proton, Nucl. Phys. B 762 (2007) 256–283.
- 2714 [58] J. Collins, Foundations of perturbative QCD, Vol. 32, Cambridge University Press, 2013.
- 2715 [59] M. G. Echevarria, T. Kasemets, P. J. Mulders, C. Pisano, QCD evolution of (un)polarized gluon  
2716 TMDPDFs and the Higgs  $q_T$ -distribution, JHEP 07 (2015) 158, [Erratum: JHEP 05, 073 (2017)].
- 2717 [60] M. G. Echevarria, Proper TMD factorization for quarkonia production:  $pp \rightarrow \eta_{c,b}$  as a study case,  
2718 JHEP 10 (2019) 144.
- 2719 [61] S. Fleming, Y. Makris, T. Mehen, An effective field theory approach to quarkonium at small  
2720 transverse momentum, JHEP 04 (2020) 122.
- 2721 [62] P. Mulders, J. Rodrigues, Transverse momentum dependence in gluon distribution and fragmen-  
2722 tation functions, Phys. Rev. D 63 (2001) 094021.
- 2723 [63] D. Boer, S. J. Brodsky, P. J. Mulders, C. Pisano, Direct Probes of Linearly Polarized Gluons inside  
2724 Unpolarized Hadrons, Phys. Rev. Lett. 106 (2011) 132001.
- 2725 [64] C. Pisano, D. Boer, S. J. Brodsky, M. G. Buffing, P. J. Mulders, Linear polarization of gluons and  
2726 photons in unpolarized collider experiments, JHEP 10 (2013) 024.
- 2727 [65] A. Efremov, N. Ivanov, O. Teryaev, QCD predictions for the azimuthal asymmetry in charm lep-  
2728 toproduction for the COMPASS kinematics, Phys. Lett. B 772 (2017) 283–289.
- 2729 [66] N. Y. Ivanov, A. Efremov, O. Teryaev, How to measure the linear polarization of gluons in unpo-  
2730 larized proton using the heavy-quark pair production, EPJ Web Conf. 204 (2019) 02006.
- 2731 [67] A. Efremov, N. Y. Ivanov, O. Teryaev, The ratio  $R = d\sigma_L/d\sigma_T$  in heavy-quark pair leptonproduction  
2732 as a probe of linearly polarized gluons in unpolarized proton, Phys. Lett. B 780 (2018) 303–307.
- 2733 [68] D. Boer, C. Pisano, Polarized gluon studies with charmonium and bottomonium at LHCb and  
2734 AFTER, Phys. Rev. D 86 (2012) 094007.
- 2735 [69] J.-W. Qiu, M. Schlegel, W. Vogelsang, Probing Gluonic Spin-Orbit Correlations in Photon Pair  
2736 Production, Phys. Rev. Lett. 107 (2011) 062001.
- 2737 [70] J.-P. Lansberg, C. Pisano, F. Scarpa, M. Schlegel, Pinning down the linearly-polarised gluons  
2738 inside unpolarised protons using quarkonium-pair production at the LHC, Phys. Lett. B 784 (2018)  
2739 217–222, [Erratum: Phys.Lett.B 791, 420–421 (2019)].
- 2740 [71] G. T. Bodwin, E. Braaten, G. Lepage, Rigorous QCD analysis of inclusive annihilation and pro-  
2741 duction of heavy quarkonium, Phys. Rev. D 51 (1995) 1125–1171, [Erratum: Phys.Rev.D 55,  
2742 5853 (1997)].

- 2743 [72] V. D. Barger, W.-Y. Keung, R. Phillips, On psi and Upsilon Production via Gluons, Phys. Lett. B  
2744 91 (1980) 253–258.
- 2745 [73] V. D. Barger, W.-Y. Keung, R. Phillips, Hadroproduction of  $\psi$  and  $\Upsilon$ , Z. Phys. C 6 (1980) 169.
- 2746 [74] R. Gai, D. Kharzeev, H. Satz, G. Schuler, K. Sridhar, R. Vogt, Quarkonium production in  
2747 hadronic collisions, Int. J. Mod. Phys. A 10 (1995) 3043–3070.
- 2748 [75] Y.-Q. Ma, R. Vogt, Quarkonium Production in an Improved Color Evaporation Model, Phys. Rev.  
2749 D 94 (11) (2016) 114029.
- 2750 [76] N. Brambilla, et al., Heavy Quarkonium: Progress, Puzzles, and Opportunities, Eur. Phys. J. C 71  
2751 (2011) 1534.
- 2752 [77] J.-P. Lansberg, New Observables in Inclusive Production of Quarkonia .
- 2753 [78] M. Butenschoen, B. A. Kniehl,  $J/\psi$  polarization at Tevatron and LHC: Nonrelativistic-QCD fac-  
2754 torization at the crossroads, Phys. Rev. Lett. 108 (2012) 172002.
- 2755 [79] M. Butenschoen, B. A. Kniehl, Next-to-leading-order tests of NRQCD factorization with  $J/\psi$   
2756 yield and polarization, Mod. Phys. Lett. A 28 (2013) 1350027.
- 2757 [80] M. Butenschoen, Z.-G. He, B. A. Kniehl,  $\eta_c$  production at the LHC challenges nonrelativistic-  
2758 QCD factorization, Phys. Rev. Lett. 114 (9) (2015) 092004.
- 2759 [81] L.-P. Sun, H. Han, K.-T. Chao, Impact of  $J/\psi$  pair production at the LHC and predictions in  
2760 nonrelativistic QCD, Phys. Rev. D 94 (7) (2016) 074033.
- 2761 [82] Z.-G. He, B. A. Kniehl, M. A. Nefedov, V. A. Saleev, Double Prompt  $J/\psi$  Hadroproduction in the  
2762 Parton Reggeization Approach with High-Energy Resummation, Phys. Rev. Lett. 123 (16) (2019)  
2763 162002.
- 2764 [83] J.-P. Lansberg, H.-S. Shao, N. Yamanaka, Y.-J. Zhang, C. Noûs, Complete NLO QCD study of  
2765 single- and double-quarkonium hadroproduction in the colour-evaporation model at the Tevatron  
2766 and the LHC .
- 2767 [84] Z.-B. Kang, J.-W. Qiu, G. Sterman, Heavy quarkonium production and polarization, Phys. Rev.  
2768 Lett. 108 (2012) 102002.
- 2769 [85] Y.-Q. Ma, K.-T. Chao, New factorization theory for heavy quarkonium production and decay,  
2770 Phys. Rev. D 100 (9) (2019) 094007.
- 2771 [86] R. Li, Y. Feng, Y.-Q. Ma, Exclusive quarkonium production or decay in soft gluon factorization,  
2772 JHEP 05 (2020) 009.
- 2773 [87] A.-P. Chen, Y.-Q. Ma, Theory for quarkonium: from NRQCD factorization to soft gluon factor-  
2774 ization .
- 2775 [88] M. Butenschoen, B. A. Kniehl, Reconciling  $J/\psi$  production at HERA, RHIC, Tevatron, and LHC  
2776 with NRQCD factorization at next-to-leading order, Phys. Rev. Lett. 106 (2011) 022003.
- 2777 [89] M. Butenschoen, B. A. Kniehl, World data of  $J/\psi$  production consolidate NRQCD factorization  
2778 at NLO, Phys. Rev. D 84 (2011) 051501.

- 2779 [90] A. V. Karpishkov, M. A. Nefedov, V. A. Saleev,  $B\bar{B}$  angular correlations at the LHC in parton  
2780 Reggeization approach merged with higher-order matrix elements, Phys. Rev. D 96 (9) (2017)  
2781 096019.
- 2782 [91] V. Saleev, M. Nefedov, A. Shipilova, Prompt  $J/\psi$  production in the Regge limit of QCD: From  
2783 Tevatron to LHC, Phys. Rev. D 85 (2012) 074013.
- 2784 [92] A. Karpishkov, M. Nefedov, V. Saleev, Spectra and polarizations of prompt  $J/\psi$  at the NICA  
2785 within collinear parton model and parton Reggeization approach, J. Phys. Conf. Ser. 1435 (1)  
2786 (2020) 012015.
- 2787 [93] V. Cheung, R. Vogt, Production and polarization of prompt  $J/\psi$  in the improved color evaporation  
2788 model using the  $k_T$ -factorization approach, Phys. Rev. D 98 (11) (2018) 114029.
- 2789 [94] A. Airapetian, et al., First measurement of the tensor structure function  $b(1)$  of the deuteron, Phys.  
2790 Rev. Lett. 95 (2005) 242001.
- 2791 [95] M. Harvey, On the Fractional Parentage Expansions of Color Singlet Six Quark States in a Cluster  
2792 Model, Nucl. Phys. A 352 (1981) 301, [Erratum: Nucl.Phys.A 481, 834 (1988)].
- 2793 [96] G. A. Miller, Pionic and Hidden-Color, Six-Quark Contributions to the Deuteron  $b_1$  Structure  
2794 Function, Phys. Rev. C 89 (4) (2014) 045203.
- 2795 [97] P. Hoyer, D. Roy, The Intrinsic gluon component of the nucleon, Phys. Lett. B 410 (1997) 63–66.
- 2796 [98] H. Mäntysaari, B. Schenke, Accessing the gluonic structure of light nuclei at a future electron-ion  
2797 collider, Phys. Rev. C 101 (1) (2020) 015203.
- 2798 [99] F. Winter, W. Detmold, A. S. Gambhir, K. Orginos, M. J. Savage, P. E. Shanahan, M. L. Wagman,  
2799 First lattice QCD study of the gluonic structure of light nuclei, Phys. Rev. D 96 (9) (2017) 094512.
- 2800 [100] J. Ashman, et al., An Investigation of the Spin Structure of the Proton in Deep Inelastic Scattering  
2801 of Polarized Muons on Polarized Protons, Nucl. Phys. B 328 (1989) 1.
- 2802 [101] D. L. Adams, et al., Measurement of the double spin asymmetry  $A_{LL}$  for inclusive multi gamma  
2803 pair production with 200-GeV/c polarized proton beam and polarized proton target, Phys. Lett.  
2804 B336 (1994) 269–274.
- 2805 [102] A. Airapetian, et al., Leading-Order Determination of the Gluon Polarization from high-p(T)  
2806 Hadron Electroproduction, JHEP 08 (2010) 130.
- 2807 [103] B. Adeva, et al., Spin asymmetries for events with high p(T) hadrons in DIS and an evaluation of  
2808 the gluon polarization, Phys. Rev. D70 (2004) 012002.
- 2809 [104] E. S. Ageev, et al., Gluon polarization in the nucleon from quasi-real photoproduction of high-p(T)  
2810 hadron pairs, Phys. Lett. B633 (2006) 25–32.
- 2811 [105] M. Alekseev, et al., Gluon polarisation in the nucleon and longitudinal double spin asymmetries  
2812 from open charm muoproduction, Phys. Lett. B676 (2009) 31–38.
- 2813 [106] C. Adolph, et al., Leading order determination of the gluon polarisation from DIS events with  
2814 high- $p_T$  hadron pairs, Phys. Lett. B718 (2013) 922–930.
- 2815 [107] C. Adolph, et al., Leading and Next-to-Leading Order Gluon Polarization in the Nucleon and  
2816 Longitudinal Double Spin Asymmetries from Open Charm Muoproduction, Phys. Rev. D87 (5)  
2817 (2013) 052018.

- 2818 [108] C. Adolph, et al., Leading-order determination of the gluon polarisation from semi-inclusive deep  
2819 inelastic scattering data, *Eur. Phys. J. C* 77 (4) (2017) 209.
- 2820 [109] A. Adare, et al., Inclusive double-helicity asymmetries in neutral-pion and eta-meson production  
2821 in  $\vec{p} + \vec{p}$  collisions at  $\sqrt{s} = 200$  GeV, *Phys. Rev. D* 90 (1) (2014) 012007.
- 2822 [110] A. Adare, et al., The Polarized gluon contribution to the proton spin from the double helicity  
2823 asymmetry in inclusive  $\pi^0$  production in polarized  $p + p$  collisions at  $\sqrt{s} = 200$ -GeV, *Phys. Rev.*  
2824 *Lett.* 103 (2009) 012003.
- 2825 [111] A. Adare, et al., Inclusive cross section and double helicity asymmetry for  $\pi^0$  production in  $p^+p$   
2826 collisions at  $\sqrt{s} = 62.4$  GeV, *Phys. Rev. D* 79 (2009) 012003.
- 2827 [112] P. Djawotho, Gluon polarization and jet production at STAR, *Nuovo Cim.* C036 (05) (2013) 35–  
2828 38.
- 2829 [113] A. Adare, et al., Double Spin Asymmetry of Electrons from Heavy Flavor Decays in  $p + p$  Colli-  
2830 sions at  $\sqrt{s} = 200$  GeV, *Phys. Rev. D* 87 (1) (2013) 012011.
- 2831 [114] A. Adare, et al., Measurements of double-helicity asymmetries in inclusive  $J/\psi$  production in  
2832 longitudinally polarized  $p + p$  collisions at  $\sqrt{s} = 510$  GeV, *Phys. Rev. D* 94 (11) (2016) 112008.
- 2833 [115] E. Leader, A. V. Sidorov, D. B. Stamenov, New analysis concerning the strange quark polarization  
2834 puzzle, *Phys. Rev. D* 91 (5) (2015) 054017.
- 2835 [116] D. de Florian, R. Sassot, M. Stratmann, W. Vogelsang, Evidence for polarization of gluons in the  
2836 proton, *Phys. Rev. Lett.* 113 (1) (2014) 012001.
- 2837 [117] D. De Florian, G. A. Lucero, R. Sassot, M. Stratmann, W. Vogelsang, Monte Carlo sampling  
2838 variant of the DSSV14 set of helicity parton densities, *Phys. Rev. D* 100 (11) (2019) 114027.
- 2839 [118] J. J. Ethier, N. Sato, W. Melnitchouk, First simultaneous extraction of spin-dependent parton dis-  
2840 tributions and fragmentation functions from a global QCD analysis, *Phys. Rev. Lett.* 119 (13)  
2841 (2017) 132001.
- 2842 [119] J. J. Ethier, E. R. Nocera, Parton Distributions in Nucleons and Nuclei, *Ann. Rev. Nucl. Part. Sci.*  
2843 (70) (2020) 1–34.
- 2844 [120] D. de Florian, R. Sassot, M. Stratmann, W. Vogelsang, Global Analysis of Helicity Parton Densi-  
2845 ties and Their Uncertainties, *Phys. Rev. Lett.* 101 (2008) 072001.
- 2846 [121] C. AIDALA, G. BUNCE, E. AL., Research plan for spin physics at rhic. .
- 2847 [122] M. Anselmino, E. Andreeva, V. Korotkov, F. Murgia, W. D. Nowak, S. Nurushev, O. Teryaev,  
2848 A. Tkabladze, On the physics potential of polarized nucleon-nucleon collisions at HERA, in:  
2849 Future physics at HERA. Proceedings, Workshop, Hamburg, Germany, September 25, 1995-May  
2850 31, 1996. Vol. 1, 2, 1996.
- 2851 [123] E. Leader, Spin in particle physics, Cambridge University Press (2011).
- 2852 [124] Y. Feng, H.-F. Zhang, Double longitudinal-spin asymmetries in  $J/\psi$  production at RHIC, *JHEP*  
2853 11 (2018) 136.
- 2854 [125] W. Vogelsang, Prompt photon production in polarized hadron collisions, in: Deep inelastic scat-  
2855 tering. Proceedings, 8th International Workshop, DIS 2000, Liverpool, UK, April 25-30, 2000,  
2856 2000, pp. 253–254.

- 2857 [126] L. E. Gordon, W. Vogelsang, Inclusive prompt photon production in polarized p p collisions at  
2858 HERA-N(polarized), Phys. Lett. B387 (1996) 629–636.
- 2859 [127] L. E. Gordon, Constraints on Delta G from prompt photon plus jet production at HERA-N (polar-  
2860 ized), Phys. Lett. B406 (1997) 184–192.
- 2861 [128] Q.-h. Xu, Z.-t. Liang, Probing gluon helicity distribution and quark transversity through hyperon  
2862 polarization in singly polarized pp collisions, Phys. Rev. D70 (2004) 034015.
- 2863 [129] A. Efremov, O. Teryaev, On Spin Effects in Quantum Chromodynamics, Sov. J. Nucl. Phys. 36  
2864 (1982) 140.
- 2865 [130] A. Efremov, O. Teryaev, QCD Asymmetry and Polarized Hadron Structure Functions, Phys. Lett.  
2866 B 150 (1985) 383.
- 2867 [131] J.-w. Qiu, G. F. Sterman, Single transverse spin asymmetries, Phys. Rev. Lett. 67 (1991) 2264–  
2868 2267.
- 2869 [132] A. Efremov, V. Korotkiian, O. Teryaev, The twist - three single spin asymmetries of pion produc-  
2870 tion, Phys. Lett. B 348 (1995) 577–581.
- 2871 [133] D. W. Sivers, Single Spin Production Asymmetries from the Hard Scattering of Point-Like Con-  
2872 stituents, Phys. Rev. D 41 (1990) 83.
- 2873 [134] D. Boer, C. Lorcé, C. Pisano, J. Zhou, The gluon Sivers distribution: status and future prospects,  
2874 Adv. High Energy Phys. 2015 (2015) 371396.
- 2875 [135] U. D’Alesio, F. Murgia, C. Pisano, Towards a first estimate of the gluon Sivers function from  $A_N$   
2876 data in pp collisions at RHIC, JHEP 09 (2015) 119.
- 2877 [136] M. Anselmino, M. Boglione, U. D’Alesio, A. Kotzinian, F. Murgia, A. Prokudin, Extracting  
2878 the Sivers function from polarized SIDIS data and making predictions, Phys. Rev. D 72 (2005)  
2879 094007, [Erratum: Phys.Rev.D 72, 099903 (2005)].
- 2880 [137] M. Anselmino, M. Boglione, U. D’Alesio, A. Kotzinian, S. Melis, F. Murgia, A. Prokudin,  
2881 C. Turk, Sivers Effect for Pion and Kaon Production in Semi-Inclusive Deep Inelastic Scatter-  
2882 ing, Eur. Phys. J. A 39 (2009) 89–100.
- 2883 [138] S. Kretzer, Fragmentation functions from flavor inclusive and flavor tagged  $e^+ e^-$  annihilations,  
2884 Phys. Rev. D 62 (2000) 054001.
- 2885 [139] D. de Florian, R. Sassot, M. Stratmann, Global analysis of fragmentation functions for pions and  
2886 kaons and their uncertainties, Phys. Rev. D 75 (2007) 114010.
- 2887 [140] R. M. Godbole, A. Kaushik, A. Misra, V. Rawoot, B. Sonawane, Transverse single spin asymmetry  
2888 in  $p + p^\uparrow \rightarrow J/\psi + X$ , Phys. Rev. D 96 (9) (2017) 096025.
- 2889 [141] M. Anselmino, M. Boglione, U. D’Alesio, E. Leader, F. Murgia, Accessing Sivers gluon distribu-  
2890 tion via transverse single spin asymmetries in p(transv. polarized) p  $\rightarrow$   $\bar{c}$  D X processes at RHIC,  
2891 Phys. Rev. D 70 (2004) 074025.
- 2892 [142] Y. Koike, S. Yoshida, Probing the three-gluon correlation functions by the single spin asymmetry  
2893 in  $p^\uparrow p \rightarrow DX$ , Phys. Rev. D 84 (2011) 014026.
- 2894 [143] Z.-B. Kang, J.-W. Qiu, W. Vogelsang, F. Yuan, Accessing tri-gluon correlations in the nucleon via  
2895 the single spin asymmetry in open charm production, Phys. Rev. D78 (2008) 114013.

- 2896 [144] R. M. Godbole, A. Kaushik, A. Misra, Transverse single spin asymmetry in  $p + p^\uparrow \rightarrow D^+ X$ , Phys. Rev. D94 (11) (2016) 114022.  
2897
- 2898 [145] N. Hammon, B. Ehrnsperger, A. Schaefer, Single-transverse spin asymmetry in prompt photon production, J. Phys. G24 (1998) 991–1001.  
2899
- 2900 [146] K. Kanazawa, Y. Koike, Single transverse-spin asymmetry for direct-photon and single-jet productions at RHIC, Phys. Lett. B720 (2013) 161–165.  
2901
- 2902 [147] D. Boer, W. Vogelsang, Asymmetric jet correlations in p p uparrow scattering, Phys. Rev. D69 (2004) 094025.  
2903
- 2904 [148] U. D’Alesio, F. Murgia, C. Pisano, P. Taelis, Probing the gluon Sivers function in  $p^\uparrow p \rightarrow J/\psi X$  and  $p^\uparrow p \rightarrow DX$ , Phys. Rev. D 96 (3) (2017) 036011.  
2905
- 2906 [149] U. D’Alesio, F. Murgia, C. Pisano, S. Rajesh, Single-spin asymmetries in  $p^\uparrow p \rightarrow J/\psi + X$  within a TMD approach: role of the color octet mechanism, Eur. Phys. J. C 79 (12) (2019) 1029.  
2907
- 2908 [150] D. L. Adams, et al., Measurement of single spin asymmetry for direct photon production in p p collisions at 200-GeV/c, Phys. Lett. B345 (1995) 569–575.  
2909
- 2910 [151] S. Kumano, Q.-T. Song, Gluon transversity in polarized proton-deuteron Drell-Yan process, Phys. Rev. D 101 (5) (2020) 054011.  
2911
- 2912 [152] J. Soffer, M. Stratmann, W. Vogelsang, Accessing transversity in double-spin asymmetries at the BNL-RHIC, Phys. Rev. D 65 (2002) 114024.  
2913
- 2914 [153] A. Mukherjee, M. Stratmann, W. Vogelsang, Next-to-leading order QCD corrections to A(TT) for prompt photon production, Phys. Rev. D 67 (2003) 114006.  
2915
- 2916 [154] R. Jaffe, A. Manohar, NUCLEAR GLUONOMETRY, Phys. Lett. B 223 (1989) 218–224.  
2917
- 2918 [155] O. Teryaev, Shear forces and tensor polarization, PoS DIS2019 (2019) 240.  
2919
- 2918 [156] P. Hoodbhoy, R. Jaffe, A. Manohar, Novel Effects in Deep Inelastic Scattering from Spin 1 Hadrons, Nucl. Phys. B 312 (1989) 571–588.  
2919
- 2920 [157] F. Close, S. Kumano, A sum rule for the spin dependent structure function  $b_1(x)$  for spin one hadrons, Phys. Rev. D 42 (1990) 2377–2379.  
2921
- 2922 [158] A. Efremov, O. Teryaev, ON HIGH P(T) VECTOR MESONS SPIN ALIGNMENT, Sov. J. Nucl. Phys. 36 (1982) 557.  
2923
- 2924 [159] A. Efremov, O. Teryaev, On the oscillations of the tensor spin structure function, in: International Symposium: Dubna Deuteron 93, 1994.  
2925
- 2926 [160] O. Teryaev, Nucleon spin and orbital structure: 20 years later, Mod. Phys. Lett. A 24 (2009) 2831–2837.  
2927
- 2928 [161] O. Teryaev, Spin structure of nucleon and equivalence principle .  
2928
- 2929 [162] O. Teryaev, Sources of time reversal odd spin asymmetries in QCD, Czech. J. Phys. 53 (2003) 47–58A.  
2930
- 2931 [163] O. Teryaev, Equivalence principle and partition of angular momenta in the nucleon, AIP Conf. Proc. 915 (1) (2007) 260–263.  
2932

- 2933 [164] O. Teryaev, Gravitational form factors and nucleon spin structure, *Front. Phys. (Beijing)* 11 (5)  
2934 (2016) 111207.
- 2935 [165] G. Y. Prokhorov, O. V. Teryaev, V. I. Zakharov, Unruh effect for fermions from the Zubarev density  
2936 operator, *Phys. Rev. D* 99 (7) (2019) 071901.
- 2937 [166] M. V. Polyakov, H.-D. Son, Nucleon gravitational form factors from instantons: forces between  
2938 quark and gluon subsystems, *JHEP* 09 (2018) 156.
- 2939 [167] S. Kumano, Q.-T. Song, Spin asymmetry for proton-deuteron Drell-Yan process with tensor-  
2940 polarized deuteron, in: 22nd International Symposium on Spin Physics, 2017.
- 2941 [168] M. Aghasyan, et al., First measurement of transverse-spin-dependent azimuthal asymmetries in  
2942 the Drell-Yan process, *Phys. Rev. Lett.* 119 (11) (2017) 112002.
- 2943 [169] B. Parsamyan, Transversely polarized Drell-Yan measurements at COMPASS, *PoS DIS2019*  
2944 (2019) 195.
- 2945 [170] C. Brown, et al., Letter of Intent for a Drell-Yan Experiment with a Polarized Proton Target .
- 2946 [171] A. Chen, et al., Probing nucleon spin structures with polarized Drell-Yan in the Fermilab Spin-  
2947 Quest experiment, *PoS SPIN2018* (2019) 164.
- 2948 [172] J. C. Collins, A. V. Efremov, K. Goeke, S. Menzel, A. Metz, P. Schweitzer, Sivers effect in semi-  
2949 inclusive deeply inelastic scattering, *Phys. Rev. D* 73 (2006) 014021.
- 2950 [173] S. V. Goloskokov, P. Kroll, The Longitudinal cross-section of vector meson electroproduction,  
2951 *Eur. Phys. J. C* 50 (2007) 829–842.
- 2952 [174] S. V. Goloskokov, P. Kroll, The Role of the quark and gluon GPDs in hard vector-meson electro-  
2953 production, *Eur. Phys. J. C* 53 (2008) 367–384.
- 2954 [175] Y. Hagiwara, Y. Hatta, R. Pasechnik, M. Tasevsky, O. Teryaev, Accessing the gluon Wigner dis-  
2955 tribution in ultraperipheral  $pA$  collisions, *Phys. Rev. D* 96 (3) (2017) 034009.
- 2956 [176] O. V. Teryaev, Analytic properties of hard exclusive amplitudes, in: 11th International Conference  
2957 on Elastic and Diffractive Scattering: Towards High Energy Frontiers: The 20th Anniversary of  
2958 the Blois Workshops, 17th Rencontre de Blois (EDS 05) Chateau de Blois, Blois, France, May  
2959 15-20, 2005, 2005.
- 2960 [177] S. V. Goloskokov, P. Kroll, O. V. Teryaev, in progress .
- 2961 [178] E. V. Shuryak, Two Scales and Phase Transitions in Quantum Chromodynamics, *Phys. Lett. B* 107  
2962 (1981) 103–105.
- 2963 [179] A. Manohar, H. Georgi, Chiral Quarks and the Nonrelativistic Quark Model, *Nucl. Phys. B* 234  
2964 (1984) 189–212.
- 2965 [180] V. Komarov, On the possibility of revealing the transition of a baryon pair state to a six-quark  
2966 confinement state, *Phys. Part. Nucl. Lett.* 15 (1) (2018) 69–75.
- 2967 [181] V. Komarov, B. Baimurzinova, A. Kunsafina, D. Tsirkov, Centrality criteria of inelastic nucleon-  
2968 nucleon collisions .
- 2969 [182] A. Faessler, V. Kukulin, M. Shikhalev, Description of intermediate- and short-range NN nuclear  
2970 force within a covariant effective field theory, *Annals Phys.* 320 (2005) 71–107.



- 2971 [183] T. Hatsuda, T. Kunihiro, POSSIBLE CRITICAL PHENOMENA ASSOCIATED WITH THE  
2972 CHIRAL SYMMETRY BREAKING, *Phys. Lett. B* 145 (1984) 7–10.
- 2973 [184] D. Blaschke, Y. Kalinovsky, A. Radzhabov, M. Volkov, Scalar sigma meson at a finite temperature  
2974 in a nonlocal quark model, *Phys. Part. Nucl. Lett.* 3 (2006) 327–330.
- 2975 [185] L. Frankfurt, E. Piasetsky, M. Sargsian, M. Strikman, Probing short range nucleon correlations in  
2976 high-energy hard quasielastic p d reactions, *Phys. Rev. C* 51 (1995) 890–900.
- 2977 [186] L. Frankfurt, E. Piasetzky, M. Sargsian, M. Strikman, On the possibility to study color trans-  
2978 parency in the large momentum transfer exclusive d (p, 2 p) n reaction, *Phys. Rev. C* 56 (1997)  
2979 2752–2766.
- 2980 [187] L. Frankfurt, M. Sargsian, M. Strikman, Feynman graphs and Gribov-Glauber approach to high-  
2981 energy knockout processes, *Phys. Rev. C* 56 (1997) 1124–1137.
- 2982 [188] A. Mueller, Proceedings of 17th rencontre de Moriond, Moriond, 1982 Van (Editions Frontieres,  
2983 Gif-sur-Yvette, France, 1982) Vol. I p.13.
- 2984 [189] S. Brodsky, Proceedings. of the 13th Int. Symposium on Multiparticle Dynamics, W. Kittel, W.  
2985 Metzger and A. Stergiou (eds.) Singapore 1982,) p.963.
- 2986 [190] G. Farrar, H. Liu, L. Frankfurt, M. Strikman, Transparency in Nuclear Quasiexclusive Processes  
2987 with Large Momentum Transfer, *Phys. Rev. Lett.* 61 (1988) 686–689.
- 2988 [191] L. Frankfurt, M. Strikman, Hard Nuclear Processes and Microscopic Nuclear Structure, *Phys.*  
2989 *Rept.* 160 (1988) 235–427.
- 2990 [192] C. G. Granados, M. M. Sargsian, Quark Structure of the Nucleon and Angular Asymmetry of  
2991 Proton-Neutron Hard Elastic Scattering, *Phys. Rev. Lett.* 103 (2009) 212001.
- 2992 [193] D. G. Crabb, et al., Spin Dependence of High p-Transverse\*\*2 Elastic p p Scattering, *Phys. Rev.*  
2993 *Lett.* 41 (1978) 1257.
- 2994 [194] L. Frankfurt, T. Lee, G. Miller, M. Strikman, Chiral transparency, *Phys. Rev. C* 55 (1997) 909–  
2995 916.
- 2996 [195] L. Frankfurt, M. Sargsian, M. Strikman, Recent observation of short range nucleon correlations in  
2997 nuclei and their implications for the structure of nuclei and neutron stars, *Int. J. Mod. Phys. A* 23  
2998 (2008) 2991–3055.
- 2999 [196] O. Hen, G. Miller, E. Piasetzky, L. Weinstein, Nucleon-Nucleon Correlations, Short-lived Excita-  
3000 tions, and the Quarks Within, *Rev. Mod. Phys.* 89 (4) (2017) 045002.
- 3001 [197] R. Arndt, W. Briscoe, I. Strakovsky, R. Workman, Updated analysis of NN elastic scattering to  
3002 3-GeV, *Phys. Rev. C* 76 (2007) 025209.
- 3003 [198] M. Sawamoto, S. Wakaizumi, ANALYSIS OF ELASTIC P P SCATTERING AT 6-GEV/C WITH  
3004 SPIN ORBIT AND SPIN SPIN COUPLING EIKONALS, *Prog. Theor. Phys.* 62 (1979) 563–565.
- 3005 [199] A. Sibirtsev, J. Haidenbauer, H.-W. Hammer, S. Krewald, U.-G. Meissner, Proton-proton scatter-  
3006 ing above 3 GeV/c, *Eur. Phys. J. A* 45 (2010) 357–372.
- 3007 [200] W. P. Ford, J. Van Orden, Regge model for nucleon-nucleon spin-dependent amplitudes, *Phys.*  
3008 *Rev. C* 87 (1) (2013) 014004.

- 3009 [201] M. Platonova, V. Kukulín, Refined Glauber model versus Faddeev calculations and experimental  
3010 data for  $pd$  spin observables, *Phys. Rev. C* 81 (2010) 014004, [Erratum: *Phys.Rev.C* 94, 069902  
3011 (2016)].
- 3012 [202] A. Temerbayev, Y. Uzikov, Spin observables in proton-deuteron scattering and T-invariance test,  
3013 *Phys. Atom. Nucl.* 78 (1) (2015) 35–42.
- 3014 [203] M. N. Platonova, V. I. Kukulín, Theoretical study of spin observables in  $pd$  elastic scattering at  
3015 energies  $T_p = 800$ -1000 MeV, *Eur. Phys. J. A* 56 (5) (2020) 132.
- 3016 [204] Y. Uzikov, J. Haidenbauer, A. Bazarova, A. Temerbayev, Spin observables of proton-deuteron  
3017 elastic scattering at SPD NICA energies within the Glauber model and pN amplitudes, Talk at  
3018 NUCLEUS-2020, (11-17 October, 2020; S-Petersburg, Russia).
- 3019 [205] V. Abramov, Phenomenology of single-spin effects in hadron production at high energies, *Phys.*  
3020 *Atom. Nucl.* 72 (2009) 1872–1888.
- 3021 [206] V. Matveev, R. Muradian, A. Tavkhelidze, Automodellism in the large - angle elastic scattering  
3022 and structure of hadrons, *Lett. Nuovo Cim.* 7 (1973) 719–723.
- 3023 [207] S. J. Brodsky, G. R. Farrar, Scaling Laws at Large Transverse Momentum, *Phys. Rev. Lett.* 31  
3024 (1973) 1153–1156.
- 3025 [208] G. Bizard, et al., EXPERIMENTAL STUDY AND BARYONIC EXCHANGE INTERPRETA-  
3026 TION OF THE REACTION H-2 (D, N) HE-3 IN THE INTERMEDIATE-ENERGY REGION,  
3027 *Phys. Rev. C* 22 (1980) 1632–1637.
- 3028 [209] Y. Uzikov, Indication of asymptotic scaling in the reactions  $dd \rightarrow p$  3-H,  $dd \rightarrow n$  3-He and  $pd$   
3029  $\rightarrow pd$ , *JETP Lett.* 81 (2005) 303–306.
- 3030 [210] A. Terekhin, V. Ladygin, Y. Gurchin, A. Isupov, A. Kurilkin, P. Kurilkin, N. Ladygina, S. Piyadin,  
3031 S. Reznikov, A. Khrenov, Differential Cross Section for Elastic Deuteron–Proton Scattering at the  
3032 Energy of 700 MeV per Nucleon, *Phys. Atom. Nucl.* 80 (6) (2017) 1061–1072.
- 3033 [211] A. Terekhin, et al., The differential cross section in deuteron-proton elastic scattering at 500, 750  
3034 and 900 MeV/nucleon, *Eur. Phys. J. A* 55 (8) (2019) 129.
- 3035 [212] Y. N. Uzikov, Search for scaling onset in exclusive reactions with the lightest nuclei, *Eur. Phys. J.*  
3036 *A* 52 (8) (2016) 243.
- 3037 [213] P. Kurilkin, et al., Measurement of the vector and tensor analyzing powers for dp- elastic scattering  
3038 at 880 MeV, *Phys. Lett. B* 715 (2012) 61–65.
- 3039 [214] P. Kurilkin, et al., Investigation of the angular dependence of the analyzing powers in the deuteron-  
3040 proton elastic scattering at the nuclotron, *Phys. Part. Nucl. Lett.* 8 (2011) 1081–1083.
- 3041 [215] A. D. Kovalenko, Y. N. Filatov, A. M. Kondratenko, M. A. Kondratenko, V. A. Mikhaylov, Polar-  
3042 ized deuterons and protons at nica@jinr, *Physics of Particles and Nuclei* 45 (1) (2014) 325–326.
- 3043 [216] A. Kovalenko, et al., The nica facility in polarized proton operation mode, IPAC11, San Sebastian,  
3044 Spain, 4-9 Sept, TUPZ004 .
- 3045 [217] Y. S. Derbenev, et al., Spin-flipping systems for storage rings, Proceedings of XIV Advanced  
3046 Research Workshop on High Energy Spin Physics (DSPIN-11) (2011) 377–384.

- 3047 [218] A. D. Kovalenko, A. V. Butenko, V. D. Kekelidze, V. A. Mikhaylov, A. M. Kondratenko, M. A.  
3048 Kondratenko, Y. N. Filatov, Nica facility in polarized proton and deuteron mode, *International*  
3049 *Journal of Modern Physics: Conference Series* 40 (2016) 1660096.  
3050 URL <https://doi.org/10.1142/S201019451660096X>
- 3051 [219] Y. N. Filatov, A. D. Kovalenko, A. V. Butenko, A. M. Kondratenko, M. A. Kondratenko, V. A.  
3052 Mikhaylov, Polarized proton beam acceleration at the nuclotron with the use of the solenoid  
3053 siberian snake, *Physics of Particles and Nuclei* 45 (1) (2014) 262–264.  
3054 URL <https://doi.org/10.1134/S1063779614010274>
- 3055 [220] Y. Filatov, et al., Orbital parameters of proton beam in nuclotron with solenoid siberian snake,  
3056 *Proceedings of XV Advanced Research Workshop on High Energy Spin Physics (DSPIN-13)*  
3057 (2013) 371–374.
- 3058 [221] A. D. Kovalenko, A. V. Butenko, V. D. Kekelidze, V. A. Mikhaylov, M. A. Kondratenko, A. M.  
3059 Kondratenko, Y. N. Filatov, Numerical calculation of ion polarization in the nica collider, *Journal*  
3060 *of Physics: Conference Series* 678 (1) (2016) 012023.  
3061 URL <http://stacks.iop.org/1742-6596/678/i=1/a=012023>
- 3062 [222] A. D. Kovalenko, A. V. Butenko, V. A. Mikhaylov, M. A. Kondratenko, A. M. Kondratenko, Y. N.  
3063 Filatov, Spin transparency mode in the nica collider with solenoid siberian snakes for proton and  
3064 deuteron beam, *Journal of Physics: Conference Series* 938 (1) (2017) 012025.  
3065 URL <http://stacks.iop.org/1742-6596/938/i=1/a=012025>
- 3066 [223] A. D. Kovalenko, A. V. Butenko, V. A. Mikhaylov, M. A. Kondratenko, A. M. Kondratenko,  
3067 Y. N. Filatov, Acceleration of polarized protons up to 3.4 gev/c in the nuclotron at jinr, *Journal of*  
3068 *Physics: Conference Series* 938 (1) (2017) 012018.  
3069 URL <http://stacks.iop.org/1742-6596/938/i=1/a=012018>
- 3070 [224] G. S. Atoian, V. V. Issakov, O. V. Karavichev, T. L. Karavicheva, A. A. Poblaguev, M. E. Zeller,  
3071 *Development of Shashlyk calorimeter for KOPIO*, *Nucl. Instrum. Meth. A* 531 (2004) 467–480.
- 3072 [225] <https://afi.jinr.ru/ADC64>.
- 3073 [226] <http://hvsys.ru/>.
- 3074 [227] V. M. Abazov, G. D. Alexeev, Y. I. Davydov, V. L. Malyshev, V. V. Tokmenin, A. A. Piskun,  
3075 *Comparative analysis of the performance characteristics of mini-drift tubes with different design*,  
3076 *Instruments and Experimental Techniques* 53 (3) (2010) 356–361.
- 3077 [228] V. M. Abazov, G. D. Alexeev, Y. I. Davydov, V. L. Malyshev, A. A. Piskun, V. V. Tokmenin,  
3078 *Coordinate accuracy of mini-drift tubes in detection of an induced signal*, *Instruments and Exper-*  
3079 *imental Techniques* 53 (5) (2010) 648–652.
- 3080 [229] V. M. Abazov, et al., *The Muon system of the run II D0 detector*, *Nucl. Instrum. Meth. A* 552  
3081 (2005) 372–398.
- 3082 [230] P. Abbon, et al., *The COMPASS experiment at CERN*, *Nucl. Instrum. Meth. A* 577 (2007) 455–  
3083 518.
- 3084 [231] G. D. Alekseev, M. A. Baturitsky, O. V. Dvornikov, A. I. Khokhlov, V. A. Mikhailov, I. A. Odnok-  
3085 loubov, V. V. Tokmenin, *The eight-channel ASIC bipolar transresistance amplifier DOM AMPL-*  
3086 *8.3*, *Nucl. Instrum. Meth. A* 462 (2001) 494–505.

- 3087 [232] G. Alexeev, M. Baturitsky, O. Dvornikov, V. Mikhailov, I. Odnokloubov, V. Tokmenin, The eight-  
3088 channel fast comparator iclthe research described in this publication was partly funded by award  
3089 no. rp1-189 of the us civilian research and development foundation for the independent states of  
3090 the former soviet union (crdf).1, Nuclear Instruments and Methods in Physics Research Section  
3091 A: Accelerators, Spectrometers, Detectors and Associated Equipment 423 (1) (1999) 157 – 162.  
3092 URL <http://www.sciencedirect.com/science/article/pii/S0168900298011851>
- 3093 [233] G. D. Alekseev, M. A. Baturitsky, O. V. Dvornikov, A. I. Khokhlov, V. A. Mikhailov, I. A. Odnok-  
3094 loubov, A. A. Shishkin, V. V. Tokmenin, S. F. Zhirikov, The D0 forward angle muon system  
3095 front-end electronics design, Nucl. Instrum. Meth. A473 (2001) 269–282.
- 3096 [234] Hamamatsu S12572-010P Datasheet.  
3097 URL <http://www.hamamatsu.com/jp/en/S12572-010P.html>
- 3098 [235] A.V.Tishevsky et al., talk at ICAPP2020, submitted to J.Phys.:Conf.Ser.
- 3099 [236] I. G. Alekseev, et al., RHIC p C CNl polarimeter: Experimental setup and physics results, AIP  
3100 Conf. Proc. 675 (2003) 812–816, [,812(2003)].
- 3101 [237] S. Trentalange, talk "STAR Spin Analysis Update", 2004 .
- 3102 [238] D. L. Adams, et al., Comparison of spin asymmetries and cross-sections in pi0 production by 200  
3103 GeV polarized anti-protons and protons, Phys. Lett. B261 (1991) 201–206.
- 3104 [239] D. L. Adams, et al., Analyzing power in inclusive pi+ and pi- production at high x(F) with a  
3105 200-GeV polarized proton beam, Phys. Lett. B264 (1991) 462–466.
- 3106 [240] C. E. Allgower, et al., Measurement of analyzing powers of pi+ and pi- produced on a hydrogen  
3107 and a carbon target with a 22-GeV/c incident polarized proton beam, Phys. Rev. D65 (2002)  
3108 092008.
- 3109 [241] A. Adare, et al., Inclusive cross section and single transverse spin asymmetry for very forward  
3110 neutron production in polarized p+p collisions at s=200 GeV, Phys. Rev. D88 (3) (2013) 032006.
- 3111 [242] B. Z. Kopeliovich, I. K. Potashnikova, I. Schmidt, J. Soffer, Single transverse spin asymmetry of  
3112 forward neutrons, Phys. Rev. D84 (2011) 114012.
- 3113 [243] C. Adler, A. Denisov, E. Garcia, M. J. Murray, H. Strobele, S. N. White, The RHIC zero degree  
3114 calorimeter, Nucl. Instrum. Meth. A470 (2001) 488–499.
- 3115 [244] D. Steffen, et al., Overview and Future Developments of the intelligent, FPGA-based DAQ (iF-  
3116 DAQ) of COMPASS, PoS ICHEP2016 (2016) 912.
- 3117 [245] M. Bodlak, V. Frolov, V. Jary, S. Huber, I. Konorov, D. Levit, J. Novy, R. Salac, M. Virius, De-  
3118 velopment of new data acquisition system for compass experiment, Nuclear and Particle Physics  
3119 Proceedings 273-275 (2016) 976 – 981, 37th International Conference on High Energy Physics  
3120 (ICHEP).
- 3121 [246] I. Konorov, Data acquisition system for the spin physics detector, 2018 .
- 3122 [247] M. Kavatsyuk, E. Guliyev, P. Lemmens, H. Löhner, G. Tambave, VHDL implementation of  
3123 feature-extraction algorithm for the PANDA electromagnetic calorimeter, in: 2010 IEEE Nuclear  
3124 Science Symposium, Medical Imaging Conference, and 17th Room Temperature Semiconductor  
3125 Detectors Workshop, 2010, pp. 785–788.

- 3126 [248] M.Ziembicki, Workshop feetdaq2019, munchen 11–13 feb 2019, [https://indico.cern.ch/](https://indico.cern.ch/event/783347)  
3127 event/783347 .
- 3128 [249] M.Suchenek, Workshop feetdaq2019, munchen 11–13 feb 2019, [https://indico.cern.ch/](https://indico.cern.ch/event/783347)  
3129 event/783347 .
- 3130 [250] I.Konorov, Workshop feetdaq2019, munchen 11–13 feb 2019, [https://indico.cern.ch/](https://indico.cern.ch/event/783347)  
3131 event/783347 .
- 3132 [251] I.Konorov, Compass front-end, trigger and daq workshop, cern 02–03 march 2020, [https://](https://indico.cern.ch/event/863068/)  
3133 [indico.cern.ch/event/863068/](https://indico.cern.ch/event/863068/) .
- 3134 [252] B.M.Veit, COMPASS Front-End, Trigger and DAQ Workshop, CERN 02–03 March 2020,  
3135 <https://indico.cern.ch/event/863068/> .
- 3136 [253] S.Huber, Compass front-end, trigger and daq workshop, cern 02–03 march 2020, [https://](https://indico.cern.ch/event/863068/)  
3137 [indico.cern.ch/event/863068/](https://indico.cern.ch/event/863068/) .
- 3138 [254] V.Frolov, Compass front-end, trigger and daq workshop, cern 02–03 march 2020, [https://](https://indico.cern.ch/event/863068/)  
3139 [indico.cern.ch/event/863068/](https://indico.cern.ch/event/863068/) .
- 3140 [255] C. Ghabrous Larrea, K. Harder, D. Newbold, D. Sankey, A. Rose, A. Thea, T. Williams, IPbus: a  
3141 flexible Ethernet-based control system for xTCA hardware, JINST 10 (02) (2015) C02019.
- 3142 [256] D. Gaisbauer, Y. Bai, S. Huber, I. Konorov, D. Levit, S. Paul, D. Steffen, Unified communication  
3143 framework, in: 20th IEEE-NPSS Real Time Conference, 2016.
- 3144 [257] J. Serrano, P. Alvarez, M. Cattin, E. Garcia Cota, J. Lewis, P. Moreira, T. Wlostowski, G. Gaderer,  
3145 P. Loschmidt, J. Dedic, R. Bär, T. Fleck, M. Kreider, C. Prados, S. Rauch, The White Rabbit  
3146 Project, Tech. Rep. CERN-ATS-2009-096, CERN, Geneva (Nov 2009).  
3147 URL <https://cds.cern.ch/record/1215571>
- 3148 [258] White Rabbit .  
3149 URL <https://ohwr.org/project/white-rabbit>
- 3150 [259] I. Konorov, L. Schmitt, B. Grube, Compass tcs documentation, compass note, date: 20 june 2001  
3151 .
- 3152 [260] D. Baranov, S. Mitsyn, P. Goncharov, G. Ososkov, The Particle Track Reconstruction based on  
3153 deep Neural networks, EPJ Web Conf. 214 (2019) 06018.
- 3154 [261] G. Ososkov, et al., Tracking on the BESIII CGEM inner detector using deep learning, Computer  
3155 Research and Modeling 10 (20) 1–24.
- 3156 [262] F. B. Megino, et al., PanDA: Evolution and Recent Trends in LHC Computing, Procedia Comput.  
3157 Sci. 66 (2015) 439–447.
- 3158 [263] F. Stagni, A. Tsaregorodtsev, L. Arrabito, A. Sailer, T. Hara, X. Zhang, DIRAC in Large Particle  
3159 Physics Experiments, J. Phys. Conf. Ser. 898 (9) (2017) 092020.
- 3160 [264] M. Barisits, T. Beermann, F. Berghaus, et al., Rucio: Scientific data management., Comput. Softw.  
3161 Big Sci. 3 (2019) 11.
- 3162 [265] A. Frohner, J.-P. Baud, R. M. Garcia Rioja, G. Grosdidier, R. Mollon, D. Smith, P. Tedesco, Data  
3163 management in EGEE, J. Phys. Conf. Ser. 219 (2010) 062012.

- 3164 [266] M. Al-Turany, D. Bertini, R. Karabowicz, D. Kresan, P. Malzacher, T. Stockmanns, F. Uhlig, The  
3165 FairRoot framework, *J. Phys. Conf. Ser.* 396 (2012) 022001.
- 3166 [267] T. Sjostrand, S. Ask, J. R. Christiansen, R. Corke, N. Desai, P. Ilten, S. Mrenna, S. Prestel, C. O.  
3167 Rasmussen, P. Z. Skands, An Introduction to PYTHIA 8.2, *Comput. Phys. Commun.* 191 (2015)  
3168 159–177.
- 3169 [268] B. Andersson, G. Gustafson, B. Nilsson-Almqvist, A Model for Low p(t) Hadronic Reactions,  
3170 with Generalizations to Hadron - Nucleus and Nucleus-Nucleus Collisions, *Nucl. Phys. B* 281  
3171 (1987) 289–309.
- 3172 [269] B. Nilsson-Almqvist, E. Stenlund, Interactions Between Hadrons and Nuclei: The Lund Monte  
3173 Carlo, Fritiof Version 1.6, *Comput. Phys. Commun.* 43 (1987) 387.
- 3174 [270] S. Bass, et al., Microscopic models for ultrarelativistic heavy ion collisions, *Prog. Part. Nucl. Phys.*  
3175 41 (1998) 255–369.
- 3176 [271] M. Bleicher, et al., Relativistic hadron hadron collisions in the ultrarelativistic quantum molecular  
3177 dynamics model, *J. Phys. G* 25 (1999) 1859–1896.
- 3178 [272] S. Agostinelli, et al., GEANT4—a simulation toolkit, *Nucl. Instrum. Meth. A* 506 (2003) 250–303.
- 3179 [273] J. Allison, et al., Geant4 developments and applications, *IEEE Trans. Nucl. Sci.* 53 (2006) 270.
- 3180 [274] J. Allison, et al., Recent developments in Geant4, *Nucl. Instrum. Meth. A* 835 (2016) 186–225.
- 3181 [275] J. Rauch, T. Schlüter, GENFIT — a Generic Track-Fitting Toolkit, *J. Phys. Conf. Ser.* 608 (1)  
3182 (2015) 012042.  
3183 URL <https://github.com/GenFit/GenFit>
- 3184 [276] S. Gorbunov, I. Kisel, Reconstruction of decayed particles based on the kalman filter, Tech. Rep.  
3185 CBM-SOFT-note-2007-003, CBM Collaboration (2007).
- 3186 [277] M. Al-Turany, et al., ALFA: The new ALICE-FAIR software framework, *J. Phys. Conf. Ser.*  
3187 664 (7) (2015) 072001.
- 3188 [278] Key4hep software.  
3189 URL <https://key4hep.github.io/key4hep-doc/index.html>
- 3190 [279] Offline framework for the spd experiment.  
3191 URL <https://git.jinr.ru/nica/spdroot>
- 3192 [280] A. A. Baldin, I. G. Voloshina, E. E. Perepelkin, R. V. Polyakova, N. S. Rossiyskaya, T. V. Shavrina,  
3193 I. P. Yudin, Numerical simulation of the field distribution produced by the SP-40 magnet of the  
3194 MARUSYA setup and comparison of simulation results with experimental data, *Technical Physics*,  
3195 52 (2007) 1397-1406 .
- 3196 [281] A. A. Baldin, et al., Measurement of the spatial magnetic field distribution of MARUSYA spec-  
3197 trometer, JINR Preprint P13-2006-67 .
- 3198 [282] A. A. Baldin, et al., Magnet for Marusya Experiment, *Phys. Part. Nucl. Lett.* 7 (1 (157)).
- 3199 [283] A. A. Baldin, Polarization Studies at MARUSYA Setup, Proceedings of International Workshop  
3200 "Relativistic Nuclear Physics from Hundreds MeV to TeV, (2008) .

- 3201 [284] A. A. Baldin, et al., Experimental Study of Asymmetries in Inclusive  $\pi^+$ , p, d Spectra in Interac-  
3202 tion of Polarized Protons and Deuterons with Carbon Targets at MARUSYA Setup, JINR Preprint  
3203 P1-2007-180 .
- 3204 [285] I. N. Meshkov, G. V. o. Trubnikov, NICA Technical Desigh Report, Dubna, (2015) .
- 3205 [286] A. N. Sissakian, A. S. Sorin, V. D. Kekelidze, et al., The MultiPurpose Detector – MPD to study  
3206 Heavy Ion Collisions at NICA (Conceptual Design Report), Dubna, (2014) .
- 3207 [287] J. Adam, et al., Determination of the event collision time with the ALICE detector at the LHC,  
3208 Eur. Phys. J. Plus 132 (2) (2017) 99.
- 3209 [288] P. Aurenche, R. Baier, M. Fontannaz, Prompt Photon Production at Colliders, Phys. Rev. D42  
3210 (1990) 1440–1449.
- 3211 [289] M. Bonesini, et al., High Transverse Momentum  $\pi^0$  Production by  $\pi^-$  and  $\pi^+$  on Protons at  
3212 280-GeV/c, Z. Phys. C37 (1987) 39–50.
- 3213 [290] M. Bonesini, et al., Production of High Transverse Momentum Prompt Photons and Neutral Pions  
3214 in Proton Proton Interactions at 280-GeV/c, Z. Phys. C38 (1988) 371.
- 3215 [291] [http://www.jinr.ru/wp-content/uploads/JINR\\_Docs/Regulation\\_for\\_the\\_](http://www.jinr.ru/wp-content/uploads/JINR_Docs/Regulation_for_the_)  
3216 [organization\\_of\\_experiments\\_eng.doc](http://www.jinr.ru/wp-content/uploads/JINR_Docs/Regulation_for_the_organization_of_experiments_eng.doc) .